Estimation of blood velocity vectors using ultrasound

Munk, Peter

Publication date:
2000

Document Version
Publisher's PDF, also known as Version of record

Estimation of Blood Velocity Vectors using Ultrasound

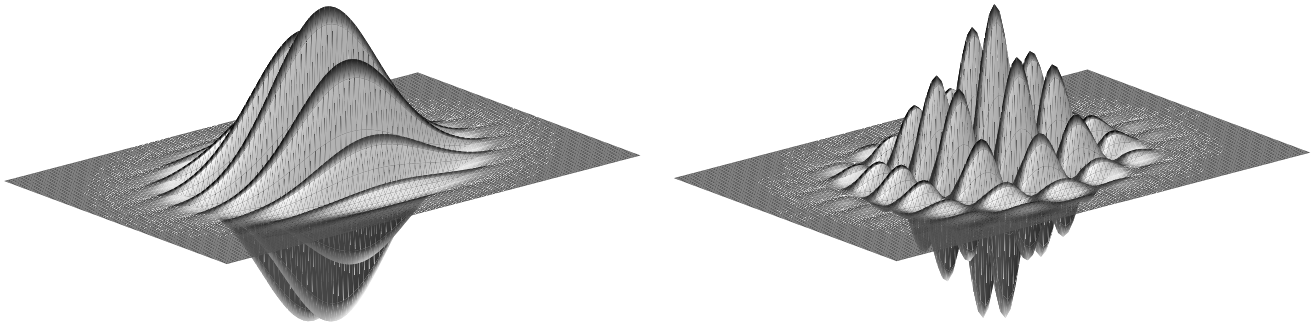

Peter Munk

Februar 29, 2000

Industrial partner:
B-K Medical A/S, Sandtoften 9,
DK-2820 Gentofte, Denmark.

University Department:
Oersted DTU
Bldg. 348, Technical University of Denmark
DK-2800 Kgs. Lyngby, Denmark.

This dissertation is submitted as a partial fulfillment of the requirements for obtaining the Ph.D. degree at the Technical University of Denmark, DTU.

Resumé (Abstract in Danish)

Dette Ph.D. projekt blev udført ved Institut for Informationsteknologi, Danmarks Tekniske Universitet(IT, DTU). Målsætningen for projektet var at udvikle en ny metode til måling af hastighedsvektorer. Den grundlæggende ide bag metoden er generel anvendelig, hvor bølger reflekteres af bevægende objekter, og det tilbagespredte felt registreres på et array af transducere.

Dette arbejde er rettet mod estimering af blodflow v.h.a. ultralyd. Kommercielt tilgængelige medicinske ultralydskannere har en grundlæggende begrænsning ved estimering af blodflow. Den anvendte metode tillader kun måling af en hastighedskomponent. Denne komponent måles parallelt med udbredelsesretningen af den udsendte akustiske puls. I det tilfælde, hvor udbredelsesretning og flowretning ikke er parallelle, er den estimerede hastighed lig prikproduktet af de to vektorer, dvs. projektionen af hastighedsvektoren på vektoren parallel med udbredelsesretningen. Det betyder, at hastighedsestimatet vil være vinkelafhængigt, og derfor vil der ikke registreres noget flow, hvis udbredelsesvektoren og flowvektoren er ortogonale.
Formålet med dette arbejde var, at eliminere denne begrænsning ved at udvikle en metode til måling af vektorielle bevægelser, som er brugbar for kommercielle medicinske ultralydskannere. Den nye metode måler blodflow uafhængigt af vinklen mellem flowretning og udbredelsesretningen. Hermed bliver det muligt at måle flow i blodkar parallelt med hudoverfladen, hvilket er hovedparten af kar i den menneskelige krop. Desuden vil det være muligt af afbilde turbulent flow kvantitativt i modsætning til nuværende kvalitative metoder, såsom varians af den estimerede middelhastighed. Herved introducerer denne nye metode mulighed for en mere korrekt og forbedret diagnose af (kardio)vaskulære tilstande i det menneskelige flow system.
Den nye metode er baseret på betragtninger vedr. den akustiske målesituation, og grundlaget for at kunne estimere hastighedsvektoren er et specielt akustisk puls-ekko felt. For at skabe dette specielle felt, skal der anvendes en array transducer og en beamformer. Desuden skal beamformeren være istand til at processere flere linier parallelt, hvis retningen (højre/venstre) af hastigheden skal bestemmes.

I den traditionelle målesituation anvendes et puls-ekko felt med oscillationer i den aksielle retning. Den nye metode er baseret på princippet om transvers spatial modulation, som skabes ved et akustisk felt med spatiale oscillationer vinkelret på den aksielle retning. En transvers retning skal bruges for at estimere 2D vektorer, og to transverse retninger for 3D vektorer. Alle retninger skal være ortogonale. På samme måde som det traditionelle pulsede Doppler flow målesystem, skabes informationen til brug for hastighedsestimation ved at udsende et antal akustiske pulser i samme retning. Denne fremgangsmåde gør det muligt, at registrere flytningen fra skud til skud, som sammen med tiden mellem de enkelte skud gør det muligt at beregne hastigheden i denne retning. Et puls-ekko felt med både aksielle og transverse

oscillationer forårsager, at signalet til hastighedsestimering vil være påvirket af bevægelse i den aksielle og den transverse retning. Den transverse modulation kan genereres ved brug af en traditionel 'delay-and-sum' beamformer. For at skabe denne transverse oscillation er det nødvendigt med en speciel apodiserings- og fokuseringsopsætning af beamformeren. I dette projekt er metoden behandlet for 2D målesituationen, men den kan umiddelbart udbygges til måling af 3D vektorer, idet signalerne til brug for estimering af 2D vektorer i to ortogonale planer, (x, z) og (y, z), kan beamformes parallelt og uafhængigt af hinanden.

I et forsøg på at finde en optimeret apodiserings- og fokuseringsopsætning blev en ny metode til planbølge dekomposition udviklet. Metoden knytter et ønsket akustisk felt med den tilhørende opsætning af beamformeren og er baseret på pulseret planbølge dekomposition af det akustiske felt. De plane bølger kan propageres til det akustiske apertur, og den komplekse opsætning af beamformeren kan beregnes. Denne metode giver en præcis relation mellem beamformeropsætningen og det tilhørende akustiske felt, og udgør dermed et godt værktøj til design af et nyt akustisk felt. Den beregnede beamformeropsætning til vektor flow metoden er brugt til at validere en tilnærmelse, som gennemgående er anvendt i projektet. På grundlag af denne tilnærmede opsætning af beamformeren, er der udviklet en metode til at skabe og kontrollere det transverse oscillerende felt dynamisk som funktion af dybden. Med denne opsætning for den akustiske målesituation, blev signaler genereret af reflektorer i bevægelse i det akustiske felt og anvendt til at evaluere nye 2D estimatorer.

Det er valideret, at den transverse oscillerende egenskab ved det akustiske felt kan bruges til at estimere den transverse flowkomponent. Sammenlignet med tidligere resultater er standardafvigelsen reduceret med en faktor 4-5 og den transverse strålebredde er reduceret med en faktor 6. Det er generelt for alle resultater, at standard afvigelsen for den transverse hastighedskomponent er større end standard afvigelsen for den aksielle hastighedskomponent. Der er præsenteret resultater for simuleringer med Field II og målinger foretaget med en svamp i bevægelse, der emulerer et speckle genererende medium. Desuden er effekten af dynamisk modulation demonstreret.
Som et biprodukt, ved at arbejde med 2D signaler og estimatorer, opstod der en ny ide til estimering af den aksielle hastighedskomponent. Ideen er baseret på 2D-FFT og Radon transformation. Resultaterne er opnået v.h.a. 3D simuleringer med Field II og viser en forbedring af standardafvigelsen på middelestimatet på en faktor 4 i forhold til den traditionelle autokorrelationsmetode.

Abstract

This work was carried out as a Ph.D. project at the Department of Information Technology, Technical University of Denmark (IT, DTU). The objective of the work was to develop a new method to evaluate flow by estimation of velocity vectors. The idea behind the method is generally applicable where waves interact with moving objects and the scattered field is monitored by a transducer array.
The work is directed towards estimation of blood flow using ultrasound. Commercially available medical ultrasound scanners have a basic limitation in doing blood flow estimation. The applied method allows only one component of the velocity vector to be measured. The component is measured in the direction parallel to the propagation direction (axial) of the emitted acoustic pulse. In case the propagation vector and the flow vector are not parallel, the estimated velocity is the dot product of the two vectors, *i.e.* the projection of the velocity vector onto the vector of the propagation direction. Thus, the estimated velocity will show an angle dependence, and therefore no flow will be detected, if the propagation vector and the flow vector are perpendicular.
The purpose of this work was to eliminate this limitation by developing a method to measure the vectorial movement applicable for commercial medical ultrasound scanners. The new method measures the blood flow independently of the angle between the flow direction and the propagation direction. With this degree of freedom it is possible to measure flow in vessels parallel to the skin surface, which is the case for a major part of vessels in the human body. Also, it will be possible to depict turbulent flow in a quantitative way compared to present qualitative methods such as variance of the estimated mean velocity. Thus, the new method introduces a significant improvement for correct and improved diagnosis of cardiovascular conditions in the human circulatory system.
The new method is founded on considerations of the acoustic measurement situation, and the basis for estimating the velocity vector is created by a special pulse-echo acoustic field. To make the special acoustic field, an array transducer and a beamformer are needed. Furthermore, the capability of parallel beamforming is required to estimate the transverse direction (left/right) of the velocity vector.

The traditional measurement situation has a pulse-echo field with oscillations in the axial direction. The new method is based on the principle of transverse spatial modulation, which is created by a pulse-echo field with spatial oscillations perpendicular to the axial direction. One transverse direction is required for estimation of 2D velocity vectors, and two transverse directions for the 3D vector. All directions are perpendicular. Like a traditional pulsed Doppler flow measurement system, the information used to estimate the velocity is obtained by emitting a number of acoustic pulses in one direction. This approach allows the inter-pulse movement for this specific direction to be recorded and the velocity to be estimated based on the movement and the time between pulses. Having a pulse-echo field with both axial and transverse oscillations, makes the signal for velocity estimation influ-

enced by motion in the axial and transverse directions. Such a transverse modulation can be generated by a traditional delay-and-sum beamformer. The setup of the beamformer needed to generate transverse oscillations is given by a special apodization- and focusing-scheme. In this work the method is evaluated for the 2D case, but it is straight forward extendable to measurement of the 3D-velocity vector, since the signals used to estimate the 2D vectors in the two orthogonal planes can be beamformed in parallel and independently of each other.

In the effort to evaluate an optimized apodization and delay scheme to create the desired acoustic field, a new approach to plane wave decomposition was developed. A method, that relates a desired acoustic field and the associated beamformer setup, is presented. The method is based on a pulsed plane wave decomposition of an acoustic field. The plane waves can be propagated to the acoustic aperture and a complex setup for the beamformer can be calculated. This method gives a precise relation between the beamformer setup and the desired acoustic field, making it a powerful tool in the process of designing a new acoustic field. The calculated beamformer setup given by this method is used to validate an approximation to be used through out this work. Based on an approximated method for calculating the beamformer setup, an approach for creating and controlling such a transverse oscillating field dynamically as a function of depth, is developed. With this setup for the acoustic measurement situation, the signals generated by scatterers moving in the acoustic field were used to evaluate new 2D velocity estimators. The work includes both simulated results using Field II, and experimental results based on measurements performed in a water tank using an array transducer and a moving scattering object. The simulation tool is used to develop the acoustic fields and to evaluate the initial performance of the proposed estimators under controlled conditions. The measurements are used to validate the correct control of the acoustic probing field and the final performance of the velocity estimators.

It is validated that the transverse oscillating nature of the acoustic field can be used to estimate the transverse velocity component. Compared to previous work, the standard deviation on the transverse velocity component is reduced by a factor of 3-4 and the transversal beamwidth has been reduced by a factor of 6. For all situations considered, the standard deviation on the transverse velocity component is larger than the standard deviation on the estimate of the axial velocity component. Results are shown for simulations of flow using Field II and for measurements using a moving sponge as a speckle generating medium. The effect of dynamic control of the transverse modulation period is presented.
As a spin-off, working with 2D-signals and estimators, a new idea for an improved estimator for the axial velocity component arouse. The presented idea is based on a 2D-FFT and a Radon transform. The results obtained by 3D-simulations with Field II show an improvement on the standard deviation of the mean estimate of a factor of 4 as compared to the traditional autocorrelation method.

Acknowledgement

I would like to thank my main advisor, Jørgen Arendt Jensen, and B-K Medical A/S for setting up this opportunity to obtain a Ph.D. degree and to express my great pleasure of doing this project. A long term dream and a goal for my professional life have been fulfilled. Scientifically, the project was initiated by an idea patented by Jørgen Arendt Jensen, with whom I share the interest for ultrasound and signal processing, and the wish to improve present performance of ultrasound scanners. Financially, I would like to thank B-K Medical A/S and the Danish Academy of Technical Sciences (ATV) for providing financial support. The project would not have been possible without the in kind and patient involvement and support of B-K Medical A/S.
I would like to thank my advisors in steering committee

- Jørgen Arendt Jensen for being very inspiring by his enthusiasm for ultrasound in specific and science in general, for letting me work independently, for many fruitful scientific discussions and for giving me some rules of life with respect to academic work. Also for creating a good atmosphere in the CFU group both on a daily basis and through social arrangements.

- Villy Brænder for always having the time to deal with my problems in a trust-worthy and fair manner. His view on human relations is an inspiration to me.

- Ole Trier Andersen for careful proof-reading on papers and my dissertation, and good advises based on his long term employment at DTU.

I would also like to thank past and present colleagues at Oersted•DTU, in particular

- Søren Kragh Jespersen, my great former office colleague, for valuable discussions on acoustics and signal processing, and for his willingness to help me out on computer problems, especially with MATLAB and Linux.

- Jens Wilhjelm for sharing his knowledge of MATLAB and ultrasound in many discussions on a daily basis.

- Malene Schlaikjer for being a good office colleague always supportive and willing to discuss, give suggestions and help out on daily problems, especially, with MATLAB, Linux and Latex, and for proof-reading my dissertation.

- Thanassis Misaridis, for proof-reading my dissertation, dealing with MATLAB issues, and for many inspiring discussions on technical and non-technical issues.

- Svetoslav Nikolov, for helping on all sorts of computer related problems with Linux, MATLAB, Lyx and Latex, and for proof-reading my dissertation.

- Kim Gammelmark for helping out on graphical problems with MATLAB.

- Henrik Laursen for computer support related to Linux and Unix.
- Benny Johansen for computer support related to Windows NT.

I would like to thank people for making my stay at Duke a pleasure, especially

- Gregg Trahey for his hospitality and for making my stay at Duke possible giving me an opportunity to obtain real-time experimental data necessary for my work.
- Martin E. Anderson for being a great colleague helping me to obtain the experimental data. Without his experience and his assistance in handling the experimental Duke scanner, it would not have been possible to evaluate the project on the basis of experimental data. Also for his and his wife Rachel's hospitality which contributed to making it a great stay.
- Bob McGough for being a new good friend that made my stay a personal pleasant experience.
- Stephan Baumann for being a new good friend and room made that made my daily life easy and enjoyable.

I would also like to thank my friends

- Bjarne Stage for being a source of inspiration to me many years ago, which, non-intentionally, made me pursue a Ph.D. degree and for his valuable encouragements, advises and discussions, and finally for proof-reading my dissertation.
- Frans Hansen and Henrik Munk for finding the time to deal with problems related to the graphical layout.

Finally, but not least, my life companion Sandra is highly appreciated for her patience and support throughout the whole period. We have lost so much time together on behalf of my ambitions. One day, I hope to be able to give what she did.

Preface

The impetus for this project is based on the results obtained during the fulfillment of a M.Sc. project, carried out at the Department of Information Technology, DTU, in the autumn 1995. By simulation it was basically proven that acoustic transverse modulation could create signals sensitive to transverse movement and thereby making it possible to estimate flow vectors. The results obtained, were based on a estimation scheme with a high variance, up to 30 % of the pure lateral mean velocity component, and an acoustic field with a large lateral extension, approximately 30 mm with a center frequency of 3 MHz, both not applicable for commercial use. The estimation was performed with 50 lines per estimate. The ability to measure velocity vectors has a commercial aspect by the interest of B-K Medical A/S, a Danish manufacturer of medical ultrasound scanners, to exploit the idea for blood flow imaging. Based on the preliminary results documented in the M.Sc. thesis, this Ph.D. project was established as a collaboration between B-K Medical A/S, as a company partner, and with the Department of Information Technology, Technical University of Denmark (DTU) as the academic institution. This research collaboration is enabled through a program managed by the Danish Academy of Technical Sciences (ATV), which is established in order to create a fruitful sphere for collaboration between industry and academics within the Ph.D. programe in Denmark. Therefore, this project has been sponsored by B-K Medical A/S and ATV.
The study was initiated in September 1996. The study plan is described in details in [Mun97]. In summary the tentative plan was to

- Investigate improved acoustic properties of the modulation field in order to make the method commercially feasible, *i.e.*, smaller acoustic sample volume.
- Develop a method to evaluate an optimized setup of the beamformer for the transverse oscillating acoustic pulse-echo field
- Develop new 2-D estimators, which calculate the axial and the transverse component of the velocity vector independent of each other and with a reduced variance compared to previous results.
- Stay at Duke University, North Carolina, USA, for a period of 6 months, to obtain experimental data to verify the results found by simulations, and to exchange ideas and discuss ultrasound in general, in specific learn more about speckle and K-space.
- Evaluate the new acoustic modulation field and the developed estimators based on simulated and experimental data.
- Make the initial attemps to implement the estimation scheme on a new digital scanner from B-K Medical A/S.
- Finally, draw up the dissertation.

This plan was, as plans often are, exposed to changes. The development of new estimators was more tricky and time consuming than expected. The extension of the time schedule for this part of the project was compensated by the planned implementation period. The implementation on the hardware did not become possible during the study period. The project for the development of a digital scanner at B-K Medical A/S has been delayed, and the status, at July 1999, did not allow any special programming of the hardware, especially for the beamformer, to be made. The foundation to implement the new feature, is though present, making it possible to handle the special case of vector flow on the scanner in the future. A special slot with the appropiate data connection is allocated for an optional future PCB-board specifically for vector flow estimation. Software wise the database system has been prepared to handle setup parameters for the transverse flow, thus making it possible to pass data to the intermediate RTSC[1] software layer between the application software and the hardware. It is verified that optional software in the RTSC layer can be implemented in order to control the beamformer setup for vector flow.
As a step to have an intermediate independent hardware platform to investigate and develop specific algorithms for transverse flow, a M.Sc. project was initiated in March 1999 and handed in November 1999. The project, on which I functioned as a co-advisor, defines a hardware interface which enables data transfer at the maximum data rate possible for the new scanner to a high performance PCI signal processing board (TI, TMS320C6701). The interface is based on a FPGA and a memory bank. The FPGA is able to decode the active status of the ultrasound scanner and handle the data stream to an output format which is properly organized for further processing on the TI board. Taking the steps described, charts a good course for future work on the final commercial development of this new flow imaging modality.

Publications

During the study I have authored or co-authored a number of conference and journal publications as listed below:

- Jørgen Arendt Jensen, Claus Buelund, Allan Jørgensen and **Peter Munk**: Estimation of the blood velocity spectrum using a recursive lattice filter , IEEE Ultrasonics Symposium Proceedings, November, 1996.
- Jørgen Arendt Jensen and **Peter Munk**: Computer phantoms for simulating ultrasound B-mode and CFM-images, Acoustical Imaging, Vol. 23, pp. 75-80, 1997.
- Jørgen Arendt Jensen and **Peter Munk**: A New Method for Estimation of Velocity Vectors, IEEE Transactions on Ultrasonics, Ferroelectrics and Frequency Control Vol. 45, pp. 837-851, May 1998.
- Jørgen Arendt Jensen and **Peter Munk**: Vector Velocity Estimation using a Single Transducer, 23rd International Symposium on Ultrasonic Imaging and Tissue Characterization, Arlington, VA, U.S.A., June, 1998.
- **Peter Munk** and Jørgen Arendt Jensen: Performance of a vector velocity estimator, IEEE Ultrasonics Symposium Proceedings, October, 1998.

[1] Real Time Scan Control

- **Peter Munk** and Jørgen Arendt Jensen: A new approach for estimation of the axial velocity using ultrasound, Ultrasonics International '99, Technical University of Denmark, Copenhagen, June, 1999
- Jørgen Arendt Jensen and **Peter Munk**: An improved estimation and focusing scheme for vector velocity estimation. IEEE Ultrasonics Symposium Proceedings, October, 1999.

Organization of the dissertation

Finally, an overview of the dissertation is given. To solve the problem, knowledge from several technical disciplines is required. The frame work for this dissertation is based on

- acoustics
- simulation and modeling
- linear systems
- multidimensional signal analysis
- array signal processing

In this project, all these disciplines comes together. The problem is divided in to an acoustical part and a signal processing part.
The acoustical part defines the measurement setup, which creates signals with the velocity vector information encoded. The signal processing part defines the estimation procedure, where the information is decoded to independent velocity estimates of the vector components. The estimation procedures developed are directly related to the measurement situation. In order to evaluate the acoustic measurement situation, a relation between the required pulsed acoustic field and the beamformer setup is needed. This relation can be established through the use of pulsed plane wave decomposition. It turns out that the requirements for the beamformer setup to obtain the 'ideal' field can not be meet by the conventional digital beamformers. The outcome is therefore used as a guideline for an approximation to the beamformer setup. The performance of the acoustical measurement setup is evaluated by both simulations and experimental work. The estimators are then developed based on knowledge of the measurement situation. Several approaches, all along the same path, with increasing complexity are investigated. The performance of the estimators are evaluated by synthetic, simulated and experimental data.
The reader is expected to have knowledge at a technical level corresponding to a M.Sc. familiar with differential equations, acoustics and signal processing in 1D and 2D.
The dissertation is divided into 6 chapters and the outline reflects the process of solving the problem.

- Chapter 1 gives a brief introduction to ultrasonic imaging. Most emphasis is put on the velocity imaging.
- Chapter 2 is a brief review of acoustics. It gives the theoretical background of the methods used for evaluation and understanding of the acoustical requirements associated with the development of the new estimation method. The approximations and limitations introduced, in order to obtain an appropriate description, are pointed out

during the review. Different methods to calculate acoustical fields are presented, and two in specific are worked into some details. This is the FFT approach and the spatial impulse response approach.

- Chapter 3 describes the approach used for flow modeling. It presents the considerations related to the model used for simulations of blood flow in acoustic fields. Stationary and pulsatile flow is presented along with simulation examples. These examples give a visualization of the signal conditions for velocity estimation.

- Chapter 4 describes the traditional 1D flow measurement system. It is a pulsed wave system and its functionality is described on the basis of a simple model. The signal model given, is used for the evaluation of the velocity estimators in the following chapters. The signal created by the movement of an object has a nature that makes it possible to estimate the velocity using an autocorrelation approach. This insight to the actual functionality of a 1D velocity estimation system, gives the seed to the development of new vector velocity estimation methods. Finally a new method to estimate the axial velocity component is presented. The method is based on the 2D-FFT combined with the Radon transform.

- Chapter 5 contains a presentation of the 2D-measurement situation and associated 2D-estimators. Simulation results for different 2-D velocity estimators are used for comparison of performance, and the ability to detect angle and amplitude is demonstrated. The influence of dynamic modulation is also evaluated.

- Chapter 6 summarizes the results.

Table of Contents

List of Figures

List of Tables

List of Acronyms

A-mode	: Amplitude mode
B-mode	: Brigthness mode
CFM	: Color Flow Mapping
CW	: Continuous Wave
DOI	: Depth of Interest
FFT	: Fast Fourier Transform
M-mode	: Motion mode
PSF	: Point Spread Function
PW	: Pulse Wave
RF	: Radio Frequency
ROI	: Region of interest
SNR	: Signal to Noise Ratio
TGC	: Time Gain Control
OF	: Offset of peak in apodization function
ZF	: Depth of interaction

Chapter 1

Introduction

This chapter gives a brief introduction to ultrasonic imaging with the emphasis on velocity imaging. The basic imaging modalities are briefly presented. Basically the term imaging covers display of both structures/morphology and flow. Morphological imaging is very briefly presented followed by a description of velocity imaging with some historical background.

1.1 Basics of ultrasonic imaging

The term ultrasonic imaging covers the whole area in which sound waves above 20 kHz are used to produce image information. The frequency range goes from kHz in the sonar applications to GHz in the microscopy applications. For medical imaging applications the typical applied frequency range is from 1 to 10 MHz, and for special applications, such as intra vascular scannings, frequencies up to 50 MHz are used. From a medical point of view, the use of ultrasonic waves has two major advantages: it is non-ioning and the speed of sound makes real-time imaging feasible. The sound velocity for the human tissue is approximately 1540 $\frac{m}{s}$ making it possible to record 3000 lines per second at a penetration depth of 25 cm. The development within ultrasonic imaging has resulted in three key modalities: intensity mapping, pulse-echo mapping and phase-amplitude techniques. The last item covers the area of holography and tomography. The pulse-echo mapping is the basis for the development of the new velocity estimator described here. Compared to X-ray[1] the ultrasonic signal is reflected at boundaries of very small local difference in acoustic properties defined by density ρ and velocity c, and is therefore an excellent approach towards imaging tissue properties and morphology.

1.2 Ultrasonic morphological imaging

The pulse-echo technique was first applied during World War I in sonar systems. With the scientific development, the technique has emerged to applications within the medical area. The pioneering work within the medical application can be traced back to the early 1950s. The reports at that time demonstrated the possible use of ultrasound to image soft tissue. Originally, the acoustic information was obtained using a piezoelectric transducer held in a stationary position. The result of this measurement was a single signal, a Radio Frequency line (RF-line). This information was displayed as the amplitude detected (envelope) response

[1] X-rays primarily maps the electron density as an intensity and therefore does not contain essential information of the tissue properties and morphology

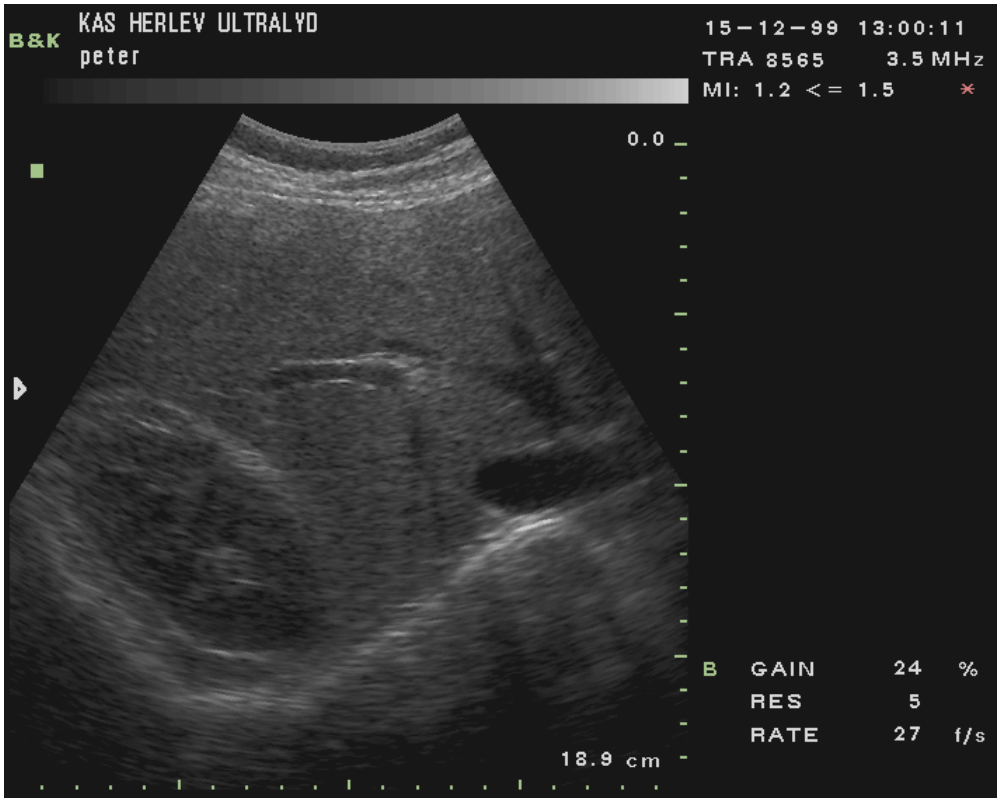

Figure 1.1: B-mode image of liver and kidney. Some veins are observed at the center and the right part of the image.

versus time/depth and was named A-mode (**A**mplitude). The amplitude at a given time reflects the local difference in density and velocity. Observing this line as a function of time results in a new type of display called M-mode (**M**otion). The display is 2D with time as abscissa and gray or color mapped A-mode lines as ordinate. With this display mode, the movement of the scatterers in *one* specific recording direction are shown. Recording lines in a sweep of *different* directions provides the basis for displaying 2D-images. The amplitude response for each line is envelope detected and displayed as a grey level line. The higher the tissue reflectivity at a given depth, the higher grey level for the respective pixel. This type of display is referred to as B-mode (**B**rightness). The change of scanning direction can be obtained by either rotating a single crystal (as used in the early systems) or by electronically steering of a multi-element transducer (a technology that has become available during the last two decades). An example of a B-mode image of the human liver is shown in Figure 1.1. The major liver veins are seen as dark regions and the gray area with a granulate appearance is the tissue. The granulate appearance is related to the phenomenon of speckle which is also known from optics and radar. The kidney is observed as the bean shaped area to the left of the image.

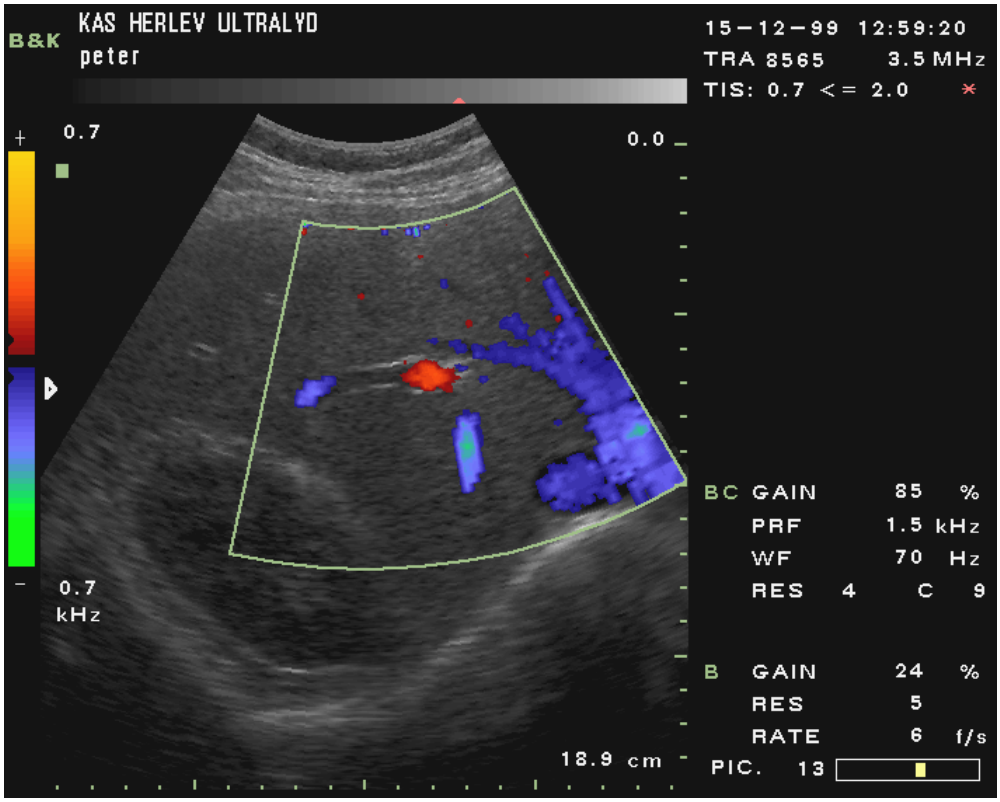

Figure 1.2: B- and CFM-mode image of liver and kidney. The coloring of veins are observed at the center and the right part of the image.

1.3 Ultrasonic velocity imaging

1.3.1 1-D velocity imaging

Like in sonar and radar systems, information on movement of scatterers or objects[2] can be extracted from a measurement situation were waves are applied. This is referred to as the Doppler information and in medical aspects it is used to monitor the blood circulatory system of the human body. Only the pulsed wave system is considered in this section. The signals used for estimation of blood flow originate from much weaker scattering than tissue and consequently the received signals are much weaker. The blood velocity estimation is based on signals originating from the dark regions in Figure 1.1.
Similar to morphological imaging, flow information can be calculated for each imaging direction. Again this is done for a sweep of directions in order to form a 2D-flow image. The estimated velocities in these kind of images are the mean value of the axial velocity distribution in a given sample volume, *i.e.* a small part of the RF-line. Typically, the velocity information is superimposed onto the grey level B-mode image as a color image. This imaging mode is referred to as CFM (**C**olor **F**low **M**apping). The color scale used in CFM can be coded as one pleases, but traditionally the blue/red color mapping is preferred. One color indicates flow away from the transducer and the other flow towards the transducer, and the intensity of the color scales to the magnitude of the axial velocity component. For comparison, the approximate same scanning situation as shown in Figure 1.1 is carried out using the CFM modality and is shown in Figure 1.2

[2]Scatterers are considered to be point-like reflectors with Rayleigh scattering properties and all other reflectors are considered objects.

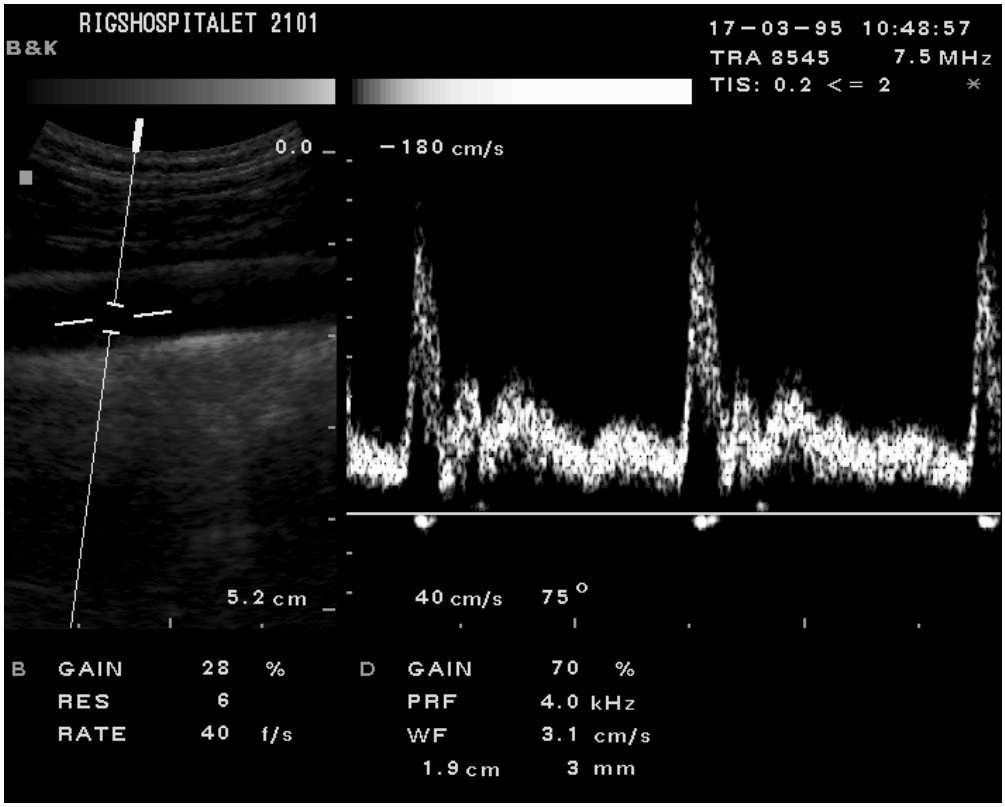

Figure 1.3: Combined B-mode and FFT-Doppler. The anatomy displayed is the carotid artery, and the FFT display of the flow in the artery shows pulsatile characteristics.

If the information represented by the mean flow is not adequate, it is also possible to display the velocity *distribution* within one specific sample volume. This mode is named FFT-Doppler since the frequency content in a demodulated RF-data segment is calculated using the FFT method for frequency estimation, and the frequency distribution relates directly to the velocity distribution in the sample volume through the Doppler equation

$$f_d = \frac{2v_z}{c} f_0 \tag{1.1}$$

where c is the speed of sound, v_z is the axial velocity component, f_0 is the center frequency of the emitted acoustic pulse, and f_d is the frequency of the demodulated data. Thus, the velocity spectrum is determined through a scaling of the FFT estimated spectrum of the demodulated RF-data segment. The velocity spectrum is displayed as a function of time (abscissa) with a grey level or color coded line (ordinate), same display type as M-mode. An example of a combined display mode is shown in Figure 1.3 with a B-mode image on the left side with indication of the interrogation sample volume and the FFT-Doppler result shown to the right.

1.3.2 2D/3D velocity imaging

The area of velocity imaging is subject to continuous research for improvement and development of new measurement methods, as well as estimation and filtering techniques. Within the medical application of ultrasound, the use of blood velocity estimation has become an important part of the daily routine examination. Therefore, the interpretation of the infor-

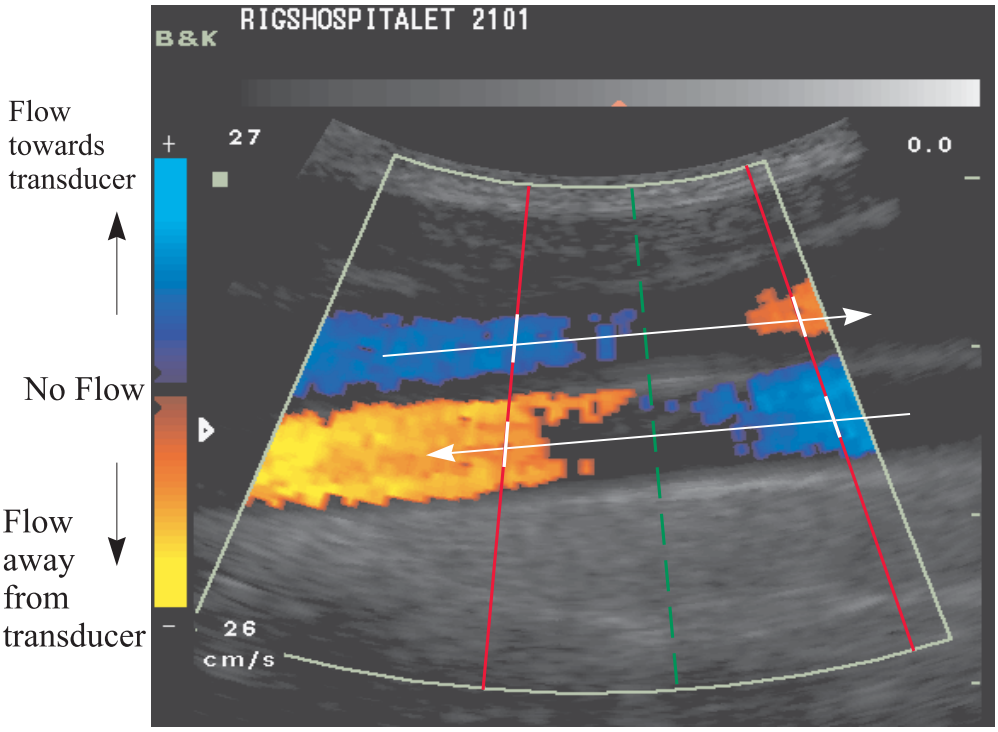

Figure 1.4: Color flow image showing the angle dependence for the used estimation method.

mation is performed by a growing group in the medical environment. Being an every day tool, it results in a less critical use in the technical sense. The qualitative value is beyond dispute, but the quantitative aspect is probably attributed too high a value. There are many factors that influence the final value of a given velocity estimate, and one must be careful in not interpreting the presented information too rigorously.
One factor to be considered is that the conventional systems only measure the speed in the direction of the pulse propagation and not the real velocity[3]. This causes the estimated velocity to be angle dependent. The angle-dependence can be seen in Figure 1.4. The figure shows a color flow image of the carotid artery and the jugular vein scanned with a convex array transducer. The use of a convex array causes the angles between flow direction and the ultrasound beam to change over the image. The sector around the dashed line at a perpendicular angle to the flow has no flow information, and the change of angle between the ultrasound beam and the velocity vector around the dashed line causes a change in estimated flow direction for both the artery and the vein. So quite a different presentation of the same velocity profile is seen as a function of angle.

Since most vessels in the human body are parallel to the skin surface, this angle dependence is a main limitation in current ultrasound flow systems. Being able to estimate the velocity vector in 2-D or 3-D would improve the information quality level and inevitably reduce the number of misinterpretations in flow diagnosis thereby improving the medical science.
The development on flow systems is partly aimed at new ways to estimate the velocity vector. Another very important aspect of flow systems is the separation of tissue and flow signals. This aspect is not taken into consideration in this work.

[3]Velocity by definition is a vector having a amplitude and direction. Throughout the text the term velocity will be used with no distinction between speed and velocity. The term velocity component will be used to distinguish the direction.

The attempt to measure the velocity vector goes back to the seventies based on ideas from optics and lasers. A crossed-beam technique was suggested by Fox [Fox78] with a system using two emitting and one receiving apertures. The velocity vector can then be found through a triangulation scheme. The variance and hence the accuracy of the transverse component of the velocity is affected by the angle between the two beams. The small angle between beams at large depths in tissue results in a high measurement variance, *i.e.* low precision. The use of two transducers or a single large array also makes probing between the ribs of a person difficult, and can result in loss of contact for one of the transducers. A good accuracy was demonstrated in an experiment with a rotating disc. This system could be expanded for 3-D velocity estimation by the use of six transducers. In 1985, Fox presented a new solution for the evaluation of the 2-D vector by use of two transducers. This idea was further developed in 1988 to 3-D velocity estimation [FG88]. A similar system with one transmit and two receive transducers was presented by Overbeck [OB92]. Using this principle a study of the flow dynamics in a vessel branch was done by Tamura [TCJ90]. Two parts of an array have also been used by Fei [FFBK94] giving good results, and several ways of displaying the velocity vector were suggested. This method is preferable because only one transducer is needed. On the basis of an array transducer 2-D velocity reconstruction strategies were examined by Maniatis [MCJ94]. Another method to estimate the velocity is given by Coultard and evolves from the use of flow meters for measurement of flow in accessible tubes, see [Cou73] and [Cou83]. This principle uses parallel acoustic beams and cross correlation. The idea has been used by several authors. Bonnefous [Bon88] suggested the use of a 2D-array transducer configured for operation with one transmit aperture and several receive apertures. By use of the cross-correlation method the lateral displacement can be estimated on the basis of a reconstructed lateral beam. More recently, the principle has been proposed by Hein [Hei93], [Hei95] to estimate the full 3-D velocity vector by the use of a special lens system. The latter confirms, by means of measurements, the results of the first report (where only simulation were used). The results obtained by this method do have a high variance, and there are problems with the lens system that generates the three parallel acoustic beams using three transducers. There are too many reverberations and the signal-to-noise ratio is not good enough to be used to measure real blood flow. Only flow phantoms are applicable at this instant. The drawback of this method is the requirement of several transducers. A different scheme was proposed by Newhouse: estimation of the velocity perpendicular to the acoustic beam by use of only one circular transducer [NCV$^+$87]. This applied method is based on the transit time broadening effect of the spectrum [NBV76]. A general discussion on transverse Doppler is given in [CNVO88]. The case of rectangular aperture is presented in [NCC91] which is supported by experimental studies. Also, a method using two transducers and spectral width is given for estimation of the 3-D velocity vector [NDCC94a]. Another experimental review can be found in [TGGA94]. The concept of 2D speckle tracking has been thoroughly developed by Gregg Trahey's group in numerous publications. Some can be found in [TSvR86], [TAvR87], [THvR88], [WT94].
Despite all these efforts during the past two decades, no commercial scanner available offers the option of estimation of a 2-D velocity vector.
Recently, an approach for estimating the transverse components of the flow vector was presented by Anderson in [And97] and [And98], which suggests to exploit the relation between the time signals in the beamformer and the acoustic sensitivity to create one version of spatial quadrature. The spatial quadrature is created by a special scheme of a Hilbert transform on the time signals in the beamformer. This approach creates, on the basis of a normal focused beamformation, a second beam which in envelope characteristics has an approximate spatial Hilbert relation to the first beam. By the first impression, this method resembles the

approach presented in this work and will be commented in more details.
In general the development of new 2D and 3D velocity estimators will be based on calculation methods with an increasing computational load. As the technology moves on with an incredible escalation in available CPU- and signal-processing power per dollar, the classic limitation given by the hardware performance, will experience a still reduced significance when ideas develop into products. Therefore, the invention and implementation of much more complicated algorithms can be expected in future medical ultrasound systems. The method presented in this work is one example.

Chapter 2

An acoustic foundation

Perception of the measurement situation is of great importance in the development of the estimation approach presented in this work. This chapter gives a description of basic acoustics, and sets up a frame to comprehend the measurement situation created for the estimation of the velocity vector. In this chapter terms and equations related to wave propagation in liquids will be reviewed under certain simplifying assumptions. The assumptions used for the derivation of the homogeneous wave equation are presented. The wave equation can take on many forms depending on the actual problem, and is the essential tool in linear acoustics. It is presented in order to give an understanding for the importance of some basic solutions given by plane and spherical waves, to be used subsequently for this work. As it will be shown later, the measurement situation created to make the estimation of the velocity vector possible, is in principle based on the interference of two waves. The theory of radiation is briefly summarized for three reasons. First, to make the introduction to a more approximative method given by the Fourier relations between the acoustic aperture and the acoustic field. This method is used to evaluate the basic characteristics linking the aperture and the acoustical field. Second, to describe the foundation of Field II, which is the simulation tool used throughout this work. The program uses the spatial impulse response to calculate the acoustical field based on the Rayleigh integral. Third, pinpoint the use of the Fresnel and the Fraunhofer approximations.
Further, a method which decomposes an acoustic field into a set of pulsed plane waves is presented in order to determine an optimal beamformer setup for the estimation of the velocity vector. The use of pulsed plane wave decomposition gives in details a relationship between the acoustic aperture and the acoustic field.
The following introduction to acoustics is based on references to [Pie81], [Sku71], [Kin82] and [MI68], which are excellent books on acoustics.

2.1 Theory of wave propagation

2.1.1 Wave motion

Sound is mechanical waves or vibrations. Waves are disturbances from an equilibrium in an elastic medium. Due to the elasticity of the media, the vibration initiated at one location can travel to more distant parts of the medium. It is the movement of the particles and not the particles themselves that propagates. The time evolution of the disturbance in a given point in space can be decomposed into harmonics by the use of the Fourier transform. These oscillations traveling in space are fundamentally a 4-dimensional (space and time) phenomenon, but also simpler cases exist. For example, the vibrating string can be described by 2 dimensions.
Mechanical waves can be very complicated in their behavior, and in the attempt to describe different acoustic phenomena, several wave modes are introduced. The two most often encountered are shear (transverse) and longitudinal waves. These are the least complex of possible wave modes, and consequently the most simple to describe mathematically. Defining these two kinds of waves involves the propagation direction of the vibration and the particle movement. In case of shear waves, the particle movement is normal to the direction of propagation. For longitudinal waves, the particle movement is parallel to the direction of propagation. Shear waves can only exist if the medium can sustain strain, such as solids. Gases and liquids do not have this ability; they can resist a change in volume but not in shape. The dominant wave mode in liquids and gases is longitudinal waves, which also can exist in solids.
The propagation of elastic waves is subject to certain physical laws. These laws are in the general case non-linear. For liquids, the waves will propagate according to the hydro-dynamic laws and for gases to the aero-dynamic laws. To apply theory in practice, some simplifying assumptions must be introduced. In this context only the propagation in liquids will be treated. The medium must be an ideal liquid which implies no viscosity. As a consequence, only longitudinal[1] waves can exist in ideal liquids.
Many models for ultrasound propagation in tissue assume that the ultrasonic propagation in tissue behaves directly analogous to the relaxational behavior for ultrasonic propagation in aqueous solutions of certain small molecules and biological macromolecules in the range of 0.1 to 10 MHz [Hus75]. This means that the shear viscosity of a liquid is not zero and has the consequence that not only longitudinal, but also shear waves can propagate through the tissue. The latter, known as viscous waves, have a very high absorption coefficient and can therefore be neglected [Bha67].
Acoustic longitudinal waves are cyclic compression and expansion of regions in the medium. The liquid particles are moved back and forth in the direction of propagation of the wave and are thereby producing adjacent regions of compression and decompression due to the elastic properties of the media. Compression causes the pressure to increase in a particular region of the liquid and expansion the pressure to decrease. At a particular spatial point the wave will pass with the propagation speed c and oscillate with the temporal frequency f giving the perceived wavelength of λ. Taking a snapshot at a particular instant, the spatial period (given by the distance between two consecutive maxima/minima) is the wavelength λ. The relation between these three variables is

$$\lambda = \frac{c}{f} = \frac{2\pi c}{\omega} \tag{2.1}$$

[1] Longitudinal waves are also referred to as compressional waves.

where ω is the temporal angular frequency which is related to the frequency by $\omega = 2\pi f$. The direction for the traveling wave is given by the wavenumber vector $\mathbf{k}$, which is the directional spatial frequency. The magnitude is

$$k = |\mathbf{k}| = \frac{2\pi}{\lambda} = \frac{\omega}{c} = \frac{2\pi f}{c} \tag{2.2}$$

The variation of the temporal angular frequency ω, as a function of the wave number magnitude k, is defined as the dispersion relation for the media. In (2.2) the fraction $\frac{\omega}{k}$ is considered constant and the medium is non-dispersive. Dispersive waves occur in dispersive media, which are characterized by different propagation speeds for components with different wavelengths, thus $\frac{\omega}{k}$ is not constant. The feature of dispersive waves can be introduced as a complex wavenumber resulting in a complex propagation velocity.

2.1.2 Equations of linear acoustics

In the following derivation it is assumed that the disturbances are small compared to an ambient state. The ambient state for a fluid can be described by the pressure, density and fluid velocity $(p_0, \rho_0, \mathbf{v}_0)$. Here the velocity is zero and the medium is homogeneous, *i.e.* the ambient quantities are independent of the position. The following approach is often referred to as the linear approximation or the acoustic approximation, and results in the linear acoustic equations. The variables with no subscription denotes the disturbance dynamics. Here p is the acoustic pressure at an arbitrary position in space $\mathbf{s}$, $\mathbf{v}$ is the particle velocity, ρ is the density at an arbitrary position. Three fundamental equations must be considered. The differential equation for conservation of mass in an ideal fluid:

$$\frac{\partial \rho}{\partial t} + \rho_0 \nabla \cdot \mathbf{v} = 0 \tag{2.3}$$

Euler's equation of motion for a fluid:
The general description is complicated. Using the assumption that the fluid is ideal and that the second and higher order terms in the relation between the pressure disturbance and the density disturbance can be neglected, the simplified equation becomes:

$$\rho_0 \frac{\partial \mathbf{v}}{\partial t} = -\nabla p. \tag{2.4}$$

Relation between pressure and density:
The process is assumed adiabatic

$$p = c^2 \rho \tag{2.5}$$

where c is the speed of sound in the medium for longitudinal waves given by

$$c^2 = \left(\frac{\partial p}{\partial \rho} \right) \Big|_o . \tag{2.6}$$

The notation $|_0$ indicates the ambient state.

2.1.3 The wave equation

Pressure

The sound propagation is subject to the physical laws introduced in Section 2.1.2. These laws form the basis for the homogeneous wave equation, which is a good model for sound propagation in liquids. This equation can be derived by a combination of three fundamental equations presented in the previous section. Using equation (2.5) in (2.3) and then differentiating with respect to time, the result becomes

$$\frac{1}{c^2}\frac{\partial p}{\partial t} + \rho_0 \nabla \cdot \mathbf{v} = 0 \tag{2.7}$$

$$\frac{\partial}{\partial t}\left(\frac{1}{c^2}\frac{\partial p}{\partial t} + \rho_0 \nabla \cdot \mathbf{v}\right) = 0 \tag{2.8}$$

$$\frac{1}{c^2}\frac{\partial^2 p}{\partial t^2} + \rho_0 \nabla \cdot \frac{\partial \mathbf{v}}{\partial t} = 0 \tag{2.9}$$

and with (2.4) inserted in (2.9) the result becomes the acoustic wave equation for the pressure function

$$\nabla^2 p - \frac{1}{c^2}\frac{\partial^2 p}{\partial t^2} = 0. \tag{2.10}$$

As a consequence of the applied assumptions, this is the wave equation in its linearized form and it is only valid for a homogeneous medium. The wave equation is a sufficient description of most encountered phenomena observed for wave propagation with small amplitudes in non-moving fluids [MI68].

The velocity potential

The wave equation can also be expressed for one of the others variables ρ or $\mathbf{v}$. If the pressure and the particle velocity must be calculated, two equations must be solved. The wave equation for p or $\mathbf{v}$ can be used with (2.4) to establish the relation between the spatial variation of the pressure and the temporal variation of the particle velocity, *i.e.* the acceleration. The velocity potential $\Phi(\mathbf{s}, t)$ is introduced to simplify the calculations. It is not a physical variable and has no direct physical interpretation, but it can lead to an alternative formulation of the wave equation. To apply the following it is assumed that the acoustic field has no curl *i.e.*

$$\nabla \times \mathbf{v} = \text{const} \equiv 0. \tag{2.11}$$

This condition is satisfied for sound fields under normal circumstances. Then, the relation between Φ and $\mathbf{v}$ is unambiguous and given by

$$\mathbf{v} = \text{grad}\,(\Phi) = \nabla \Phi(\mathbf{s}, t) \tag{2.12}$$

Using (2.4), the pressure is

$$p = -\rho_0 \frac{\partial \Phi(\mathbf{s}, t)}{\partial t}. \tag{2.13}$$

Substituting (2.13) into (2.10) and integrating with respect to time shows that Φ also satisfies the wave equation. The wave equation in terms of Φ takes the form

$$\nabla^2\Phi(\mathbf{s},t) - \frac{1}{c^2}\frac{\partial^2\Phi(\mathbf{s},t)}{\partial t^2} = 0 \tag{2.14}$$

Based on a solution of the velocity potential, p and $\mathbf{v}$ can be calculated using (2.12) and (2.13).
The solutions of the wave equation must refer to a coordinate system. In Appendix A, the notation of three different coordinate systems are given. The coordinate systems are the rectangular, the spherical and the cylindrical.

2.1.4 Simple solutions to the wave equation

The derivation of the wave equation pinpoints the assumptions to be made in order to obtain a fairly simple equation to describe wave propagation. These assumptions must be bared in mind when solutions are evaluated.
Many advanced and complex solutions exist to the wave equation depending on the initial and boundary conditions for the acoustic situation. The conditions reflect the actual acoustical problem and the intended purpose of the acoustic field. This will be illustrated when dealing with radiation problems in Chapter 2.2. Taking no initial or boundary conditions into account, three simple wave fields play a central role in the field of acoustics. It is the plane, the spherical and the cylindrical wave which occur as basic solutions for the wave equation in the respective coordinate systems. Here properties for the plane wave and the spherical wave are considered. In principle a plane wave is characterized by the fact that all acoustic variables are functions of only one spatial component with the proper choice of coordinate system. Thus, the term plane wave has to be associated to a specific coordinate system. Classically, the term plane wave implicitly refer to the rectangular coordinate system. The spherical wave is a plane wave in the spherical coordinate system.
There are two classical ways of solving the wave equation, named d'Lambert's method and Bernoulli's method. The first method presumes that the sound field can be considered as a sum of two wave fields, one converging and one diverging. The latter presumes that the solution to the wave equation can be written as a product of functions that depend on one variable. This method is also referred to as separation of the variables and is a standard method for finding a solution when confronted with a partial differential equation [Han76].

Plane wave

If an observation point is situated at a sufficiently large distance from the wave source, the acoustic field will have plane wave characteristics. If the coordinate system is chosen such that the plane wave propagates parallel to the x-axis, the wave equation reduces to one dimension:

$$\frac{\partial^2\Phi(x,t)}{\partial x^2} = \frac{1}{c^2}\frac{\partial^2\Phi(x,t)}{\partial t^2}. \tag{2.15}$$

According to the d'Lambert method, the general solution can be found as two propagating waves of the form :

$$\Phi(x,t) = f_1(ct-x) + f_2(ct+x). \tag{2.16}$$

The first function represents a wave traveling in the positive direction and the second a wave traveling in the negative direction. Any initial conditions can be met since f_1 and f_2 are two arbitrary functions. For the monochromatic case, the solution is written as:

$$\Phi(x,t) = f_1\left(\frac{c}{\omega}(\omega t - kx)\right) + f_2\left(\frac{c}{\omega}(\omega t + kx)\right). \tag{2.17}$$

A complex form of the harmonic solution for the velocity potential is

$$\Phi(x,t) = A\exp(j(\omega t - kx)) + B\exp(j(\omega t + kx)) \tag{2.18}$$

where the constants A and B must meet the initial conditions. According to this method, an arbitrary plane wave field can be described physically as an interference of two waves propagating in opposite directions on the x-axis. Typically in acoustic radiation problems, the converging/reflected wave is non existent. In 3 dimensions the solution, for a diverging propagating plane wave with $\mathbf{s} = (x, y, z)$ and $\mathbf{k} = (k_x, k_y, k_z)$, becomes

$$\Phi(\mathbf{s},t) = A\exp(j(\omega t - \mathbf{ks})) \tag{2.19}$$

where $\mathbf{s} = (x, y, z)$ is a point in space in the rectangular coordinate system.
Substituting this form into the wave equation we obtain

$$k_x^2\Phi(\mathbf{s},t) + k_y^2\Phi(\mathbf{s},t) + k_z^2\Phi(\mathbf{s},t) = \frac{\omega^2\Phi(\mathbf{s},t)}{c^2}. \tag{2.20}$$

This implies a constraint on the wave number coefficients

$$k_x^2 + k_y^2 + k_z^2 = \left(\frac{\omega}{c}\right)^2. \tag{2.21}$$

The solution is referred to as a monochromatic plane wave[2] . The relation given in (2.21) is essential for plane wave decompositions such as the angular spectrum. It tells us that not all combinations of k_x, k_y, k_z are possible for real k_x, k_y, k_z. For large values of k_x and k_y, as an example, k_z could become complex. With complex values of k_z an extra exponential function is added to the plane wave amplitude function. These waves are referred to as evanescent waves, and they come into play when plane wave decomposition is done with the Angular Spectrum method.

Spherical wave

The Laplace operator (A.7) in the spherical coordinate system given in Appendix A is applied to the wave equation, and the general spherical wave equation can be written as

$$\frac{1}{r^2}\frac{\partial}{\partial r}(r^2\frac{\partial\Phi}{\partial r}) + \frac{1}{r^2\sin\vartheta}\frac{\partial}{\partial\vartheta}(\sin\vartheta\frac{\partial\Phi}{\partial\vartheta}) + \frac{1}{r^2\sin^2\vartheta}\frac{\partial^2\Phi}{\partial\varphi^2} = \frac{1}{c^2}\frac{\partial^2\Phi}{\partial t^2} \tag{2.22}$$

[2]The term 'monochromatic' meaning one color refers to the temporal behavior of Φ. The term 'plane wave' arises because at an instant of time t_0 the value of $\Phi(\mathbf{s}, t_0)$ is the same at all points lying in a plane given by $k_x x + k_y y + k_z z = C$.

General solutions involve Bessel functions and associated Legendre polynomials. A solution in the spherical system with plane wave properties, *i.e.* the solution that depends only on time and one spatial variable r, and independent of φ and ϑ, is named a spherical wave. The spherical wave is obtained using

$$\frac{\partial \Phi}{\partial \varphi} = \frac{\partial \Phi}{\partial \vartheta} = 0 \tag{2.23}$$

which reduces (2.22) to

$$\frac{1}{r^2}\frac{\partial}{\partial r}(r^2\frac{\partial \Phi(r,t)}{\partial r}) = \frac{1}{c^2}\frac{\partial^2 \Phi(r,t)}{\partial t^2} \tag{2.24}$$

A formal identity for any function Φ is

$$\frac{1}{r^2}\frac{\partial}{\partial r}(r^2\frac{\partial \Phi(r,t)}{\partial r}) = \frac{1}{r}\frac{\partial^2 (r\Phi(r,t))}{\partial r^2} \tag{2.25}$$

and applying (2.25) in (2.24), gives

$$\frac{1}{r}\frac{\partial^2 (r\Phi(r,t))}{\partial r^2} = \frac{1}{c^2}\frac{\partial^2 \Phi(r,t)}{\partial t^2} \tag{2.26}$$

and using the substitution

$$\Psi(r,t) = r\Phi(r,t) \tag{2.27}$$

results in a new one dimensional wave equation

$$\frac{\partial^2 \Psi(r,t)}{\partial r^2} = \frac{1}{c^2}\frac{\partial^2 \Psi(r,t)}{\partial t^2}. \tag{2.28}$$

Again, the most general solution is of the form

$$\Psi(r,t) = f_1(ct-r) + f_2(ct+r). \tag{2.29}$$

The first function $f_1(ct-r)$ is referred to as a diverging spherical wave. Similarly $f_2(ct+r)$ represents a converging spherical wave. The solution for the velocity potential is

$$\Phi(r,t) = \frac{1}{r}f_1(ct-r) + \frac{1}{r}f_2(ct+r) \tag{2.30}$$

Note that Ψ does not change its form propagating away from the origin, but Φ decreases by the factor $\frac{1}{r}$. The solution for Φ has a singularity at $r = 0$. The most important diverging spherical wave is harmonic. Such waves are represented in complex form by

$$\Phi(r,t) = \frac{A}{r}\exp(j(\omega t - kr)) \tag{2.31}$$

Using $\Phi(r,t) = r\Phi(r,t)$ in (2.28) it shows that k and ω are related by $k^2 = \omega^2/c^2$ and the diverging spherical wave can be written without explicit dependence on k as

$$\Phi(r,t) = \frac{A}{r}\exp(j\omega(t - \frac{r}{c})) \tag{2.32}$$

Spherical waves can in principle also be used to decompose an acoustic field. Using spherical waves the radial amplitude dependence has to be accounted for making it more cumbersome than the plane wave approach. The spatial impulse response, which is described in Section 2.3.4, is a method used for calculation of pulsed wave fields based on a spherical wave approach. In medical ultrasound most beamforming [JD93] is performed in the near field of the acoustic transducer on the basis of a spherical waves assumption. A brief discussion on beamforming is given in Section 2.6.

2.1.5 Complex solutions to the wave equation

If one applies the linear properties of the wave equation and the Fourier theorem, it can be shown that any signal, irrespective of the shape in space and time, satisfies the wave equation [Dud84]. In this work acoustic pulses are of interest. Equivalent representations for the pulse can be written in either the time or the frequency domain. If two functions $\Phi_1(\mathbf{s},t)$ and $\Phi_2(\mathbf{s},t)$ satisfy the wave equation, then the linear combination $a\Phi_1(\mathbf{s},t)+b\Phi_2(\mathbf{s},t)$, where a and b are scalars, is also a solution. Because $A\exp(j(\omega t-\mathbf{k}\cdot\mathbf{s}))$ is a solution to the wave equation, it is possible to describe more complicated solutions as a sum or integral of complex exponentials. With the plane wave as a basic solution this leads to the application of either Fourier series or Fourier integrals as shown in the following.
One dimensional Fourier transform can undertake different forms and a general introduction to the Fourier transform can be found in [Bra78]. Here the applied form is

$$P(\omega) = \int_{-\infty}^{\infty} p(t)\exp(-j\omega t)dt \tag{2.33}$$

$$p(t) = \frac{1}{2\pi}\int_{-\infty}^{\infty} P(\omega)\exp(j\omega t)d\omega. \tag{2.34}$$

Using the basic theorems, time scaling and time shift, for the Fourier transform properties, the propagating wave in the x-direction of an arbitrary shape is given by

$$p(x,t)=p_1(t-\frac{x}{c}) = \frac{1}{2\pi}\int_{-\infty}^{\infty} P(\omega)\exp(j\omega(t-\frac{x}{c}))d\omega \tag{2.35}$$

$$= \frac{1}{2\pi}\int_{-\infty}^{\infty} P(\omega)\exp(j(\omega t-kx))d\omega \tag{2.36}$$

which is a sum of harmonic plane waves. $P(\omega)$ is a characteristic feature independent of time and position, since a plane wave does not change amplitude when propagating. This representation in one dimension can be used in a three-dimensional description of the pulse by its 3-D Fourier transform

$$p(\mathbf{s},t)=\left(\frac{1}{2\pi}\right)^3\int_{-\infty}^{\infty} P(\mathbf{k})\exp(j(\omega t-\mathbf{k}\cdot\mathbf{s}))d\mathbf{k}. \tag{2.37}$$

As shown, the transformation kernel is a propagating harmonic plane wave. Since a 3-D wave is described spatially by the $\mathbf{k}$ vector, the transform is performed with respect to this plane wave function basis. Note that for a $\mathbf{k}$ plane wave $p(\mathbf{s},t)$ does not change form as it propagates in the $\mathbf{k}$-direction. $P(\mathbf{k})$ can be regarded as a three dimensional generalization of the Angular Spectrum known from optics [Goo68]. Here $P(\mathbf{k})$ is the Fourier transform of

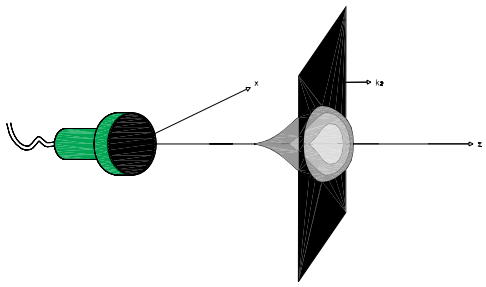

Figure 2.1: Plane iso-phase surface for integration on the $\mathbf{k}=\mathbf{k_1}$ plane.

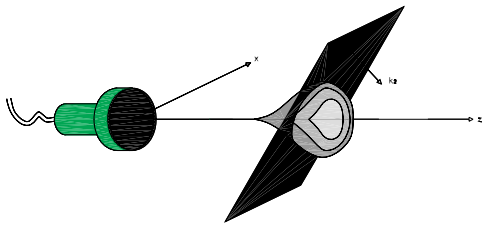

Figure 2.2: Plane iso-phase surface for integration on the $\mathbf{k}=\mathbf{k_2}$ plane.

$p(\mathbf{s},t)$. The other part in the transformation pair is given by

$$P(\mathbf{k}) = \int_{-\infty}^{\infty} p(\mathbf{s},t)\exp(-j(\omega t - \mathbf{k}\cdot\mathbf{s}))d\mathbf{t}. \tag{2.38}$$

Calculating this 3D Fourier transform can be rather cumbersome. Methods for calculating the 3D Fourier transform are given in [TAL93].
This approach of describing the acoustic field has been developed and used by Leeman and co-workers. As a consequence of investigations on diffraction-free measurements [LSF$^+$85], the group developed a large aperture hydrophone (**D**iffraction-**F**ree) for measurements and calibration of fields [CLRS86]. Usually, the acoustic fields from ultrasonic transducers are measured with a point hydro-phone, and the results are very sensitive to spatial positions due to diffraction. The idea with the **DF**-hydrophone is to measure a plane wave component of the pulse. In theory the **DF**-hydrophone performs a surface integral of the acoustical pressure present at the hydrofone plane. The direction of wavenumber $\mathbf{k}$ being measured is the one orthogonal to the surface of the DF-hydrophone. The principle is illustrated in Figure 2.1 and Figure 2.2 for two different $\mathbf{k}$-values.

This measurement is diffraction free, meaning that the pulse measured with the **DF**-hydrophone is independent of the distance from the transducer [CL89]. With this method, the acoustic field is decomposed into a set of harmonic plane waves. These plane waves can be propagated by simple means and therefore it is possible to predict the acoustic field at

any given location. Also the effects of nonlinearities and loss/damping can be treated, see [CLH88],[FHLC90], [LCH91]and [HBL94]. Further, the measurement approach can be used for evaluation of acoustical power output [LHFJ90] and it makes it much easier to perform reflectivity measurements of materials when no diffraction effects are present [CLJ90].
Finally, it is pointed out that the spherical wave can be used to build up more complicated solutions to the spherical wave equation by superimposing complex exponentials, just like plane waves. In this case, however, the wave shape is altered, as the wave propagates outward from the origin, because of the factor $\frac{1}{r}$. The method is elucidated for the one dimensional case, now in spherical notation,

$$p(r,t) = \frac{1}{r}p(t-\frac{r}{c}) \tag{2.39}$$

the result of the spherical decomposition becomes

$$p(r,t) = \frac{1}{2\pi r}\int_{-\infty}^{\infty} P(\omega)\exp(j\omega(t-\frac{r}{c}))d\omega \tag{2.40}$$

$$= \frac{1}{2\pi r}\int_{-\infty}^{\infty} P(\omega)\exp(j(\omega t-kr))d\omega \tag{2.41}$$

Again $P(\omega)$ is the Fourier transform of $p(r,t)$. The Fourier relations imply that any pulse shape in space and time can be decomposed into a sum of spherical waves. These Fourier relations will be further exploited in Chapter 2.7.
The approaches presented here gives a foundation to understand how more complicated acoustic fields can be interpreted and thereby improve the ability to comprehend more complex acoustic problems.

2.2 Theory of radiation and diffraction

The wave equation describes the propagation of the acoustic waves. In the theory of radiation the acoustic source and the wave propagation are linked together. The geometry of the vibrating source and the medium form the boundary conditions for the wave equation. In Harris, [Har81a], [Har81b], four different methods of solving the boundary value problem are presented. These are the most frequently encountered in determining the field of a baffled planar piston. The methods are the Rayleigh surface integral, the King integral, the Schoch solution and the convolution integral. These integrals are related to different ways of calculating the radiated field.
The theory of radiation and diffraction is included in a short and condensed form to give an understanding of the approximations used in the calculation of a radiated field.

2.2.1 The Rayleigh integral

Finding analytical solutions to the acoustic wave equation is, in general, a very complex task. Pressure field calculations involve solutions of the wave equation for both source (vibration problem) as well as the surrounding medium (acoustic problem). In order to develop a simple mathematical model, it is assumed that the vibrating source is mounted in an infinite baffle. Two examples of baffles will be given: rigid and soft. The problem is then formulated as a classical boundary value problem. For this kind of problem different solutions exist, which can be found in a review by Harris, [Har81a], [Har81b]. Here the Rayleigh integral is reviewed. With reference to Figure 2.3, the boundary problem is given by the following.

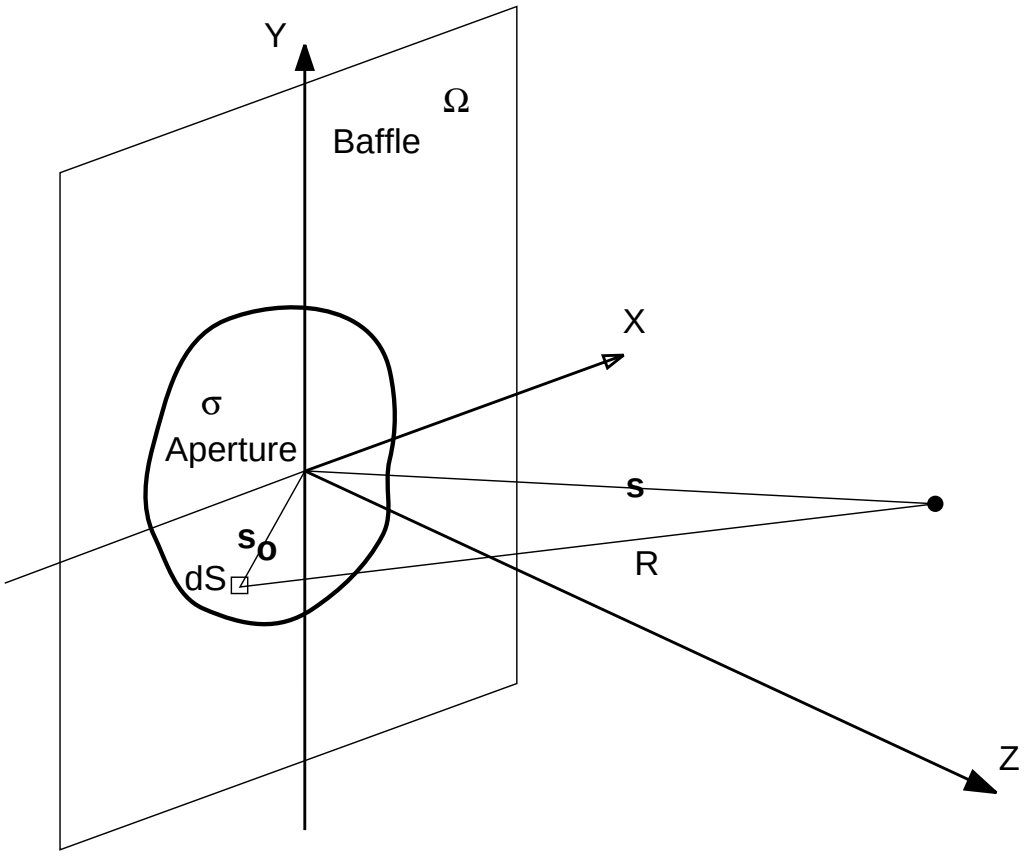

Figure 2.3: Schematic for calculation of boundary problems.

Consider the problem of determining the pressure as a function of time and spatial position in the half-space Υ, defined by $z > 0$, caused by a specified normal velocity $\nu_n(\mathbf{s}_0, t)$ of the piston area, denoted σ, which is situated in the xy-plane Ω, *i.e.* $z = 0$. A rigid baffle constraints the displacement at the boundary to zero, thus the normal velocity is set to zero for this area. The problem is defined for the velocity potential $\Phi(\mathbf{s}, t)$

$$\begin{aligned} \nabla^2\Phi(\mathbf{s},t) &= \frac{1}{c^2}\frac{\partial^2\Phi(\mathbf{s},t)}{\partial t^2} \\ \frac{\partial\Phi}{\partial z} &= \nu_n(\mathbf{s}_0,t) \quad ,\mathbf{s}_0 \in \sigma \\ \nu_n(\mathbf{s}_0,t) &= 0 \quad ,\mathbf{s}_0 \notin \sigma \wedge \mathbf{s}_0 \in \Omega \\ \Phi(\mathbf{s},t) &= \frac{\partial\Phi(\mathbf{s},t)}{\partial t} = 0 \qquad ,\mathbf{s}_0 \notin \sigma \wedge \mathbf{s}_0 \in \Omega \end{aligned} \tag{2.42}$$

A rigorous solution for the acoustic pressure field, when considering harmonic radiated fields, is described by the Kirchoff-Helmholtz integral. A simplification of the Kirchoff-Helmholtz integral gives the solution for the time-dependent velocity potential to this problem by the Rayleigh integral

$$\Phi(\mathbf{s},t) = \int_S \frac{\nu_n(\mathbf{s}_0, t - \frac{R}{c})}{2\pi R} dS \tag{2.43}$$

and the solution for the pressure is

$$p(\mathbf{s},t) = -\rho \int_S \frac{\frac{\partial}{\partial t}\nu_n(\mathbf{s}_0, t - \frac{R}{c})}{2\pi R} dS. \tag{2.44}$$

If the baffle is acoustically soft, the boundary conditions change. With a soft baffle the pressure, *i.e.* the time derivative of the velocity potential, will be zero at the baffle surface. The problem is then defined as

$$\begin{aligned}
\nabla^2\Phi(\mathbf{s},t) &= \frac{1}{c^2}\frac{\partial^2\Phi(\mathbf{s},t)}{\partial t^2} \\
\frac{\partial\Phi}{\partial z} &= \nu_n(\mathbf{s}_0,t) \quad ,\mathbf{s}_0 \in \sigma \\
p(\mathbf{s}_0,t) &= -\rho\frac{\partial\Phi(\mathbf{s},t)}{\partial t} = 0 \quad ,\mathbf{s}_0 \notin \sigma \wedge \mathbf{s}_0 \in \Omega \\
\Phi(\mathbf{s},t) &= \frac{\partial\Phi(\mathbf{s},t)}{\partial t} = 0 \qquad ,\mathbf{s}_0 \notin \sigma \wedge \mathbf{s}_0 \in \Omega.
\end{aligned} \tag{2.45}$$

The simplified solution to this problem is known as the Rayleigh-Sommerfeld integral and is equivalent to the Rayleigh integral except for a factor $\cos\nu$, which is called the obliquity factor. It represents the angular sensitivity of the basic modeling spherical wave. The velocity potential is given by

$$\Phi(\mathbf{s},t) = \int_S \frac{\nu_n(\mathbf{s}_0, t-\frac{R}{c})}{2\pi R}\cdot\cos\nu\; dS \tag{2.46}$$

and the pressure by

$$p(\mathbf{s},t) = -\rho\int_S \frac{\frac{\partial}{\partial t}\nu_n(\mathbf{s}_0, t-\frac{R}{c})}{2\pi R}\cdot\cos\nu\; dS. \tag{2.47}$$

The two examples show the impact of the boundary conditions on the solutions. The examples represent the extreme cases, rigid and soft. Thus, when modeling an acoustic radiator the boundary conditions must be evaluated. Kino [Kin87] points out two examples. A transducer element submerged in liquid or positioned in an array has different responses somewhere between examples of the rigid baffle case and the soft baffle, also named the pressure release baffle.
In the simulation approach used in this work, array transducers are modeled as individual elements in a rigid baffle, not taking the other elements into consideration. The solutions given are only valid for planar transducers and, therefore, secondary diffraction effects[3] are neglected. Solving the Rayleigh integral, even for simple geometrical setups, still gives very complicated analytical solutions.

2.2.2 The Fresnel and Fraunhofer integral

Further simplifications can be obtained by geometrical considerations, such as the maximum size of the transducer aperture and a minimum distance from the observation point to the transducer. The regions for which these approximations are valid are named the Fresnel region (the near-field) and the Fraunhoffer region (the far-field).
The Fresnel approximation is less restrictive than the Fraunhoffer approximation, thus the

[3]In principle curved transducers introduce reflection of waves generated by the transducer it self.

Fresnel region includes the Fraunhofer region. As shown in the following, the approximations are concerned with an exponential factor that arises in the Rayleigh integral

$$\Phi(\mathbf{s},t) = \int_S \frac{\nu_n(\mathbf{s}_0, t-\frac{R}{c})}{2\pi R} dS \tag{2.48}$$

when using the Huygen's principle for calculation.
In this derivation, a continuous wave and a constant displacement velocity u_0 over the aperture are assumed. Let the aperture be divided into a number of elements e_{dS} with the area dS . When $dS \to 0$ the elements become equivalent to a simple source[4] with the strength $u_0 dS$. Further it is assumed that the individual elements e_{dS} are not affected by the presence of other correlated sources. The resulting velocity potential at a given point in space is

$$\Phi(\mathbf{s},t) = \frac{2u_0}{4\pi}\exp(j\omega t)\int_S \frac{\exp(-jkR)}{R} dS \tag{2.49}$$

or the pressure

$$p(\mathbf{s},t) = \rho\frac{\partial\Phi}{\partial t} = j\omega\rho\frac{u_0}{2\pi}\exp(j\omega t)\int_S \frac{\exp(-jkR)}{R} dS. \tag{2.50}$$

This integral, called the Huygens-Rayleigh integral, represents a special case of the Huygen's principle, *i.e.* every point on a plane vibrating surface can be considered as the center of an outgoing spherical wave. The Huygen-Rayleigh integral is exact, if the radiating surface is plane and is enclosed in a rigid baffle, so that no sound is reflected or diffracted at the boundaries.
As stated previously, the approximations are applied to the exponential within the integral. Let the aperture border function be a convex function, and the maximum cross section of the aperture that intersects the center of gravity, CG, be denoted by Γ, see Figure 2.4. A point (x_0, y_0, z_0) in a plane parallel to the aperture plane at the distance z_0 is considered. The distance from the field point to CG is

$$R_0 = \sqrt{x_0^2 + y_0^2 + z_0^2} \tag{2.51}$$

and the distance from the aperture point $(x, y, 0)$ to the field point (x_0, y_0, z_0) is

$$R^2 = (x - x_0)^2 + (y - y_0)^2 + z_0^2 \tag{2.52}$$

since the field point is situated in a plane parallel to the aperture surface. The field point defines $\mathbf{r_0} = (x_0, y_0, z_0)$ and using

$$\gamma^2 = x^2 + y^2 \tag{2.53}$$
$$x_0 = R_0\sin(\vartheta)\cos(\varphi) \tag{2.54}$$
$$y_0 = R_0\sin(\vartheta)\sin(\varphi) \tag{2.55}$$

where ϑ is the angle between $\mathbf{r_0}$ and the z-axis and φ is the angle between $\mathbf{r_0}$ and the x-axis, then

$$R^2 = R_0^2\left(1 + \frac{\gamma^2}{R_0^2} - \frac{2xx_0}{R_0^2} - \frac{2yy_0}{R_0^2}\right) \tag{2.56}$$

[4] A simple source is a point with an omnidirectional radiation pattern.

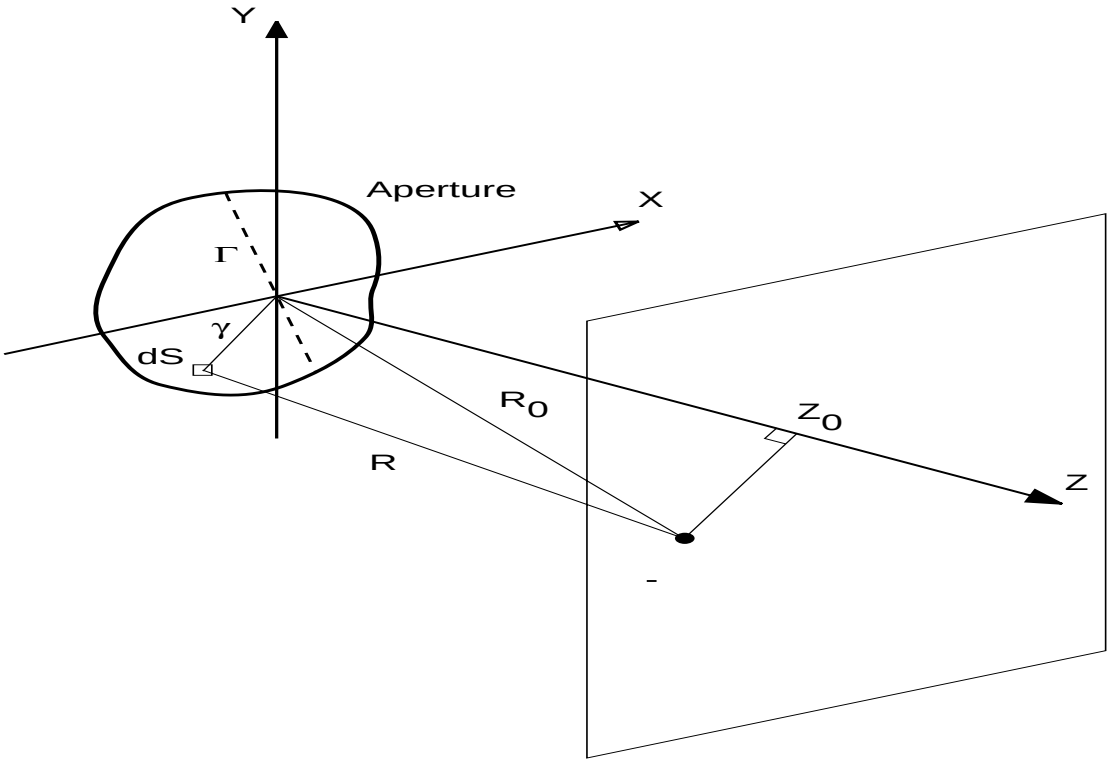

Figure 2.4: Geometry for Fresnel and Fraunhofer approximations for a radiation problem.

and R as a function of depth R_0 and angles ϑ and φ becomes

$$R = R_0 \left(1 + \frac{\gamma^2}{R_0^2} - \frac{2xx_0}{R_0^2} - \frac{2yy_0}{R_0^2}\right)^{1/2} \tag{2.57}$$

$$= R_0 \left(1 + \frac{\gamma^2}{R_0^2} - \frac{2x}{R_0}\sin(\vartheta)\cos(\varphi) - \frac{2y}{R_0}\sin(\vartheta)\sin(\varphi)\right)^{1/2}. \tag{2.58}$$

The square root can be developed into a power series using

$$\sqrt{1+b} = 1 + \frac{b}{2} - \frac{b^2}{8} + \ldots \tag{2.59}$$

and (2.58) becomes

$$R = R_0 \left(1 + \frac{1}{2}\frac{\gamma^2}{R_0^2} - \left(\frac{x}{R_0}\sin(\vartheta)\cos(\varphi) + \frac{y}{R_0}\sin(\vartheta)\sin(\varphi)\right)\right) \tag{2.60}$$

$$-\frac{1}{2}\left(\frac{x}{R_0}\sin(\vartheta)\cos(\varphi) + \frac{y}{R_0}\sin(\vartheta)\sin(\varphi)\right)^2 + \ldots \tag{2.61}$$

where only one component of b^2 is shown. Assuming that $R_0 >> \Gamma/2$ or $\gamma << R_0$ then

$$R \approx R_0 + \frac{\gamma^2}{2R_0} - x\sin(\vartheta)\cos(\varphi) + y\sin(\vartheta)\sin(\varphi) - \frac{1}{2R_0^2}\left(x\sin(\vartheta)\cos(\varphi) + y\sin(\vartheta)\sin(\varphi)\right)^2 \tag{2.62}$$

which shows that R has a linear and a quadratic term with respect to the off axis position relative to the z-axis and a component that depends on the size of the aperture. The variables x and y are the integration variables in the exponential in the Rayleigh integral given by (2.49) or (2.50).
The *Fresnel* approximation (often named the paraxial approximation) is obtained by retaining the terms up to second order in the exponential.
The *Fraunhofer* (or the far field) approximation is obtained by retaining the terms up to first order *i.e.* the phase-front curvature is ignored. The use of the Fraunhofer approximation will be further developed in Section 2.3.2 to point out the Fourier relation between an aperture and the CW radiation pattern.
The actual regions will depend on the geometry of the aperture and the frequency. The most common rule of thumb is given for the circular aperture. Let the radius be noted a and $ka >> 1$, ($k = 2\pi/\lambda$). With these assumptions the regions demands becomes [Kin87]:

- The Fresnel approximation: $a << R_0$.
- The Fraunhofer approximation: $\frac{a^2}{\lambda} < R_0$.

2.3 Calculation methods for radiated acoustic fields

Different methods can be used to calculate the radiated acoustical field of a transducer. Four methods presented in this section have been considered, and some have been used during this work. The methods are

- Numerical integration method
- Fourier transform method
- The replica pulse method
- Spatial impulse response method

The Fourier transform and the spatial impulse response have both been used for this work and are therefore described in details.

2.3.1 Numerical integration method

A numerical implementation of the Rayleigh integral is the most straight forward method and a robust way to calculate the acoustic field. This method is very cumbersome with a high number of operations needed to perform the computation for a time-dependent field.

2.3.2 Fourier transform method

With the Fraunhofer approximations applied to the Rayleigh integral, the relation between the aperture and the acoustical field is given by the Fourier transform.
It can be shown that the radiation pattern for a line-aperture is the one-dimensional Fourier transform of the apertures excitation function [Ste76a]. This method is valid for continuous wave (CW) in the far field of the aperture. It also applies to two dimensional cases which involve a two-dimensional Fourier transform, see [Goo68]. In both the 1D and 2D case it can be shown that the relations are valid for focused transducers at the focal depth for

a restricted off-axis distance. The method is included because it is used to evaluate the acoustic field pattern for vector velocity estimation.
Here the one-dimensional problem will be presented for a line with length L on the x-axis. Initially we have

$$p(x,R,t) = \rho\frac{\partial\Phi}{\partial t} = j\omega\rho\frac{u_0}{2\pi}\exp(j\omega t)\int_L a(x)\frac{\exp(-jkR)}{R}dS \tag{2.63}$$

where $a(x)$ is the aperture function on L. With a one dimensional aperture the geometry becomes

$$R^2 = (x-x_0)^2 + z_0^2 \tag{2.64}$$

or

$$R^2 = R_0^2\left(1 + \frac{x^2}{R_0^2} - \frac{2xx_0}{R_0^2}\right). \tag{2.65}$$

Using (2.59) the approximative expression becomes

$$R \approx R_0\left(1 + \frac{x^2}{2R_0^2} - \frac{xx_0}{R_0}\right) = R_0 + \frac{x^2}{2R_0} - \frac{xx_0}{R_0}. \tag{2.66}$$

With the Fresnel approximation, $\frac{L}{R_0} << 1$, the amplitude can be considered constant, *i.e.* $R = R_0$, and with $u = \sin(\vartheta) = \frac{x_0}{R_0}$ the pressure can be expressed as

$$\begin{aligned} p(x_0,R_0,t) &= \rho\frac{\partial\Phi}{\partial t} && (2.67)\\ &= j\omega\rho\frac{u_0}{2\pi}\exp(j\omega t)\frac{\exp(-jkR_0)}{R_0}\cdot \\ &\quad \int_L a(x)\exp\left[jk\left(xu - \frac{x^2}{2R_0}\right)\right]dx && (2.68)\end{aligned}$$

The normalized complex radiation pattern is defined as

$$\mathsf{R}(u) = \frac{p(x,R,t)}{p(0,R,t)} \tag{2.69}$$

resulting in

$$\mathsf{R}(u) = \int_{line} a_n(x)\exp\left[jk\left(xu - \frac{x^2}{2R_0}\right)\right]dx \tag{2.70}$$

where $a_n = \frac{a(x)}{a(0)}$ is the normalized aperture function, *apodization function*. The first term in the integral is the Fraunhofer kernel $\exp(jkxu)$ and the second term is the Fresnel kernel $\exp(-jkx^2/2R_0)$. Using the Fraunhofer approximation

$$\frac{L^2}{\lambda} < R_0$$

the integral becomes

$$\mathsf{R}(u) = \int_{line} a_n(x)\exp(jkxu)dx. \tag{2.71}$$

This shows that the normalized complex radiation pattern $\mathsf{R}(u)$ in the far field, can be calculated as the Fourier transform of the normalized aperture function $a_n(x)$. If x is normalized to the wavelength λ, $x' = x/\lambda$, then

$$\mathsf{R}(u) = \int_{line} a_n(x') \exp(j2\pi x'u) dx \tag{2.72}$$

which is the Fourier transform in the most often applied version.
If linear system theory is applied, the time evolution in a given direction can be calculated using a Fourier transform method. This is a consequence of the convolution theorem. The application for a one-dimensional problem can be found in [BC81] and for a two-dimensional problem in [GP85] and [Cob84]. The two dimensional application is developed on the basis of the angular spectrum technique [Goo68], which is a method for monochromatic waves (CW). In this work the Fourier relation will be used to point out the basic requirements for the acoustic aperture to make a transverse oscillating acoustic field.

2.3.3 Replica pulse method

The replica pulse method is an approximative method, but it is very useful to obtain a basic understanding of the evolution of a pulsed acoustic field. It is a tool which feeds the intuition. The basic idea is that the wave field can be decomposed in a geometric plane wave of cross section equal to that of the radiator and of an edge wave emanating from the rim of the radiator. It is based on the Schoch solution to the wave equation, which shows that the acoustic field can be decomposed as a plane wave and an edge wave. This method has been employed by A. Freedman and further information can be found in several articles from the sixties and the seventies (see [Fre70a] and [Fre70b]) and more recently in [Fre94]. The replica pulse method links a mathematical problem to a practical tool. The method is mentioned to imply its worth, when acoustical problems have to be mentally visualized as a help to understand a problem.

2.3.4 Spatial impulse response method

The spatial impulse response method applies linear system theory to the wave equation, and it separates the temporal and spatial characteristics of the acoustical field, which is apprehended as a spatial filter. The approach assumes the wave propagation to be linear in a non-attenuating and homogeneous medium. It is a powerful technique that evaluates the Rayleigh integral as a convolution between the normal velocity $\nu_n(\mathbf{s}_0, t)$, and a function $h(\mathbf{s}, t)$ named the spatial impulse response. The physical interpretation of the spatial impulse response is that it relates the acoustical field impulse response to the geometry of the radiating source.
The first derivation of a transient field for a circular piston in a rigid baffle was published by Oberhettinger, [Obe61b], [Obe61a]. The development of the explicit use of a spatial impulse response and a convolution method is ascribed to Tupholme and the method has further been developed by Stephanishen (also named the 'local observer' approach), [Ste71a], [Ste71b].
Based on the Rayleigh integral the time evolution of the velocity potential in a spatial point is

$$\Phi(\mathbf{s}, t) = \int_S \frac{\nu_n(\mathbf{s}_0, t - \frac{R}{c})}{2\pi R} dS \tag{2.73}$$

The velocity function can be expressed as a temporal integral term

$$\nu_n(\mathbf{s}_0, t - \frac{R}{c}) = \int \nu_n(\mathbf{s}_0, t_o)\delta(t - \frac{R}{c} - t_0)dt \tag{2.74}$$

and with the application of this term, the excitation pulse is separated from the transducer geometry in (2.73)

$$\Phi(\mathbf{s}, t) = \int_S \int_T \frac{\nu_n(\mathbf{s}_0, t_0)\delta(t - \frac{R}{c} - t_0)}{2\pi R}\, dt_0\, dS \tag{2.75}$$

In order to demonstrate the nature of convolution, it is assumed that the surface velocity is uniform, *i.e.* $\nu_n(\mathbf{s}_0, t) = \nu_n(t)$ then

$$\Phi(\mathbf{s}, t) = \nu_n(t) \underset{t}{*} \int_S \frac{\delta(t - \frac{R}{c})}{2\pi R}\, dS \tag{2.76}$$

where $\underset{t}{*}$ represents the convolution with respect to the subscript; in this case the time. The last term in (2.76)

$$h(\mathbf{s}, t) = \int_S \frac{\delta(t - \frac{R}{c})}{2\pi R}\, dS \tag{2.77}$$

is defined as the spatial impulse response. The integral is an example of Huygens' principle where the contributions from all the infinitesimally small areas that make up the aperture are integrated. The velocity potential can be written as

$$\Phi(\mathbf{s}, t) = \nu_n(t) \underset{t}{*} h(\mathbf{s}, t). \tag{2.78}$$

Alternatively the pressure is given by

$$p(\mathbf{s}, t) = \rho \frac{\partial \nu_n(t)}{\partial t} \underset{t}{*} h(\mathbf{s}, t) \tag{2.79}$$

or

$$p(\mathbf{s}, t) = \rho \nu_n(t) \underset{t}{*} \frac{\partial h(\mathbf{s}, t)}{\partial t}. \tag{2.80}$$

The impulse response $h(\mathbf{s}, t)$ often has very high derivatives with respect to time, whereas the normal velocity $\nu_n(\mathbf{s}_0, t)$ is an oscillating function with a very smooth envelope having well-behaved derivatives. For numerical evaluation, the most often applied convolution method is (2.79).

When calculating $h(\mathbf{s}, t)$, an approach other than summing up the contributions from the aperture at a specific spatial position, can be used. This is a consequence of the acoustic reciprocity theorem, which implies that the source and the receiver can be interchanged [MI68], [Pie81]. The consequence of this powerful theorem is that the spatial impulse response can be calculated as the length of the intersection between a spherical wave emitted from the point of interest and the aperture.

The impulse response for different kinds of apertures has been derived. For the plane circular aperture see [Ste71b], for the concave circular see [PL76], for the concave annulus see [AFH81], for the flat rectangular see [LW73], for the elliptic see [Ste77] and for the triangular

see [Jen96b]. This method is the most applied for calculation of pulsed acoustic fields. The references are numerous. A good introduction and an extension of the method can be found in [TT82]. For simple transducer geometry it directly offers a computationally fast method and it can be further developed for calculations of pulse-echo fields.

2.4 Calculation method of pulse-echo acoustic fields

The former methods introduced in Section 2.3.4 feature the possibility of calculating the fields by their free field properties, *i.e.* the transmit field or the receive field individually, but the applications of interest within ultrasonic imaging rely on a pulse-echo measurement situation. Therefore some considerations are needed on this matter in order to device a calculation method based on the spatial impulse response. The scattering problem can be formulated is a number of ways depending on the physical aspect considered. The solution for a single scatter response and a multiple scatters response will be presented. For a general discussion on scattering refer to Ishimaru [Ish78a], [Ish78b].

Response of single scatterer

For a single scatterer the spatial pulse-echo impulse response corresponds to the convolution of the spatial impulse response of the transmit and receive aperture, [Ste81], [HAF83] and [FC84]. This is also intuitively understandable since the point of reflection equals a spatial impulse response of $\delta(x_0, y_0, z_0)$ and the system modeled is considered to be linear due to the governing homogeneous linear equation.

Response of multiple scatterers

This situation of multiple scatterers is not straightforward as in the single scatterer situation. To describe this phenomenon of an inhomogeneous medium it is necessary to involve scattering in the deduction of the wave equation. As a result, the wave equation becomes inhomogeneous as well. A solution for an equation where the scattering term is a function of density and propagation velocity perturbations has been presented in [GL77] based on results in [MI68]. The method has been further evolved in [Jen91] to the application of the impulse response for an arbitrary transducer configuration to calculate the field response in a scattering medium. The basic assumption relies on weak scattering for the use of the first Born approximation, as illustrated in Figure 2.5. The emitted field is symbolized by the large arrow. The scattered field from the individual scatterers are indicated by the 'snowflakes'. Every scatterer is a Rayleigh scatterer having a omnidirectional directivity function. The Born approximation allows the individual scatterer responses to be added up without any secondary scattering effects, *i.e.* neglecting multiple scattering in which the propagation direction changes more than once from transmission to reception. Another approximation introduced, is the assumption of separability of the excitation and the transducer geometry. Under these assumptions the result for the backscattered signal becomes, in convolution terms [Jen91],

$$p_r(\mathbf{s}, t) = v_{pe}(t) \underset{t}{*} f_m(\mathbf{s}) \underset{\mathbf{s}}{*} h_{pe}(\mathbf{s}, t) \tag{2.81}$$

The first term v_{pe} includes the transducer excitation and the electromechanical response

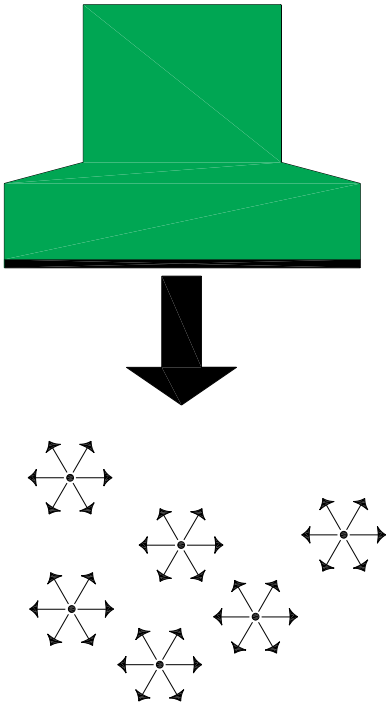

Figure 2.5: Illustration of multiple scattering. Rayleigh scattering is assumed for the used point scatterers and the Born approximation for summing the individual contributions.

during emission and reception. The second term is

$$f_m(\mathbf{s}) = \frac{\Delta\rho(\mathbf{s})}{\rho_0} - \frac{2\Delta c(\mathbf{s})}{c_0} \tag{2.82}$$

which accounts for the inhomogeneities in the tissue due to density and propagation velocity perturbations that cause the scattered signal. The third term is

$$h_{pe}(\mathbf{s},t) = \frac{1}{c_0^2}\frac{\partial^2(h_T(\mathbf{s},t) \underset{t}{*} h_R(\mathbf{s},t))}{\partial t^2} \tag{2.83}$$

which is the modified pulse-echo spatial response that relates the transducer configuration to the spatial extent of the scattered field. Often the transmit and receive transducer geometry are different, which is indicated in (2.83) by $h_T(\mathbf{s},t)$ and $h_R(\mathbf{s},t)$. For the implementation of the method, it is numerically inconvenient to differentiate the combined impulse response. Instead, the double differentiation is performed on v_{pe} .

2.5 Acoustical resolution

An imaging system is often characterized by the ability to depict a point scatterer using the resolution cell. In this context three directional properties are used. It is the axial, the lateral and the elevational resolution as illustrated in Figure 2.6.

The axial and the lateral resolution are directly visible in the image. The elevational resolution is the one orthogonal to the image plane. Sometimes the term transversal is used

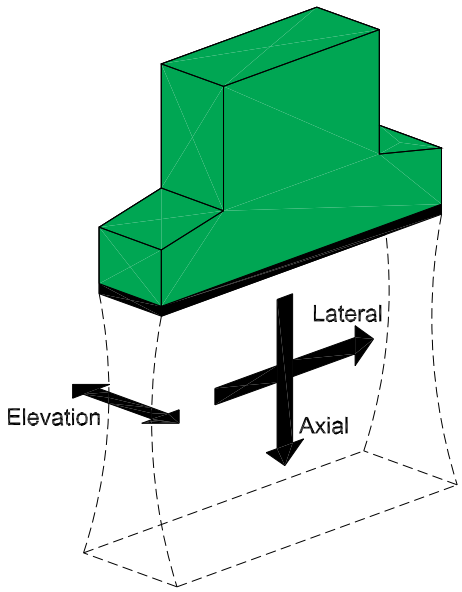

Figure 2.6: Definitions of direction in an ultrasound image.

instead of elevational and should not be confused with the term *transverse*, which is used for flow components. The resolution cell is defined by a border that has a given level (e.g. -3dB, -6dB, -10dB, -20dB) relative to the maximum envelope response from a specific depth. The maximum response varies, and the resolution cell changes shape, as a function of depth. An illustration of this 3-D measure is given in Figure 2.7. The axial resolution is determined by the length of the pulse emitted from the transducer. The lateral and transverse resolution are basically related to the size of the active acoustic aperture.
Resolution is of great importance to the image quality, because it defines the imaging system ability to resolve details. In conventional flow imaging, the method used to calculate the axial velocity component is based on an autocorrelation approach. The quality of the estimated velocity increases with the pulse length, *i.e.* the variance of the estimate decreases with increased pulse length. Thus, there is a conflict of interest in axial resolution capability and quality of the flow estimation.

2.6 Beamforming

A short description of time-domain [5] beamforming is included to facilitate the use of the special apodization and delay scheme used for the vector estimation. Beamforming and

[5]Beamforming can also be performed by frequency domain methods. For further information on this topic see books by Johnson [JD93] and Soumekh [Sou94]. This kind of beamforming can be based on a FFT approach and is referred to as FFT-beamforming. The possible use of these methods have not been investigated.

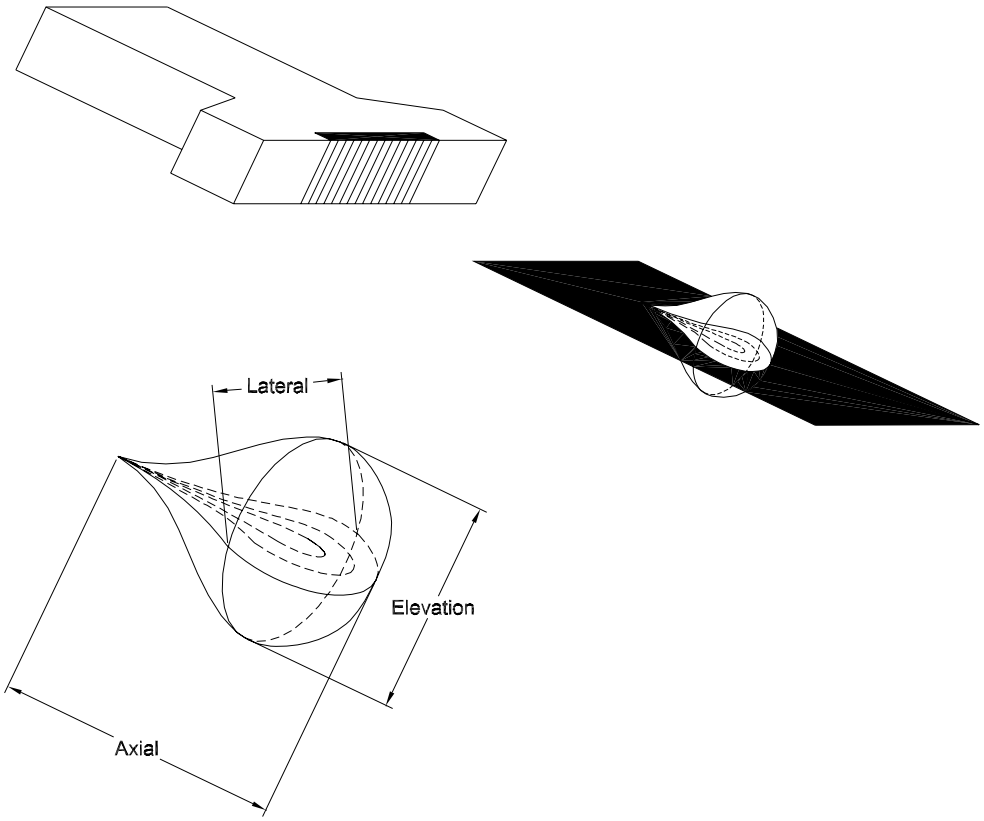

Figure 2.7: The resolution cell in the image plane and an example of a contour volume.

multi-element transducers are inevitably bundled. This kind of configuration, beamformer and array/matrix transducer, enables control of the directivity characteristics in both space and time of the acoustic field. The basic purpose is to obtain as good a resolution as possible with the restriction of an overall homogeneous image resolution with a minimum of sidelobe and grating lobe artifacts.
The non-axial resolution limits of an imaging system are mainly determined by the dimensions of the acoustic transducer. Within these limits, the beamformer controls the actual resolution, basically by a summing scheme. Beamforming is used both for the transmit and the receive situation. The control of an imaging system can be either static or dynamic. Static means that the acoustic focusing does not change with time during recording of one RF-line. Dynamic control of the acoustic focusing of an imaging system is possible with a beamformer. In conventional[6] imaging dynamic control is performed only during receive mode. Beamforming is a science in itself, and the publications are numerous. Many advanced methods originate from radar [Mai94] and sonar [Dud84], [JD93], where adaptive and optimization schemes are employed. Array signal processing is a common description for this field of research. It can be shown that there is a relation between the frequency

[6]The term conventional is used to differentiate from imaging with dynamic control in both transmit and receive using a synthetic aperture approach.

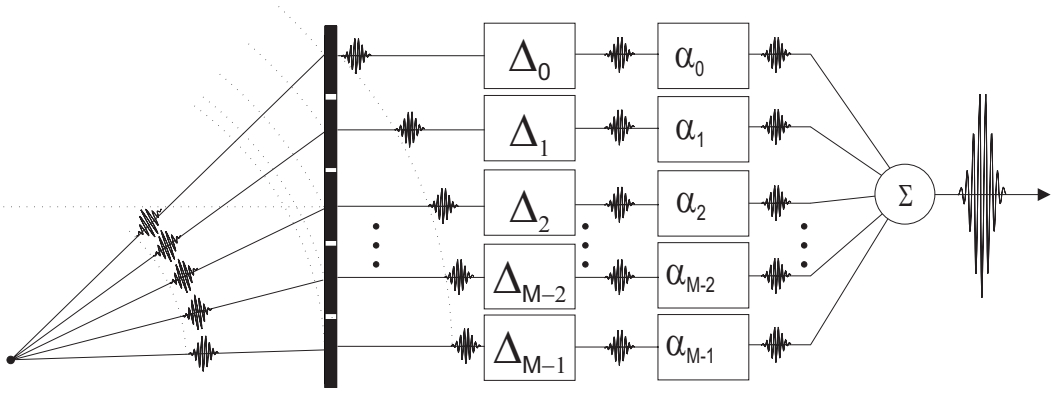

Figure 2.8: Delay-and-sum beamformer.

estimation techniques and beamforming techniques, where directions of arrival correspond to temporal frequencies [AG96], [MEAG96]. Thus, methods originally developed for spectral estimation, parametric and non-parametric, can be transferred to beamforming.
The terminology used to describe the transmit and the receive situation is different. In transmit mode, the beamformer creates an acoustic pulse and the term acoustic field is used in this frame. In receive mode, the beamformer is used to create a specific spatial sensitivity obviously within the limitations of the imaging system and the term acoustic sensitivity is used. This sensitivity is most often controlled to be as limited as possible in space and to have a smooth overall shape, like a Gaussian function. Thus, when a pulse-echo system is described, it must be in terms of sensitivity. In the general case the total pulse-echo sensitivity can not be calculated in some straight forward manner. The result is a complicated interaction between the transmitted acoustic field and the spatial receive sensitivity.
Two types of beamformers are presented, both for the receive application. First, the delay-and-sum beamformer which is a simple approach, and second, the filter-and-sum beamformer, which is a more general approach.

Delay-and-sum beamformer

The delay-and-sum beamformer is the most commonly used beamformer in medical ultrasound imaging. Even though delay-and-sum beamforming is the simplest array signal processing algorithm, it still remains a powerful approach towards acoustic focusing and beamsteering. The underlying idea is quite simple: If a propagating signal is present in a receiving arrays aperture, the sensor outputs, delayed by appropriate amounts of time and added together, reinforce the signal with respect to waves propagating from a specific location (spherical wave) or direction (plane wave). The delays that reinforce the signal are directly related to the difference in propagation time to the different sensors for a given wavefront. To visualize the beamform technique, a pulse emitted from a point source is shown at the transducer elements, before and after delay and after summation, see figure 2.8. The waveform measured by the m'th sensor is $y_m(t)$. The array samples the wave field spatially at each sensor location. The delay-and-sum beamformer consists of applying a delay Δ_m and amplitude weight α_m to the output of each sensor, then summing the resulting signals, see figure 2.8. The amplitude weighting is called the array shading or apodization. Typically, the delays are adjusted to focus the array beam on signals propagating from a particular point $\mathbf{s}_0$. Thus, the array sensitivity to waves propagating from a particular location/direction in space can be optimized by choosing appropriate delays. The shape of the

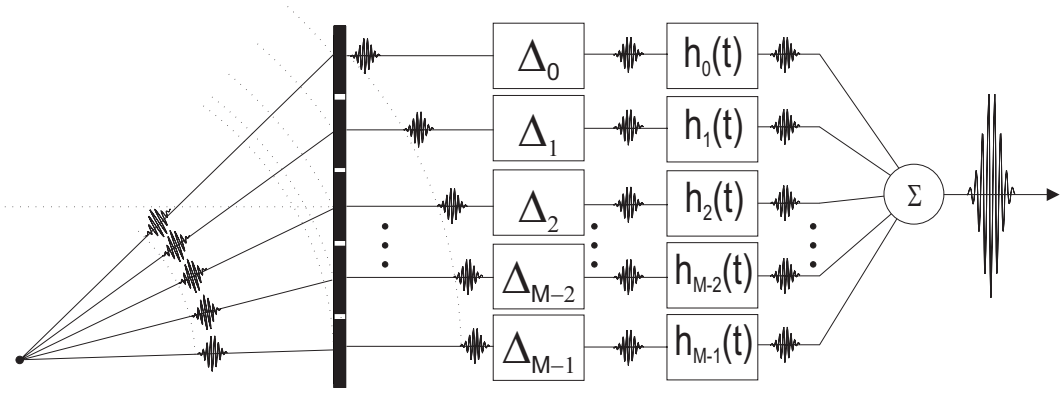

Figure 2.9: Filter-and-sum beamformer.

sensitivity function (beam function) orthogonal to the beamforming direction is determined by the apodization of the array. For B-mode imaging purposes, the function has a maximum in the imaging direction and the shape varies with depth. The beam function depicts how a point reflector will appear in the image. The delay-and-sum beamformers output signal is given by

$$z\left(t\right)=\sum_{m=1}^{M}\alpha_m y_m\left(t-\Delta_m\right). \tag{2.84}$$

The process of beamforming is simple, but the actual acoustical characteristics (4-dimensional function of space and time) created by this processing approach is quite complicated. Often time and space are treated separately in the control of the beamformer, which results is a limited use of the beamformer capabilities. The method presented in Section 2.7, represents a precise method to calculate the beamformer setup for a given desired pulsed acoustic field characteristic. To meet the requirements to the beamformer capabilities, a filter and sum approach must be employed.

Filter and sum beamformer

The general beamformer, illustrated in Figure 2.9, shows how each channel is processed individually and finally summed. Each channel has a linear filter with the impulse response $h_m(t)$, a delay filter with unit amplitude and delay Δ_m, and an apodization factor α_m. The apodization is incorporated into the linear filter. The delay can be divided into a coarse and a fine delay. Usually only the fine delay is incorporated into the filter. If the input signal at a given channel is named $x_m(\mathbf{s},t)$, the output of the filter is

$$y_m(t)=\int_o^{\infty} h_m\left(\tau\right)x_m\left(\mathbf{s},t-\tau d\tau\right) \tag{2.85}$$

and the output of the beamformer is

$$z\left(t\right)=\sum_{m=1}^{M}\alpha_m y_m\left(t-\Delta_m\right) \tag{2.86}$$

This architecture allows both spatial and temporal filtering. The choice of filters is not a straight forward problem. For example, the filters could be used to compensate for known angular distortion. In Section 2.7 a method is described which calculates impulse responses of the filters, delays and apodization to be used in order to obtain a specified acoustic field.

This type of beamformer is not commonly used for medical ultrasound where a typical channel number ranges from 64 to 256. The beamformers are implemented in ASIC and adding a filter to each channel increases the complexity dramatically. Instead the simpler delay-and-sum beamformer is used.

2.7 Propagation of acoustic fields

This section describes the decomposition of a pulsed acoustic field into a set of pulsed plane waves. The decomposition makes it possible to propagate a desired pulse shape described in space and time from one location to another. With this method it is possible to determine the excitation needed on an array transducer, element by element, in order to obtain a close approximation to the original desired bounded pulse. The approximation arises due to the limited size of the acoustic aperture and spatial sampling property of the used array transducer. Thus, the acoustical field can be designed according to the imaging needs. Only fields symmetrical to the axis of the propagation direction are considered.

2.7.1 Theory

The decomposition method is based on calculation of the 2D or 3D spatial Fourier transforms for each temporal frequency. A 3D propagating plane wave, unbounded in space and time, is described by

$$e\left(\mathbf{s},t\right)=\exp(j(\omega_0 t-\mathbf{k_0}\cdot\mathbf{s})) \tag{2.87}$$

where the plane wave is characterized by the wavenumber $\mathbf{k_0}$ and the angular frequency ω_0. The time is t and $\mathbf{s}$ is the observation point in space. The function (2.87) is considered to be an elemental function in the 4D Fourier transform pair [Dud84]

$$p(\mathbf{s},t) = \frac{1}{(2\pi)^4}\int_{-\infty}^{\infty}\iiint_{-\infty}^{\infty} P(\mathbf{k},\omega)\exp(j(\omega t-\mathbf{k}\cdot\mathbf{s}))\,d\mathbf{k}\,d\omega \tag{2.88}$$

$$P(\mathbf{k},\omega) = \int_{-\infty}^{\infty}\iiint_{-\infty}^{\infty} p(\mathbf{s},t)\exp(-j(\omega t-\mathbf{k}\cdot\mathbf{s}))\,d\mathbf{s}\,dt, \tag{2.89}$$

where $\mathbf{k}$ is the wavenumber, which determines the propagation direction and, thus, is perpendicular to any iso-phase plane of the wave. Basically formula (2.88) shows that any function of space and time can be decomposed in temporal frequency and 3D plane waves. The formulas (2.88) and (2.89) are valid for general functions and must be restricted to functions that satisfy the wave equation. An applicable function must meet the condition

$$\omega^2=c^2|\mathbf{k}|^2=c^2k^2, \tag{2.90}$$

which is valid for a lossless medium. An attractive feature of an unbounded harmonic plane wave is that the propagation of such waves can be handled as a simple phase shift. For a pulsed/bounded plane wave, the propagation delay in the $\mathbf{k}$-direction to reach a point $\mathbf{s_0}$ is given by the time

$$\Delta=\frac{\mathbf{k}\cdot\mathbf{r}}{c} \tag{2.91}$$

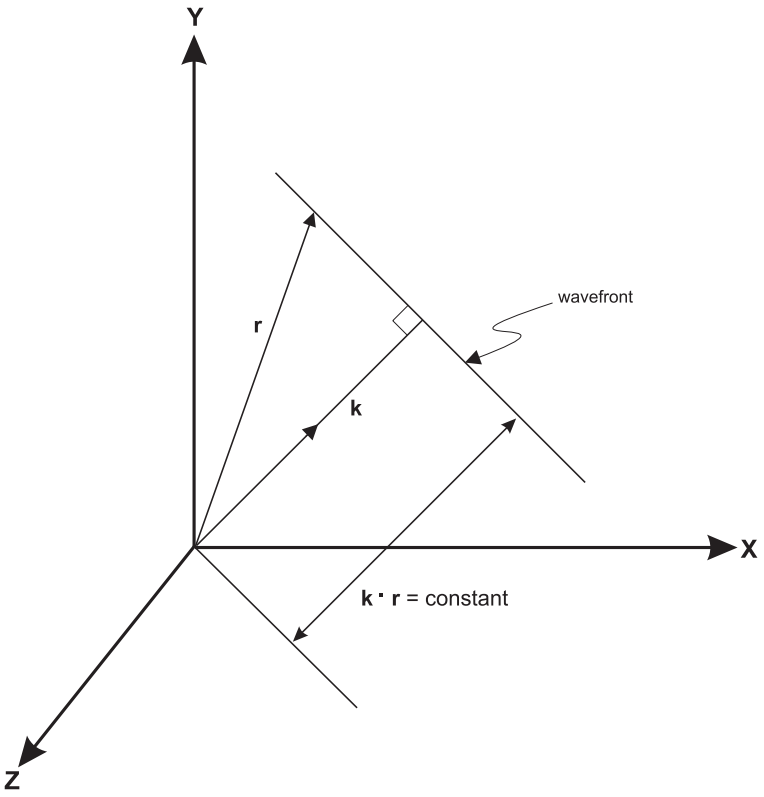

Figure 2.10: Illustration of a wavefront and the notation used to describe a propagating plane wave.

where $\mathbf{r}$ is the vector from a chosen reference point at the plane wave to $\mathbf{s_0}$ and c is the propagation velocity, see Figure 2.10.

Thus, in this framework of pulsed plane waves, propagation is handled as a time delay, rather than a phase delay. In order not to alter the pulse shape, a lossless medium must be assumed.

Using (2.89), the Fourier transform of $e\left(\mathbf{s},t\right)$ gives

$$E\left(\mathbf{k},\omega\right)=\delta\left(\mathbf{k}-\mathbf{k_0}\right)\delta\left(\omega-\omega_0\right) \tag{2.92}$$

which shows that each point in the $(\mathbf{k},\omega)$ domain corresponds to one plane wave propagating in the $\mathbf{k}$-direction with an angular temporal frequency of ω. If the plane wave bounded in time is described by

$$p\left(\mathbf{s},t\right)=a\left(\mathbf{s},t\right)\exp(j(\omega t-\mathbf{k_0}\cdot\mathbf{s})) \tag{2.93}$$

then the 4D Fourier transform will be

$$P\left(\mathbf{k},\omega\right)=\delta\left(\mathbf{k}-\mathbf{k_0}\right)\otimes A(\mathbf{k},\omega)=A(\mathbf{k_0},\omega) \tag{2.94}$$

Traditionally, plane wave decomposition is referred to as the Angular Spectrum Decomposition. The method is used to propagate fields, but the use is limited for backpropagation, due to the nature of evanescent waves where the amplitude grow exponentially with the backpropagated distance. The presence of evanescent waves is a consequence of the chosen formalism of the angular spectrum method and these are non-physical waves.

The evanescent waves can be eliminated using a projection of the acoustic field as described by Leeman [LH97]. The projection is carried out as an integration onto a plane in the 3D

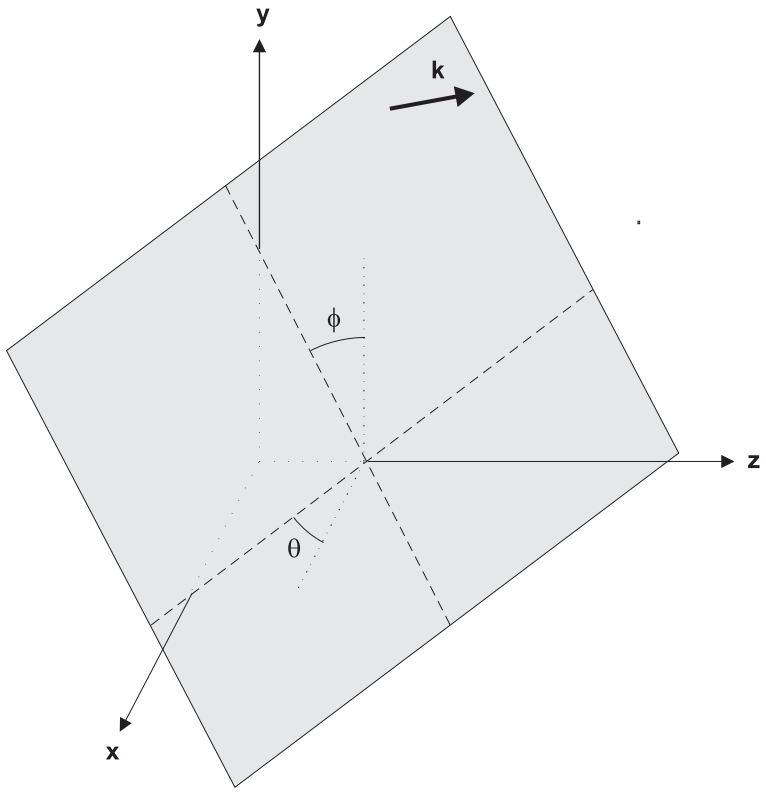

Figure 2.11: Projection plane used for integration of the pulsed field.

space, see also Section 2.1.5. The method emerged in the mid 80s [LSF+85] and has recently been described by Leeman [LH97] and Healey [HL97]. A plane projection is an example of the Fourier slice theorem in the theory of reconstruction from projections. The approach was originally developed in the effort to obtain diffraction free acoustic/ultrasound measurements using a large aperture hydrophone. The hydrophone, having a diameter of 8-10 cm, performs the plane integral since the applied PVDF covers the whole acoustic energy volume.

In the papers given on this topic it has not been specifically pointed out that the approach assumes local spatial stationarity because time and propagation distance are related through the propagation velocity, and they are interchanged in the derivation of the theory. In acoustic terms this means that there is a limit to how strong focused fields the method can handle. To deal with the related time and space measure, two time measures are introduced. The propagating pulse being evaluated is frozen at a specific time t_0, which is referred to as global time, thus a point in time (*i.e.* depth), where the spatial 3D distribution of the pulse is recorded. This frozen pulse has an oscillatory nature in the propagation direction, which, in a very complex manner, is related to the time signal exciting the transducer. Spatial displacements in the 3D frozen image in the propagation direction of the pulse can be regarded as time assuming local stationarity. This time is referred to as local time τ, which is the time difference to global time t_0, thus $\tau = t - t_0$.

The projections are performed on a plane in space with normal vector $\mathbf{k}$, denoted $\mathbf{k}$-plane, and all planes considered rotate around a pivot point[7] on the axis of propagation. The orientation of the projection plane is illustrated in Figure 2.11.

The coordinate system $\mathbf{s} = (x, y, z)$ is chosen to have the z-axis parallel to the propagation

[7] A unique point of rotation shared by all projection planes.

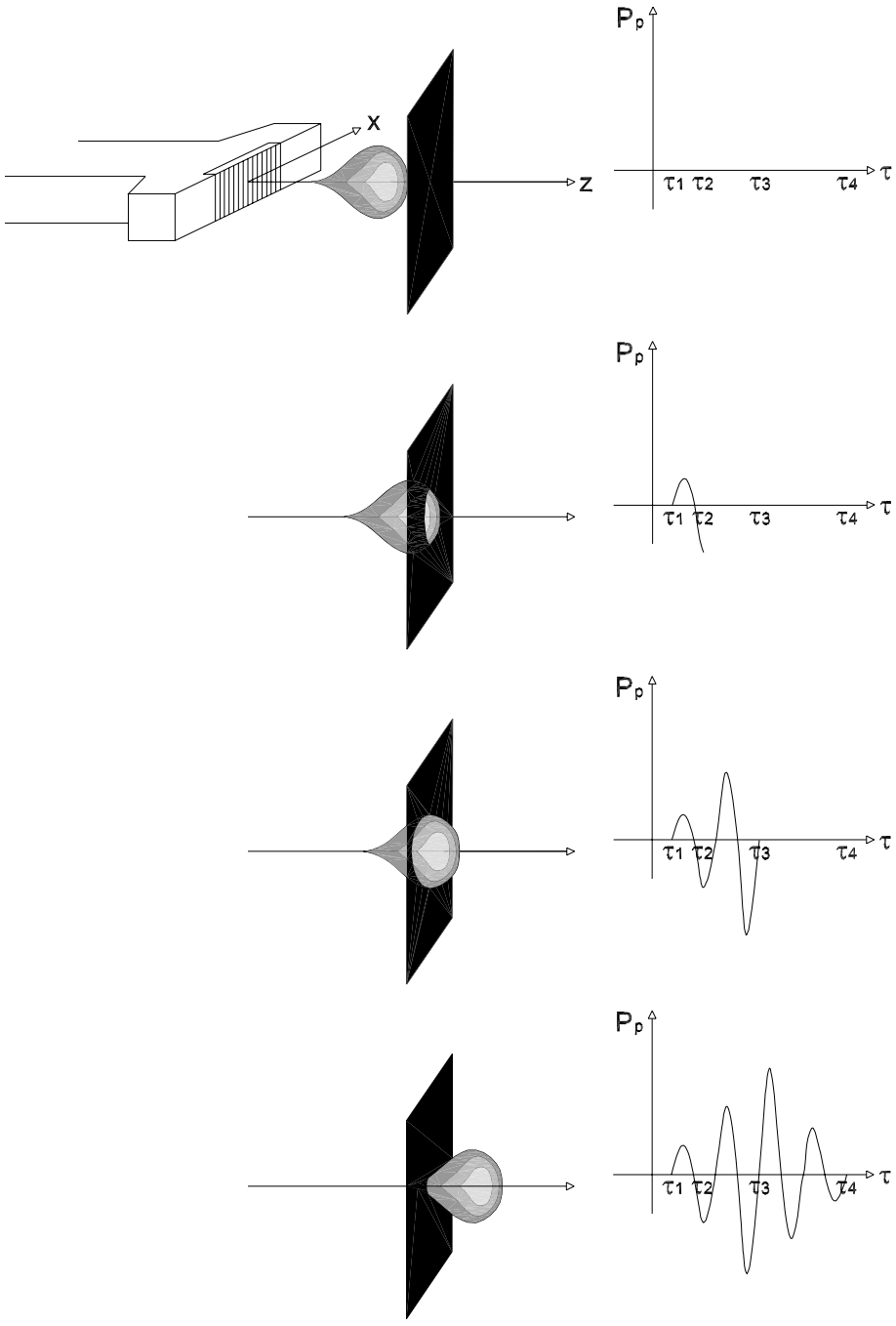

Figure 2.12: Illustration of the integration procedure. The 3D pulse is integrated over the projection plane as it propagates.

direction of the acoustic pulse, and k_x, k_y and k_z are the components of the normal vector $\mathbf{k}$ along the x-, y-, z-axes respectively. For plane waves, an iso-phase surface in space is a 3D plane with a constant value. It defines the wavefront, and the surface can be described as $\mathbf{k} \cdot \mathbf{s} = k_x x + k_y y + k_z z = \text{constant}$.
A 1D signal is calculated for the propagating pulse passing through the projection plane over which the integration is performed. Performing an integral over a $\mathbf{k}$-plane results in a time function describing the pulse shape for this particular plane wave propagating in the $\mathbf{k}$ direction. The situation is illustrated in Figure 2.12
. Each value in the temporal function $P(\mathbf{k}, \tau)$ for a pulse $p(\mathbf{s}, t_0)$ at a specific time t_0 is

calculated as the integral of the pulse in the plane given by $\mathbf{k}$. The surface integral, using the $\mathbf{k}$-plane, of the propagating pulse at a specific time is calculated. Thus, for each value of $\mathbf{k}$ there is a local time function as a result of the surface integration. Compared to previous work of Leeman and Healey, this approach incorporates time dependence in the directivity function, named $P(\mathbf{k}, \tau)$. Here the time is local time. The propagation of the bounded plane wave is performed in the global time domain on $P(\mathbf{k}, \tau)$ according to the time delay from one location of the axis of the propagation direction to the new location. This approach is referred to as pulsed plane wave decomposition and is closely related to the Leeman approach. The key issue is the use of plane wave projections.
The projections are calculated as the integral over the $\mathbf{k}$-plane. The orientation of the integration plane is given by two angles θ and ϕ. A new rectangular coordinate system is introduced, that is rotated relative to first one in order to describe the mathematical foundation of the calculation method. One coordinate system is used to describe the propagating pulse and the other to describe the integration over the $\mathbf{k}$-plane. A rotation of the coordinate system is used to align the new coordinate system to the $\mathbf{k}$-plane. The coordinates change from $\mathbf{s}$ to $\mathbf{s^k}$. The origin of the coordinate system is the pivot point of the integration plane. With the proper choice of angle definitions, the Jacobian for the coordinate rotations will be one, *i.e.*

$$dxdydz = dx^k dy^k dz^k. \tag{2.95}$$

This relation makes it possible to perform an integration with respect to a coordinate system that follows the wave number of the integration plane.
The integration over the plane, with reference to the rotated coordinate system, is given by

$$P_{(p)}\left(z^k, t\right) = \int \int_{-\infty}^{\infty} dx^k dy^k p(x^k, y^k, z^k, t). \tag{2.96}$$

The new coordinate system $\mathbf{s^k} = (x^k, y^k, z^k)$ is chosen to have the z^k-axis parallel to the normal vector $\mathbf{k}$. The new coordinate system simplifies the plane integral and the result is an projection onto the (z^k, t)-plane.
A relation between $P(\mathbf{k}, t)$ and the projection $P_{(p)}\left(z^k, t\right)$ will be established in the following. In the context of pulsed propagating plane waves only the 3-D spatial Fourier transform must be considered because the global time dimension is fixed at t_0. Thus, (2.88) and (2.89) becomes

$$p(\mathbf{s}, t_0) = \frac{1}{(2\pi)^3} \int\int\int_{-\infty}^{\infty} P(\mathbf{k}, t_0) \exp(j(\omega t_0 - \mathbf{k} \cdot \mathbf{s}))\, d\mathbf{k} \tag{2.97}$$

$$P(\mathbf{k}, t_0) = \int\int\int_{-\infty}^{\infty} p(\mathbf{s}, t_0) \exp(-j(\omega t_0 - \mathbf{k} \cdot \mathbf{s})\, d\mathbf{s}. \tag{2.98}$$

The local time τ, *i.e.* a displacement $\varepsilon = c\tau$ in the propagation direction z^k, is introduced as a third variable relative to the position $\mathbf{s}$

$$p(\mathbf{s}, t_0, \tau) = \frac{1}{(2\pi)^3} \int\int\int_{-\infty}^{\infty} P(\mathbf{k}, t_0, \tau) \exp(j(\omega t_0 - \mathbf{k} \cdot \mathbf{s}))\, d\mathbf{k} \tag{2.99}$$

$$P(\mathbf{k}, t_0, \tau) = \int\int\int_{-\infty}^{\infty} p(\mathbf{s}, t_0, \tau) \exp(-j(\omega t_0 - \mathbf{k} \cdot \mathbf{s})\, d\mathbf{s}. \tag{2.100}$$

$P(\mathbf{k}, t_0, \tau)$ is the time function that describes the bounded pulsed plane wave with the wave number vector $\mathbf{k}$ at a specific time instant t_0. Equation (2.99) describes a pulsed decomposition of any pulsed wave field. Using (2.99) in (2.96) the plane integral becomes

$$P_{(p)}\left(z^k, t_0, \tau\right) = \frac{1}{(2\pi)^3} \int \int_{-\infty}^{\infty} dx^k dy^k \iiint_{-\infty}^{\infty} P(\mathbf{k}, t_0, \tau) \exp(j(\omega t_o - \mathbf{k} \cdot \mathbf{s}))\, d\mathbf{k}. \quad (2.101)$$

The local time τ, which is in the z-direction, can be written as an exponential in the Fourier integral, and writing the vector in coordinate components gives

$$P_{(p)}\left(z^k, t_0, \tau\right) = \frac{1}{(2\pi)^3} \int \int_{-\infty}^{\infty} dx^k dy^k \iiint_{-\infty}^{\infty} dk_x^k dk_y^k dk_z^k P\left(k_x^k, k_y^k, k_z^k\right) \quad (2.102)$$

$$\cdot \exp\left(-j\left(k_x^k x^k + k_y^k y^k + k_z^k z^k + \omega\tau + \omega t_0\right)\right). \quad (2.103)$$

Using the definition of the delta function by its Fourier integral

$$\delta(k) = \frac{1}{2\pi} \int_{-\infty}^{\infty} dx \exp(jkx) \quad (2.104)$$

and

$$\omega = k_z c = k_z^k \frac{c}{\cos\theta \cos\phi} = k_z^k c^k \quad (2.105)$$

the plane integration becomes

$$P_{(p)}\left(z^k, t_0, \tau\right) = \frac{1}{2\pi} \int_{-\infty}^{\infty} dk_z^k P\left(0, 0, k_z^k\right) \exp\left[jk_z^k\left(z^k - c^k\tau - c^k t_0\right)\right] \quad (2.106)$$

in which $P\left(0, 0, k_z^k\right)$ indicates the collapse of two dimensions. The use of (2.104) in the x and y direction collapses the integration over $\mathbf{k}$ to the k_z-direction. The one projection $P_{(p)}$ can be written as a displacement to a location corresponding to t_1 as

$$P_{(p)}\left(z^k, t_1, \tau\right) \equiv P_{(p)}(z^k - c^k(t_0 - t_1), t_0, \tau). \quad (2.107)$$

If a pulsed field, given at a time instant t_0, has been decomposed into a set of pulsed plane waves, each of these plane waves can be propagated to any location in space and the pulsed wave field can be constructed at a new location. Here it must be emphasized that the velocity c_k used to propagate the plane wave $\mathbf{k}$ is adjusted according to the angle between the propagation direction z and the normal vector k (equal to z^k).
With this method a desired pulse at a given time t_0 can be decomposed into pulsed plane waves. Each of these plane waves can be propagated to each of the elements of an array transducer. The contribution of each propagated plane wave to a transducer element is summed up resulting in one pulse per transducer element. The pulses calculated for the elements can now be used as the excitation for the array transducer to create the original desired pulse. Thus, this tool presents a way of calculating a setup for a beamformer to create a desired field without involving any optimization scheme. The element pulses can also be used as time filters in receive mode to create a desired sensitivity function.

2.7.2 An example

Two examples are given to clarify the approach. The choice of examples is directly related to the acoustic fields used for vector velocity estimation. The examples are given in 2D in the xz-plane. The time is fixed at t_0 and the point spread function is described in xz-space. The envelope of the PSF is defined by a 2D Gaussian function where the standard deviations

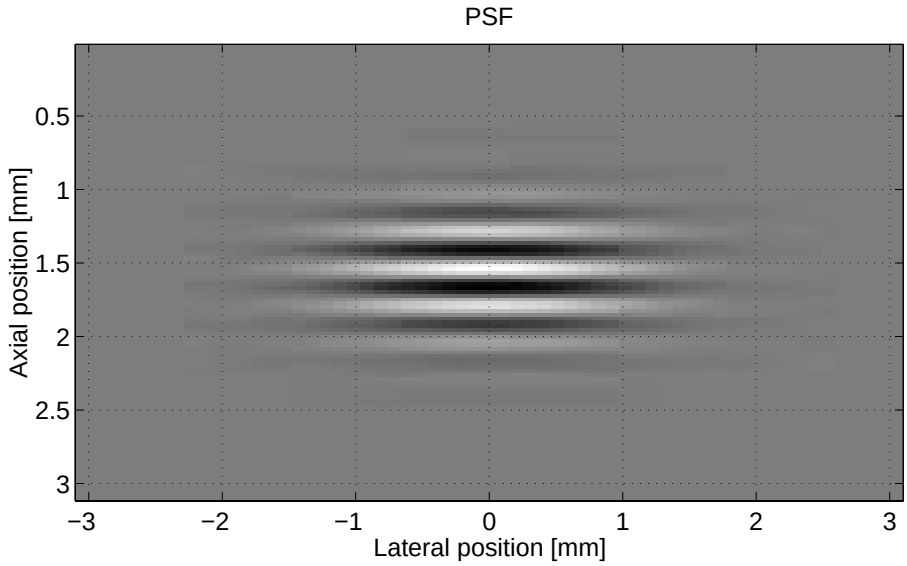

Figure 2.13: Conventional Gaussian enveloped pulsed pressure field

determine the axial and the lateral resolution. The functions limited by the envelope are harmonic functions. Either one dimensional, in the axial direction, or two dimensional, in the axial and lateral direction. These acoustic fields are analogous to the ones used for measurement of the velocities in either 1D or 2D, respectively. The results for the pulsed plane wave decomposition are calculated analytically. The calculated set of plane waves are propagated to an array transducer and summed numerically for each array element. The result reflects the required excitation for the transmit beamformer setup or the filter impulse response with delay for receive beamforming using a filter and sum beamformer.
The examples will operate only on two spatial dimensions, the lateral x- and the axial z-direction. The reduction from 3 to 2 dimensions causes the plane integral to become a line integral. The angle between the line of integration and the axis of propagation, z, is denoted θ. The integration line is named the θ-line.
The two pulses considered are

- case 1: a conventional Gaussian pulse oscillating in the axial direction with the frequency f_0, see Figure 2.13
- case 2: a 2D double oscillating field with an axial and a lateral/transverse oscillation. The lateral frequency is f_x and has the unit of $[m^{-1}]$, see Figure 2.14

The conventional Gaussian pulse is a special case of the double oscillating field. The oscillation function is denoted $f(x, z, t)$. In both cases the pulse is bounded in the axial and lateral direction by a 2D Gaussian envelope function $g(x, z, t)$. The extension of the pulse is controlled by the axial standard deviation σ_z and the lateral standard deviation σ_x. The oscillating function is

$$\begin{aligned} f(x,z,t) &= \cos(2\pi f_x x)\cos\left(2\pi f_0 \frac{z}{c} - 2\pi f_0 t\right) \\ &= \frac{1}{2}\cos\left(2\pi f_0\left(\frac{z}{c} - t\right) - 2\pi f_x x\right) + \frac{1}{2}\cos\left(2\pi f_0\left(\frac{z}{c} - t\right) + 2\pi f_x x\right) \\ &= f_1(x,z,t) + f_2(x,z,t) \end{aligned} \tag{2.108}$$

and the envelope function is

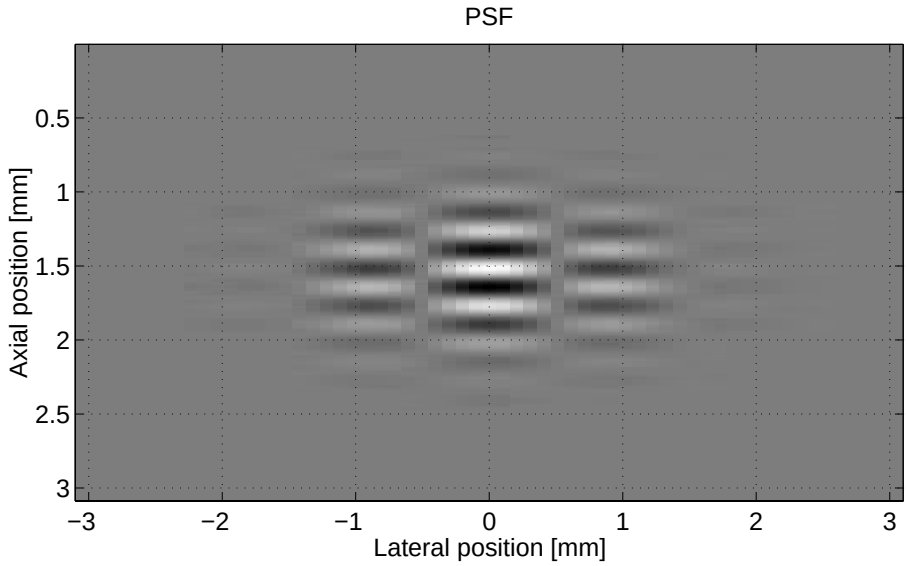

Figure 2.14: Double oscillating Gaussian enveloped pulsed pressure field

$$g(x,z,t) = \frac{1}{2\pi}\frac{1}{\sigma_x\sigma_z}\exp\left(-\frac{1}{2}\left[\left(\frac{x}{\sigma_x}\right)^2 + \left(\frac{z-ct}{\sigma_z}\right)^2\right]\right). \tag{2.109}$$

With this description, there is a geometric relation between x and z, which gives the shape of the pulse, and a time dimension which allows propagation of the pulse in local time. The field sensitivity is given by

$$h(x,z,t) = f(x,z,t)g(x,z,t) \tag{2.110}$$

and the line integral is denoted

$$H(t;\theta) = \int_{\theta-line} h(x,z,t)dxdz. \tag{2.111}$$

Thus, the pressure function in the xz plane is decomposed in the 2D-space by line integrals to a number of time functions. A line in the xz-plane is given by $z = x\tan\theta$, which is used for making the integral dependent on one variable x. An analytical solution to the line integration with θ as a parameter is given. The function $h(x,z,t)$ is divided in two functions

$$h(x,z,t) = h_1(x,z,t) + h_2(x,z,t) \tag{2.112}$$

where

$$h_1(x,z,t) = f_1(x,z,t)g_1(x,z,t) \tag{2.113}$$

$$\tag{2.114}$$

$$h_2(x,z,t) = f_2(x,z,t)g_2(x,z,t) \tag{2.115}$$

$$\tag{2.116}$$

and $h(x,z,t)$ is written as

$$
\begin{aligned}
h(x,z,t) &= h_1(x,z,t) + h_2(x,z,t) \\
&= \frac{1}{4\pi}\frac{1}{\sigma_x\sigma_z}\exp\left(-\frac{1}{2}\left[\left(\frac{x}{\sigma_x}\right)^2+\left(\frac{z-ct}{\sigma_z}\right)^2\right]\right)\cos\left(2\pi f_0\left(\frac{x\,\tan\theta}{c}-t\right)-2\pi f_x x\right) \\
&+ \frac{1}{4\pi}\frac{1}{\sigma_x\sigma_z}\exp\left(-\frac{1}{2}\left[\left(\frac{x}{\sigma_x}\right)^2+\left(\frac{z-ct}{\sigma_z}\right)^2\right]\right)\cos\left(2\pi f_0\left(\frac{x\,\tan\theta}{c}-t\right)+2\pi f_x x\right)
\end{aligned}
\tag{2.117}
$$

$h_1(x,z,t)$ and $h_2(x,z,t)$ are rewritten in the form

$$
\begin{aligned}
h_1(x,z,t) =& \frac{1}{4\pi}\frac{1}{\sigma_x\sigma_z}\exp\left(-x^2\left(\frac{1}{2\sigma_x^2}+\frac{\tan^2\theta}{2\sigma_z^2}\right)+x\frac{ct\,\tan\theta}{\sigma_z^2}-\frac{c^2t^2}{2\sigma_z^2}\right) \\
&\cdot\cos\left(x\left(2\pi\frac{f_0}{c}\tan\theta+2\pi f_x\right)-2\pi f_0 t\right)
\end{aligned}
\tag{2.118}
$$

$$
\begin{aligned}
h_2(x,z,t) =& \frac{1}{4\pi}\frac{1}{\sigma_x\sigma_z}\exp\left(-x^2\left(\frac{1}{2\sigma_x^2}+\frac{\tan^2\theta}{2\sigma_z^2}\right)+x\frac{ct\,\tan\theta}{\sigma_z^2}-\frac{c^2t^2}{2\sigma_z^2}\right) \\
&\cdot\sin\left(x\left(2\pi\frac{f_0}{c}\tan\theta+2\pi f_x\right)+2\pi f_0 t\right)
\end{aligned}
\tag{2.119}
$$

The integration in the form of

$$
\int_{-\infty}^{\infty}\exp\left(-\left(ax^2+2bx+d\right)\right)\cos\left(px^2+2qx+r\right)dx \tag{2.120}
$$

can be solved analytically, see Appendix B. The integration of $h(x,z,t)$ and the result $H_n(t;\theta)$ becomes

$$
H_n(t;\theta) = \frac{1}{4\pi}\frac{1}{\sigma_x\sigma_z}\sqrt{\frac{\pi}{a}}\exp\left(\frac{b^2}{a}-d-\frac{q_n^2}{a}\right)\cos\left(-2\frac{b}{a}q_n+r\right) \tag{2.121}
$$

with $n = 1, 2$ and

$$
\begin{aligned}
a &= \frac{1}{2}\left(\frac{1}{\sigma_x^2}+\frac{\tan^2\theta}{\sigma_z^2}\right) = \frac{1}{2\sigma_{tot}^2} \\
b &= -\frac{ct\tan\theta}{2\sigma_z^2} \\
d &= \frac{c^2t^2}{2\sigma_z^2} \\
p &= 0 \\
q_1 &= \pi\frac{f_0}{c}\tan\theta-\pi f_x \\
q_2 &= \pi\frac{f_0}{c}\tan\theta+\pi f_x \\
r &= -2\pi f_0 t.
\end{aligned}
\tag{2.122}
$$

The final solution is

$$
H(t;\theta) = H_1(t;\theta) + H_2(t;\theta)
$$

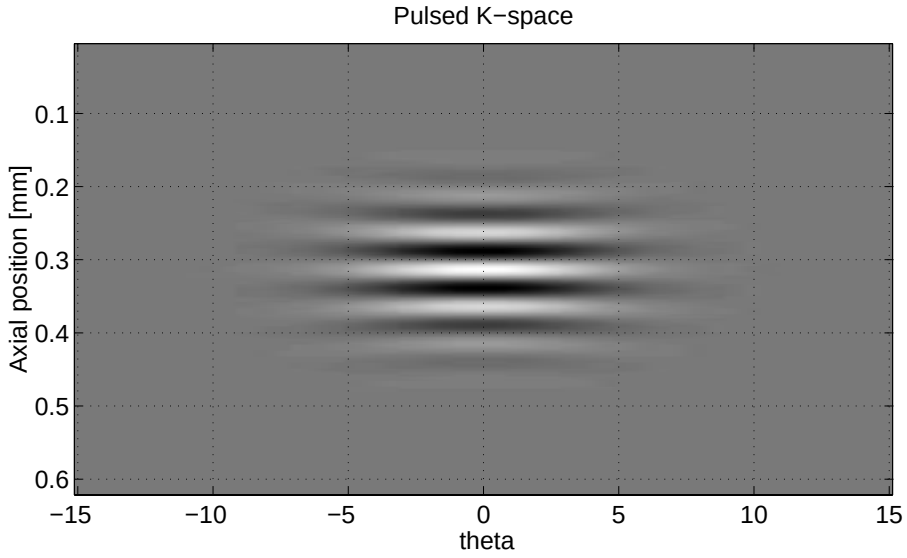

Figure 2.15: Pulsed K-space for conventional Gaussian pulse.

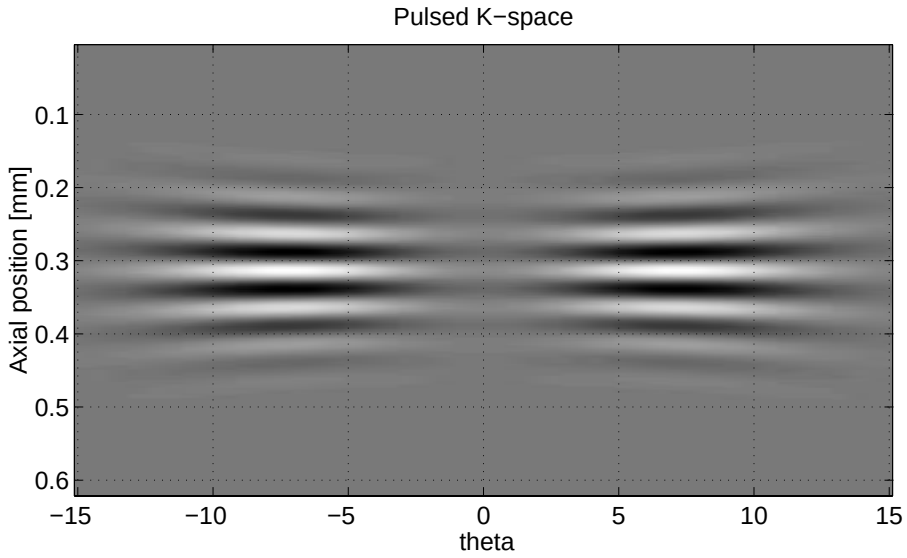

Figure 2.16: Pulsed K-space for double oscillating Gaussian pulse.

The pulsed k-space for the two examples is shown in Figure 2.15 and Figure 2.16. The abscissa is the angle between a line parallel to the x-axis and the integration line. The ordinate is the axial dimension of the pulsed plane wave. There is one time function for each angle θ.
The solution might seem a bit overwhelming and therefore some specific observations are presented to clarify some of the properties of this function.
If $\theta = 0$ then

$$H(t;0) = \frac{1}{2\pi}\frac{1}{\sigma_x\sigma_z}\exp\left(-2\pi(f_x\sigma_x)^2\right)\exp\left(-\frac{1}{2}\left(\frac{ct}{\sigma_z}\right)^2\right)\cos\left(-2\pi f_0 t\right) \tag{2.123}$$

The Gaussian enveloped axial oscillation of f_0 can be identified as the exp- and cos-terms, and the amplitude diminishes with increasing f_x or σ_x. This would be expected, since an increase in f_x or σ_x results in an increase in the number of oscillations at the integration

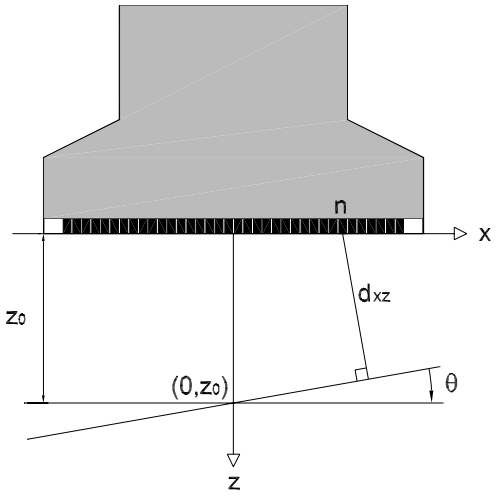

Figure 2.17: Schematics for delay calculation applied for backpropagation.

line, which causes the integrated value to diminish. Maximum axial amplitude is obtained for f_x or σ_x equals zero. Thus, no lateral oscillating field is present.
If $t = 0$ then

$$\begin{aligned} H(0;\theta) =& \frac{1}{4\pi}\frac{1}{\sigma_x\sigma_z}\exp\left(-\frac{2}{\frac{1}{\sigma_x^2}+\frac{\tan^2\theta}{\sigma_z^2}}\left(2\pi\frac{f_0}{c}\left(\tan\theta-\frac{c}{f_0}f_x\right)\right)^2\right) \\ &+ \frac{1}{4\pi}\frac{1}{\sigma_x\sigma_z}\exp\left(-\frac{2}{\frac{1}{\sigma_x^2}+\frac{\tan^2\theta}{\sigma_z^2}}\left(2\pi\frac{f_0}{c}\left(\tan\theta+\frac{c}{f_0}f_x\right)\right)^2\right). \end{aligned} \tag{2.124}$$

Again a Gaussian function can be identified. As a function of $\tan\theta$ the mean value is correctly controlled by the lateral frequency f_x. The axial wavelength is $\lambda_0 = \frac{c}{f_0}$ and the lateral oscillation period is $d_x = \frac{1}{f_x}$ therefore the mean value of the Gaussian function can be described as

$$\tan\theta = \pm\frac{\lambda_0}{d_x}.$$

This shows that an increase in f_x corresponds to a higher mean value of the Gaussian distribution in k-space. The maximum variance occurs for $\tan\theta = 0$ and decreases with increasing θ. The variance in $H(0;\theta)$ is dominated by the σ_x and the higher σ_x the narrower a distribution in k-space. As a marginal example, this demonstrates that an unbounded 2D oscillating field is made using two intersecting plane waves. This observation is in accordance with general linear acoustic theory.
Now the plane wave distribution $H(t;\theta)$ is known and the individual pulsed plane waves can be propagated to an acoustic aperture at any location in the xz-plane in order to evaluate the needed spatial distributed excitation function. The distance d_{xz} from a given integration line to an element on a linear array transducer, see Figure 2.17 for the schematics, is

$$d_{xz}(\theta, z_0, n) = p(n-\frac{1}{2})\sin\theta + z_0\cos\theta, \tag{2.125}$$

transducer	linear array
number of physical elements	128
center frequency [MHz]	6
pitch [λ]	0.05
kerf [λ]	0.95
height [mm]	2
relative bandwidth	0.60
system parameters	
sampling frequency [MHz]	300
sound speed [m/s]	1540
Number of active elements in transmit	128
Number of active elements in receive	128

Table 2.1: Parameters for transducer and system setup used for backpropagation and FieldII simulation

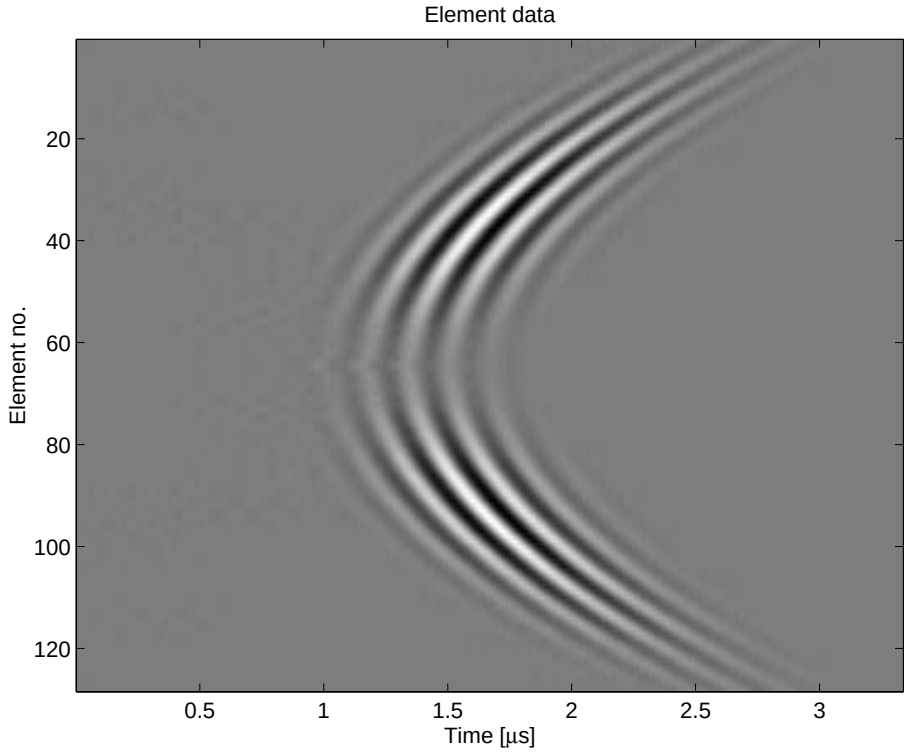

Figure 2.18: Excitation matrix for the array transducer, one row for each element.

where n is the element number, p is the pitch[8], z_0 is the rotation point on the z-axis, θ is the angle of the plane wave considered. The velocity applied to each of the θ-plane waves is corrected according to θ. The corrected velocity is

$$c_\theta = \frac{c}{\cos\theta} \tag{2.126}$$

The propagation is done for the double oscillating case, and the acoustic aperture is an array transducer defined in Table 2.1.
Figure 2.18 shows the resulting excitation for each element. The matrix has one column for

[8]Pitch is the center to center distance for two adjacent elements in an array transducer

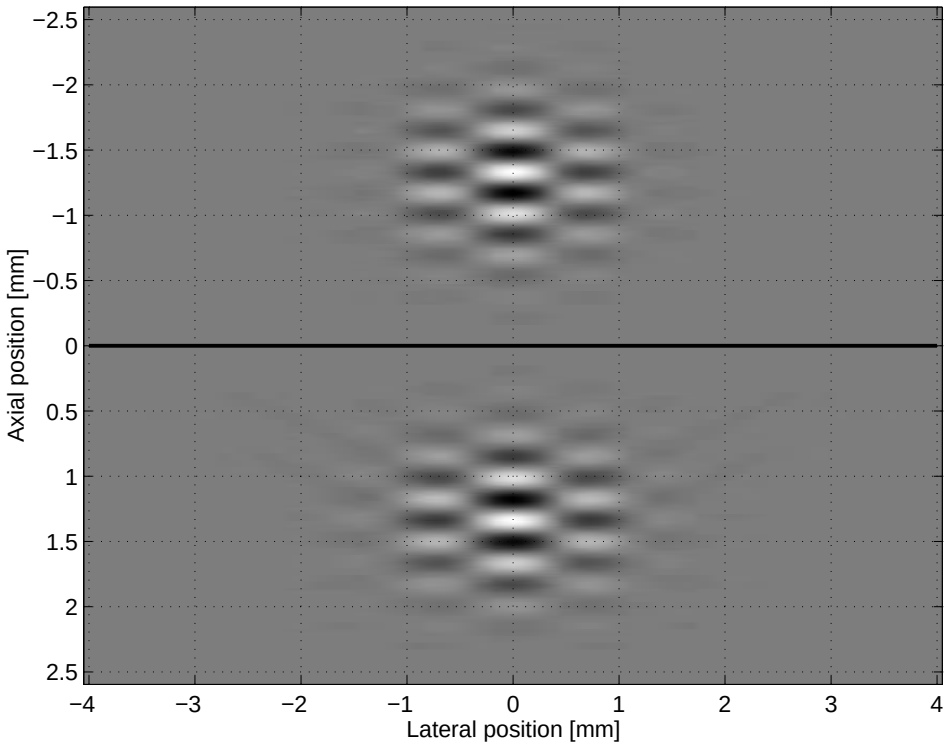

Figure 2.19: Comparison between the desired (top) field and the decomposed-backpropagated-transmitted field.

each time sample. The size of the column corresponds to the number of array elements. Thus each row is the time function associated with an element. The calculated element excitation is used for a simulation using Field II to make a comparison of the desired field with the simulated field. The result can be seen in Figure 2.19. The result shows that it is possible to analytically decompose a pulsed field into pulsed plane waves, propagate these waves to the positions of the array elements, sum up the contribution for all plane waves at the individual element, and use the analytical result of the summed pulse as an excitation for the elements of an array transducer to obtain the desired acoustic field. Figure 2.19 shows two pulsed fields which are in close agreement. The top field is the desired field and the bottom field is the beamformed field. The lateral oscillation has the correct period and the part of the simulated field, which double oscillates, resembles the original desired field.
This example also demonstrates the ability to form a desired field sensitivity by using the calculated time signal for each channel as an element temporal matched filter as described in Section 2.6 formula (2.85) and (2.86), where the beamformer is introduced. The spectrum for each element is calculated and shown in Figure 2.20 as a filled contour plot.
The maximum value in the frequency plot is found at 6 MHz at the group of elements that defines the location of the `sinc`peaks of the apodization function used in Chapter 5. The contour plot also indicates that the center frequency changes as a function of element number. To emphasize the behaviour of the center frequency and the bandwidth of each element, a normalized plot for each element is calculated and displayed in Figure 2.21.
The normalized plot shows the shift in center frequency from 5 MHz at the edge elements towards 6 MHz at the maximum frequency value and increasing slightly towards the center elements. The spectrum at the center elements are corrupted because sampling is introduced when the time traces of the individual elements are calculated by the backpropagation routine. Even though, the plot indicates the need of individual element filters to create a pulsed

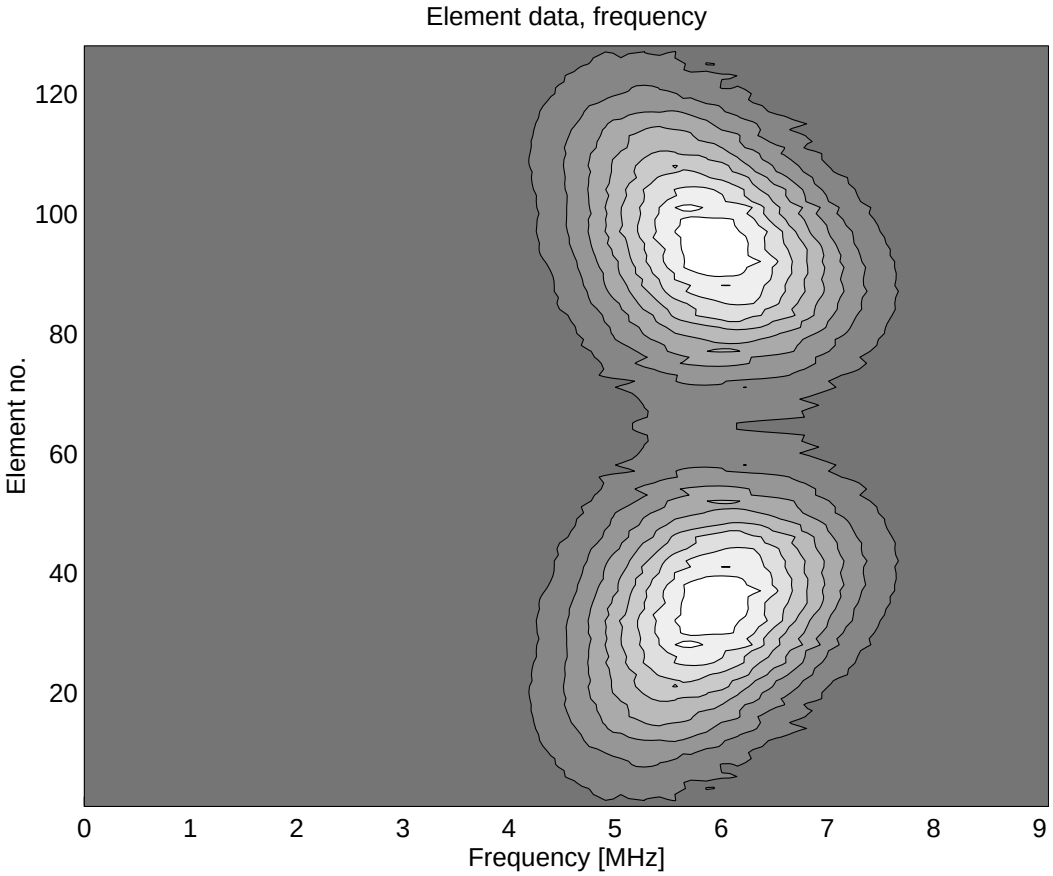

Figure 2.20: Frequency plot of element data.

field with no side lobes. Also the delay profile has to be reconsidered according to Figure 2.18.

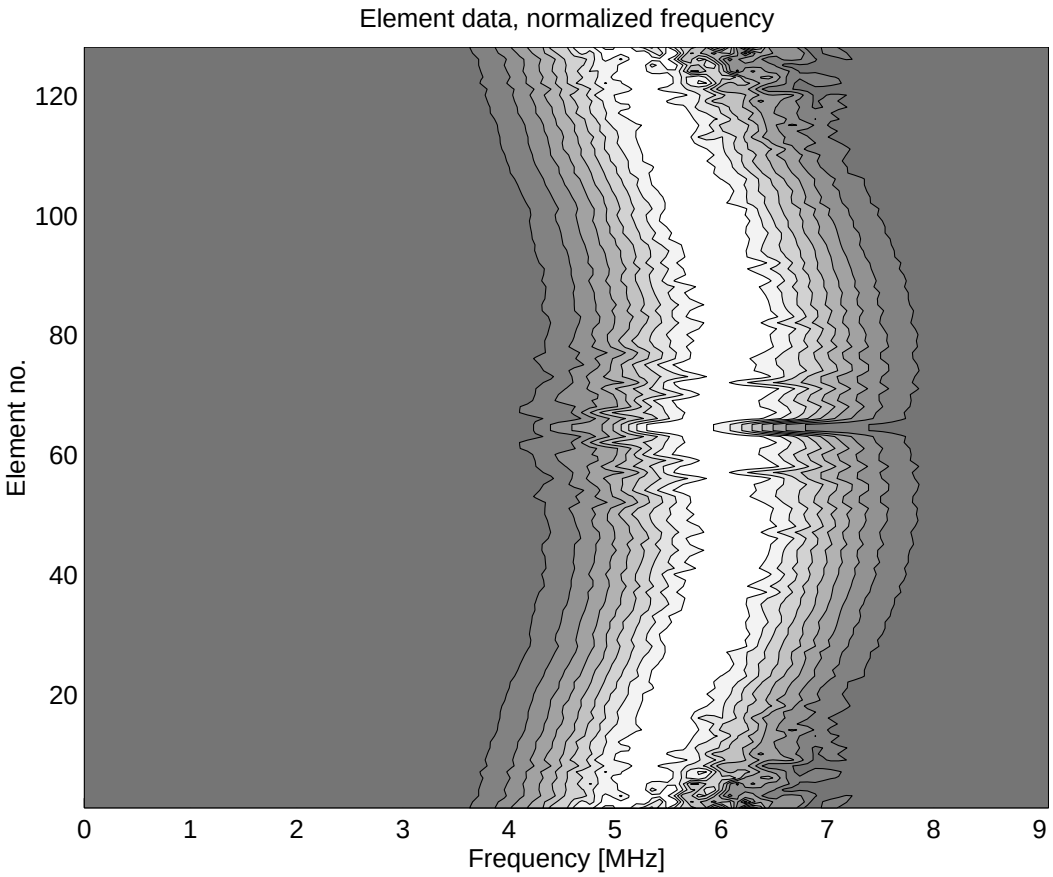

Figure 2.21: Normalized frequency plot of element data.

Chapter 3

Modeling blood flow in acoustic fields

This chapter introduces the models of laminar flow with stationary and pulsatile time functions. The models are used to move scatterers in order to simulate 3D blood flow. Basic concepts related to the physics of blood scattering and the modeling are presented. The response of the modeled scatterers moving in the acoustic field is simulated using Field II [JS92]. Imaging systems are evaluated by phantoms, which can be emulated using the method presented in Section 2.4. Forming a phantom by a group of point scatterers, images can be created to evaluate the characteristics of the interacting acoustical field [JM97].
In modern ultrasound imaging systems blood vessels are usually depicted as anechoic structures surrounded by echogenic solid soft tissues. Basically, three signal levels appear in an ultrasound image,

- the low-level: signals scattered from blood
- the mid-level: scattered from soft tissue, *e.g.* liver, spleen
- the high-level: scattered/reflected from hard tissue, *e.g.* ligament, vessel wall, organ boundaries

The early ultrasonic pulse-echo imaging systems lacked sufficient dynamic range or sensitivity for the echoes from blood to be detected due to poor SNR, and therefore flow detection was not possible. Today, state-of-the-art imaging systems depict vessels as anechoic regions in normal setup, but in some flow situations, with the imaging system set at a high gain, the flow can be seen directly in the B-mode imaging. A high dynamic range of approximately 100 dB is needed to visualize the sporadic appearance of the scattered signal from the blood in a B-mode image. The scattering strength of the vessel wall and tissue can be up to 60-80 dB higher than the scattering strength of blood. Due to the spatial extension of the propagating acoustic pulse of 4-8 wavelengths, the weak flow signal scattered from blood interferes with the strong non-flow signal reflected from the surroundings. The situation with a signal condition of a strong pseudo-stationary[1] signal and a weak flow signal, calls for advanced filtering strategies to remove the impact of the strong signal. The choice of a proper filtering method is a science on its own, and the purpose of this work is not to evaluate the influence of stationary echo canceling, but to verify the basic ability of the proposed method to estimate vector flow. Therefore, a simple simulation scheme was used. The influence of the vessel wall and surrounding tissue on the scattered flow signals is not taken into account.

[1]The term pseudo-stationary is used since the surrounding vessel walls and tissue also move due to the pulsatile nature of the flow.

The simulation tool Field II gives a 3D frame for calculating the acoustic pulse-echo response from an infinitesimally small point reflector located at a specified position. Placing numerous scatterers in the 3D acoustic sample volume as presented in Section 2.5, and summing up the calculated response from all the scatterers, a resulting signal with speckle characteristics can be generated. This kind of signal is characterized by abrupt phase shifts. These phase shifts and the stochastic noise present in ultrasound systems are major causes for the deterioration of the performance of an estimator scheme. Thus, signals with speckle characteristics are essential for the evaluation of an estimation scheme. Models of the stochastic nature of speckle can be devised, but it must be kept in mind that the created signal depends on the characteristics of the acoustic pulse and that the acoustic pulse globally is spatially non-stationary. Therefore the stochastic characteristics of the received signal change with position. Field II is used in order to incorporate the influence of the acoustic sample volume. Models for three different profiles are devised:

- stationary plug flow,
- stationary parabolic flow,
- pulsatile parabolic flow.

The stationary plug and parabolic flow profile are used for testing the estimators. The pulsatile parabolic flow is used to visualize the signal conditions present for flow estimation, and to underline the possible use of line detection by the new 2D FFT-Radon approach given in Chapter 4.

3.1 Modeling Flow

This section gives a short description of basic flow physics. The flow is modeled for rigid circular tubes and it is assumed that there are no entrance effects.

3.1.1 Motion equation

In 1955, Womersley established an equation that describes the motion of a liquid in a tube with time-varying circular symmetric laminar flow $v(r,t)$ given by [NO90]

$$\frac{\partial^2 v(r,t)}{\partial r^2} + \frac{1}{r}\frac{\partial v(r,t)}{\partial r} + \frac{1}{\mu}\frac{\partial p(r,t)}{\partial z_{tube}} = \frac{1}{\Lambda}\frac{\partial v(r,t)}{\partial t}. \tag{3.1}$$

The liquid has density ρ and viscosity μ, and it is assumed Newtonian. The kinematic viscosity is defined by

$$\Lambda = \frac{\mu}{\rho}. \tag{3.2}$$

The velocity parallel to the tube axis z_{tube} is $v(r,t)$. The distance r is measured from the center of the straight circular tube and is limited by the radius of the tube R.

3.1.2 Stationary flow

The flow model can be simplified considerably for stationary conditions, *i.e.* no time dependence,

$$\frac{\partial v\left(r,t\right)}{\partial t}=0. \tag{3.3}$$

With this condition the partial differential equation becomes

$$\frac{\partial^2 v\left(r,t\right)}{\partial r^2}+\frac{1}{r}\frac{\partial v\left(r,t\right)}{\partial r}=-\frac{1}{\mu}\frac{\partial p\left(r,t\right)}{\partial z_{tube}}=\text{const.} \tag{3.4}$$

The parabolic flow profile is a solution given by

$$v\left(r\right)=v_0\left(1-\left(\frac{r}{R}\right)^2\right) \tag{3.5}$$

where v_0 is the maximum velocity at the center of the tube, R is the radius of the tube, and r is the radial position. The plug flow, which defines the velocity to be constant and independent of the radial position, is also a solution

$$v\left(r\right)=v_0. \tag{3.6}$$

These two profiles are used to evaluate the estimators presented in Chapter 5.

3.1.3 Pulsatile flow

In this section a brief presentation of a model for pulsatile flow is given. It is included to give the foundation used for simulation of pulsatile flow data.
For pulsatile flow, the profile changes as function of time, and therefore is a more complicated phenomenon to model. The analysis of pulsatile flow can be performed by separation of space and time. The time function is decomposed into its harmonics, and the flow profile is treated separately for each frequency component.
Let the spatial function be a rotationally symmetric profile and the time function harmonic. The harmonic pressure difference is given by $\Delta P\cos(\omega t-\phi)$ and the flow rate $Q\left(t\right)$. According to Womersley [Wom55] the pressure difference and the volume flow rate are related by

$$\begin{aligned} Q\left(t\right) &= \frac{8M'_{10}}{R_f\alpha^2}\Delta P\sin\left(\omega t-\phi+\varepsilon'_{10}\right) \\ \alpha &= R_f\sqrt{\frac{\rho}{\mu}\omega} \\ R_f &= \frac{8\mu L}{\pi R^4} \end{aligned} \tag{3.7}$$

where α is named Womersley's number and ϕ is a constant phase shift and ω is the angular frequency. The wave is determined by the amplitude M'_{10} and the phase ε'_{10}. For calculation of M'_{10} and ε'_{10} refer to Appendix C.

For a steady state pulsatile flow, the flow profile can be calculated as a function of time based on the flow rate. For each temporal harmonic m, the velocity $v_m\left(t, \frac{r}{R}\right)$ as a function of radius and time is calculated by Evans [Eva2a], [Eva2b]

$$\begin{aligned} v_m\left(t, \frac{r}{R}\right) &= \frac{1}{\pi R^2} Q_m \left|\Psi_m\left(\frac{r}{R}, \tau_{\alpha_m}\right)\right| \cos\left(\omega_m t - \phi_m + \chi_m\right) \\ \Psi_m\left(\frac{r}{R}, \tau\right) &= \frac{\tau_{\alpha_m} J_0\left(\tau_{\alpha_m}\right) - \tau_{\alpha_m} J_0\left(\tau_{\alpha_m} \frac{r}{R}\right)}{\tau_{\alpha_m} J_0\left(\tau_{\alpha_m}\right) - 2 J_1\left(\tau_{\alpha_m}\right)} \\ \chi_m &= \angle\left(\Psi_m\left(\frac{r}{R}, \tau\right)\right) \\ \tau_{\alpha_m} &= J^{\frac{2}{3}} R \sqrt{\frac{\rho}{\mu} \omega_m} \end{aligned} \tag{3.8}$$

where $J_n(\cdot)$ is the nth order Bessel function of the first kind. The mean spatial velocity $\overline{v}(t)$ is related to the volume flow rate by the area of the tube by:

$$Q(t) = A\overline{v}(t) \tag{3.9}$$

The flow profile can be calculated, spatially and temporally, on the basis off the mean velocity using (3.8), (3.8) and (3.9). The approach is as follows: The temporal function of the mean spatial velocity is decomposed into its Fourier coefficients. For each harmonic, the resulting time-dependent flow profile can be calculated using (3.8). Assuming linearity, the resulting time-dependent velocity profile can be determined by summation of each harmonic solution to (3.8). Linearity can be assumed for Newtonian fluids. The following reconstruction formula summarizes the calculation method for the pulsatile flow profile on the basis of a known mean spatial velocity:

$$v\left(t, \frac{r}{R}\right) = 2v_0\left(1 - \frac{r^2}{R^2}\right) + \sum_{m=1}^{\infty} |V_m| \left|\Psi_m\left(\frac{r}{R}, \tau_{\alpha_m}\right)\right| \cos\left(\omega_m t - \phi_m + \chi_m\right) \tag{3.10}$$

where V_m is amplitude of the mth harmonic of the mean velocity $\overline{v}(t)$. Note that the first term in (3.10) corresponds to the stationary flow and is a parabolic profile. The function $\Psi_m\left(\frac{r}{R}, \tau_{\alpha_m}\right)$ links the spatial and temporal dependence of the profile solutions.
This model is used to calculate RF data from a computer phantom with pulsatile flow.

3.2 Scattering by blood.

This section briefly discusses the physics of blood scattering and how it is modeled to be used with the Field II program.

3.2.1 Physics of blood scattering

Scattering from blood is caused by particles suspended in blood. The blood is a complex fluid with several components and it has been established that the erythrocytes (the red blood cells) are the dominant scattering components [SSR76], when ultrasound interacts with blood. An individual erythrocyte is a biconcave disk, about 7 μm in diameter and with a maximum thickness of 2 μm. The mean corpuscular volume is 87 μm^3. The ratio of the total erythrocyte volume to the total blood volume is the haematocrit. The haematocrit is typical 40% for healthy adults. Typically it is 5% higher for men and 5% lower for women.

For a blood sample with a haematocrit of 45 %, the average distance between two red cells is about 10 percent of its diameter. Therefore, their motion will be hindered by the presence of other particles. Thus, the particles can not be considered independent on each other. There are approximately $5 \cdot 10^9$ erythrocytes per milliliter of whole blood which accounts for 98 % of the blood particles.
A cubic blood sample, each side equal to the wavelength of a 3 MHz pulse, will contain over a million red blood cells. At the ultrasonic frequency of 3 MHz, the wavelength is 0.5 mm. Thus, an individual erythrocyte is two orders of magnitude smaller than the wavelength. It thereby fulfills the condition to be a Rayleigh scatterer and is considered as such. When Rayleigh scattering is present the backscattered power increases with the fourth power of the frequency. The choice of the ultrasonic frequency that gives the maximum signal-to-noise ratio for echoes detected from blood is determined by the compromise between the backscattering of blood, which increases with frequency, and the attenuation of the ultrasound carrier, which also increases with frequency. The backscattered power versus haematocrit has been published by Shung [SSR76].

3.2.2 Modeling blood scattering

Several suggestions for modeling blood scattering can be found in the literature. A few will be reviewed here and the method employed in this work will be presented.
There are different ways to approach the problem of simulating signals from blood. Two basic approaches are briefly described. First, the statistical characteristics of the backscattered signal can be calculated with a mathematical model of the interaction between the scattering medium and the acoustic pulse. Second, a simulation of the acoustic field, 2D/3D, is used to calculate responses from individual scatterers, which are finally summed. In general terms, the first method emphasizes the complexity of the scattering medium and the second method emphasizes the complexity of the acoustic field. The second method is named the particle approach.
In modeling the scattering process, blood can be treated as a suspension of point scatterers [BM74]. This approach assumes that the scatterers to behave as uncorrelated scatterers, which neglects the fact that the erythrocytes interact strongly, because they are quite closely packed. Angelsen [Ang80] incorporated the interaction in his model by treating blood as a continuous medium characterized by fluctuations in mass density and compressibility. The situation is further complicated by the tendency of erythrocytes to aggregate, forming rouleaux that can survive under normal flow conditions, as described by Machi [MSB+83]. This indicates that even more complicated models could be developed. On the other hand, sometimes simple methods are needed to give an overview. In the work by Mo [MC86], a stochastic model for CW-Doppler signals is presented. With some simplifications, it is concluded that the basic statistic properties of ultrasound backscattered by blood can be characterized as a zero-mean, stationary Gaussian random process. This allows the signal to be completely specified by its autocorrelation function. Some of the different approaches suggested in the literature are categorized in another work by Mo et al. [MC92], in which an unifying approach towards the description of Doppler signals is presented.
In this work the particle approach is used to calculate the scattered response. The signal generated by numerous scatterers interacting with a 3D acoustic field is based on a summation of the complex acoustical responses of the individual scatterers. The argument against this approach is that it does not include the close packing of the erythrocytes. The applied flow model in this work does only include laminar flow for the evaluation of the estimators. Thus, the scatterers will have the same relative position which causes the scatterers to ap-

pear closely packed. The primary goal is not to develop a detailed model for blood scattering that includes all subtle phenomena of blood dynamics, but to obtain scattered signals that exhibit the random fluctuations denoted as speckle. The choice of scatterer density is subject to a compromise to make the calculation time feasible. Matching the density of the red blood cells of approximately $5 \cdot 10^9$ erythrocytes per milliliter, the calculation load would be unrealistic. The simulation time is linearly proportional to the number of scatterers. In order to obtain a reasonable simulation time, it is necessary to reduce the scatterer density to a much lower level than implied by the number of red blood cells. The imaging system can be described by its resolution cell (volume). The size of this cell is determined by the 3-D point spread function defined by the 6 dB limits for the axial, lateral and transversal dimension. The limit in wavelengths for a typical Doppler burst is 10 λ, for the lateral beam width 6 λ, and for transversal beam width 10 λ. which equals a volume of 600 λ^3. As a rule of thumb, to obtain fully developed speckle, the number of scatters in the resolution cell must exceed 10 [RMZ90]. The density of scatterers is chosen to $2/\lambda^3$.
Finally, the scatterer characteristics must be defined. A scatterer can have different properties depending on the size and form, and the physical properties, *i.e.* rigid or elastic. For a rigid body, Rayleigh scattering occurs when the circumference is much smaller, *i.e.* 10 times, than the wavelength. Every scatterer is considered to be a rigid and infinitesimal small reflector having an omnidirectional directivity function. The scatterers are modeled by a real reflection coefficient with a value given by a Gaussian distribution with zero mean and a variance that controls the scattering strength. The larger the variance, the stronger the scattering. The position of the scatterers are uniform distributed in space, which will provide a random phase, when summing up the individual contributions.

3.3 Simulation of blood flow

This section presents the procedure used for blood flow simulations. The tools used are MATLAB by Mathworks and Field II. The Field II program is written in C, which interfaces to MATLAB, where the advanced toolboxes, *e.g.* signal processing, statistics and image processing, and display facilities are available. Field II has numerous features and presents an effective acoustic simulation toolbox to evaluate imaging systems by fast and simple means. Several predefined transducers exist, like single piston, 1D-array and 2D-array, and both transmitted and pulse-echo field characteristics can be calculated.
In this work 1D-arrays are used. The transducer is defined by its geometry and the beamformer setup. The scatterers are defined by position and amplitude. The scatterers are moved according to the flow profile for each time instant to calculate the scattered responses.

3.3.1 Distribution of scatterers in a tube

The scatterers have to be distributed according to the flow configuration considered. The most common used flow phantom is the straight tube of a given length and radius. The number of scatterers to be used is determined according to the acoustic sample volume. The position and scattering amplitude of the scatterers are determined by random numbers. In MATLAB, random numbers can only be generated with a Gaussian and a uniform distribution. The uniform distribution is ascribed values between 0 and 1, and is named Π_0^1. The Gaussian distribution has a zero mean with variance 1. Other distributions are calculated on the basis of the uniform and the Gaussian distribution.
The position of the scatterers must be in rectangular coordinates, (x, y, z). Because the

tube is modeled in polar coordinates (r, θ) and the scatterers are distributed randomly by a uniform distribution in rectangular coordinates in space, a transformation process is needed. If a stochastic variable with a known distribution function is used as an argument for a function, then the distribution function of the result can be calculated [Jøe87]. Under certain restrictions this holds for both one- and two-dimensional problems. The distribution function corresponds to the density function of the scatterers. The following derivation is from [Mun96].
The unscaled distribution function required for this simulation is

$$h(y,z) = \begin{cases} \frac{1}{\pi} & \text{for} \quad y^2 + z^2 < 1 \\ 0 & \text{for} \quad y^2 + z^2 > 1 \end{cases} \tag{3.11}$$

The transform of the stochastic variables from a polar coordinate system to rectangular coordinate system is

$$\begin{aligned} Y &= R \cdot \cos\Theta \\ Z &= R \cdot \sin\Theta \end{aligned} \tag{3.12}$$

or written in a compact form

$$\varphi(R,\Theta) = (\varphi_1(R,\Theta), \varphi_2(R,\Theta)) = \tau^{-1}(R,\Theta) = (R\cos\Theta, R\sin\Theta) \tag{3.13}$$

giving the inverse function $\varphi^{-1} = \tau$ of

$$\tau(Y,Z) = \left(Y^2 + Z^2, \arctan\left(\frac{Z}{Y}\right)\right) \tag{3.14}$$

According to [Jøe87], the two dimensional stochastic variable

$$(R,\Theta) = \tau(Y,Z) = (\tau_1(Y,Z), \tau_2(Y,Z)) \tag{3.15}$$

has the distribution function of

$$k(r,\theta) = \begin{cases} h(\varphi_1(r,\theta)\,\varphi_2(r,\theta)) \left|\det \varphi'(r,\theta)\right| & \text{for} \quad 0 < r < 1\ ,\ 0 < \theta < 2\pi \\ 0 & \text{otherwise} \end{cases} \tag{3.16}$$

where det is the Jacobi determinant. For this problem the derivatives of φ are

$$\begin{aligned} \frac{\partial\varphi_1}{\partial r} &= \cos\theta \\ \frac{\partial\varphi_1}{\partial\theta} &= -r\sin\theta \\ \frac{\partial\varphi_2}{\partial r} &= \sin\theta \\ \frac{\partial\varphi_2}{\partial\theta} &= r\cos\theta \end{aligned} \tag{3.17}$$

yielding the determinant

$$\det\left(\varphi'(r,\theta)\right) = \begin{vmatrix} \cos\theta & -r\sin\theta \\ \sin\theta & r\cos\theta \end{vmatrix} = r \tag{3.18}$$

Thus the distribution becomes

$$k(r,\theta) = \begin{cases} \frac{r}{\pi} & \text{for} \quad 0 < r < 1\ ,\ 0 < \theta < 2\pi \\ \\ 0 & \text{for} \qquad\quad \text{otherwise} \end{cases} \tag{3.19}$$

which can be written as two stochastically independent variables $k(r,\theta) = k_r(r) \cdot k_\theta(\theta)$. Using that, the problem is rotation symmetric then

$$k_r(r) = \begin{cases} 2r & \text{for} \quad 0 < r < 1 \\ 0 & \text{otherwise} \end{cases} \tag{3.20}$$

$$k_\theta(\theta) = \begin{cases} \frac{1}{2\pi} & \text{for} \qquad 0 < \theta < 2\pi \\ 0 & \text{otherwise} \end{cases} \tag{3.21}$$

The problem is now simplified to find the function that transforms the uniform distribution to a ramp distribution function. If $R = \tau(X)$ where X has the distribution function $f(x)$ the frequency function for R is given by

$$k_r(r) = \begin{cases} f(\tau^{-1}(r)) \cdot \left|(\tau^{-1})'(r)\right| & \text{for} \quad 0 < r < 1 \\ 0 & \text{otherwise.} \end{cases} \tag{3.22}$$

With $f(x) = \Pi_0^1$ then $f(\tau^{-1}(r)) = 1$ and the problem becomes straightforward. The function τ must satisfy

$$\left(\tau^{-1}\right)'(r) = 2r \tag{3.23}$$

yielding

$$r = \tau(x) = x^{1/2}. \tag{3.24}$$

The procedure to generate the scatterer field is briefly summarized in the following. The angular distribution is Π_0^1, scaled by 2π, and the radius distribution is the square root of Π_0^1, scaled by the radius of the tube. These two data set are transformed to y and z positions. Further the x position is Π_0^1 , scaled to the length of the tube used for the simulation. This gives a description in rectangular coordinates of a tube of scatterers with a random distribution in space. The scattering amplitude of the scatterers is Gaussian with mean zero and variance one. The variance controls the scattering strength of a volume with scatterers. In imaging phantoms, different scattering strengths are obtained, using different variances for different areas. In this work only one level of scattering strength is needed to evaluate flow and the variance is chosen to be one.

3.3.2 Moving the scatterers

The scatterers are moved according to the flow profile. Only laminar flow is considered and the scatterers are displaced according to their radial positions in the circular tube. The scattered signal is repeatedly calculated with a time interval T_{prf}. The scatterers are moved from one pulse emission to the next. Because the number of scatterers determine the simulation time, the size of tube should be minimized. The choice of radius of the tube is based on considerations on the imaging frequency, the pulse length and desired signal length.

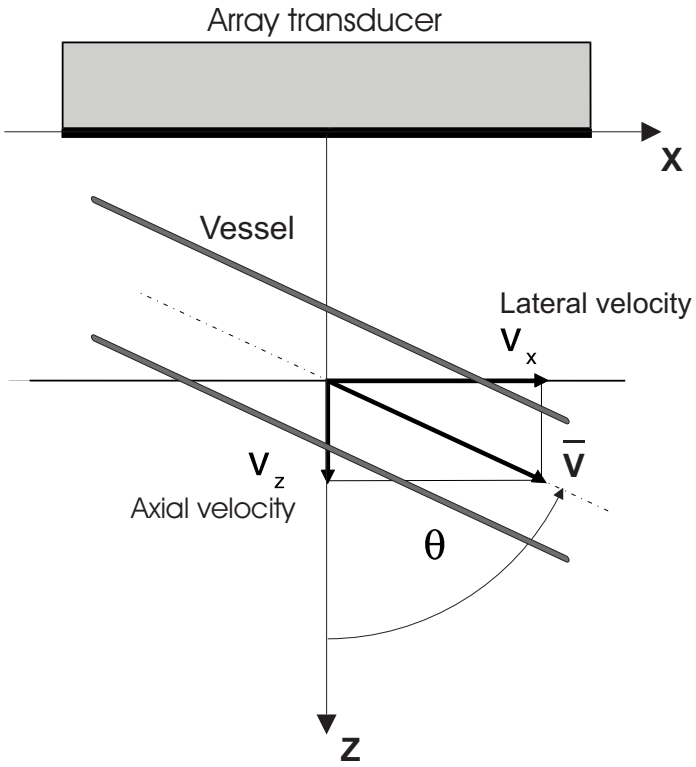

Figure 3.1: Simulation setup. The vessel is rotated by θ and displaced to depth z_0.

To minimize the number of scatterers, the length of the tube should correspond to the lateral extension of the acoustic field. The shorter the tube, the fewer scatterers, and the faster the simulation. In order not to keep track of the scatterer density, a recycle strategy is applied. Since only laminar flow is considered, it is easy to reposition the scatterers as they move beyond the tube delimitation. The scatterers are moved accordingly to their radial position and do not change radial position. The movement for a given radial position depends on the type of flow profile chosen. When the scatterers are recycled, they are assigned new radial positions and amplitudes. The axial position is changed by the length of the tube. The reassignment of radial position and amplitude is necessary to avoid repeated patterns in the RF-data.
The tube can be positioned at any spatial location and rotated by an angle. To keep the calculations simple, the displacement of the scatterers are performed for the tube axis parallel with the x-axis. This approach, causes the translation to be calculated in only one dimension. Subsequently the tube is rotated according to the flow angle and translated to a specified position in depth.

3.3.3 Positioning the scatterers

The positioning is illustrated in Figure (3.1). In matrix notation the rotation and the displacement of the position matrix to the specified depth z_0 in the field, becomes

$$\begin{pmatrix} x_f \\ y_f \\ z_f \end{pmatrix} = \begin{pmatrix} \cos\theta & 0 & \sin\theta \\ 0 & 1 & 0 \\ -\sin\theta & 0 & \cos\theta \end{pmatrix} \cdot \begin{pmatrix} x \\ y \\ z \end{pmatrix} + \begin{pmatrix} 0 \\ 0 \\ z_0 \end{pmatrix} \tag{3.25}$$

3.3.4 Field II procedure

The Field II program utilizes MATLAB as the interface for the setup of the simulation. The basic setup for preparing a simulation can briefly be listed as

- define position of scatterers/reflectors
- define physical layout of transducer
- define sampling frequency
- define active transmit aperture
- define transmit impulse response
- define transmit calculation reference point
- define active receive aperture
- define receive impulse response
- define receive calculation reference point
- define excitation pulse
- define transmit apodization
- define transmit delay
- define receive apodization
- define receive delay

The setup can for some part be calculated based on parameters *e.g.* focus point (x, y, z) or be fully controlled by delay and apodization matrices calculated by the user. For a given setup several options for field calculations are given. The emitted pressure field, the pulse-echo field, and the summed voltage trace from a collection of scatterers have been the most used in this work. For further details refer to 'Users guide for the Field II program'[2].
The diagram of the simulation procedure is shown in Figure (3.2).

3.4 Flow examples

Three types of flow examples are shown to illustrate the signal conditions present for flow estimation. These are:

- plug flow
- parabolic flow
- pulsed flow

[2]All program files and documentation are available at http://www.it.dtu.dk/~jaj/field.

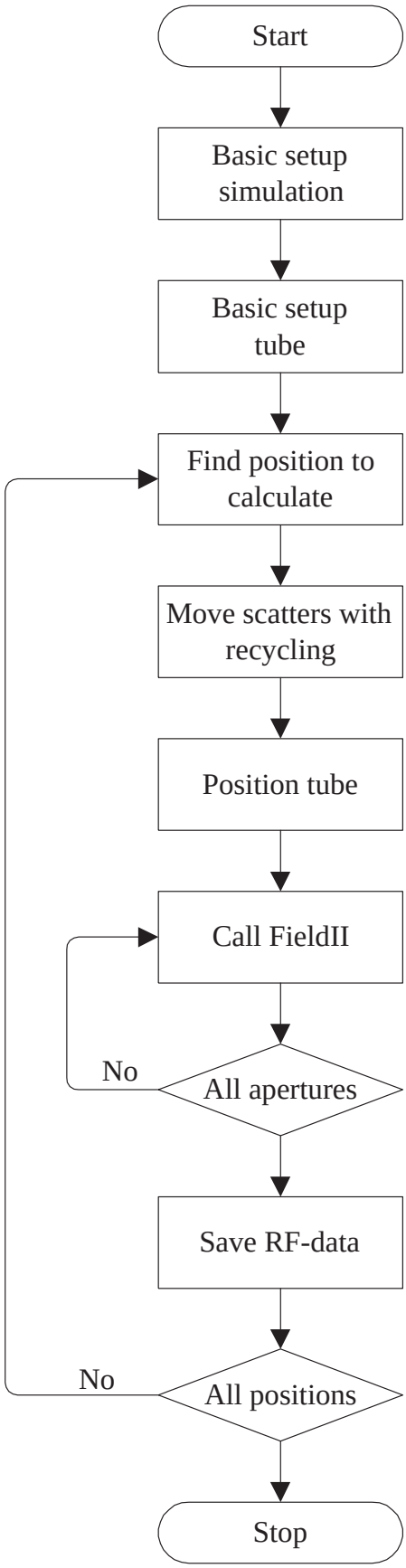

Figure 3.2: Procedure for simulation of blood flow using Field II.

transducer	linear array
number of physical elements	128
center frequency [MHz]	6
pitch [mm]	0.156
kerf [mm]	0.025
height [mm]	7
relative bandwidth	0.40

Table 3.1: Transducer parameters used for simulation.

system parameters	
sampling frequency [MHz]	100
pulse repetition frequency [kHz]	10
sound speed [m/s]	1540
transmit focal point (x,y,z) [mm]	(0 0 38.5)
number of active elements in transmit	64
receive depth (x,y,z) [mm]	(0 0 38.5)
number of active elements in receive	128

Table 3.2: System parameters used for simulation.

The results using plug and parabolic flow profiles are shown in Figure 3.3 and Figure 3.4. The basic underlying mechanism that make velocity estimation possible, is the correlation between RF-signals scattered from one emission to the next. When the blood scatterers are moving with an axial velocity component, the received signals will be displaced from one emission to the next. If the recorded RF-data are arranged in a matrix with one column for each emission and displayed, lines will appear. The slope of these lines are proportional to the axial velocity component. The principle behind a pulsed velocity estimation system is explained in more details in Chapter 4.
The simulation setup used for the plug and parabolic flow is given in Table 3.1, Table 3.2 and Table 3.3.
The transducer setup is shown in Table 3.1
The system setup is given in Table 3.2
The flow setup is given in Table 3.3
The result using a plug flow profile, given in Figure 3.3, shows the same displacement for all depths. The scattering strength decreases towards the edge of the tube because the number of scatterers interacting with the acoustic pulse decreases. The flow is towards the transducer and a constant displacement from one emission to the next can be seen. No clear lines are present due to the phenomenon of speckle.

flowparameters	
flow depth [mm]	38.5
length of tube [mm]	8
max blood velocity [m/s]	0.5
radius of tube [mm]	4
flow angle [degrees]	30

Table 3.3: Flow parameters used for simulation.

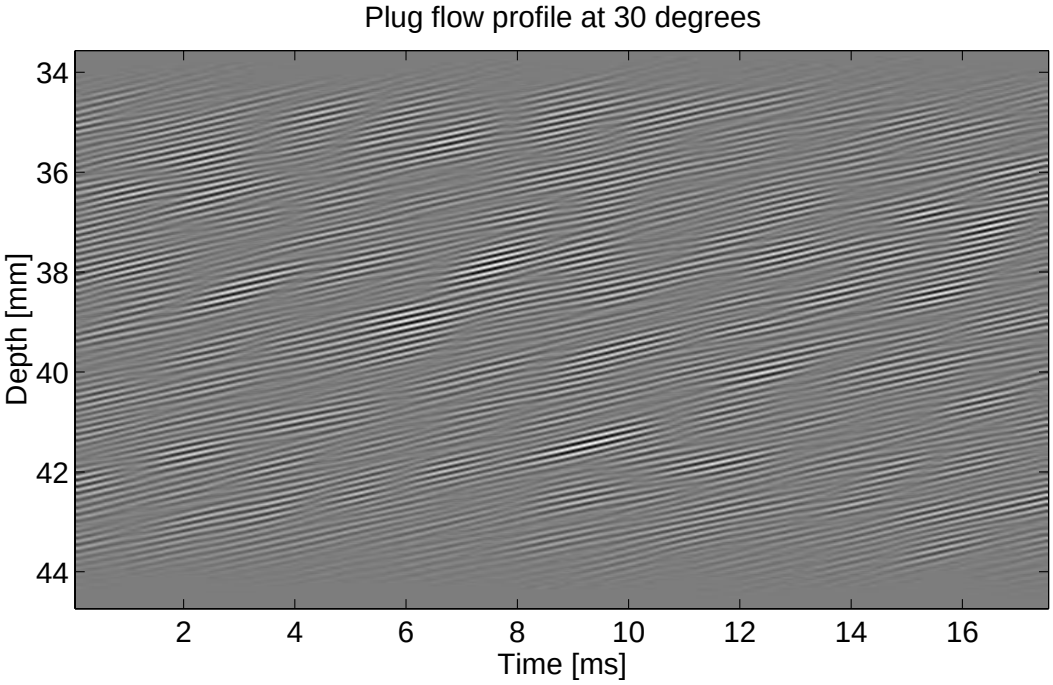

Figure 3.3: RF-lines generated using a plug flow profile.

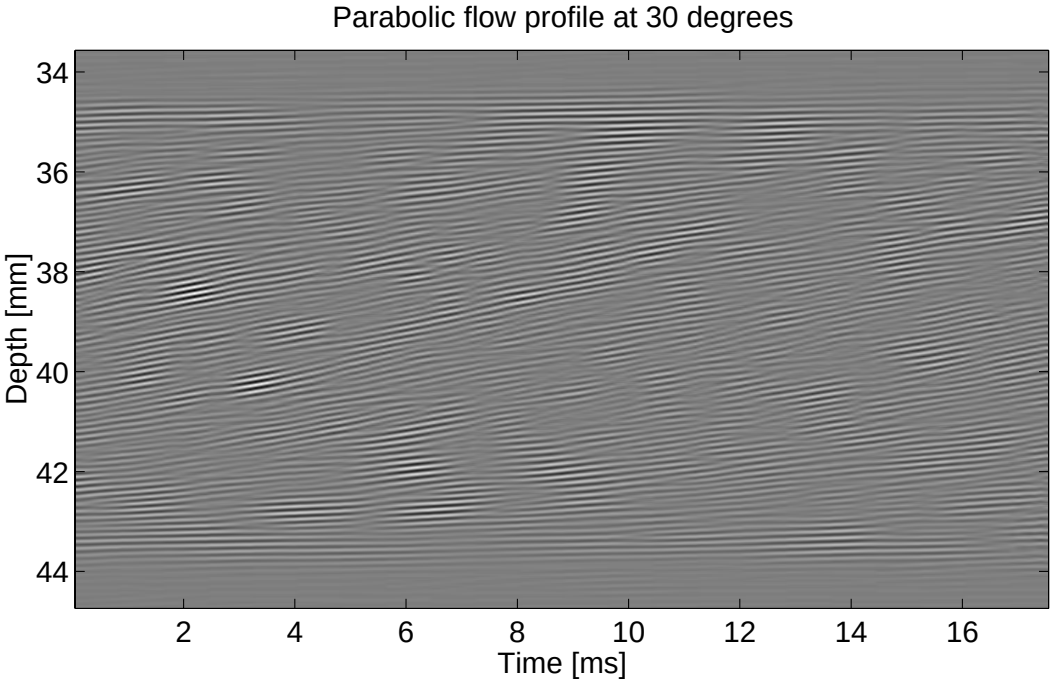

Figure 3.4: RF-lines generated using a parabolic flow profile.

The result using a parabolic flow profile, given in Figure 3.4, shows an increasing displacement towards the center of the tube. This corresponds to the position of maximum velocity. At the edge the velocity approaches zero. The angles of the lines in the image reflects the displacement of the scatterers. The slope is maximum in the center of the vessel and decreases towards zero slope at the edge of the vessel. Again the scattering strength decreases towards the edge of the tube.

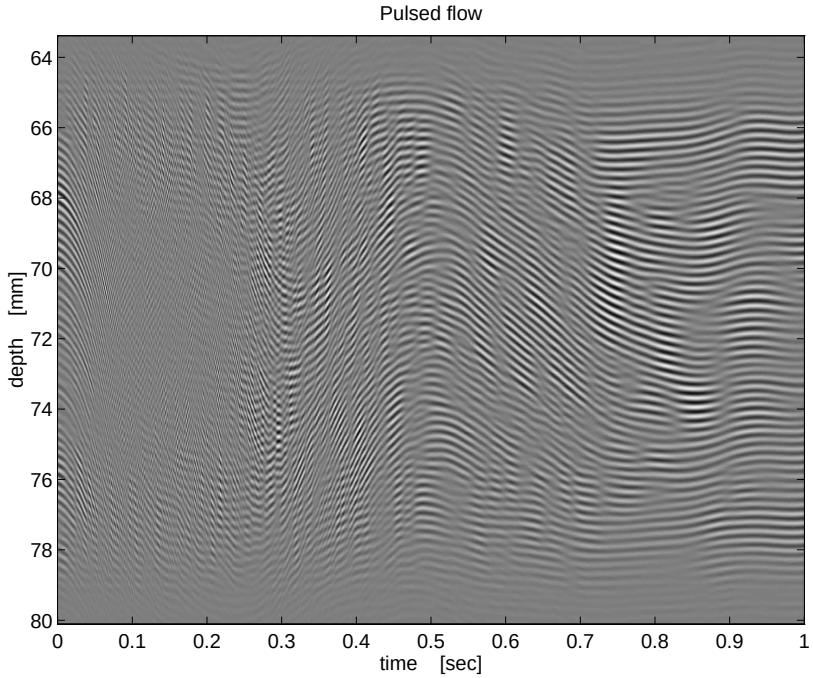

Figure 3.5: RF-lines generated using a pulsatile parabolic flow profile.

To give an impression of the dynamics of flow, and thereby the nature of a real flow signal, one cycle of a pulsed flow profile was simulated. Based on figures listed in Table 3.2 in Jensen [Jen96a], a common femoralis flow is calculated using (3.10). The profile evolution is calculated for ten equidistant samples in a whole heart cycle with a pulse of 62 beats/sec. The simulation results are from [Mun96] and are based on a different setup than the plug and parabolic flow. The primary differences are : the center frequency (3 MHz), the flow depth (70 mm) and the vessel size. The first image shown in Figure 3.5 displays the whole cycle. The dynamics of the diastole in the time period from 0 to 0.4 s is not properly visible. Approximately time 0.4 to 1 s the change of slope as a function of time and position can be seen.

In order to visualize the rapid change that occurs at the start of the cycle, two subsamples are shown in Figure 3.6 and Figure 3.7.

We see how fast and slow changes of the line slope appears at different time instants of the heart cycle, and that positive and negative velocities result in positive and negative slopes of the lines, respectively. In principle, the estimation techniques calculate the average of the line slope. To obtain a useful estimate, several pulses must be emitted in one direction, the more pulses, the better the estimate. The number of pulses should be kept at a minimum out of consideration to the frame rate and to obtain a unbiased estimate of the instant line slope.

The simulations also show the influence of speckle in all three types of flow. The speckle phenomenon causes the lines to have abrupt changes, introducing decorrelation and low signal to noise ratio. These sudden phase shifts affects the estimation of the mean velocity and is, together with electrical noise, the main reason for using averaging over multiple pulses.

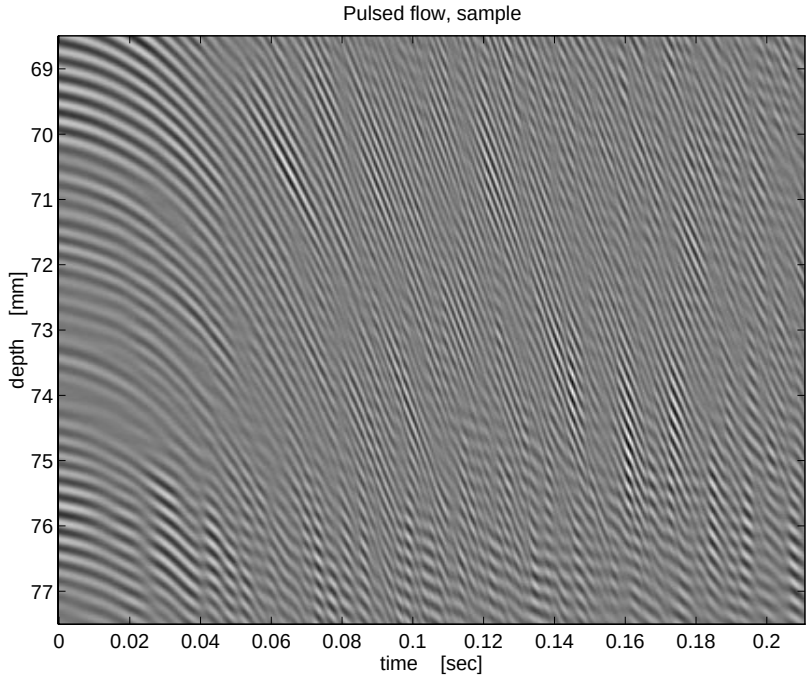

Figure 3.6: Subsample of Figure 3.5, which show the fast change of slope in the beginning of the heart cycle.

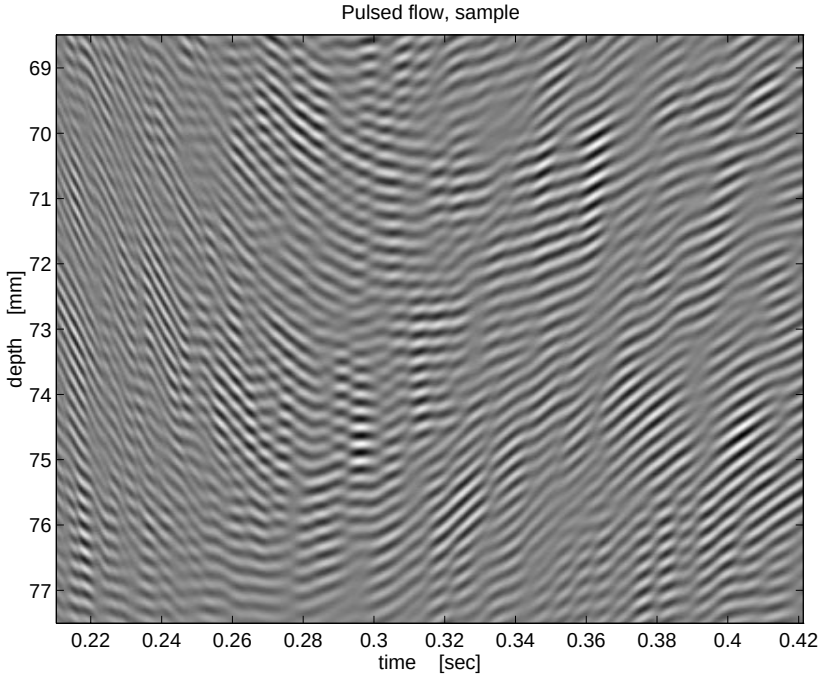

Figure 3.7: Subsample of Figure 3.5, which show the slow change of slope and direction in the middle of the heart cycle.

Chapter 4

1D flow

The 1D-flow measurement is included to give a basic understanding of the velocity estimation approach used in present scanners, and to point out the close relation to the new 2D method presented in Chapter 5.
Basically, the 1D-velocity component can be calculated by either frequency domain or time domain processing. The two methods are fundamentally different. The frequency domain approach is essentially a narrowband technique (often referred to as the Doppler technique), whereas the time domain approach is a broadband technique. The difference reflects the desire to obtain a good resolution for the estimation.
The Doppler technique consequently operates best with long pulses, which gives a poor axial resolution. The method used to estimate the mean velocity is based on the autocorrelation approach and is performed in the time domain. The breakthrough for real time velocity estimation came about in 1982 using the autocorrelation approach. The method was first briefly presented by Namekawano [NKTK82], [NKKO82], and in more details by Kasai et al. [KNKO85]. The time domain estimation is based on the cross-correlation approach, as described by Dotti et al. [DGS$^+$76] and Bonnefous et al. [BPB86], which relies on a good axial resolution since the method depends on temporal tracking of the spatial position of individual coherent blood target ensembles. The cross-correlation method (time processing) is a high bandwidth technique and has no aliasing problems, as compared to the narrow band technique of the autocorrelation (phase processing). The major drawback of the cross-correlation is the high computational requirement compared to the autocorrelation approach. The cross-correlation technique has only been implemented in one commercial scanner and is not available at the market today.
All contemporary commercially available systems use the autocorrelation approach for velocity estimation.
The flow imaging is based on pulsed wave (PW) systems, which are briefly introduced, and two estimation methods are presented: The classical velocity estimation using the autocorrelation approach is reviewed and a new Fourier-Radon approach is introduced. The autocorrelation approach is presented to give the basis for an extension to the 2D estimator developed for the vector estimation. The Fourier-Radon approach is a spin-off of the work carried out and it is a result of working with 2D data in order to devise new methods for 2D estimators.

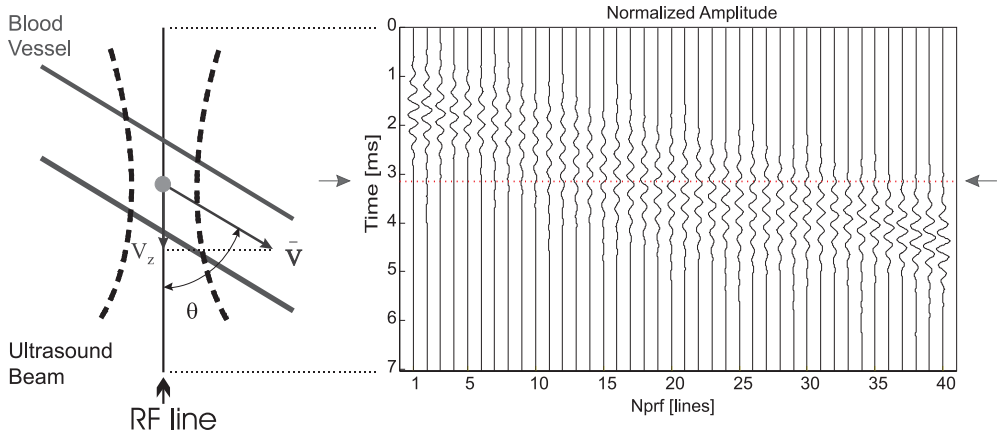

Figure 4.1: Consecutive received RF signals for a pulsed wave system with one scatterer moving slowly past the range gate indicated by the dashed line at the arrows.

4.1 Measurement situation

4.1.1 Pulse wave system

A good description of a PW-system able to detect velocity was given by Baker [Bak70]. He gave a detailed description of the sampling operation on the received backscattered signal from blood. Baker stated that the system tracked the slow movement of the scatterers through the range gate. Baker ascribed the ability to estimate the velocity to the Doppler effect. A different description was given by Magnin [Mag86], [Mag87] and Bonnefous [BP86], where it is argued that the velocity is estimated by the time shift from one emission to the other, and not the Doppler shift in a classical context. For a further discussion on Doppler systems refer to Jensen [Jen96a].
The acoustical measurement situation for a traditional pulsed Doppler system for blood velocity estimation is illustrated in Figure 4.1 in a simplified manner with only one scatterer. The measurement situation is shown to the left in the figure. A transducer is positioned so that the emitted pulsed field intersects the blood vessel. The acoustic field (indicated by the dashed lines) interacts with the blood particle and is scattered towards the transducer and the time response (RF data) is recorded. A number of consecutive ultrasound pulses are emitted in one direction in order to track the displacement of the blood scatterer from one emission to the other.

Between two emissions the scatterer has moved a distance proportional to the velocity component v_z in the direction of the ultrasound beam, *i.e.* the axial direction. The time shift t_s of the RF signal from pulse to pulse is

$$t_s = \frac{2v_z}{c} T_{prf} \tag{4.1}$$

where c is the speed of sound, and T_{prf} is the time between pulse emissions. The RF signals corresponding to consecutive recordings are displayed on the right for a number of pulse emissions. The signals recorded are aligned vertically next to each other. It is seen how the scatterer slowly moves away from the transducer. The cross-correlation of the received pulse signal from one pulse emission to the next is proportional to the autocorrelation function of one pulse-echo signal delayed t_s. This movement can be measured by recording the signal at a specific depth marked at the horizontal line superimposed on the RF signals. Taking out one sample at a specific depth for each line gives a sampled signal with a frequency

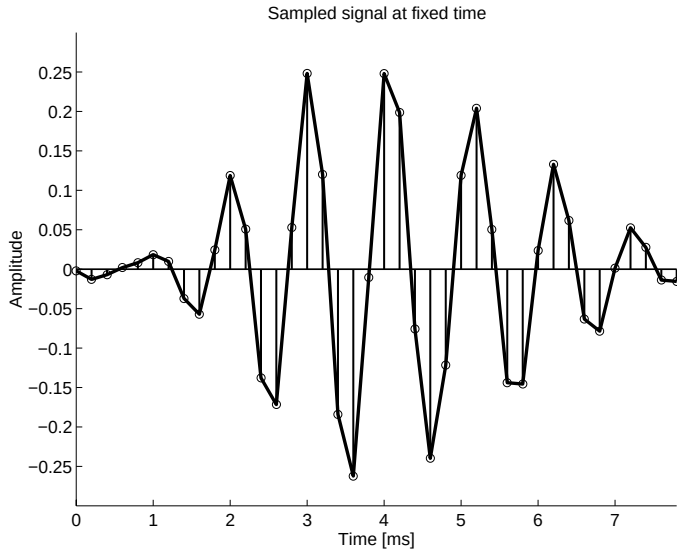

Figure 4.2: Signal sampled at a specific depth for a number of pulse emissions. The sampling frequency is f_{prf}

proportional to the scatterer velocity. A near-monochromatic sinusoidal pulse sampled in this way, gives a received signal for the ith pulse emission for a single scatterer described by [Jen96a]

$$r(i) = a(i)\sin(2\pi\frac{2v_z}{c}f_0 iT_{prf} + \theta) = a(i)\sin(2\pi f_p iT_{prf} + \theta) \tag{4.2}$$

where the variables are: $a(i)$ the envelope amplitude, f_0 the emitted frequency, and θ is a phase factor accounting for the propagation delay, *i.e.* the depth of interest.
Thus, a MHz signal is sampled with f_{prf} which is in the kHz range. The sampling operation scales the frequency of the emitted signal with a factor of $2v_z/c$. The spectrum of the received signal is a replica of the emitted spectrum [Jen96a], where the frequency axis is scaled by $2v_z/c$. The frequency of the received signal is thereby proportional to the blood velocity. The underlying mechanism, that makes it possible to estimate the axial velocity, is the sinusoidal oscillations in the emitted signal. The signal received from one depth is shown in Figure 4.2. If f_0 and c are known, this result indicates that the velocity v_z can be estimated on the basis of the frequency of the f_{prf} sampled data. Unfortunately f_0 and c are not constant, but must be assumed constant when the mean frequency is related to the axial velocity.

4.2 Flow estimation

4.2.1 Autocorrelation method

The autocorrelation approach has been used with success to estimate the mean frequency of an oscillating signal. The first publication of a possible use of the autocorrelation approach for displaying real time flow in ultrasound images was given as a conference paper by Namekawa, [NKTK82], [NKKO82]. The full value of the approach did not gain a widespread appreciation until several years later, when Kasai published a detailed paper [KNKO85]. The paper demonstrated that true real-time color flow imaging was possible using frequency estimation by the autocorrelation approach . The fundamental idea of this approach is to

estimate the phase shift on the basis of a complex sinusoidal signal. This complex signal can be generated using the Hilbert transform. It is interesting to note that the method was first developed for meteorological purposes in order to extract information from weather radar. In principle it is possible to estimate the mean frequency with only two samples[1]. Several estimators and their properties has been investigated in the seventies [MR72], [Zrn77], [Zrn79]. Considerations on practical implementation can be found in [MZ83] and a geometric interpretation of different kinds of estimators is given in [PS83]. At the same period around 1985 other groups worked towards development of new velocity estimators. Angelsen developed both theory [Ang81] and suggestions for implementation [AK83]. The same year as Kasai, Barber and his group [BEK85] published a paper with two approaches including a method corresponding to the approach given by Kasai.
The drawback of this approach is the basic assumption of a constant f_0 and c. The human tissue is an inhomogeneous propagation medium that has a frequency dependent attenuation and speckle generating characteristics. Hence there will be a random fluctuation of f_0 with a decreasing mean value with depth. Averaging has to be employed due to the statistical nature of f_0 and the low SNR present in the measurement situation. The averaging is typically done using 8-16 emissions per estimate, and the estimation is done for a number of samples in the RF line (depth direction). The final estimate is the mean of the velocity for a given depth (RF averaging). Usually the number of RF samples used for averaging corresponds to the length of the pulse applied for emission, which usually is in the range of 4-8 periods of the center frequency f_0. To deal with the problem of the statistical properties of f_0, an approach has been proposed by Loupas and Gill [LPG95b], [LPG95a]. The authors extend the traditional autocorrelation approach to estimate both the axial RF frequency f_0 and the sampled frequency f_p. The model employed still assumes sinusoidal phase relationship between RF samples in order to estimate the two frequencies.
To illustrate the basics of the autocorrelation method, an enveloped monochromatic, continuous time signal is assumed. The Hilbert transform is employed to create a complex signal.

$$r_{rec}(t) = x(t) + jy(t) \tag{4.3}$$

The complex signal can be written as

$$\begin{aligned} r_{rec}(t) &= g(t)\exp\left[-j\left(2\pi f_0 \frac{2v_z}{c}t - \phi_d\right)\right] && (4.4)\\ &= g(t)\exp\left[-j\phi(t)\right] && (4.5)\end{aligned}$$

Here $g(t)$ is the envelope function and the phase $\phi(t)$ is related to the axial velocity and the velocity is proportional to the phase derivative given by

$$\frac{d\phi}{dt} = -\frac{4\pi f_0}{c}v_z \tag{4.6}$$

and the velocity is

$$v_z = -\frac{d\phi}{dt}\cdot\frac{c}{4\pi f_0} \tag{4.7}$$

Thus, the velocity v_z is estimated through an estimate of phase derivative of the received signal.

[1]It is interesting to note that the first publication goes back to 1968 were two reports were published by Rummler at the Bell Telephone Labs [Rum68a] , [Rum68b].

The phase of the complex signal is

$$\phi(t) = \arctan\left[\frac{y(t)}{x(t)}\right] \tag{4.8}$$

The derivative with respect to time is

$$\begin{aligned}
\frac{d\phi(t)}{dt} &= \frac{d\arctan\left[\frac{y(t)}{x(t)}\right]}{dt} && (4.9)\\
&= \frac{1}{1+\left[\frac{y(t)}{x(t)}\right]^2}\frac{d\left[\frac{y(t)}{x(t)}\right]}{dt} && (4.10)\\
&= \frac{1}{1+\left[\frac{y(t)}{x(t)}\right]^2}\frac{x(t)\,\dot{y}\,(t)) - y(t)\,\dot{x}\,(t)}{x^2(t)} && (4.11)\\
&= \frac{x(t)\,\dot{y}\,(t) - y(t)\,\dot{x}\,(t)}{x^2(t)+y^2(t)} && (4.12)
\end{aligned}$$

with the notation

$$\dot{x}\,(t) = \frac{dx(t)}{dt} \qquad \text{and} \qquad \dot{y}\,(t) = \frac{dy(t)}{dt} \tag{4.13}$$

The derivation is valid only for a continuous function, but is useful to illustrate the relation between the complex function $r_{rec}(t)$ and the velocity through the phase derivative.
In an ultrasound scanner the received signal from a pulse measurement is a digital signal which calls for an approximation of the derivative. There are several ways to perform a numerical approximation, some of which are given in [Jen96a]. The samples $x(i)$ and $y(i)$ are taken from a particular depth and $x(i-1)$ and $y(i-1)$ is from the same depth, but from the previous recorded line. The time between the recorded lines is T_{prf}. The phase derivative is calculated as

$$\begin{aligned}
\frac{\Delta\phi(i)}{\Delta i} &= \phi(i) - \phi(i-1)\\
&= \arctan\left[\frac{y(i)}{x(i)}\right] - \arctan\left[\frac{y(i-1)}{x(i-1)}\right] && (4.14)
\end{aligned}$$

and the velocity is expressed as

$$v_z = -\frac{c}{4\pi f_0 T_{prf}}\arctan\left[\frac{y(i)x(i-1)) - x(i)y(i-1)}{x(i)x(i-1)) + y(i)y(i-1)}\right] \tag{4.15}$$

This formula devises the basic method of calculation which is referred to as the autocorrelation method. The relation to the autocorrelation function is given in the following and it shows a way of improving the estimator. The discrete complex autocorrelation function is [Pap84]

$$\begin{aligned}
R(m) &= \lim_{N\to\infty}\frac{1}{2N+1}\sum_{i=-N}^{N}\mathbf{r}^*_{rec}(i)\mathbf{r}_{rec}(i+m) && (4.16)\\
&= \Re(R(m)) + j\Im(R(m)) && (4.17)
\end{aligned}$$

where $r^*_{rec}(i) = x(i) + \mathrm{j}y(i)$. Setting $m = 1$ and using that the autocorrelation is an even function, *i.e.* $R(m) = R(-m)$, the velocity estimate can be linked to the autocorrelation function and be reformulated as

$$v_z = -\frac{c}{4\pi f_0 T_{prf}} \arctan\left[\frac{\Im(R(1))}{\Re(R(1))}\right] \tag{4.18}$$

Calculating $R(1)$ theoretically requires an infinite amount of data

$$R(1) = \lim_{N\to\infty} \frac{1}{2N+1} \sum_{i=-N}^{N} \mathbf{r}^*_{rec}(i)\mathbf{r}_{rec}(i+1) \tag{4.19}$$

In the real situation, $R(1)$ must be estimated because only a limited amount of data N_c is available. The estimated value is

$$\widehat{R}(1) = \frac{1}{N-1} \sum_{i=0}^{N_c-2} \mathbf{r}^*_{rec}(i)\mathbf{r}_{rec}(i+1) \tag{4.20}$$

Using the equivalence of the autocorrelation function, an averaging scheme using several lines to calculate v_z can be devised as

$$\begin{aligned} v_z &= -\frac{c}{4\pi f_0 T_{prf}} \arctan\left[\mathrm{Arg}\left\{\frac{1}{N-1}\sum_{i=0}^{N_c-2} \mathbf{r}^*_{rec}(i)\mathbf{r}_{rec}(i+1)\right\}\right] \\ &= -\frac{c}{4\pi f_0 T_{prf}} \arctan\left[\frac{\frac{1}{N-1}\sum_{i=0}^{N_c-2}\left(y(i)x(i+1) - x(i)y(i+1)\right)}{\frac{1}{N-1}\sum_{i=0}^{N_c-2}\left(x(i)x(i+1) + y(i)y(i+1)\right)}\right] \\ &= -\frac{c}{4\pi f_0 T_{prf}} \arctan\left[\frac{\sum_{i=0}^{N_c-2}\left(y(i)x(i+1) - x(i)y(i+1)\right)}{\sum_{i=0}^{N_c-2}\left(x(i)x(i+1) + y(i)y(i+1)\right)}\right] \end{aligned} \tag{4.21}$$

Thus, the phase contributions from several lines are averaged. This derivation corresponds to the one suggested by [KNKO85]. This relation to the autocorrelation function makes it possible to estimate the variance for the estimated velocity. The variance of the estimate is an indication of the velocity spread within the range gate. The variance of the autocorrelation function can be derived in the continuous domain. For further reading see [Jen96a], [Ang81], [KNKO85].
Finally, a compact notation for estimating the velocity for multiple depths is given. If the quadrature data for a specific depth/gate is arranged in a vector with

$$\mathbf{r}_{rec}(n) = \mathbf{x}(n) + j\mathbf{y}(n) \tag{4.22}$$

where

$$\mathbf{x}(n) = [x(n)\ \ x(n+1)\ \ x(n+2)\ldots x(n+N_c-2)] \tag{4.23}$$

and

$$\mathbf{y}(n) = [y(n)\ \ y(n+1)\ \ y(n+2)\ldots y(n+N_c-2)] \tag{4.24}$$

then (4.21) becomes

$$v_z = -\frac{c}{4\pi f_0 T_{prf}} \arctan \left[\frac{\Im \left[\mathbf{r}_{rec}(n) \cdot \mathbf{r}_{rec}^{*T}(n+1) \right]}{\Re \left(\mathbf{r}_{rec}(n) \cdot \mathbf{r}_{rec}^{*T}(n+1) \right)} \right] \tag{4.25}$$

This expression can be expanded to include all gates, indexed by m. Then the quadrature signal is a matrix

$$\mathbf{R}_{rec}(m,n) = \mathbf{X}(m,n) + j\mathbf{Y}(m,n) \tag{4.26}$$

and the velocity estimate as a function of depth can be calculated as[2]

$$v_z(m) = -\frac{c}{4\pi f_0 T_{prf}} \arctan \left[\mathrm{Arg} \left\{ \mathrm{diag} \left[\mathbf{R}_{rec}(m,n) \cdot \mathbf{R}_{rec}^{*T}(m,n+1) \right] \right\} \right] \tag{4.27}$$

4.2.2 Fourier-Radon method

The Fourier-Radon (FR) method is based on a geometrical approach towards estimation of the mean velocity. The 2D-RF data are treated as a 2D information matrix with a column for each RF-line and the number of columns corresponding to the number of emissions evaluated. The oscillating nature of the signal creates iso-phase lines in the data matrix. The slope of the iso-phase lines is proportional to the displacement from one recording to the other caused by the axial velocity component. According to (4.1) the slope at a specific range of depth for a given T_{prf} is proportional to the axial velocity of the blood particles. By geometry, the angulation of these lines can be found independently of f_0 in the 2D Fourier domain. For comparison, the autocorrelation approach calculates the average phase shift from line to line, assuming that the mean frequency is proportional to the velocity. Estimating the phase shift in the autocorrelation approach corresponds to finding the slope assuming a model which depends on a constant f_0. In Section 3.4 examples of 2D-RF data of different flow profiles were given, and the relation between the slope of the 2D-RF data and the velocity was pointed out. Lines with a negative slope indicates forward flow and lines with a positive slope indicate reverse flow. The FR method presents a new way to perform the estimation of the local slope of the RF-lines in a 2D-RF data matrix.
Previous work has been done using the 2D Fourier transform of the 2D-RF data by Wilson [Wil91] and Loupas and Gill [LG94]. These papers present the relation of the 2D Fourier domain to the velocity, and evaluate the statistical performance of the estimate of the mean value in the frequency domain. The mean value in the 2D Fourier domain is shown to be the mean value of the velocity distribution. The 2D Fourier transform is performed on the matrix with ordinate $t = n \cdot t_s$ and abscissa $T = m \cdot Tprf$. The two time measures t and T will be denoted fast and slow time respectively. In the 2D Fourier domain the axis will be denoted fast frequency f and slow frequency F. Slow frequency is the frequency related to the velocity, fast frequency describes the interacting ultrasound pulse. The slope in the time domain 2D-RF data is inversely related to the slope in the frequency domain [Rob82]. Therefore, an estimate of the slope in frequency domain can be used instead of the slope in time domain. A different approach towards the estimation of the slope in the time domain is the 'Butterfly search technique' [AB95]. The method is not defined as a Radon technique but is uses the same logic. The method sums up over lines in the time domain and searches for the maximum value.

[2] $diag[\mathbf{M}]$ takes the diagonal of a matrix and the argument of a complex number a is $Arg\{a\} = \frac{Im(a)}{Re(a)}$.

To illustrate the relation between the 2D time domain and the 2D frequency domain, a continuous sinusoid given by

$$s\left(T,t\right)=\sin\left(2\pi f_0\left(t+\frac{2v_z}{c}T\right)\right) \tag{4.28}$$

is transformed to the 2D Fourier domain as

$$S\left(F,f\right)=\frac{1}{2}\delta\left(F-f_0\frac{2v_z}{c}\right)\delta\left(f-f_0\right)+\frac{1}{2}\delta\left(F+f_0\frac{2v_z}{c}\right)\delta\left(f+f_0\right). \tag{4.29}$$

Thus, the slope in the (t,T) time domain, will be $\frac{c}{2v_z}$ of the line through the dirac pulses in the (f,F) frequency domain. The slope in the frequency domain must be defined relative to the ordinate instead of the abscissa in order to be proportional to the velocity, and it is named α. Thus, zero velocity corresponds to zero slope. In the discrete case the slope in the frequency domain will be scaled with the two sampling frequencies f_s and f_{prf} yielding

$$\alpha=\frac{2v_z}{c}\frac{f_s}{f_{prf}} \tag{4.30}$$

which shows that the slope α can be determined independently of f_0. The velocity estimate will be proportional to an estimated angle $\hat{\alpha}$ assuming that f_s, f_{prf}, and c are constant. The parameters f_s and f_{prf} are controlled by the system setup of the ultrasound scanner, leaving only c to be assumed constant.

The estimate $\hat{\alpha}$ could be calculated by finding the mass point in the 2D frequency domain. Instead, the new approach applies yet a transformation. The result is a 1D function, where a mean value is proportional to the mean velocity in the observed time period. The energy distributions in the 2D Fourier domain will be two mass centers located on a line passing through origo in the (f,F) domain, due to the symmetry of the Fourier transform. This symmetry indicates the possible application of a radial transformation, such as the Radon transform [Dea93]. The Radon transform is well known as a robust method to detect lines in noise [Tof96]. The classical transform calculates an integrated value along a line as a function of slope and displacement to origo. Thus, the output of the Radon transform is in general 2D. Calculating for all angles, the maximum value for the Radon transform will be found for a line intersecting origo, due to the symmetry in the frequency domain. Therefore, the Radon transform is only calculated for the one displacement equal to zero. The 1D output is used to calculate the estimated $\hat{\alpha}$ of the slope for the line through the two mass centers in the frequency domain. Again to demonstrate the method, a simple example based on synthetic data is given. Synthetic data are generated on the basis of

$$r_m(n)=\sin(2\pi\left(n\frac{f_0}{fs}+m\frac{2v_z}{c}\frac{f_0}{f_{prf}}\right)) \tag{4.31}$$

where $n=1\ldots N$ and $m=1\ldots M$. Here N and M equals 32. The synthetic data is used both to illustrate the method and to compare the performance of both the autocorrelation method and the 2D-FR method. In Figure 4.3 the result of the 2D-FFT transform of the 2D-RF data is shown for three different axial velocities, $v_z=0.0, 0.05$ and 0.1 m/s.

The slope in the time data increases according to the increase in axial velocity and the slope α increases in the frequency domain as the axial velocity increases. The Radon transform of the frequency spectrum for the three cases of velocity is shown in the middle row of Figure 4.4.

The full Radon transform is shown to illustrate how the two centers of mass in the 2D Fourier domain are converted into two lines and that they intersect at the zero intersection

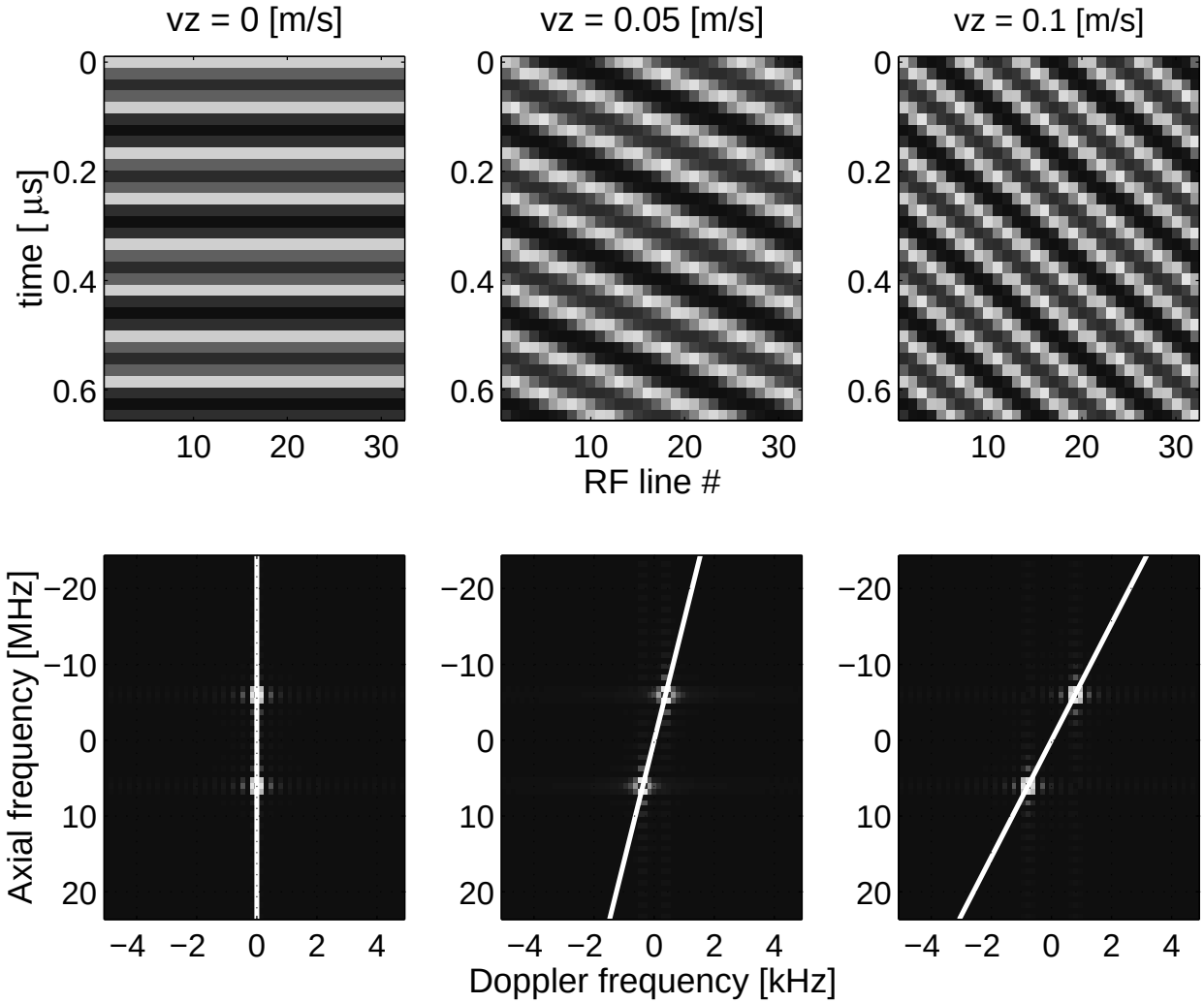

Figure 4.3: 2D-FFT results for different axial velocities. The top row is the 2D-RF data and the corresponding 2D-FFT is shown in the bottom row. The relation between the RF slope and the FFT slope is evident.

line. The zero intersection line is indicated in the second row as the dotted horizontal lines in the Radon transform results. The vertical lines are the angles expected to have the maximum values from the velocities used to generate the synthetic data sets. The bottom row shows the 1D data used to calculate the estimate $\widehat{\alpha}$. This simple example shows how Radon transform of zero intersection is a distribution with a mean value according to the applied generating velocity. This indicates the possible use for axial velocity estimation.

4.3 Comparison of the two flow estimation techniques

The autocorrelation and the Fourier-Radon transform are compared for both synthetic and simulated data. The simulated data is generated using Field II. The setup for this simulation utilizes an array transducer generating an acoustic field that interacts with a group of scatterers in a vessel moving according to a plug flow distribution. The sampling frequency is 96 MHz and the simulation result is resampled at 24 MHz. The transducer is a 6 MHz (f_o) linear array with 64 elements spaced ($\lambda_0/2$) apart. All elements are used in both transmit and receive. The array is focused at a depth of 40 mm for both transmit and receive. The applied pulse length is $4\lambda_0$ corresponding to a total of 16 RF samples. The blood vessel with

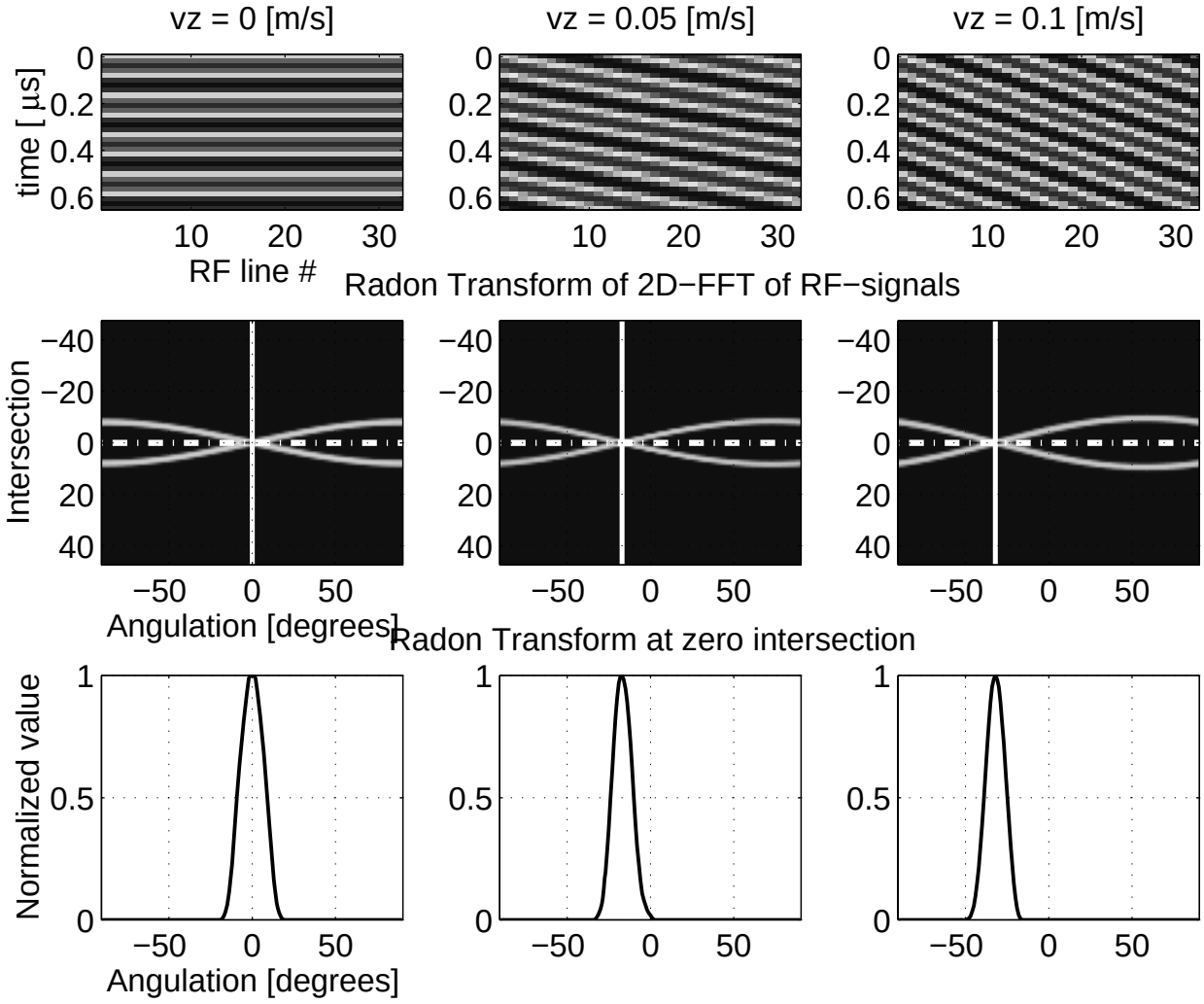

Figure 4.4: Radon transform of the 2D frequency domain and the corresponding zero intersection line, which is used to estimate the angle in the 2D Fourier domain and thereby the axial velocity component. The distribution of the zero intersection line is displaced proportional to the axial velocity component.

a radius of 5 mm was positioned at 40 mm with a 60 degree angle relative to the propagation direction. The flow velocity is 0.2 m/s in a direction away from the transducer (negative direction), thus the axial component is -0.1 m/s. Compared to the synthetic data, the simulated data is used to introduce the decorrelation in the RF signal caused by the transverse displacement of the scatterers and the statistical properties of the RF fluctuations generated by the speckle.

Results are obtained for synthetic and simulated data with 500 realizations of a 16 by 16 2D-RF data matrix (8000 RF lines). Gaussian distributed noise is added to the simulated flow signal to obtain SNRs of -6, -3, 0, 3, 6, 9 and 12 dB. The 2D-RF data is transformed to the 2D Fourier domain, and a threshold of -10 dB to the peak value in the amplitude spectrum is applied followed by a Radon transform. The angle corresponding to the maximum value in the 1D Radon domain (zero intersection line) is found and the mean for a symmetric angle range around the maximum angle is calculated yielding the velocity estimate. Finally a 3-point median filter is applied to remove the impulsive noise that can arise, when maximum detection is used. For each noise level the mean and the standard deviation of the velocity estimates are calculated. The results for the synthetic and the simulated data set are shown in Figure 4.5 and Figure 4.6. Both the synthetic and the simulated results show a smaller

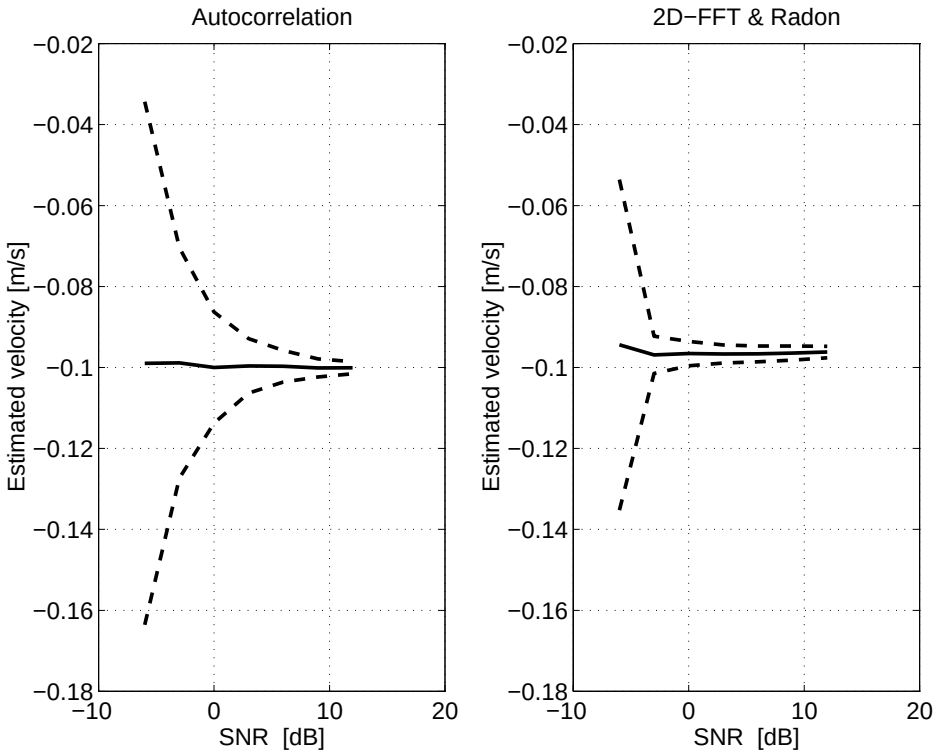

Figure 4.5: Performance on synthetic data using varying SNR. The mean value of the estimated velocity is the solid line and the dotted line is ± one standard deviation. The correct value of the velocity is -0.1 m/s.

standard deviation for the new method. The mean of the autocorrelation estimate becomes biased using simulated data. The bias is constant with respect to the data type for the new method. For comparison the relative standard deviation is depicted in Figure 4.7. A significant improvement up to a factor of 4 for the simulated data is shown. The result obtained for a SNR of -6 dB is not considered, because the ratio of the standard deviation to the mean value, indicates that the estimated values are not applicable.
The performance of the autocorrelation method as measured by the relative standard deviation is better for the synthetic data, except for a SNR of -3 and 0 dB. For the simulated data the 2D-FR performs better for all noise conditions. The main reason must be ascribed to the fact that there is no model for the phase relation anticipated in the estimation of the velocity using the new method.
Thus, it can be concluded that it is possible to estimate the axial velocity with the 2D-FR method, and the performance on the simulated data, which has the statistical characteristics of speckle, is improved compared to the traditional autocorrelation method. The results have shown an improved performance by a factor of 1.5-4 on the standard deviation of the estimated velocity. The best improvement is obtained under conditions of a SNR of -3 to 0 dB, which is a critical range for velocity estimation in modern ultrasound scanners.

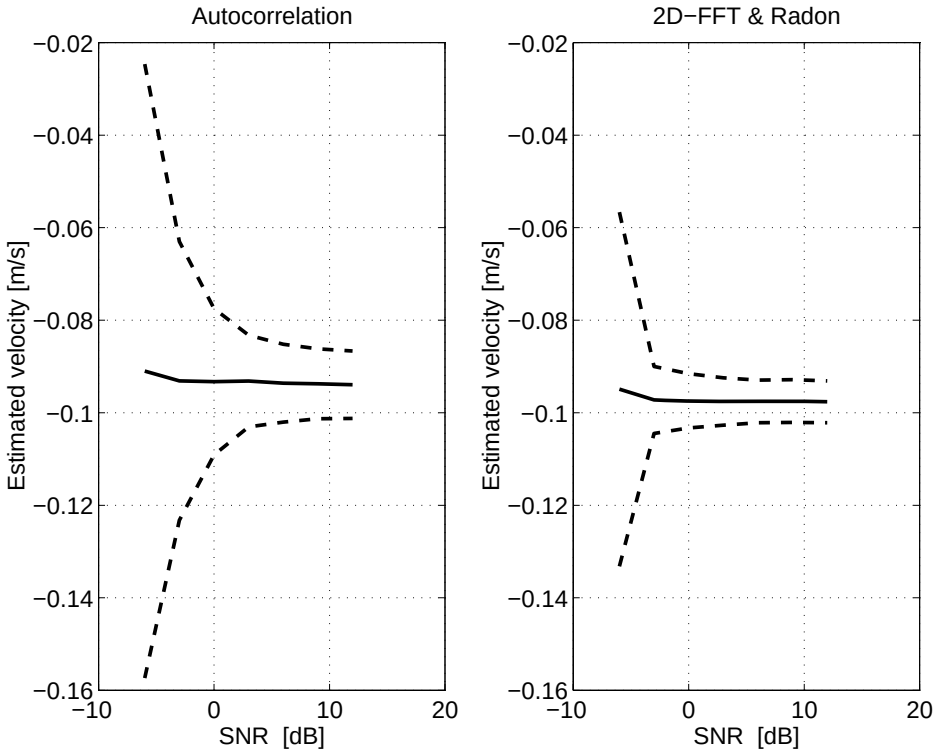

Figure 4.6: Performance on simulated data using varying SNR. The mean value of the estimated velocity is the solid line and the dotted line is ± one standard deviation. The correct value of the velocity is -0.1 m/s.

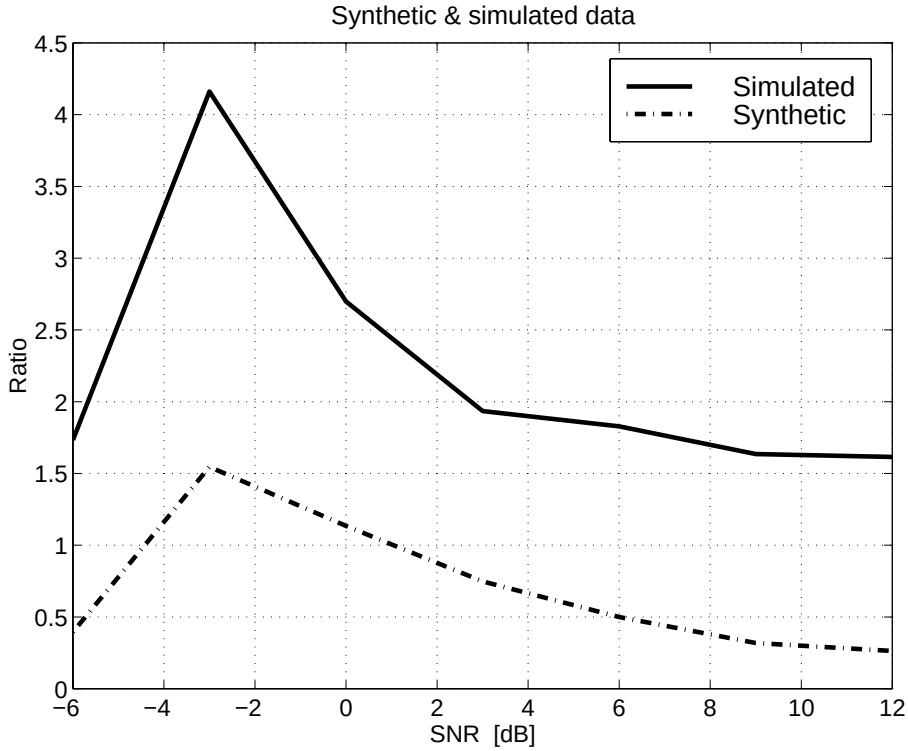

Figure 4.7: Relative improvement in standard deviation for synthetic and simulated data for the new approach relative to the standard autocorrelation approach.

Chapter 5

2D flow

Two aspects must be considered in order to develop a method to estimate the velocity vector. First, the measurement situation, which creates signals in which the vector movement is encoded, and second the calculation method used to decode the created information. This chapter describes the measurement situation which enables the estimation of vector flow, together with 4 different approaches to estimate the velocity vector.
The existing CFM systems only measure the axial velocity component yielding an angle-dependent velocity estimation. With this limitation, the next natural step for improving the velocity imaging modality is to estimate the entire velocity vector. The attempts to evaluate the vectorial flow are numerous, as referenced in Chapter 1. Still no commercially applicable solutions have been proposed.
In Chapter 4 the functionality of a pulsed Doppler system was presented using a simple model. Despite the simplicity of the model, it gives an insight to the basic and most important understanding of a pulsed wave Doppler system. The system measures a signal sampled with a frequency of f_{prf}. The mean frequency of this signal is related to the mean RF frequency by a scaling factor which includes the axial velocity component. It is the displacement of the RF-signal, due to the movement of the scatterer between pulse emissions, that creates the scaling relation. This scaled oscillating signal, sampled with T_{prf}, is used in an autocorrelation approach to estimate the mean frequency, which is related to the velocity of the scatterer. It is the oscillatory nature of the emitted RF pulse that makes it possible to estimate the mean frequency through the phase. In this manner the oscillating signal relates to the velocity. The flow angle is defined as the angle between propagation direction and flow direction. As the flow angle increases, the directions change from 0 degree (parallel directions) towards 90 degrees (perpendicular directions). With such an increasing flow angle, the impact of the axial displacement of the reflected signal decreases and thereby reduces the ability to estimate the velocity.
The idea behind the 2D measurement scheme is a straightforward extension of the scheme that is used in 1D pulsed Doppler systems. If a velocity component perpendicular to the propagation direction should be measured, a transverse oscillation in this direction of the spatial pulse-echo sensitivity function must be created.
Thus, a requirement to the measurement situation for the estimation of the 2D velocity vector is a spatial pulse-echo sensitivity function with a double oscillation, one in the axial direction and one in the transverse direction. The output signal from the beamformer will hereby be influenced by motion both axially and transversely. Such an approach has been suggested in [Mun96], [JM98] and [MJ98]. The vector flow information created by the measurement situation is extracted by the velocity estimator. The estimators presented here are, like the traditional mean axial velocity estimator, based on an autocorrelation approach. Basically,

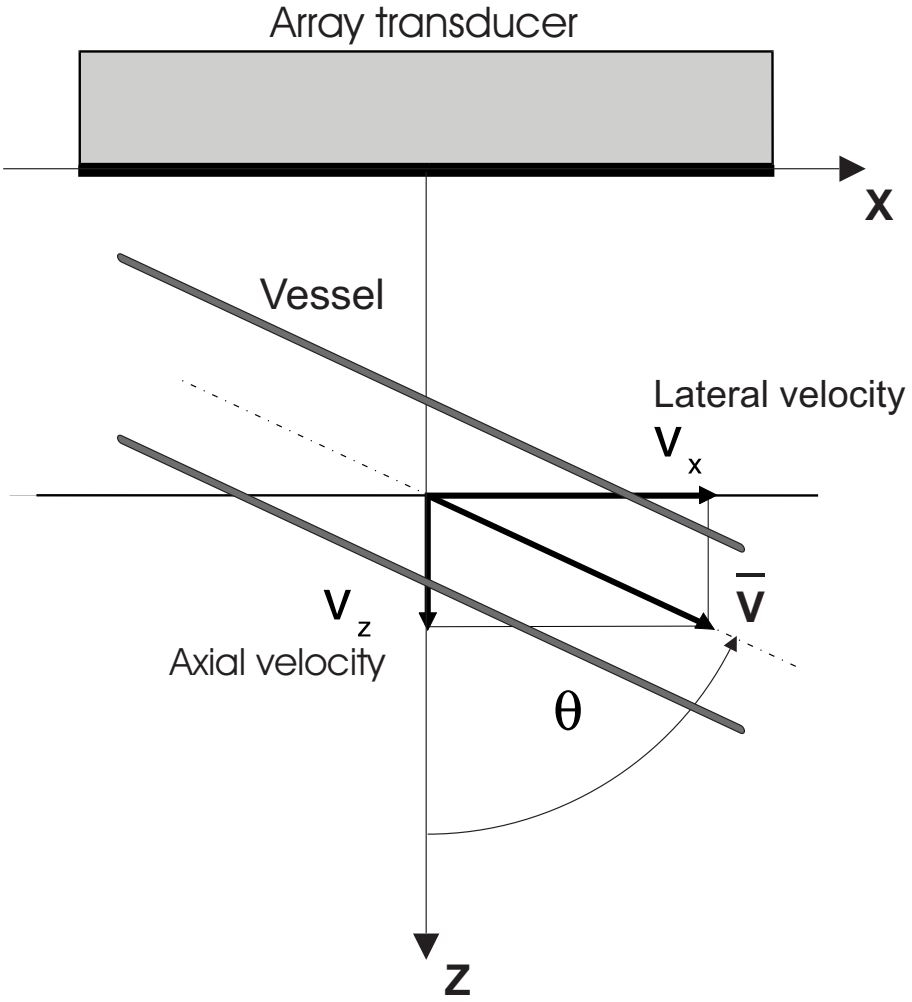

Figure 5.1: Notation for axial and lateral directions in the image plane.

the purpose of the 2D-estimator is to extract phase information in a way that separates the influence of the axial and the transverse oscillation component of the measurement situation. The work presented in this dissertation is based on the use of an 1D array transducer, and the vector is estimated in two dimensions in the image plane, (x, z)-plane. No considerations are made regarding the elevation direction. The signals used for the evaluation of the performance of the estimation schemes are based on flow signals with no interference from signals originating from stationary or slowly moving highly echogenic tissue structures.

5.1 The acoustic measurement setup

The notation used for the axial and the transverse direction in the image plane is shown in Figure 5.1
'Lateral' refers to the direction transverse to the axial direction on the image plane.[1] The notation 2D refers to the dimensions of the image plane. The basic description of the measurement situation will be presented by different means of complexity. An approximation of the required spatial pulse-echo sensitivity can be generated by proper control of the beamformer. A calculation method to devise an improved control of the beamformer was presented in Chapter 2 using pulsed plane wave decomposition. The control can be carried out in three

[1]Lateral is used according to the AIUM recommended ultrasound terminology [AIU97]

different ways, either for the emitted field, or for the received field or as a combination of both. Like in B-mode imaging one fixed transmit must be used to maintain a high frame rate. The spatial transmit field distribution will vary with depth using a fixed transmit. It will be will be too complicated to rely on a combination of the transmitted field and the receive sensitivity, since assumptions on the reflectivity properties of the medium must be made. Therefore the solution presented here is based on a fixed transmit setup with a Gaussian apodization, in order to reduce diffraction effects to a minimum, and the primary control of the transverse oscillation is carried out in the receive beamforming.

5.1.1 Synthetic field model

As an initial attempt, a basic mathematical description of the measurement situation is given. The term synthetic model is used because there is no relation between the acoustic field and the aperture. The purpose is to show how the signal created by such a measurement situation will reflect information of vectorial flow. A simple model is introduced to simplify the nature of the signal created by the measurement situation. A single scatterer interacts with a 2D acoustic field $f(x,z)$ by traversing at different angles to the propagation direction to give the measurement signal. This model results in a sampling of the 2D acoustic field along a line as a function of interaction angle θ. The signal $s(x,z)$ for a given point (x,z) with a single scatterer positioned at (x_0,z_0) is

$$\begin{aligned} s(x,z) &= f(x,z) \underset{xz}{*} \delta(x-x_0, z-z_0) \\ &= f(x-x_0, z-z_0). \end{aligned} \tag{5.1}$$

The single scatterer is moved along a straight line trajectory. The line is given by the point-slope description $z - z_1 = \alpha(x - x_1)$ where α is the slope and the point of origin is (z_1, z_1). The model of the 2D double-oscillating acoustical pulse-echo sensitivity $f(x,z)$ is based on separability $f(x,z) = f(x) \cdot f(z)$ and in general terms is described by

$$\begin{aligned} f\,(x,z) &= A_f \cdot f(x) \cdot f(z) \\ &= A_f \cdot e_x(x) \cdot \cos\left(2\pi x f_x - \phi_{x0}\right) \cdot e_z(z) \cdot \cos\left(2\pi \frac{2z}{c} f_0 - \phi_{z0}\right) \end{aligned} \tag{5.2}$$

The axial direction is z and the lateral direction is x, $e_x(x)$ and $e_z(z)$ are the envelope functions in the axial and lateral directions respectively, A_f is the overall amplitude, and ϕ_{z0} and ϕ_{x0} are initial phases. The velocity vector is $\mathbf{v} = (v_x, v_z) = (v_a \cdot \cos(\alpha), v_a \cdot \sin(\alpha))$, where $v_a = |\mathbf{v}|$. The response from the scatterer moving through the field is recorded with a time interval of T_{prf}. The received signal is denoted $r_{rec}(i) = x(i) + \mathrm{j}y(i)$ and the displacement in the axial and lateral direction for each recording i, is

$$x(i) = v_x i T_{prf} = v_a \cdot \sin(\alpha) i T_{prf} \tag{5.3}$$

$$z(i) = v_z i T_{prf} = v_a \cdot \cos(\alpha) i T_{prf} \tag{5.4}$$

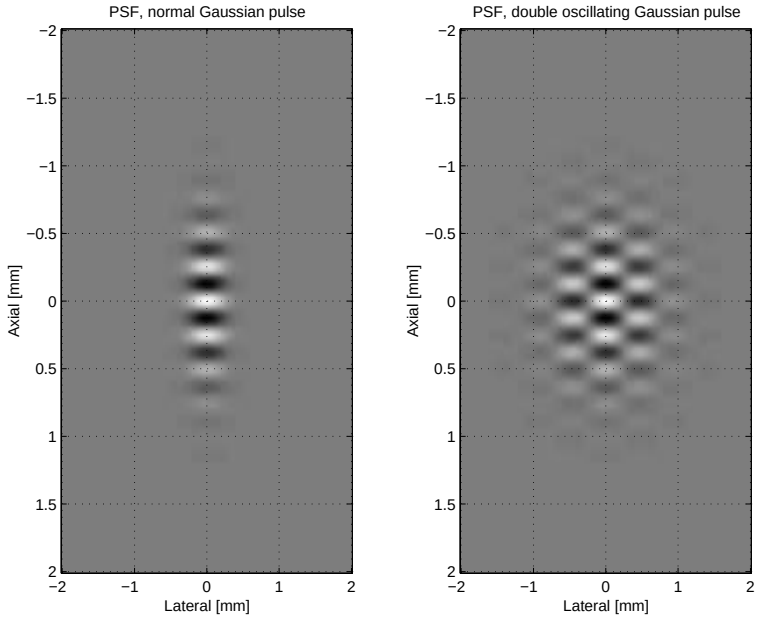

Figure 5.2: The pressure function of a normal Gaussian pulse and a double oscillating pulse.

and the received signal becomes

$$\begin{aligned} r_{x,z}(i) = A_{rec} \quad &\cdot \quad e_x(i) \cdot \cos\left(2\pi v_x f_x i T_{prf} - \phi_{x0}\right) \\ &\cdot \quad e_z(i) \cdot \cos\left(2\pi \frac{2v_z}{c} f_0 i T_{prf} - \phi_{z0}\right) \end{aligned} \tag{5.5}$$

The envelope in both the axial and lateral direction can be modeled by Gaussian functions

$$e_x(i) = k \cdot \exp\left(-2\left(B_r^x f_x \pi v_x i T_{prf}\right)^2\right) \tag{5.6}$$

$$e_z(i) = k \cdot \exp\left(-2\left(B_r^z f_0 \pi \frac{2v_z}{c} i T_{prf}\right)^2\right) \tag{5.7}$$

An example with $c = 1540$ m/s and $f_0 = 6$ MHz of a normal Gaussian pulse $f_x = 0$ m, and a double oscillating pulse, $f_x = 1000$ m is shown in Figure 5.2.

A single scatterer traverses with v_a=0.1 m/s through the PSFs to illustrate the impact of the oscillating acoustic field on the sampled signal at f_{prf}=5 kHz. The oscillatory nature and the change for different angles are demonstrated in Figure 5.3 for a normal Gaussian pulse, and a double oscillating Gaussian pulse for different angles of $0, 25, 50, 75, 90$ degrees.

The signal created from a single scatterer traversing through a double oscillating acoustic field is influenced by both axial and transverse motion. In the normal pulse, the mean frequency decreases with the angle until no oscillation is present for perpendicular directions of flow and propagation. The impact of double oscillation in the new pulse is clearly seen in the second column of Figure 5.3. At 90 degrees the pure lateral oscillation is present and in the intermediate angles a combined oscillation is seen. This example also shows the difference in modulation periods in the axial and lateral direction.

Assuming that the acoustic field is separable and invariant in time and space, and the scatterer field only is a function of two spatial dimensions, x and z, a 2D convolution approach can be applied to evaluate the impact on the signal created by the 2D oscillating field

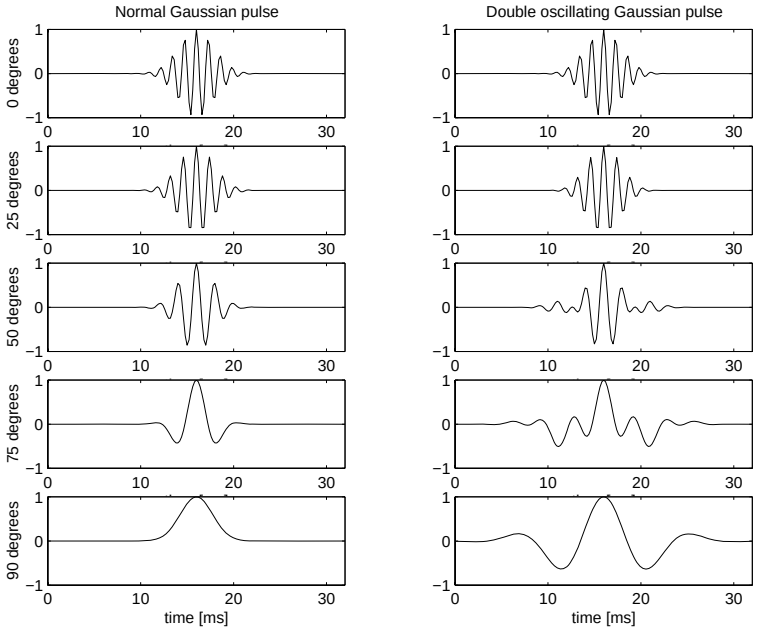

Figure 5.3: Signals generated by a single scatterer traversing two different acoustic fields at different angles.

interacting with a bundle of scatterers. The bundle of scatterers are uniformly distributed in the 2D space and the amplitude distribution is Gaussian. No results using this method is presented here.

5.1.2 CW field approximation

The results obtained by the synthetic fields show that signals can be made sensitive to movement of a scatterer transverse to the pulse propagation direction. The task is now to acoustically create a pulse-echo sensitivity that has the features of a double oscillating function. In previous work [Mun96], the CW field theory was applied to obtain the basic understanding of the requirements on the complex receive aperture function. It is a far-field approximation, which implies that no curvature of the phase front is present, *e.g.* a plane wave approximation.
The double-oscillating pulse-echo sensitivity is created based on pure receive consideration. The transmit field limits the lateral extension in which a lateral oscillation can be created. It must be stressed that the evaluation method presented here is for CW, which implies infinite extension of acoustic waves and infinite extension of the acoustic aperture. Even so it gives an insight to the major features of the acoustic measurement situation. For CW fields only relative phase within 2π is of importance, where as for pulsed fields, propagation time becomes a part of the phase considerations as well. For pulsed fields, the bounded conditions of acoustic oscillations mean that propagation time determines the local relative phase. Consider a pulsed case and the region surrounding a point of time alignment, e.g. the focus point for a curved transducer. The propagation time from this point to the aperture is constant, thus, time alignment is present. Depending on the pulse length, a region around this point can be assumed having CW-properties. The CW approximation elucidates the basic properties of the acoustic field, and the 'details' such as sidelobe characteristics are determined by the pulse length. The longer the pulse, the larger the interference region.

Fourier relations

The Fourier relations for an acoustic aperture and the associated acoustic field have been presented in Chapter 2. The far-field CW radiation pattern can be calculated by a Fourier transform of the transducers front-face velocity distribution just as radiation patterns in optics [Goo96]. The front-face distribution is in principle a complex function. The amplitude part of the distribution function is denoted the apodization function. In the theory of CW radiation patterns, constant, linear and quadratic phase terms can be handled. The constraints on validation increases as the phase function becomes more complicated.
The receive beamforming must be designed to create the lateral spatial modulation. Thus, the receive apodization function is derived from the field pattern needed. The derivation is based on the one-dimensional case in order to obtain a qualitative understanding. A full three-dimensional pulse-echo sensitivity simulation will be presented later using Field II.
When using the far-field paraxial approximation, the front-face velocity distribution $r(\eta)$ at the lateral aperture position η and the far-field radiated pressure $\mathsf{R}(x)$ at the lateral field position x are related by [Goo96]

$$\mathsf{R}(x) = k_1 \int_{-\infty}^{\infty} r(\eta) \exp\left(-j2\pi \frac{x}{\lambda z}\eta\right) d\eta. \tag{5.8}$$

Here λ is the wavelength, z is axial distance to the field point, and k_1 is a constant of proportionality that is neglected during the following derivation. The integral corresponds to a Fourier transform with a scaling of x by $1/(\lambda z)$.
The lateral beamwidth is of great significance to the clinical value of an imaging system. Thus, the pulse-echo sensitivity must be bounded in the lateral direction. The pulse-echo lateral beamwidth is influenced by both the transmit and the receive setup of the beamformer. The transmit lateral beamwidth indicates the lateral extension to which the receive beamformer can create a limited number of oscillations. One approach to describe the limited lateral pulse-echo sensitivity function is to use a lateral harmonic function multiplied by a rectangular window. The desired pattern thus consists of two terms, such as

$$\mathsf{R}(x) = \ \mathrm{rect}(L)\cos(2\pi f_x x) \tag{5.9}$$

where x is lateral distance, f_x is spatial frequency in the lateral direction, and $\mathrm{rect}(L)$ denotes a rectangular function of width L centered around $x = 0$. The lateral oscillation period is denoted $d_x = 1/f_x$. The velocity distribution of the aperture $r(\eta)$ can be calculated as a convolution of two functions, due to the Fourier relation between the aperture apodization function. The two functions are denoted $r_1(\eta)$ and $r_2(\eta)$ and the velocity distribution is

$$r(\eta) = r_1(\eta) * r_2(\eta). \tag{5.10}$$

The radiation pattern becomes

$$\mathsf{R}(x) = \mathcal{F}\{r(\eta)\} = \mathcal{F}\{r_1(\eta) * r_2(\eta)\} = \mathsf{R}_1(x)\mathsf{R}_2(x) \tag{5.11}$$

where $\mathcal{F}$ is the spatial Fourier transform and $*$ is the convolution, in this case in space.
The Fourier transform of the cosine term is

$$r_2(\eta) = \frac{1}{2z\lambda}\left[\delta\left(\frac{\eta}{z\lambda} + f_x\right) + \delta\left(\frac{\eta}{z\lambda} - f_x\right)\right] \tag{5.12}$$

and the Fourier transform of the rectangular window function of width L is

$$r_1(\eta) = \mathcal{F}\{\text{rect}(L)\} = \frac{L}{z\lambda}\frac{\sin\left(\pi\eta\frac{L}{z\lambda}\right)}{\pi\eta\frac{L}{z\lambda}} \tag{5.13}$$

Thus, a rectangular acoustic windowing field can be created if the aperture apodization function is a *sinc* function (infinite function). The width of the field is determined by the first zero crossings in the *sinc* function, *i.e.* the width of the main lobe of the *sinc* function. The first zero crossing η_0 is at

$$\eta_0 = \frac{z\lambda}{L} \tag{5.14}$$

A narrow lateral extension requires a zero far from the peak at $\eta = 0$ in the *sinc* function. If (5.12) and (5.13) are combined, the result becomes

$$r(\eta) = r_1(\eta) \otimes r_2(\eta) = \frac{L}{2z\lambda}\left(\frac{\sin\left(\pi\left(\frac{\eta}{z\lambda}+f_x\right)L\right)}{\pi\left(\frac{\eta}{z\lambda}+f_x\right)L} + \frac{\sin\left(\pi\left(\frac{\eta}{z\lambda}-f_x\right)L\right)}{\pi\left(\frac{\eta}{z\lambda}-f_x\right)L}\right) \tag{5.15}$$

which shows that a bounded lateral oscillation is generated by an aperture with an apodization of two *sinc* functions. This aperture function will give a field symmetric across the acoustic axis of the aperture. The spatial frequency f_x of the lateral modulation is determined by the distance between the peaks of the two *sinc* functions and is

$$f_x = \frac{\eta_t}{z\lambda} = \frac{1}{d_x} \tag{5.16}$$

where η_t is the positive position of the maximum of the *sinc* function. This apodization function, in simple terms, shows that the oscillating field is created by enforcing signals received at the two segments located around the centers of the *sinc* function and summing them up to create an interference pattern. The unit vectors from a point on the acoustic axis to the two *sinc* peaks on the aperture, corresponds to the wave numbers k of two interfering plane waves needed to create the interference pattern.
So far only the apodization function has been considered with the limitations put on the phase by the Fourier relation. Also the phase component of the front-face velocity distributions influences the pulse-echo sensitivity. The phase component determines the wavefront to be enforced in the beamforming [JD93]. To reinforce the oscillating properties of the receive field sensitivity at a given point on the axis of propagation, a conical delay scheme is applied, as illustrated in Figure 5.4. The conical delay scheme implies the application of plane wave approximation to the beamforming. The lateral oscillation period d_x is

$$d_x = \frac{\lambda}{\sin\alpha} \tag{5.17}$$

In Figure 5.4 the DOI (depth of region) is denoted ZF and the distance from the acoustical line to the peak value of the *sinc* function is OF . With this notation the lateral oscillation period is expressed as

$$d_x = \frac{\lambda}{\sin\left(\arctan\frac{\text{OF}}{\text{ZF}}\right)} \tag{5.18}$$

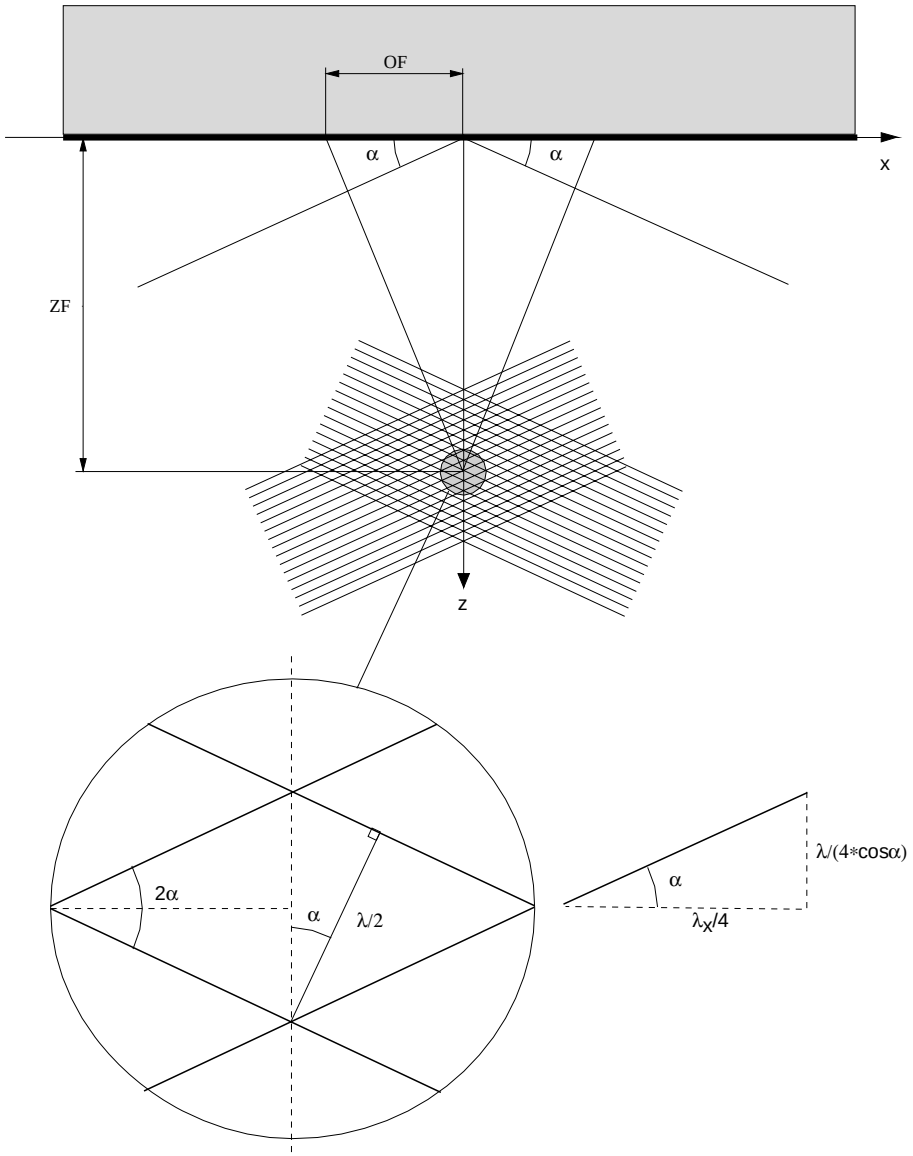

Figure 5.4: Schematics of the interference of 2 plane waves created by a conical delay profile.

Relation to pulsed plane wave decomposition

An interesting point can be made for the result obtained by the simple Fourier relations and the pulsed plane wave decomposition. The element excitation matrix calculated in Section 2.7 is sampled along the conical delay lines calculated as suggested in the previous section. The lines and the beamformer matrix are shown in Figure 5.5. The amplitude along these sampling lines is shown in Figure 5.6, and a function resembling a *sinc* can be recognized. This example illustrates the relation between pulsed fields and CW fields. The focusing introduces a time delay which from the point of view of a plane wave (each of the conical lines) corresponds to a spatial change in amplitude. The apodization of a plane wave by a *sinc* function gives the best resolution obtainable by a plane wave. This relation between the approximative CW approach and the precise pulsed plane wave decomposition suggests that the use of a *sinc* function as the apodization in combination with the conical delay profile is

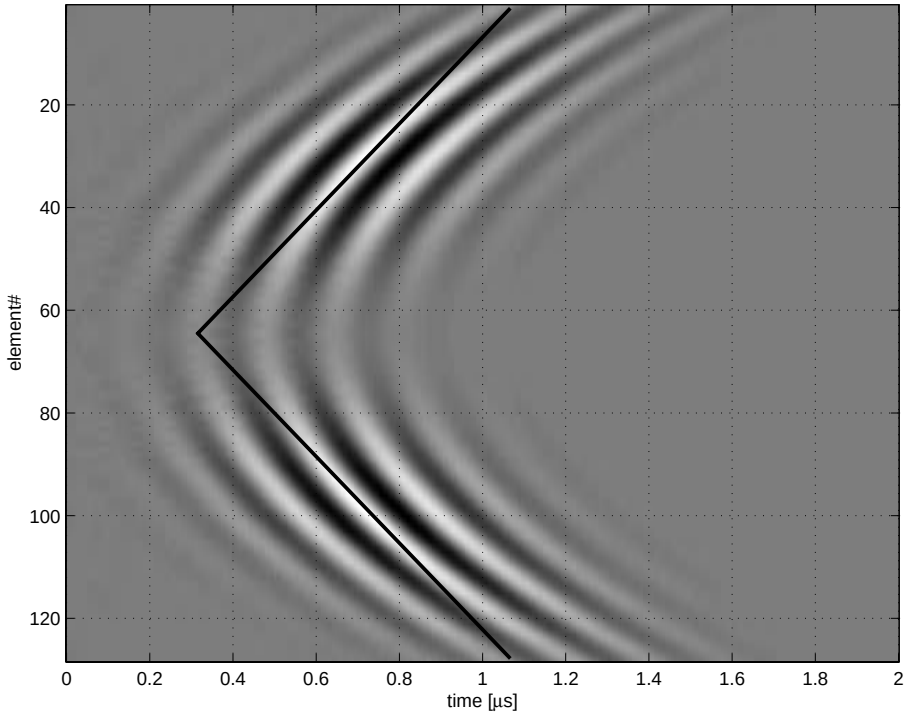

Figure 5.5: Conical delay lines in beamformer matrix for comparison of the CW and the pulsed plane wave decomposition.

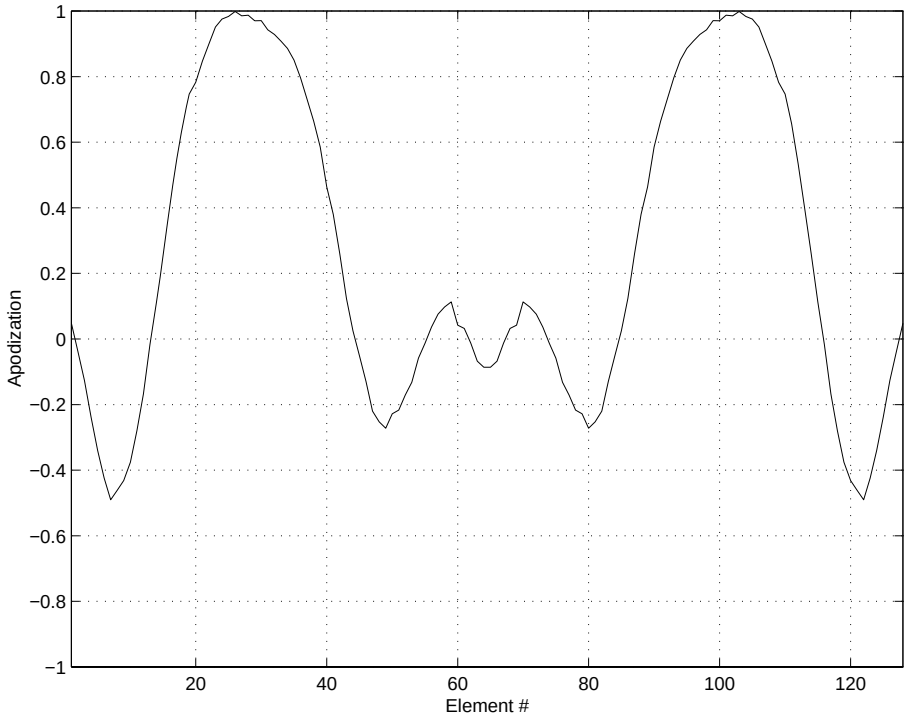

Figure 5.6: Apodization values sampled along the lines in Figure 5.5.

a good approximation for the beamformer setup to create a transverse oscillating acoustic pulse. The result obtained by the CW approach will be further used in this work, because it allows a simple programming of the beamformer when dynamic receive is considered as described in Section 5.4.3.

5.2 Spatial quadrature

In the PW Doppler systems, it is necessary to have a quadrature signal to be able to estimate the direction of the axial velocity component. In this frame, *spatial* quadrature is needed. The temporal signals are made analytically by the use of the Hilbert transformation. The spatial quadrature signal is created by two probing beams, which are displaced laterally to each other by a distance of a quarter of the lateral oscillation period. Due to the limited extent of the acoustic field, the lateral oscillation period should, in terms of the spatial Fourier domain, be referred to as the inverse of the mean value of the spatial frequency distribution. The measurement situation must correctly be described as a wideband modulation process. The received signal is a result of a modulation of the scatterer function by the spatial limited acoustic field. The displacement of the two beams is related through the narrowband approach used for quadrature detection.
The term spatial quadrature in this context is not the same as the one used by Anderson [And97], [And98], who suggests to exploit the relation between the time signals in the beamformer and the acoustic sensitivity to create one version of spatial quadrature. By first impression this approach resembles the method presented in this work. The Anderson spatial quadrature is related to the Hilbert transform on the time signals in the beamformer. The active channels on the aperture are divided in two halves, which are summed separately in a traditional manner. The two outputs from the beamformer are processed in two different ways. Either they are summed to form the output of a conventional delay-sum beamformer, or one channel is Hilbert transformed and summed with the other channel. The pulse-echo fields obtained by the two sums, form what is called 'Spatial Quadrature' because a Hilbert relation exists for the two fields in the transverse direction. This approach creates, on the basis of a normal focused beam formation, a second beam whose envelope characteristics has an approximate Hilbert relation, spatially, to the first beam. The normal focused beam can be characterized by a Gaussian envelope. Thus, the proposed method by Anderson does not have two oscillating fields as presented in this work.
The similarity of the two methods is given by a stated quadrature relation in the transverse direction. A quadrature signal is needed to find the velocity direction. The difference between the two methods is that Anderson concentrates on the quadrature relation in the sense of a spatial Hilbert relation. The method presented here is based on two channels with equal modulation characteristics, but shifted transversely to each other by a quarter of the mean lateral modulation period. In this work, the transverse modulation period is the parameter which can be controlled. In Anderson's approach only one channel has transverse oscillating characteristics, and the oscillation period is not directly controlled in his approach, but is indirectly determined by the focusing applied in the conventional beamformed channel. The signals obtained by the conventional focused field, can be described in the context of transverse Doppler [NCV+87], [NDCC94b].
Modern digital beamformers have the option of parallel beamforming. This feature allows multiple receive beams to be generated in parallel, typically 2-4 beams[2]. Thus, the two receive beams required to create a lateral spatial quadrature measurement situation can be generated simultaneously.
The beamformer setup is a complex function with an amplitude and a phase value for each channel. The two fields can be positioned by shifting them by a phase angle α and $-\alpha$, which tilts the beams by $\pm\alpha$ from the z-axis [Ste76b]. This is a Fourier approach and the associated approximations must be kept in mind. Let a linear phase shift $\exp(jk\alpha\eta)$ be

[2]Commercial real time 3D scanners use up to 64 beamformers.

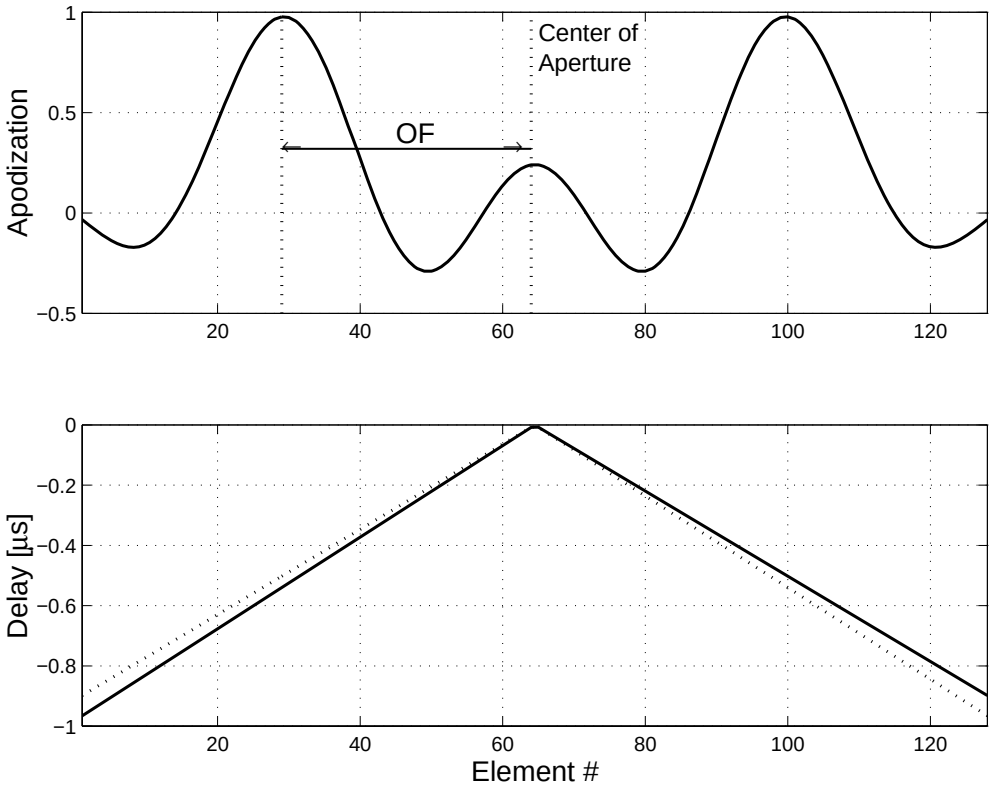

Figure 5.7: Apodization of array elements (top graph) and delay profiles (bottom graph) for the in-phase (dotted) and the quadrature (solid) receive beamformer setup.

added to an aperture apodization $r(\eta)$

$$r_{tilt}(\eta) = r(\eta)\exp(jk\alpha\eta) \tag{5.19}$$

Here α is the phase angle and $k = 2\pi/\lambda$ is the wave number. Alternatively, the beams can be displaced by shifting the complex function along the aperture line. Thus, the amplitude and the phase function are kept constant, but are shifted relative to each other according to the lateral oscillation period.

The setup for the receive beamforming is given by an apodization function and a delay function as shown in Figure 5.7. To obtain the spatial quadrature in this setup, the apodization function is kept constant and only the phase is changed between the in-phase and the quadrature channel. With spatial quadrature and time quadrature four signals are present in the measurement setup. The situation is illustrated in Figure5.8, where the geometrical positions of the measuring points are greatly exaggerated for illustration purpose. The signal pairs ($L1_I$, $L1_Q$) and ($L2_I$, $L2_Q$) are time quadrature signals and the signal pairs ($L1_I$, $L2_I$) and ($L1_Q$, $L2_Q$) are spatial quadrature signals. The spatial quadrature signals are created by the two parallel beams in the measurement setup, and the time quadrature signals are created by a Hilbert transform of the time signals. Recall that the four channels are sampled by T_{prf} (slow time) and the time Hilbert transform is performed on RF signals (fast time) in channel $L1_I$ and $L2_I$.

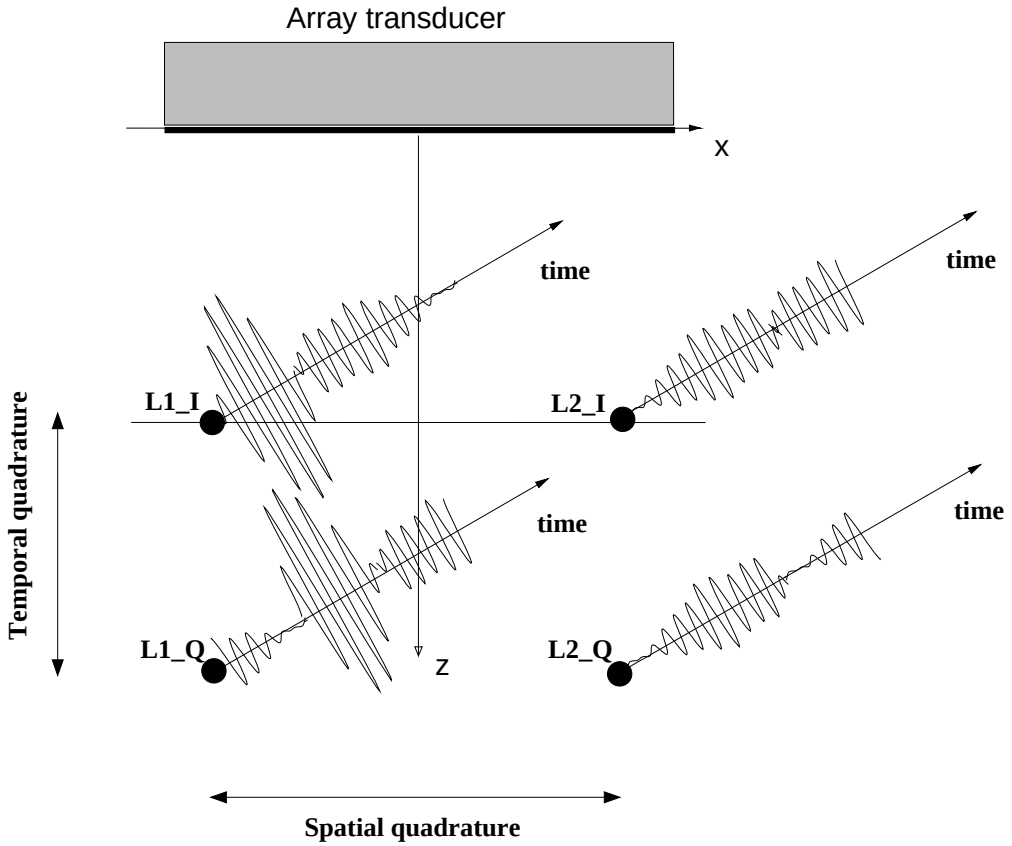

Figure 5.8: Schematics of measurement situation with 2D quadrature signals

5.3 Measures of 2D complex signals

The topic of Hilbert transforms in signal processing is treated by Hahn [Hah96]. In this work, the Hilbert transform of multidimensional complex signals is considered. The two dimensional case is of specific interest to this work. In order to be able to estimate the frequencies with no ambiguity, a single-orthant spectrum of the 2D complex signal is needed. The measurement situation is an example of 2D modulation and is, to my knowledge, the first of its kind.
The theory presented in [Hah96] is not a general theory on multidimensional analytic signals, but the book emphasizes the notation of complex signals. Based on the uniqueness theorem of the Fourier analysis, the inverse Fourier transform of a single-orthant spectrum uniquely defines a multidimensional complex signal. The multidimensional Hilbert transform is introduced. The total Hilbert transform of a nth dimensional signal $u(\mathbf{x})$ is defined as

$$v(\mathbf{x}) = \mathcal{F}_{nD}^{-1}\left\{(-\mathrm{j})^n \left(\prod_{k=1}^{n} \operatorname{sgn}\omega_k\right) U(\Omega)\right\} \tag{5.20}$$

where $\mathcal{F}_{nD}^{-1}$ is the nth dimensional inverse Fourier transform and $U(\Omega)$ is the nth dimensional Fourier transform of $u(\mathbf{x})$ and ω_k is the angular frequency.
For a signal of two dimensions, $u(x,z)$, with the 2D Fourier transform of $U(\omega_1,\omega_2)$, three Hilbert transforms exist.The total 2D Hilbert transform is defined as

$$v(x,z) = \mathcal{F}_{2D}^{-1}\left\{-\operatorname{sgn}\omega_1 \operatorname{sgn}\omega_2 U(\omega_1,\omega_2)\right\} \tag{5.21}$$

and two partial 2D transforms as

$$v_1(x,z) = \mathcal{F}_{2D}^{-1}\{-\mathrm{jsgn}\,\omega_1 U(\omega_1,\omega_2)\} \quad (5.22)$$
$$v_2(x,z) = \mathcal{F}_{2D}^{-1}\{-\mathrm{jsgn}\,\omega_2 U(\omega_1,\omega_2)\} \quad (5.23)$$

The single orthant signals related to the four quadrants are

$$\begin{array}{ll} 1.\ \text{QUADRANT:} & (u-v)+\mathrm{j}(v_1+v_2) \\ 2.\ \text{QUADRANT:} & (u+v)-\mathrm{j}(v_1-v_2) \\ 3.\ \text{QUADRANT:} & (u+v)+\mathrm{j}(v_1-v_2) \\ 4.\ \text{QUADRANT:} & (u-v)-\mathrm{j}(v_1+v_2) \end{array} \quad (5.24)$$

The single orthant 2D spectrum can be used to evaluate the lateral frequency f_x generated by the PSFs used for the velocity measurement setup. The spatial in-phase component is denoted PSF_{1I} and the quadrature PSF_{2I}. The temporal Hilbert transform of the PSF quadrants are denoted PSF_{1Q} and PSF_{2Q} respectively. Thus with $u(x,z) = PSF_{1I}$, $v(x,z) = PSF_{2Q}$, $v_1(x,z) = PSF_{1Q}$ and $v_2(x,z) = PSF_{2I}$ the calculated spectra will be single orthant. This calculation method will be used to evaluate the performance of dynamic modulation, see Section 5.4.3, and the concept of signals with single orthant spectra is used in the understanding and development of velocity estimators. An example based on the double oscillating field introduced in Chapter 2 is given. The four quadrature fields are shown in Figure 5.9. The following illustrates how the combination of the signals decreases the ambiguity in the corresponding spectra. Three examples are calculated, combining an increasing number of signals. The signals are

$$\begin{aligned} f_{4Q} &= PSF_{1I} \\ f_{2Q} &= PSF_{1I} + \mathrm{j}PSF_{2I} \\ f_{1Q} &= PSF_{1I} - PSF_{2Q} + \mathrm{j}(PSF_{1Q} + PSF_{2I}) \end{aligned} \quad (5.25)$$

and the spectra for each combination are calculated. The results are shown in Figure 5.10. The top plot is the four quadrant spectrum of f_{4Q}, the center plot is the spatial one-sided spectrum of f_{2Q} and the bottom plot is the single orthant spectrum of f_{1Q}. As the dimension of the combined signal increases, the spectral dimension decreases to a single orthant corresponding to the four-component signal. This example shows that the displacement of a quarter of the lateral oscillation period of the PSFs is a good approximation to the desired Hilbert relation between PSF_{1I} and PSF_{2I}. The single orthant spectra of the signal combinations in (5.24) are calculated and shown in Figure 5.11. Thus, by proper signal combination the resultant single orthant spectrum can be positioned in one of the quadrants. The theory presented here is developed for multidimensional signals and is thus applicable to 3 dimensional problems. This feature will be important for the future development of estimators used for 3D flow measurements.

5.4 Simulated pulse-echo acoustic field

So far only qualitative assessment of the measurement situation have been presented. The simulation program Field II is used to make a validation of previous considerations, and to

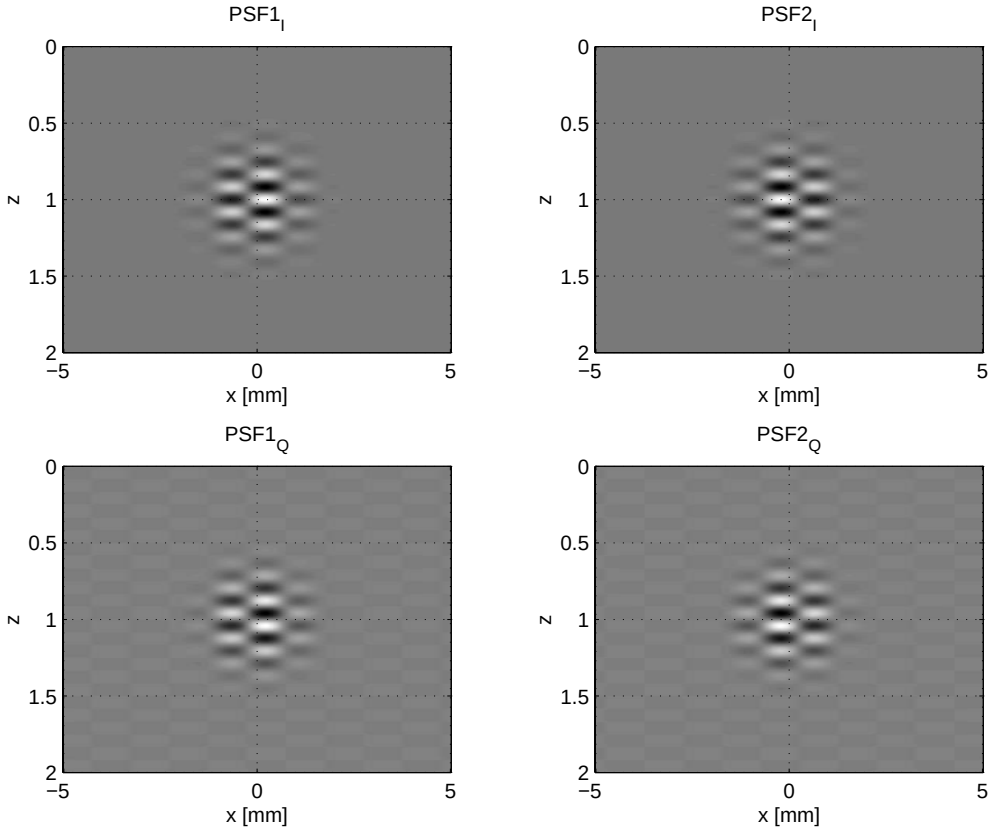

Figure 5.9: Quadrature representation of the double oscillating Gaussian enveloped acoustical field.

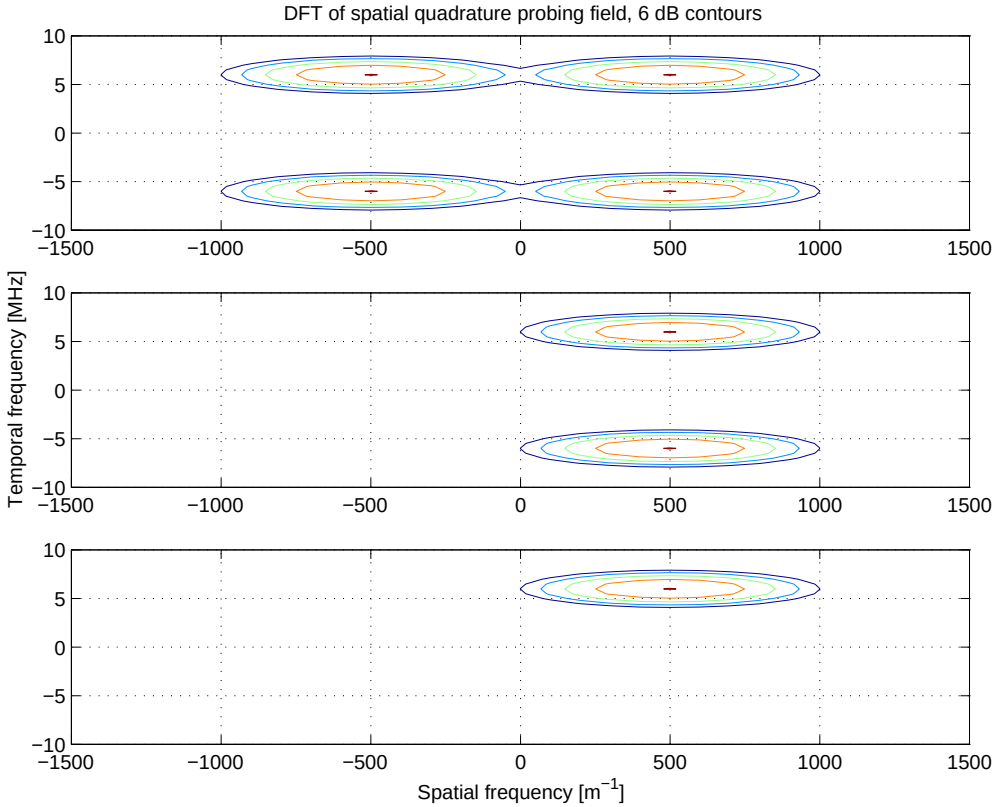

Figure 5.10: The spectral representation of combinations of the quadrature fields with 6 dB contours. A combination of all four quadrant fields results in a single orthant spectrum.

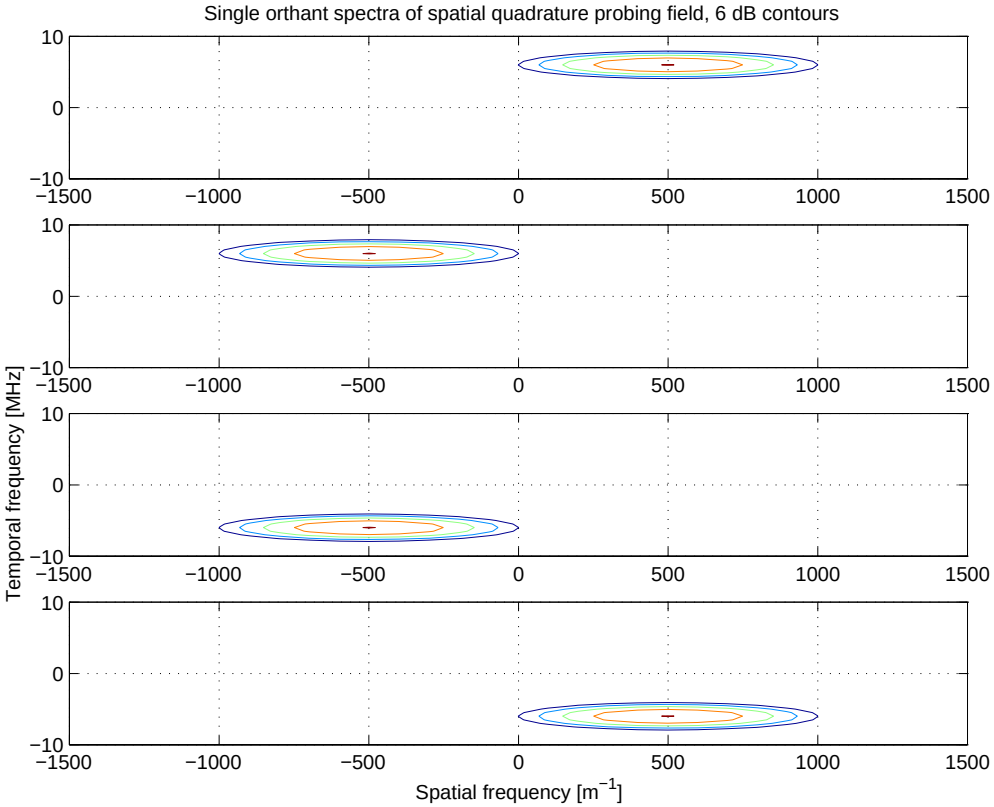

Figure 5.11: Spectral representations of different combinations of the four quadrant fields.

Array	linear
Frequency [Mhz]	6
Pitch [mm]	0.156
Kerf [μm]	25
Height [mm]	7

Table 5.1: Transducer parameters used for simulation.

demonstrate the effect of different approaches for apodization and focusing. In previous work [Mun96] the transmit field was a Gaussian bounded plane wave and the receive sensitivity was designed to create multiple oscillations laterally. The center frequency was 3 MHz and the lateral oscillation period was 4 mm resulting in a lateral extension of approximately 25 mm. In order to make the resolution applicable for medical purposes, the extent of the pulse-echo sensitivity has been diminished by the use of transmit focusing and reduced number of lateral oscillations by increasing the width of the *sinc* function used for receive apodization.

5.4.1 Simulation setup

Transducer parameters

The basic transducer parameters are given in Table 5.1. The transducer parameters correspond to the transducer used for the experiments done at Duke University. The pulse measured by a hydrophone in the experimental work is approximated in Field II by a combination of the transducer impulse response and the excitation.

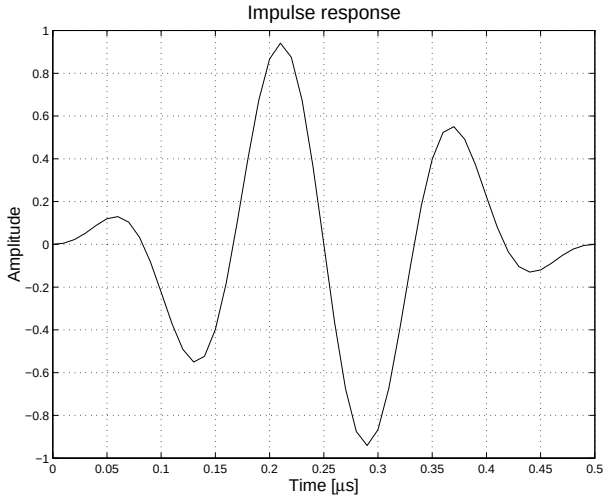

Figure 5.12: Transducer impulse response used for simulation.

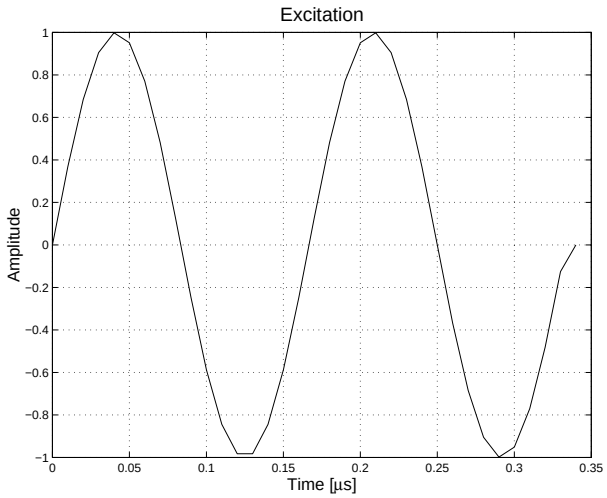

Figure 5.13: Excitation signal of two cycle sine used for simulation.

Transducer impulse response

The transducer impulse response determines the maximum bandwidth that can be used for excitation. In Field II, the transducer bandwidth is defined by the impulse response shown in Figure 5.12.

Transducer excitation

The applied excitation is a two cycle cosine and is shown in Figure 5.13. When the excitation pulse is convolved twice with the transducers impulse response, the result resembles the pulse-echo measured time response.

Transmit focus

In order to improve the spatial resolution, a transmit focus was applied with an F-number of 4. The delay profile is quadratic with a geometric focus point at 38.5 mm and the apodization is Gaussian.

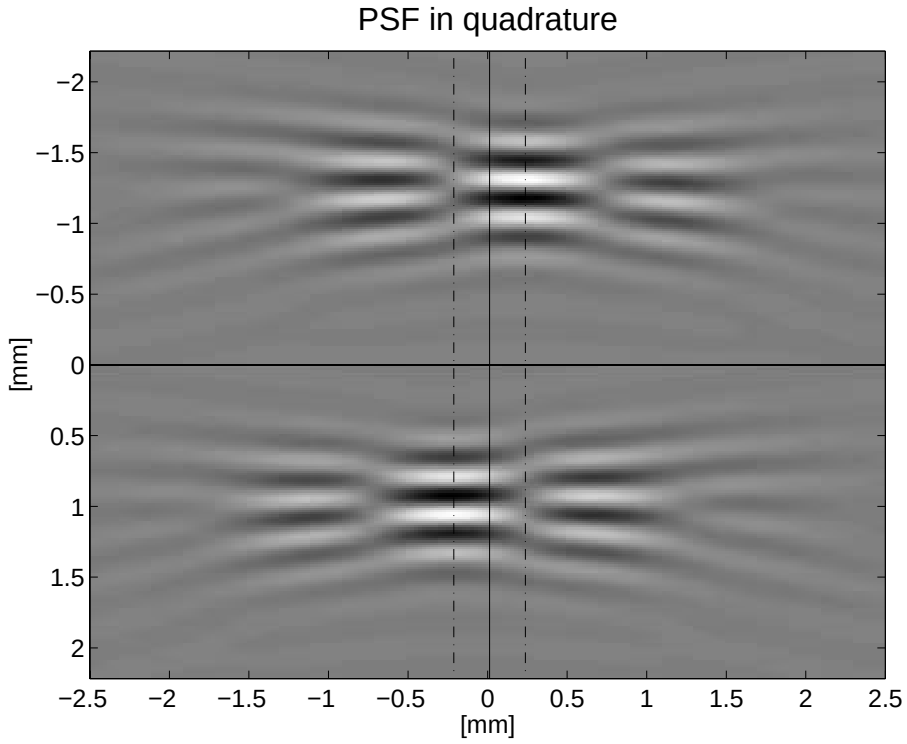

Figure 5.14: Simulated PSF in quadrature at a depth of 38.5 mm and a lateral oscillation period of 2 mm.

5.4.2 Static receive field

As an initial approach, a static receive setup was used to evaluate the performance of the vector estimation setup. With the setup shown in Figure 5.7, for a depth of 38.5 mm and a lateral oscillation period of 2 mm, the quadrature PSFs are the functions shown in Figure 5.14

The solid vertical line indicates the line of propagation and the dashed lines the position of the maximum value of the axially enveloped data for each PSF. Figure 5.14shows that the maximum value in one PSF corresponds to a zero value in the other one. The distance between the two dashed lines corresponds to one quarter of the lateral oscillation period. Thus, this simulation study supports the hypothetis to form the spatial quadrature by controling the lateral oscillation period and the displacement applying a *sinc* apodization function and a properly tilted conical delay function.

5.4.3 Dynamic receive field

One of the benefits of controlling the lateral oscillation in the receive beamforming, as opposed to the transmit beamforming, is the ability to do dynamic receive beamforming. The purpose of dynamic receive for this work is in principle the same as for the B-mode imaging: to maintain the acoustic characteristics constant for a range of depths, by tracking the acoustic pulse as it propagates in depth. In the frame of this work, it is not a matter of obtaining the smallest possible point spread function, but to obtain a constant lateral oscillation period as a function of depth, by tracking the pulse as it propagates. The term dynamic modulation will be used for this application of dynamic receive processing.

Recall, with reference to Figure 5.4 , that the lateral oscillation period d_x is

$$d_x = \frac{\lambda}{\sin\alpha} \tag{5.26}$$

where α is the cone angle.
The lateral oscillation period can also be expressed as

$$d_x = \frac{\lambda}{\sin\left(\arctan\frac{OF}{ZF}\right)} \tag{5.27}$$

where ZF is the DOI and OF is the distance from the aperture center line to the peak value of the *sinc* function.
For the analysis of the beamforming strategy, the assumption that the basic wavelength λ does not change as a function of depth, is made.[3]
According to (5.26) the conical delay profile for dynamic modulation should be static, *i.e.* α constant, to maintain a constant lateral oscillation period. The apodization scheme is determined by the ratio $\frac{OF}{ZF}$, which should be kept constant as well. Because of the limited aperture these requirements can be fulfilled only for a limited range of depths. The range for which OF can be selected is dependent on the number of zeros required for the *sinc* function used for the apodization. The number of zeros in the aperture function controls the number of oscillations. The procedure that calculates the apodization ensures that the specified number of zeros is present in the direction towards the center of the aperture. The aperture apodization function is calculated for each array element for a number of depths. Thus, to display the apodization sequence, a matrix is used. In Figure 5.15 the apodization function for a range of depths is shown. The effect of a limited aperture can be seen at a depth of 49 mm.
The first and last apodization functions are plotted in Figure 5.16 to show the different apodization functions for different depths.

The dynamic modulation is demonstrated by calculation of the lateral modulation frequency using the method presented in Section 5.3 and calculating the mass point of the single orthant spectrum. The desired lateral wavelength is 2 mm and the calculated wavelength as a function of depth is shown in Figure
5.17.
The plot shows that the lateral wavelength varies between 1.98 and 2.08 mm in the range of depth from 25 to 49 mm. For comparison the lateral wavelength with a static setup at 38.5 mm is shown in Figure 5.18.
At a first glance the static approach seems to perform more stable than the dynamic, but this is not the case. The reason for discrepancy is the use of the mass point to indicate the mean lateral spatial frequency, which indicate the change in the shape of the PSF in an ambiguous manner. To illustrate the difference between static and dynamic modulation, a series of 24 PSFs at different depths, ranging from 16-62 mm, are shown for the two cases. In Figure 5.19 and in Figure 5.20 the PSF can be compared for different locations. Figure 5.19 shows a larger variation in the 'sidelobes' than the series in Figure 5.20.

[3]The center frequency of an acoustic pulse shifts during propagation in a medium with frequency dependent attenuation. For a Gaussian pulse the shift of the center frequency can be calculated analytically. As an example with a pulse of f_0=6 MHZ and a relative bandwidth of 20 % propagating in tissue with an attenuation of 0.7 dB/cm/MHz, the shift at a depth of 5 cm is 580 kHz or 9.7 %.

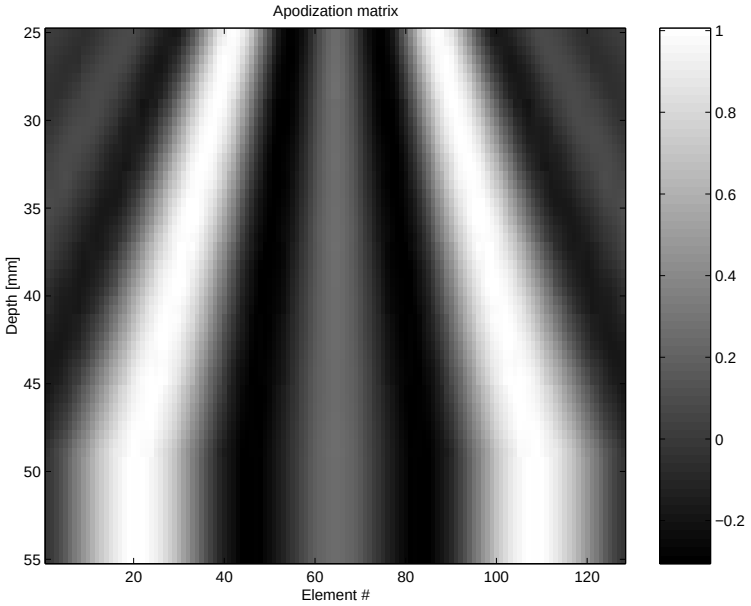

Figure 5.15: Apodization matrix for dynamic control of lateral oscillation period as a function of depth.

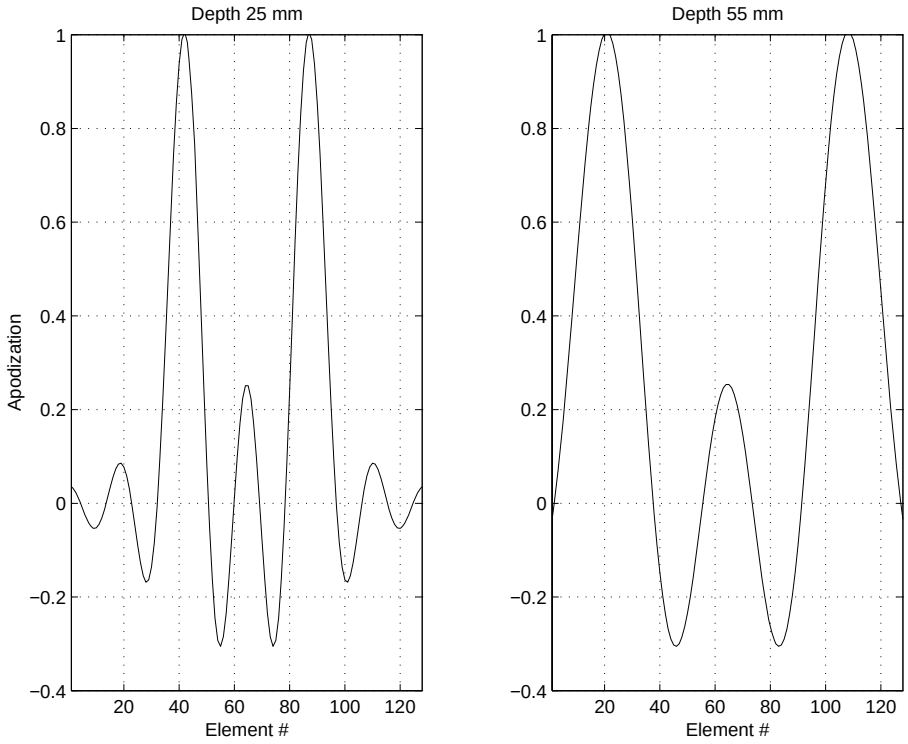

Figure 5.16: Apodization functions used for a lateral oscillation period of 2 mm at two different depths.

5.5 Measured pulse-echo acoustic field

The measurements presented here are the experimental outcome of a six-month stay at Duke University, North Carolina, USA. I was associated with one of the groups at the biomedical engineering department at Duke. The group works with adaptive imaging within medical ultrasound, and is under the supervision of Dr. Gregg Trahey. The group has the facility to obtain experimental data from a digital ultrasound scanner using an array transducer. The system is a prototype of a Siemens scanner and makes it possible to record RF-data

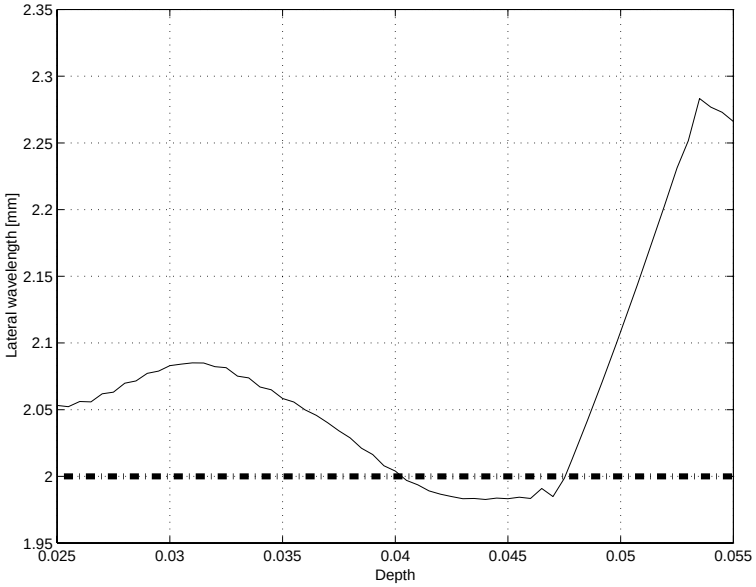

Figure 5.17: The mean lateral oscillation period as a function of depth with dynamic control.

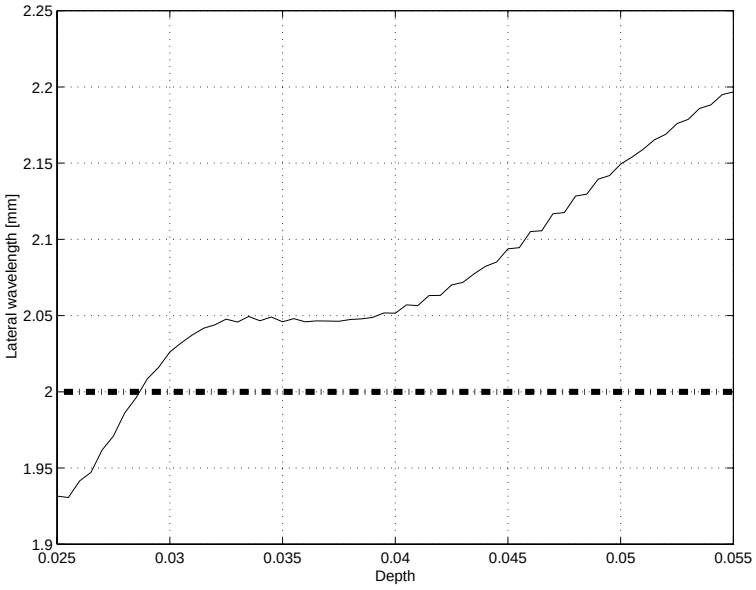

Figure 5.18: The mean lateral oscillation period as a function of depth with static control.

simultaneously from 128 channels sampled at a rate of 36 MHz. The sampled RF-data are beamformed by post processing. Data were recorded for a point reflector and a sponge, both mounted on a stepping unit. The data obtained with the point reflector were used to experimentally verify the capabilities of the proposed focusing scheme for velocity estimation. The sponge data were used to evaluate the velocity estimator on the basis of real data from a diffuse scattering medium.

The point reflector used for measurements is a spherical industrial ruby with a diameter of 1/64". The ruby has been submerged into gelatine in order to create a setup with an acoustically floating point. There is no backscattering effect[4] in the gelatine, thus, the ruby will appear as freely suspended in the media. The gelatine block was mounted on a stepping

[4]No backscattering of the propagating pulse will occur if no change in propagation velocity, density or attenuation exists.

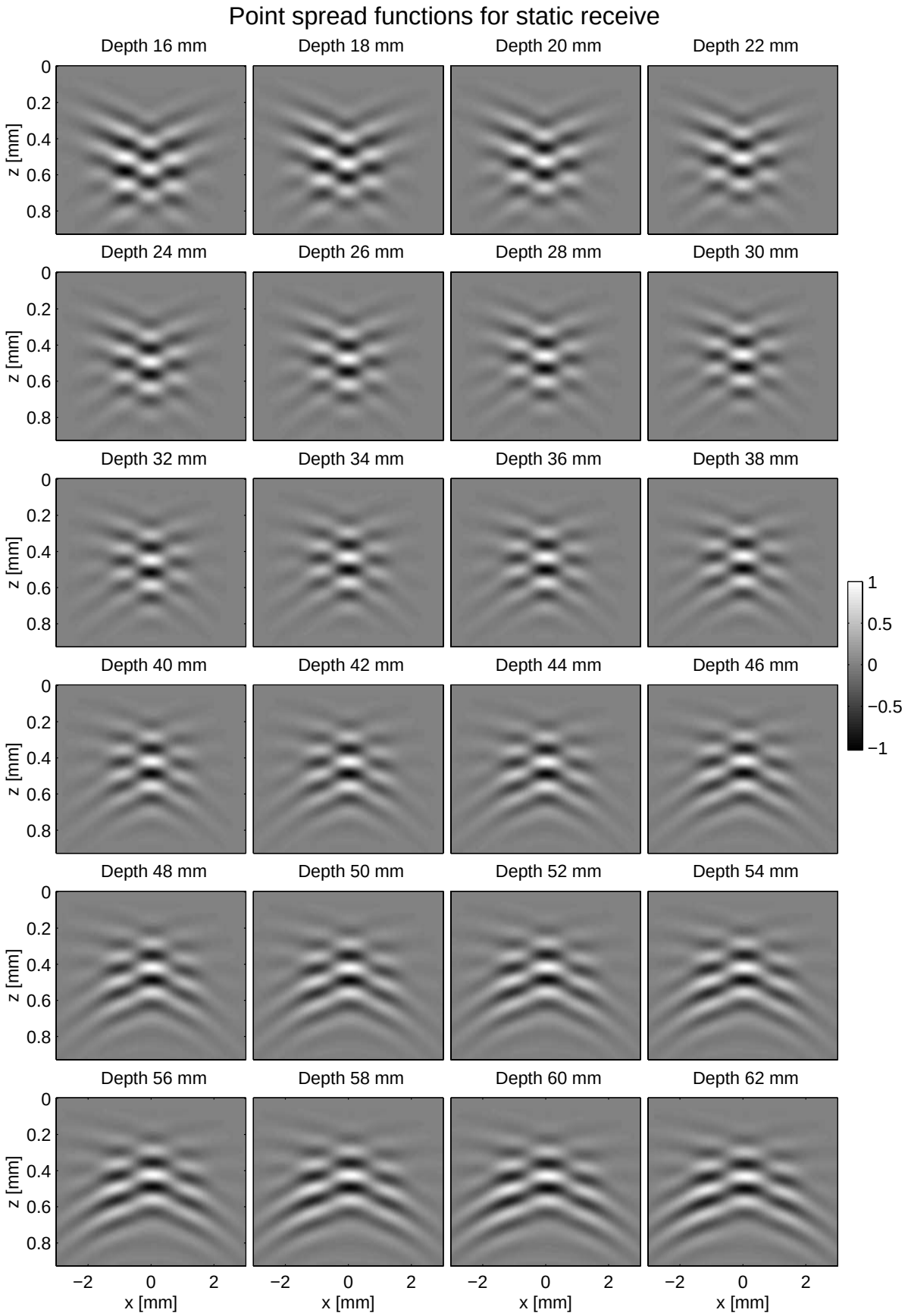

Figure 5.19: PSF at different locations with a static beamform setup.

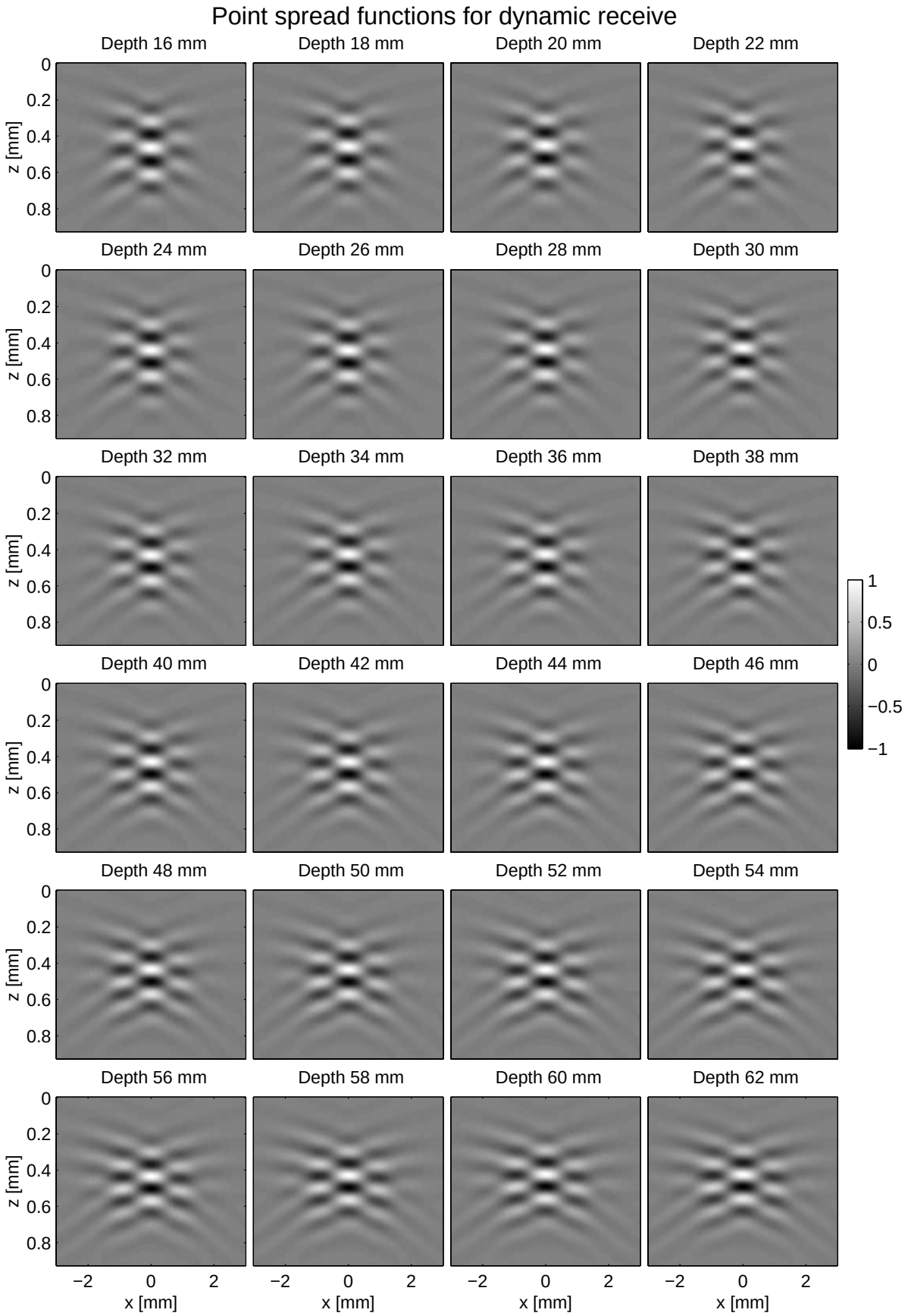

Figure 5.20: PSF at different locations with a dynamic beamform setup.

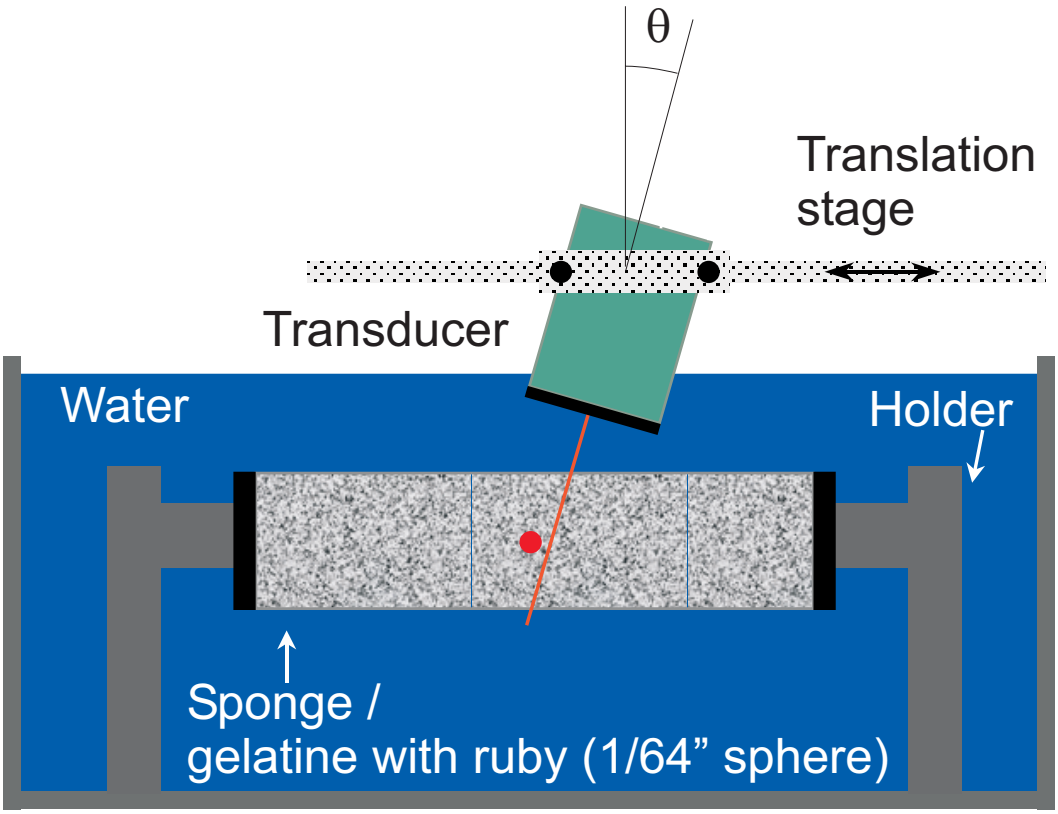

Figure 5.21: Measurement setup used for collecting experimental data with a sponge or a ruby suspended in gelatine as reflector.

device to control the displacement from one measurement to another. The measurement situation is illustrated in Figure 5.21

The ruby was positioned at a distance of 38.5 mm from the transducer surface corresponding to the acoustical transmit focus. The transmit F-number was 4 and the apodization applied a Hanning window on active elements .
The RF-data for 128 elements were recorded for each position of the ruby. The data were beamformed for each position of the ruby to form one RF line per position of the ruby. By moving the ruby parallel to the transducer surface, the 2D RF PSF can be depicted. The result is shown in Figure 5.22. The PSF is rotated a small amount counter clockwise due to a misalignment of the stepping device and the transducer surface. The overall characteristics are as expected from the previous introductory considerations based on CW assumptions. The center line shows that the pulse-echo sensitivity can be displaced to the left and right. The dashed lines show the position of the peaks of the two PSFs, which form the spatial quadrature. The resemblance between the simulated and the experimental PSF can be validated by comparison between Figure 5.22 and Figure 5.14.
Having a double oscillating field, it can be a bit troublesome to evaluate the precise displacement of the two PSFs. Therefore the axial envelope of the 2D PSF is calculated and shown in Figure 5.23. This type of display shows more precisely the displacement of the two PSFs of $\lambda_x/4$. The maximum in one PSF corresponds to the zero crossing for the other PSF and vise-versa. With this setup, the lateral extension of the acoustic field has been reduced to approximately 1.5 times the lateral oscillation period.

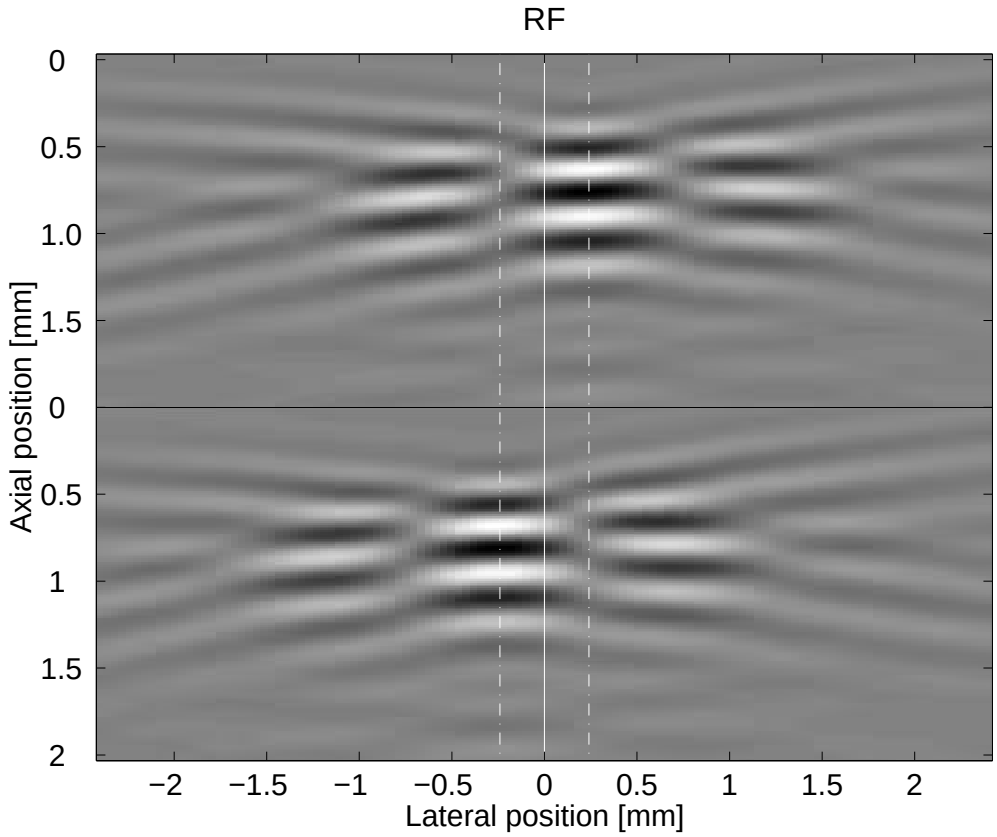

Figure 5.22: RF-data of experimental PSF in quadrature obtained with a ruby as reflector.

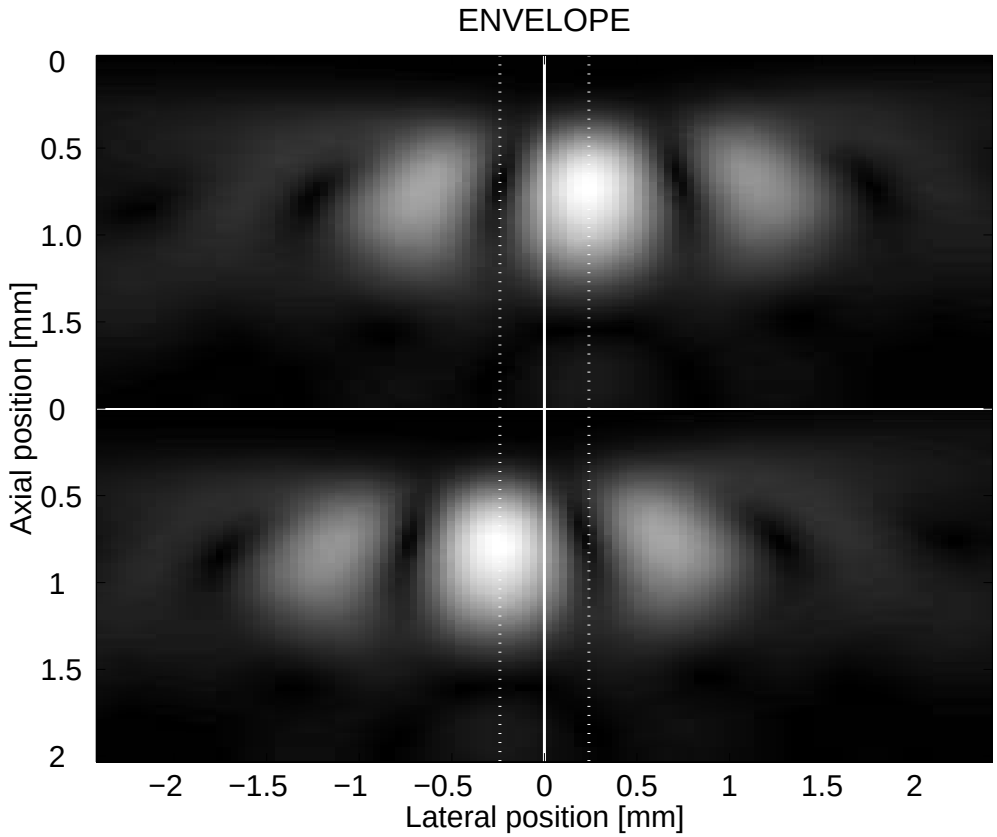

Figure 5.23: Envelope data of experimental PSF in quadrature obtained by a ruby as reflector.

5.6 Flow estimation

This section presents the derivation of the estimators to be evaluated in Chapter 6. All estimators are based on an autocorrelation approach. By principle this is a narrow-band technique, where the velocity estimation is performed by estimating the phase shift.
The derivations presented in this chapter focus on the lateral velocity component, but also an alternative method for the axial velocity estimation is given. The axial velocity component can still be calculated by a classical autocorrelation estimator by forming a received beam with conventional beamforming without the transverse modulation. This approach gives a better resolution and a lower variance of the velocity estimate at the expense of an extra receive beamformer.

5.6.1 Aliasing

The signals used to estimate the velocity components are influenced by the oscillations in the PSFs in the axial and the lateral direction. It is important to note that the phase variation for the axial movement is more rapid compared to the same lateral movement. Thus, for a flow situation with an equal axial and lateral velocity component, the phase shift of the two components, for a given time period, will be different. For a given velocity, the change in phase for the lateral signal will be smaller than the change in phase for the axial signal. To obtain the same phase shift, the lateral oscillation period must be

$$d_x = \frac{\lambda_0}{2} \tag{5.28}$$

which is not possible, because the lateral wavelength is determined by the interference of two waves with wavelength λ_0. The ratio of lateral to axial wavelength will depend on the beamforming strategy, but is typically 5 to 15. In order to obtain the same phase shift for the same velocity in the axial and lateral direction different f_{prf}s must be used.
According to the sampling theorem of a harmonic signal, the aliasing limits, in this case, are determined by the wavelengths of the modulating acoustic pulse and the f_{prf}. The harmonic signal f_1 must be sampled fast enough to limit the phase shift between two samples to π or $f_{prf} > 2 \cdot f_1$. Using the model given by 5.5, the velocity limitation in the axial velocity v_z^{max} becomes

$$2\frac{2v_z^{max}}{c} f_0 \leq f_{prf} \tag{5.29}$$

or

$$v_z^{max} = \frac{\lambda_0}{4} f_{prf} \tag{5.30}$$

and the lateral velocity limitation v_x^{max} is

$$2\frac{v_x^{max}}{d_x} \leq f_{prf} \tag{5.31}$$

or

$$v_x^{max} = \frac{d_x}{2} f_{prf} \tag{5.32}$$

To obtain the same velocity limit in the axial and lateral direction, two different PRFs, f_{prf}^z and f_{prf}^x must be used, and the relation between f_{prf}^z and f_{prf}^x is

$$\frac{f_{prf}^{z}}{f_{prf}^{x}} = 2\frac{d_x}{\lambda_0} \tag{5.33}$$

The choice will depend on the mode setup of the ultrasound scanner and the minimum acceptable framerate.

5.6.2 Estimator no. 1

This estimator is based on the assumption of a spatial quadrature relation between beams, as originally presented in the preceding M.Sc. thesis [Mun96]. The straight forward approach is improved by averaging [Jen99] and by considerations on the applied lag calculating the autocorrelation.

It was anticipated that the signals created by the measurement situation would be in temporal and spatial quadrature, and that a straight forward autocorrelation estimation method would be directly applicable to determine the lateral velocity component. The conclusion was that the lateral component could not be properly estimated due to the impact of the axial oscillation. Therefore, the use of tracking was suggested. The idea behind tracking is straight forward. The signal created in the beamformer is influenced by both the axial and lateral oscillation. Thus, the direct autocorrelation approach measures a phase change from one emission to the next created by both the axial and the lateral oscillations. In case the quadrature requirements are not met, the axial oscillation becomes a dominating error in the estimation of the lateral phase component. If the axial velocity is known, the phase contribution from the axial component can be tracked out.

To illustrate the principle, consider the following scenario. Again a simple model is used to interpret the approach. A single scatterer is traversing a double oscillating CW field. To illustrate the situation, a sampled field is shown in Figure 5.24. Each column is the recorded RF line for a given scatterer position in the field. Both the I and the Q channel for the spatial quadrature are present. The time between columns is T_{prf}=200 μs *i.e.* f_{prf}=5 kHz. The example is given for an axial frequency of 6 MHz and a lateral oscillation period of 2 mm. The velocity is 0.2 m/s with an angle θ of 60 degrees. As in a conventional pulse wave Doppler system samples are normally taken from one depth. This approach corresponds to picking samples along the horizontal trace in the data matrix show. The signals along the horizontal traces are shown in Figure 5.24, second column, trace one and three. These signals clearly show double oscillating characteristics as a result of the combined influence of the axial and the lateral oscillation in the PSF.

In order to eliminate the influence of the axial oscillation, an angled trace is applied instead of the horizontal. The choice of angle is based on the estimated axial velocity, which determines the axial displacement from one recording to another. The signals along the angled traces are shown in Figure 5.24, second column, trace two and four, having a single oscillation frequency corresponding to the influence of the lateral PSF component. The signals are now in a condition that can be used in a conventional autocorrelation approach for velocity estimation. The oscillation frequency is proportional to the lateral velocity and the two channels are in quadrature. Thus, the magnitude of the lateral velocity and the direction can be estimated.

The described case is ideal with a monochromatic field and a correct estimated axial velocity. A wrongly estimated axial component will introduce some influence of the axial oscillation on the lateral estimation, but not to the same extend as with no tracking. The obtained results demonstrate the expected effect of the tracking method.

As described in Chapter 4, the autocorrelation of lag 1 is traditionally used for estimation

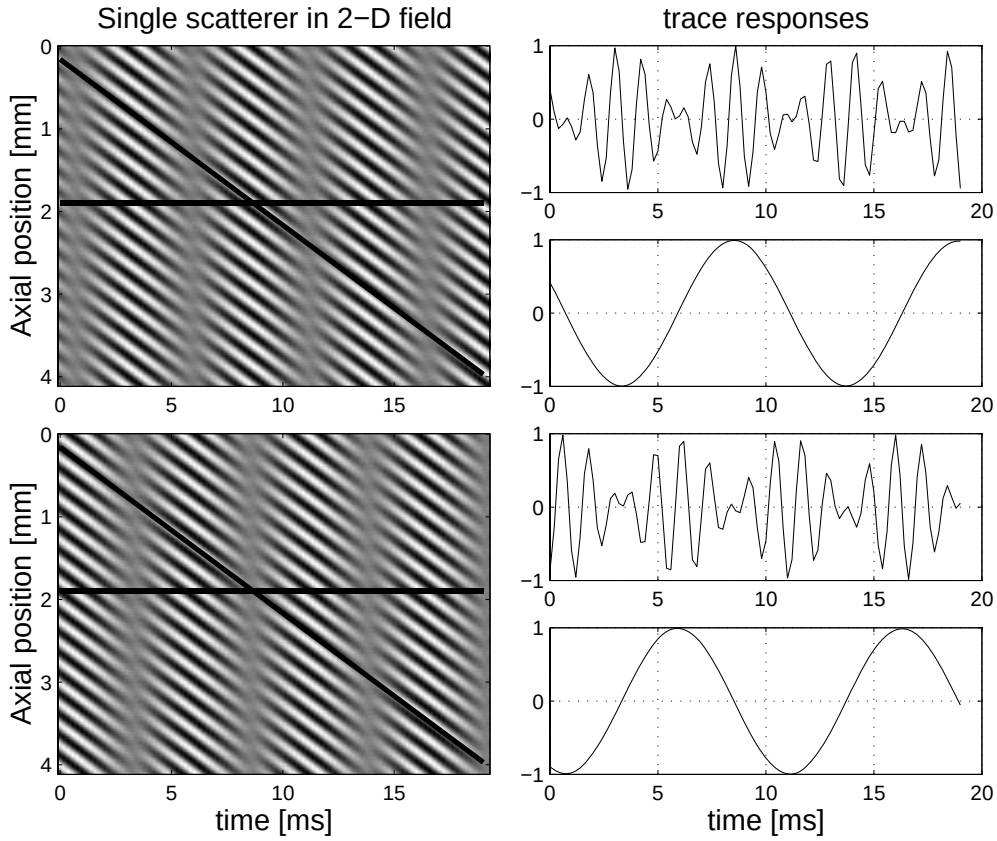

Figure 5.24: The effect of tracking on the quadrature signal.

of the velocity, but any lag can in principle be used, as long as the limit for aliasing is not exceeded. In order to find the velocity, the autocorrelation function must be estimated. The estimate of the autocorrelation is based on a number of samples. The variance of the autocorrelation estimate is inversely proportional to the number of samples employed. The number of samples available for the estimation corresponds to the number of emitted pulses per imaging direction. With a limited number of samples, for imaging purposes 4-20, the use of a higher lag number will increase the variance of the estimate [MZ83], [OS89].
The lateral modulation period is determined by the frequency and the angle between the interfering waves. With a limited aperture, the lateral modulation period is bound to be larger than the wavelength of ultrasound pulse. This suggests the use of higher lag in the estimated autocorrelation. The signal used for the velocity estimation is the phase shift and by using a higher lag, the phase signal to noise ratio can be improved. Thus, with the received signal r_{rec} the lateral velocity can be estimated by using a lag k

$$\begin{aligned} d\widehat{\Theta}_S &= \frac{1}{k}\arctan\left(\frac{\Im[\widehat{R}_S(k)]}{\Re[\widehat{R}_S(k)]}\right) \\ \widehat{R}_S(k) &= \frac{1}{N-k}\sum_{i=0}^{N-k} r^*_{rec}(i)r_{rec}(i+k), \end{aligned} \tag{5.34}$$

where N is the total number of samples used for the estimation, which equals the number of pulses emitted in one direction.
The performance of the estimator can further be improved by averaging over a number of autocorrelation estimates for a range of samples in the axial direction, *i.e.* a number of

parallel traces for different fast times t_n [Jen99]. The number of estimates to use in the axial direction is reasonably limited by the length of the applied RF-pulse. For a given sample in depth N_z, the number of pulses used is N and the number of samples for the averaging in the axial direction is N_{rf}. The estimate of the autocorrelation is

$$\widehat{R}(k;N_z) = \frac{1}{(N-k)N_{rf}} \sum_{i=0}^{N-k} \sum_{n=-\frac{N_{rf}}{2}}^{\frac{N_{rf}}{2}-1} r^*_{rec}(i,n+N_z) r_{rec}(i+k,n+N_z). \tag{5.35}$$

This expression is valid for a horizontal trace and is an extension of (5.34). For an angled trace with a slope determined by the estimated axial velocity component v_z the displacement in number of samples is

$$n_d = \text{round}\left(k\frac{2\hat{v}_z}{c}T_{prf}f_s\right). \tag{5.36}$$

With reference to N_z the axial compensated estimate of the autocorrelation $\hat{R}^c$ is

$$\widehat{R}^c(k;N_z) = \frac{1}{(N-k)N_{rf}} \sum_{i=0}^{N-k} \sum_{n_d=-\frac{N_{rf}}{2}}^{\frac{N_{rf}}{2}-1} r^*_{rec}(i,n+N_z+n_d/2) r_{rec}(i+k,n+N_z+n_d/2). \tag{5.37}$$

The estimation of the phase shift is given by

$$d\hat{\theta} = \frac{1}{k}\arctan\left(\frac{\Im\left[\widehat{R}^c(k;N_z)\right]}{\Re\left[\widehat{R}^c(k;N_z)\right]}\right) \tag{5.38}$$

where $\Im\{\widehat{R}^c(k)\}$ denotes the imaginary part of the complex autocorrelation and $\Re\{\widehat{R}^c(k)\}$ the real part at lag k.

5.6.3 Estimator no. 2

This estimator exploits the 2D quadrature relation that exists between quadrature signals in time and space for the measurement setup as defined in Figure 5.8. Compared to estimator no.1, an analysis of the measurement situation is presented. On the basis of the applied model, the estimations of the axial and the lateral component are shown to be independent and an averaging scheme is devised.
The model of the 2D double oscillating acoustical pulse-echo sensitivity $f(x,z)$ applied in this section, is used to evaluate phase relations for the signal generated. To make the analysis simple, no spatial restraints are present, *i.e.* $e_z(z) = 1$ and $e_x(x) = 1$, and $a = 1$, thus the in-phase PSF is

$$f(x,z) = \cos\left(2\pi\frac{v_z}{c}f_0 - \varphi_{z0}\right) \cdot \cos\left(2\pi x f_x - \varphi_{x0}\right) \tag{5.39}$$

and the signal received by T_{prf}-sampling, with $\phi_{z0} = 0$ and $\phi_{x0} = 0$, is

$$r_I(i) = \cos\left(\varphi_z(i)\right)\cos\left(\varphi_x(i)\right). \tag{5.40}$$

The spatial quadrature PSF is

$$f(x,z) = \cos\left(2\pi\frac{v_z}{c}f_0 - \varphi_{z0}\right) \cdot \sin\left(2\pi x f_x - \varphi_{x0}\right) \tag{5.41}$$

and giving the signal

$$r_Q(i) = \cos(\varphi_z(i)) \sin(\varphi_x(i)). \tag{5.42}$$

The two phase components, in the z- and x-direction, are noted φ_z and φ_x respectively and are given by

$$\varphi_z(i) = 2\pi \frac{2v_z}{c} f_0 i T_{prf} \tag{5.43}$$

and

$$\varphi_x(i) = 2\pi v_x f_x i T_{prf} \tag{5.44}$$

Let the acoustic field sensitivity be described by the signals $L1_I$, $L1_Q$,$L2_I$ and $L2_Q$ in the model, thus

$$\begin{aligned} L1_I &= \cos\varphi_z \cos\varphi_x \\ L1_Q &= \sin\varphi_z \cos\varphi_x \\ L2_I &= \cos\varphi_z \sin\varphi_x \\ L2_Q &= \sin\varphi_z \sin\varphi_x \end{aligned} \tag{5.45}$$

where I and Q in this notation refer to the temporal Hilbert relation. By combination of the signals, four quadrature signals are defined, two in time and two in space,

$$\begin{aligned} S1 &= L1_I + \mathrm{j}L2_I \\ S2 &= L1_Q + \mathrm{j}L2_Q \\ S3 &= L1_I + \mathrm{j}L1_Q \\ S4 &= L2_I + \mathrm{j}L2_Q. \end{aligned} \tag{5.46}$$

Using (5.46) in (5.47), the combined signals can be written as

$$S1 = \cos\varphi_z \cos\varphi_x + \mathrm{j}\cos\varphi_z \sin\varphi_x = \cos\varphi_z \exp \mathrm{j}\varphi_x \tag{5.47}$$

$$S2 = \sin\varphi_z \cos\varphi_x + \mathrm{j}\sin\varphi_z \sin\varphi_x = \sin\varphi_z \exp \mathrm{j}\varphi_x \tag{5.48}$$

$$S3 = \cos\varphi_z \cos\varphi_x + \mathrm{j}\sin\varphi_z \cos\varphi_x = \cos\varphi_x \exp \mathrm{j}\varphi_z \tag{5.49}$$

$$S4 = \cos\varphi_z \sin\varphi_x + \mathrm{j}\sin\varphi_z \sin\varphi_x = \sin\varphi_x \exp \mathrm{j}\varphi_z. \tag{5.50}$$

The phase ϕ of a complex signal $S(t) = x_s(t) + \mathrm{j}y_s(t)$ is calculated by

$$\phi(t) = \arctan\left(\frac{y_s(t)}{x_s(t)}\right). \tag{5.51}$$

To calculate the estimated velocity, the phase derivative $\theta(t) = \frac{\partial\phi}{\partial t}$ is needed, and for a discrete time signal the phase derivative is approximated in two different ways. Either by[5]

$$\theta_S(i) \approx \frac{\Delta\phi(i)}{\Delta i} = \frac{y_s(i)x_s(i-1) - x_s(i)y_s(i-1)}{x_s(i)x_s(i-1) + y_s(i)y_s(i-1)} \tag{5.54}$$

[5]The derivative can also be approximated by:

$$\theta_S(i) \approx \frac{\Delta\phi(i)}{\Delta i} = \frac{y_s(i)x_s(i-1) - x_s(i)y_s(i-1)}{x_s(i)^2 + y_s(i)^2} \tag{5.52}$$

or by the direct phase difference

$$\theta_S(i) = \frac{\Delta\phi(i)}{\Delta i} = \phi(i) - \phi(i-1) = \arctan\left(\frac{y_s(i)}{x_s(i)}\right) - \arctan\left(\frac{y_s(i-1)}{x_s(i-1)}\right) \tag{5.55}$$

With the approach given by (5.54) the phase for the 4 signals are, as expected,

$$\begin{aligned}
\theta_{S1}(i) &= \tan(\varphi_x(i) - \varphi_x(i-1)) && (5.56)\\
\theta_{S2}(i) &= \tan(\varphi_x(i) - \varphi_x(i-1)) && (5.57)\\
\theta_{S3}(i) &= \tan(\varphi_z(i) - \varphi_z(i-1)) && (5.58)\\
\theta_{S4}(i) &= \tan(\varphi_z(i) - \varphi_z(i-1)) && (5.59)
\end{aligned}$$

and for the combined signals

$$S_{1\pm2} = S1 \pm S2 = \cos\varphi_x(\cos\varphi_z + \sin\varphi_z) \pm \mathrm{j}\sin\varphi_x(\cos\varphi_z + \sin\varphi_z), \tag{5.60}$$

and

$$S_{3\pm4} = S3 \pm S4 = \sin\varphi_z(\cos\varphi_x + \sin\varphi_x) \pm \mathrm{j}\cos\varphi_z(\cos\varphi_x + \sin\varphi_x). \tag{5.61}$$

The relations for the phase difference using sum and difference of the signals are

$$\begin{aligned}
\theta_{S1\pm2}(i) &= \pm\tan(\varphi_x(i) - \varphi_x(i-1)) && (5.62)\\
\theta_{S3\pm4}(i) &= \pm\tan(\varphi_z(i) - \varphi_z(i-1)) && (5.63)
\end{aligned}$$

Applying (5.43) and (5.44), the relationship between phase and velocity for the lateral and axial velocity component can be established. The phase derivatives θ_S are calculated with autocorrelation approach given in either (5.35) or (5.37) , thus either $\theta_S = \hat{R}(k;N_z)$ or $\theta_S = \hat{R}^c(k;N_z)$

Having in mind that $S2$ is the temporal Hilbert transform of $S1$, and $S4$ of $S3$, then adding and subtracting corresponds to averaging in the case of oscillating signals in quadrature.

Further, θ_{S1+2} and θ_{S1-2} can be combined in the case of an imbalance between the spatial quadrature channels. The imbalance can be created by speckle, as well as by spatial misalignment, and reduced correlation between the PSF in the two spatial channels. The phase derivative of the signal $S_{12} = S_{1+2} + S_{1-2}$ is used to estimate the lateral velocity component with $\theta_{S12} = 0.5(\theta_{S1+2} - \theta_{S1-2})$ and the velocity component is calculated by

$$v_x = -\frac{1}{2\pi f_x T_{prf} k}\arctan\left(\frac{\Im[{R_{12}}^c(k;N_z)]}{\Re[{R_{12}}^c(k;N_z)]}\right) \tag{5.64}$$

The same approach is used for the axial direction, not to improve the temporal quadrature because the axial quadrature is calculated by the Hilbert transform, but to improve noise- and speckle-reduction by averaging. The phase derivative of the signal $S_{34} = S_{3+4} + S_{3-4}$

but the addition for harmonic signals does not apply for the phase,
i.e if $S_{12} = S_1 + S_2$ then $\theta_{S12}(i) \neq \frac{\theta_{S1}(i)+\theta_{S2}(i)}{2}$ where

$$\theta_{S1}(i) \approx \tfrac{\Delta\phi_{S1}(i)}{\Delta i} \quad \theta_{S2}(i) \approx \tfrac{\Delta\phi_{S2}(i)}{\Delta i} \quad \theta_{S12}(i) \approx \tfrac{\Delta\phi_{S12}(i)}{\Delta i} \tag{5.53}$$

is used to estimate the axial velocity component $\theta_{S34} = 0.5(\theta_{S3+4} - \theta_{S3-4})$, and the velocity component is calculated by

$$v_z = -\frac{c}{4\pi f_0 T_{prf} k} \arctan\left(\frac{\Im[R_{34}{}^c(k;N_z)]}{\Re[R_{34}{}^c(k;N_z)]}\right) \tag{5.65}$$

The derivation of (5.65) and (5.64) are based on the discrete approximation (5.54). Another approach is to use (5.55). The result is obtained in a more straightforward manner, because the phase contributions are considered at separate time instants, i and $i-1$. The phase for each quadrature signal is calculated

$$\theta_{S1} = \arctan\left(\frac{\cos\varphi_z(i)\sin\varphi_x(i)}{\cos\varphi_z(i)\cos\varphi_x(i)}\right) - \arctan\left(\frac{\cos\varphi_z(i-1)\sin\varphi_x(i-1)}{cos\varphi_z(i-1)\cos\varphi_x(i-1)}\right) \tag{5.66}$$

$$\theta_{S2} = \arctan\left(\frac{\sin\varphi_z(i)\sin\varphi_x(i)}{\sin\varphi_z(i)\cos\varphi_x(i)}\right) - \arctan\left(\frac{\sin\varphi_z(i-1)\sin\varphi_x(i-1)}{sin\varphi_z(i-1)\cos\varphi_x(i-1)}\right) \tag{5.67}$$

$$\theta_{S3} = \arctan\left(\frac{\sin\varphi_z(i)\cos\varphi_x(i)}{\cos\varphi_z(i)\cos\varphi_x(i)}\right) - \arctan\left(\frac{\sin\varphi_z(i-1)\cos\varphi_x(i-1)}{cos\varphi_z(i-1)\cos\varphi_x(i-1)}\right) \tag{5.68}$$

$$\theta_{S4} = \arctan\left(\frac{\sin\varphi_z(i)\sin\varphi_x(i)}{\cos\varphi_z(i)\sin\varphi_x(i)}\right) - \arctan\left(\frac{\sin\varphi_z(i-1)\sin\varphi_x(i-1)}{\cos\varphi_z(i-1)\sin\varphi_x(i-1)}\right) \tag{5.69}$$

which in the case of 2D quadrature becomes

$$\tag{5.70}$$

$$\theta_{S1} = \varphi_x(i) - \varphi_x(i-1) \tag{5.71}$$

$$\theta_{S2} = \varphi_x(i) - \varphi_x(i-1) \tag{5.72}$$

$$\theta_{S3} = \varphi_z(i) - \varphi_z(i-1) \tag{5.73}$$

$$\theta_{S4} = \varphi_z(i) - \varphi_z(i-1) \tag{5.74}$$

where the relation $\cot(z) = \tan(\frac{\pi}{2} - z)$ is used for calculating θ_{S3} and θ_{S4}. Using (5.43) and (5.44), a direct relation for the derivate of the phase and the velocity is found

$$\theta_{S1} = \theta_{S2} = -2\pi f_x v_x T_{prf} \tag{5.75}$$

$$\theta_{S3} = \theta_{S4} = -2\pi f_0 \frac{2v_z}{c} T_{prf}. \tag{5.76}$$

If the estimate of the phase derivative, *i.e.* of the autocorrelation function is based on (5.37), the estimate of the axial velocity component using lag k is

$$\hat{v}_z = -\frac{c}{4\pi f_0 T_{prf} k} \arctan\left(\frac{\Im[\widehat{R}^c_{S3}(k;N_z)]}{\Re[R_{S3}{}^c(k;N_z)]}\right) \tag{5.77}$$

or

$$\hat{v}_z = -\frac{c}{4\pi f_0 T_{prf} k} \arctan\left(\frac{\Im[\widehat{R}^c_{S4}(k;N_z)]}{\Re[R_{S4}{}^c(k;N_z)]}\right) \tag{5.78}$$

and the estimate of the lateral velocity component is

$$\hat{v}_x = -\frac{1}{2\pi f_x T_{prf} k} \arctan\left(\frac{\Im[\widehat{R}^c_{S1}(k;N_z)]}{\Re[R_{S1}{}^c(k;N_z)]}\right) \tag{5.79}$$

or

$$\hat{v}_x = -\frac{1}{2\pi f_x T_{prf} k} \arctan\left(\frac{\Im[\widehat{R}^c_{S2}(k;N_z)]}{\Re[{R_{S2}}^c(k;N_z)]}\right) \tag{5.80}$$

5.6.4 Estimator no. 3

This estimator is also based on the quadrature relations given by the model of 2D complex signals as described in section 5.3. The described approach was developed by Jensen and is submitted for publication [Jen99].
The velocities to be estimated can be both positive and negative, and a signal with a one-sided spectrum should be employed to calculate the velocity. Two complex signals are defined by combinations of the quadrature signals. This estimator calculates two phases, which are the sum and the difference of the phase created by the axial and the lateral oscillation. These phases are then summed and subtracted to calculate the lateral and the axial velocity components.
The acoustic fields are assumed monochromatic with unit amplitude both temporally and spatially, thus, the received and sampled spatial quadrature signal can be written as

$$S1(i) = \cos(2\pi f_p i T_{prf}) \exp(j2\pi f_x^v i T_{prf}) \tag{5.81}$$

where

$$f_p = \frac{2v_z}{c} f_0$$
$$f_x^v = f_x v_x$$

The temporal Hilbert transform of the RF signal in the two spatial quadrature channels yields

$$S2(i) = \sin(2\pi f_p i T_{prf}) \exp(j2\pi f_x^v i T_{prf}). \tag{5.82}$$

New complex signals are defined as

$$\begin{aligned}
SQ1(i) &= S1(i) + jS2(i) \\
&= \frac{1}{2}\left(\exp(j2\pi i T_{prf}(f_x^v + f_p)) + \exp(j2\pi i T_{prf}(f_x^v - f_p))\right) \\
&+ j\frac{1}{2j}\left(\exp(j2\pi i T_{prf}(f_x^v + f_p)) - \exp(j2\pi i T_{prf}(f_x^v - f_p))\right) \\
&= \exp(j2\pi i T_{prf}(f_x^v + f_p)) \qquad (5.83) \\
SQ2(i) &= S1(i) - jS2(i) \\
&= \frac{1}{2}\left(\exp(j2\pi i T_{prf}(f_x^v + f_p)) + \exp(j2\pi i T_{prf}(f_x^v - f_p))\right) \\
&- j\frac{1}{2j}\left(\exp(j2\pi i T_{prf}(f_x^v + f_p)) - \exp(j2\pi i T_{prf}(f_x^v - f_p))\right) \\
&= \exp(j2\pi i T_{prf}(f_x^v - f_p)), \qquad (5.84)
\end{aligned}$$

which gives complex exponentials with phases proportional to the sum and difference of f_p and f_x^v.

The phase changes of the complex exponentials are

$$\begin{aligned} d\theta_{SQ1} &= 2\pi T_{prf}(f_x^v + f_p) \\ d\theta_{SQ2} &= 2\pi T_{prf}(f_x^v - f_p) \end{aligned} \tag{5.85}$$

Adding $d\theta_{SQ1}$ and $d\theta_{SQ2}$ gives

$$d\theta_{SQ1} + d\theta_{SQ2} = 2\pi 2 T_{prf} f_x^v = 4\pi T_{prf} v_x f_x \tag{5.86}$$

and subtracting $d\theta_{SQ1}$ and $d\theta_{SQ2}$ gives

$$d\theta_{SQ1} - d\theta_{SQ2} = 2\pi 2 T_{prf} f_p = 4\pi T_{prf} \frac{2v_z}{c} f_0 \tag{5.87}$$

The transverse velocity component can be found by

$$v_x = \frac{(d\theta_{SQ1} + d\theta_{SQ2})}{2\pi 2 f_x T_{prf}} \tag{5.88}$$

and the axial velocity component as

$$v_z = \frac{(d\theta_{SQ1} - d\theta_{SQ2})c}{2\pi 4 T_{prf} f_0}. \tag{5.89}$$

The result shows that this estimator also calculates the axial and transverse velocity component independently of each other. The combination of the signals results in complex signals, where the real and the imaginary part are combined by diagonals in the model illustrated in Figure 5.8 that relates $SQ1 = (L1_I - L2_Q) + \mathrm{j}(L1_Q + L2_I)$ and $SQ2 = (L1_I + L2_Q) + \mathrm{j}(L1_Q - L2_I)$.
The phase change θ is calculated using (5.34). The calculation of the transverse velocity component (5.88) depends on two arc-tangents. To improve phase aliasing problems of two components, the relation

$$\tan(A \pm B) = \frac{\tan(A) \pm \tan(B)}{1 \mp \tan(A)\tan(B)} \tag{5.90}$$

can be used and the result becomes

$$\begin{aligned} \tan(d\theta_{SQ1} + d\theta_{SQ2}) &= \tan\left(\arctan\left(\frac{\Im[\widehat{R}^c_{SQ1}(k)]}{\Re[\widehat{R}^c_{SQ1}(k)]}\right) + \arctan\left(\frac{\Im[\widehat{R}^c_{SQ2}(k)]}{\Re[\widehat{R}^c_{SQ2}(k)]}\right)\right) \\ &= \frac{\Im[\widehat{R}^c_{SQ1}(k)]\Re[\widehat{R}^c_{SQ2}(k)] + \Im[\widehat{R}^c_{SQ2}(k)]\Re[\widehat{R}^c_{SQ1}(k)]}{\Re[\widehat{R}^c_{SQ1}(k)]\Re[\widehat{R}^c_{SQ2}(k)] - \Im[\widehat{R}^c_{SQ1}(k)]\Im[\widehat{R}^c_{SQ2}(k)]} \end{aligned} \tag{5.91}$$

where $R_{SQ1}(k)$ is the complex lag k autocorrelation value for $SQ1(i)$ and $R_{SQ2}(k)$ is the complex lag k autocorrelation value for $SQ2(i)$. A similar expression can be derived for the

axial velocity, and the estimators are:

$$v_x = \frac{d_x}{2\pi 2T_{prf}} \arctan\left(\frac{\Im[\widehat{R}^c_{SQ1}(k)]\Re[\widehat{R}^c_{SQ2}(k)] + \Im[\widehat{R}^c_{SQ2}(k)]\Re[\widehat{R}^c_{SQ1}(k)]}{\Re[\widehat{R}^c_{SQ1}(k)]\Re[\widehat{R}^c_{SQ2}(k)] - \Im[\widehat{R}^c_{SQ1}(k)]\Im[\widehat{R}^c_{SQ2}(k)]}\right) \tag{5.92}$$

and

$$v_z = \frac{c}{2\pi 4T_{prf} f_0} \arctan\left(\frac{\Im[R_{SQ1}(k)]\Re[R_{SQ2}(k)] - \Im[R_{SQ2}(k)]\Re[R_{SQ1}(k)]}{\Re[R_{SQ1}(k)]\Re[R_{SQ2}(k)] + \Im[R_{SQ1}(k)]\Im[R_{SQ2}(k)]}\right). \tag{5.93}$$

Compared to previous estimators, this approach involves fourth order moments in the estimation procedure.

5.6.5 Estimator no. 4

This section presents a further combined development of the approaches used for estimator no. 2 and no. 3. The idea is to exploit the averaging approach used for estimator no. 2 and the creation of signals with one-sided spectra, as used for estimator no. 3. The development of estimator no. 3 anticipates that the signals generated by the four channels are in 2D quadrature as defined in Section 5.3. The signal $SQ1$ created in the derivation of estimator no. 3 is analogous to a 2D complex signal with a 1'st. quadrant one-sided spectrum. The phenomena of speckle will prevent the generated signals to have 2D quadrature relations. Thus, an averaging scheme is suggested to improve the quadrature relation of the 2D signals. The 2D spectrum can be calculated in four different ways using the signal pairs $(L1_I, L1_Q)$ and $(L2_I, L2_Q)$, one for each quadrant in the 2D frequency domain. A short notation of the quadrature signals is introduced

$$\begin{aligned} u &= L1_I \qquad (5.94)\\ u_1 &= L2_I \\ u_2 &= L1_Q \\ v &= L2_Q \qquad (5.95) \end{aligned}$$

The relation between signal combinations and quadrant spectra is given by

$$\begin{aligned} &1.\ \text{QUADRANT:} && (u-v) + \mathrm{j}(v_1+v_2) \\ &2.\ \text{QUADRANT:} && (u+v) - \mathrm{j}(v_1-v_2) \\ &3.\ \text{QUADRANT:} && (u+v) + \mathrm{j}(v_1-v_2) \\ &4.\ \text{QUADRANT:} && (u-v) - \mathrm{j}(v_1+v_2) \end{aligned} \tag{5.96}$$

The four single orthant spectra are depicted in Figure 5.25 as the circles $Q1, Q2, Q3$ and $Q4$, where the number refers to the quadrant definition. Figure 5.25 illustrates the possible combinations to use for calculation of f_x and f_p. The approach used in estimator 3 is illustrated in Figure 5.25. Different gray levels are used. The medium grey circles reflect the calculation of the phase of $Q1$ and $Q2$ signals. The dark gray circles indicate the sum and difference of the $Q1$ and $Q2$ phases, which are used to estimate the axial and lateral velocity components. The light grey circles show the option of using $Q3$ and $Q4$, and the alternative summations and subtractions. The measurement setup gives 4 signals, which are supposed to be in a 2D Hilbert relation. The four signals are combined to form two complex signals

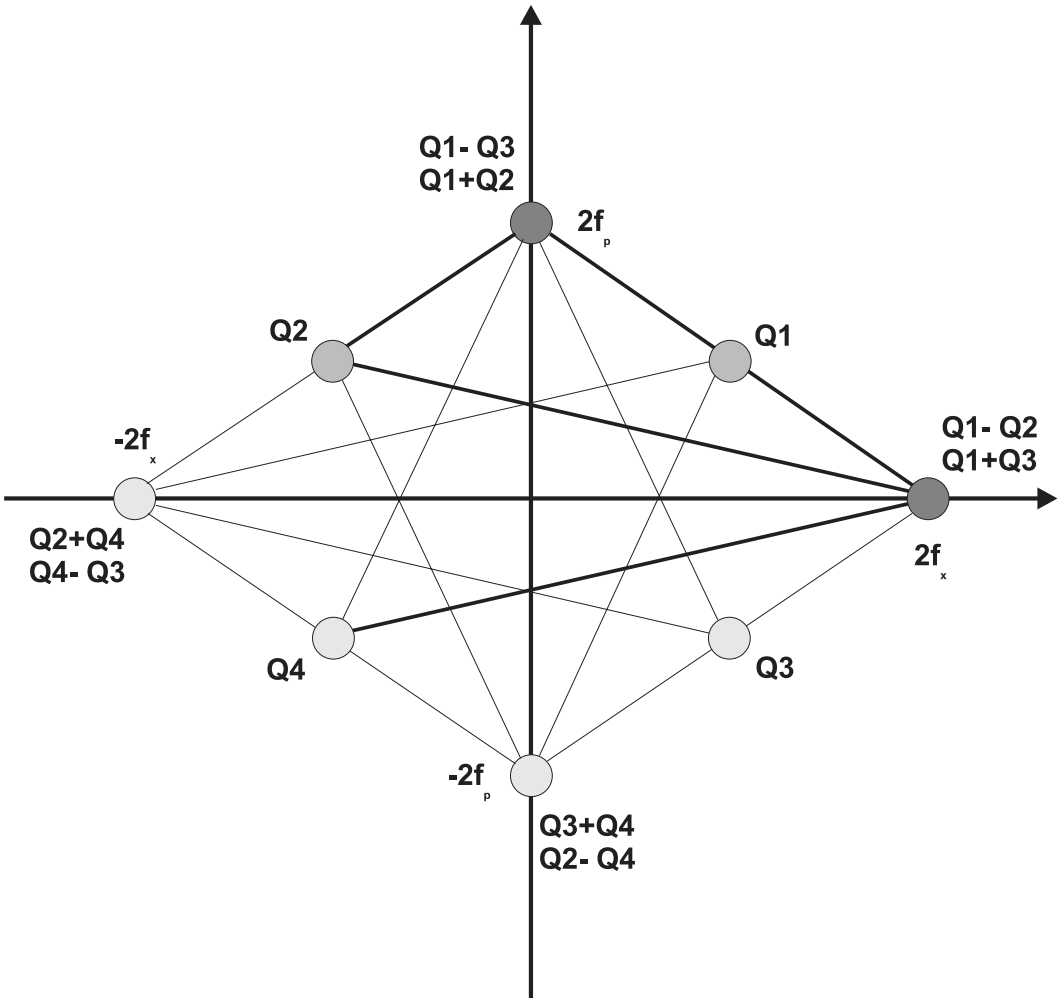

Figure 5.25: Complex signals in the four quadrants. The phases of two complex signals can be combined to estimate either f_x or f_p. Sum and difference of $Q1$ and $Q2$ is given as an example. Other possibilities are indicated.

to calculate two phases. Thus, there is no degree of freedom to use other combinations for averaging in the velocity estimation. Several combinations are suggested at $-2f_x$, $2f_x$, $-2f_p$ and $2f_p$.

If the relation between the four channels is given by 2D Hilbert transforms, then the spectra will be the same in all four quadrants as shown in Figure 5.11. In case of quadrature imbalance these four combinations can be used for averaging to reduce bias in the 2D spectra. The estimator proposed here is based on combination of all four signals both in the real and the imaginary part of the complex signals created for phase estimation. To reduce the extension of the formulas, two phases are introduced as

$$\varphi_z(i) = 2\pi f_0 \frac{2v_z}{c} iT_{prf} = 2\pi f_p iT_{prf} \tag{5.97}$$

$$\varphi_x(i) = 2\pi v_x f_x iT_{prf} = 2\pi f_x^v iT_{prf} \tag{5.98}$$

The temporal and spatial fields are assumed monochromatic with unit amplitude. Four combinations are considered:

1. Quadrant

$$\begin{aligned} SQ1(i) &= (u(i) - v(i) - v_1(i) - v_2(i)) + \mathrm{j}(u(i) - v(i) + v_1(i) + v_2(i)) \\ &= \cos(\varphi_x(i) + \varphi_z(i)) - \sin(\varphi_x(i) + \varphi_z(i)) \\ &+ \cos(\varphi_x(i) + \varphi_z(i)) + \sin(\varphi_x(i) + \varphi_z(i)) \\ &= \exp[\mathrm{j}(\varphi_x(i) + \varphi_z(i))](1 + \mathrm{j}) \end{aligned}$$

2. Quadrant

$$\begin{aligned} SQ2(i) &= (u(i) + v(i) - v_1(i) + v_2(i)) + \mathrm{j}(u(i) + v(i) + v_1(i) - v_2(i)) \\ &= \cos(\varphi_x(i) - \varphi_z(i)) - \sin(\varphi_x(i) - \varphi_z(i)) \\ &+ \cos(\varphi_x(i) - \varphi_z(i)) + \sin(\varphi_x(i) - \varphi_z(i)) \\ &= \exp[\mathrm{j}(\varphi_x(i) - \varphi_z(i))](1 + \mathrm{j}) \end{aligned}$$

3. Quadrant

$$\begin{aligned} SQ3(i) &= (u(i) - v(i) + v_1(i) + v_2(i)) + \mathrm{j}(-u(i) + v(i) + v_1(i) + v_2(i)) \\ &= \cos(\varphi_x(i) + \varphi_z(i)) + \sin(\varphi_x(i) + \varphi_z(i)) \\ &- \cos(\varphi_x(i) + \varphi_z(i)) + \sin(\varphi_x(i) + \varphi_z(i)) \\ &= \exp[\mathrm{j}(\varphi_x(i) + \varphi_z(i))](1 - \mathrm{j}) \end{aligned}$$

4. Quadrant

$$\begin{aligned} SQ4(i) &= (u(i) + v(i) + v_1(i) - v_2(i)) + \mathrm{j}(-u(i) - v(i) + v_1(i) - v_2(i)) \\ &= \cos(\varphi_x(i) - \varphi_z(i)) + \sin(\varphi_x(i) - \varphi_z(i)) \\ &- \cos(\varphi_x(i) - \varphi_z(i)) + \sin(\varphi_x(i) - \varphi_z(i)) \\ &= \exp[\mathrm{j}(\varphi_x(i) - \varphi_z(i))](1 - \mathrm{j}) \end{aligned}$$

The changes in phase in the complex exponentials are

$$d\theta_{SQ1} = 2\pi T_{prf}(f_x^v + f_p) \tag{5.99}$$
$$d\theta_{SQ2} = 2\pi T_{prf}(f_x^v - f_p) \tag{5.100}$$
$$d\theta_{SQ3} = 2\pi T_{prf}(f_x^v + f_p) \tag{5.101}$$
$$d\theta_{SQ4} = 2\pi T_{prf}(f_x^v - f_p). \tag{5.102}$$

The summation of the phase changes yields

$$d\theta_{SQ_x} = d\theta_{SQ1} + d\theta_{SQ2} + d\theta_{SQ3} + d\theta_{SQ4} = 8\pi T_{prf} f_x^v \tag{5.103}$$

and the lateral velocity component is determined by

$$v_x = \frac{d_x}{8\pi T_{prf}} d\theta_{SQx}. \tag{5.104}$$

By a proper combination of phase changes given by

$$d\theta_{SQ_z} = d\theta_{SQ1} - d\theta_{SQ2} + d\theta_{SQ3} - d\theta_{SQ4} = 16\pi f_0 \frac{2v_z}{c} T_{prf} \tag{5.105}$$

the axial velocity component can be calculated as

$$v_z = \frac{c}{16\pi f_0 T_{prf}} d\theta_{SQz}. \tag{5.106}$$

The estimation of the phase changes will involve four arguments. The general phase change $d\theta_{SQ}$ can be evaluated as

$$\begin{aligned} d\theta_{SQ} &= \tan(d\theta_{SQ1} \pm d\theta_{SQ2} + d\theta_{SQ3} \pm d\theta_{SQ4}) \\ &= \tan\left[(d\theta_{SQ1} + d\theta_{SQ3}) \pm (d\theta_{SQ2} + d\theta_{SQ4})\right] \\ &= \frac{\tan\left(d\theta_{SQ1} + d\theta_{SQ3}\right) \pm tan\left(d\theta_{SQ2} + d\theta_{SQ4}\right))}{1 \mp \tan\left(d\theta_{SQ1} + d\theta_{SQ3}\right)\tan\left(d\theta_{SQ2} + d\theta_{SQ4}\right))} \end{aligned} \tag{5.107}$$

The notation

$$\tan\left(d\theta_{SQ1} + d\theta_{SQ3}\right) = \frac{A}{B} \tag{5.108}$$

$$\tan\left(d\theta_{SQ2} + d\theta_{SQ4}\right)) = \frac{C}{D} \tag{5.109}$$

is used to reduce the extension of the expressions. Using (5.90) in (5.107) gives

$$\begin{aligned} \tan(d\theta_{SQ1} \pm d\theta_{SQ2} + d\theta_{SQ3} \pm d\theta_{SQ4}) &= \frac{\frac{A}{B} \pm \frac{C}{D}}{1 \mp \frac{A}{B}\frac{C}{D}} \\ &= \frac{AD \pm BC}{BD \mp AC} \end{aligned} \tag{5.110}$$

With

$$\tan\left(d\theta_{SQN}\right) = \frac{\Im[R_{SQN}(k)]}{\Re[R_{SQN}(k)]} \tag{5.111}$$

the four variables, $N = 1, 2, 3, 4$, become

$$\begin{aligned} A &= \Im[R_{SQ1}(k)]\Re[R_{SQ3}(k)] + \Im[R_{SQ3}(k)]\Re[R_{SQ1}(k)] \\ B &= \Re[R_{SQ1}(k)]\Re[R_{SQ3}(k)] - \Im[R_{SQ1}(k)]\Im[R_{SQ3}(k)] \\ C &= \Im[R_{SQ2}(k)]\Re[R_{SQ4}(k)] + \Im[R_{SQ4}(k)]\Re[R_{SQ2}(k)] \\ D &= \Re[R_{SQ2}(k)]\Re[R_{SQ4}(k)] - \Im[R_{SQ2}(k)]\Im[R_{SQ4}(k)] \end{aligned} \tag{5.112}$$

and the products can be calculated as

$$
\begin{aligned}
AD &= \Im[R_{SQ1}(k)]\Re[R_{SQ2}(k)]\Re[R_{SQ3}(k)]\Re[R_{SQ4}(k)] \\
&- \Im[R_{SQ1}(k)]\Im[R_{SQ2}(k)]\Re[R_{SQ3}(k)]\Im[R_{SQ4}(k)] \\
&+ \Re[R_{SQ1}(k)]\Re[R_{SQ2}(k)]\Im[R_{SQ3}(k)]\Re[R_{SQ4}(k)] \\
&- \Re[R_{SQ1}(k)]\Im[R_{SQ2}(k)]\Im[R_{SQ3}(k)]\Im[R_{SQ4}(k)]
\end{aligned} \tag{5.113}
$$

$$
\begin{aligned}
BC &= \Re[R_{SQ1}(k)]\Im[R_{SQ2}(k)]\Re[R_{SQ3}(k)]\Re[R_{SQ4}(k)] \\
&+ \Re[R_{SQ1}(k)]\Re[R_{SQ2}(k)]\Re[R_{SQ3}(k)]\Im[R_{SQ4}(k)] \\
&- \Im[R_{SQ1}(k)]\Im[R_{SQ2}(k)]\Im[R_{SQ3}(k)]\Re[R_{SQ4}(k)] \\
&- \Im[R_{SQ1}(k)]\Re[R_{SQ2}(k)]\Im[R_{SQ3}(k)]\Im[R_{SQ4}(k)]
\end{aligned} \tag{5.114}
$$

$$
\begin{aligned}
BD &= \Re[R_{SQ1}(k)]\Re[R_{SQ2}(k)]\Re[R_{SQ3}(k)]\Re[R_{SQ4}(k)] \\
&- \Re[R_{SQ1}(k)]\Im[R_{SQ2}(k)]\Re[R_{SQ3}(k)]\Im[R_{SQ4}(k)] \\
&- \Im[R_{SQ1}(k)]\Re[R_{SQ2}(k)]\Im[R_{SQ3}(k)]\Re[R_{SQ4}(k)] \\
&+ \Im[R_{SQ1}(k)]\Im[R_{SQ2}(k)]\Im[R_{SQ3}(k)]\Im[R_{SQ4}(k)]
\end{aligned} \tag{5.115}
$$

$$
\begin{aligned}
AC &= \Im[R_{SQ1}(k)]\Im[R_{SQ2}(k)]\Re[R_{SQ3}(k)]\Re[R_{SQ4}(k)] \\
&+ \Im[R_{SQ1}(k)]\Re[R_{SQ2}(k)]\Re[R_{SQ3}(k)]\Im[R_{SQ4}(k)] \\
&+ \Re[R_{SQ1}(k)]\Im[R_{SQ2}(k)]\Im[R_{SQ3}(k)]\Re[R_{SQ4}(k)] \\
&+ \Re[R_{SQ1}(k)]\Re[R_{SQ2}(k)]\Im[R_{SQ3}(k)]\Im[R_{SQ4}(k)]
\end{aligned} \tag{5.116}
$$

The lateral and the axial velocity component using this estimation approach can now be devised. Using (5.104) the lateral velocity component is estimated by

$$
\begin{aligned}
v_x &= \frac{d_x}{8\pi T_{prf}} d\theta_{SQx} \\
&= \frac{d_x}{8\pi T_{prf}} \arctan\left(\frac{AD+BC}{BD-AC}\right).
\end{aligned}
$$

and the axial velocity component is estimated by

$$
\begin{aligned}
v_z &= \frac{c}{16\pi T_{prf}} d\theta_{SQz} \\
&= \frac{c}{16\pi f_0 T_{prf}} \arctan\left(\frac{AD-BC}{BD+AC}\right).
\end{aligned}
$$

With this estimation approach, eight order moments appear in the formulas. The purpose is to reduce the variance of the estimated velocities.

Chapter 6

Summarizing results

The results are organized according to the different kind of data types used for evaluation of the estimators. For each data type a range of angles are evaluated. The performance of the estimators is evaluated as a function of the level of superimposed Gaussian distributed white noise and the number of lines/emissions applied in the estimation of the mean velocity. Four different estimators are evaluated. A distinct number of SNR levels and lines per estimate are chosen and all combinations possible are exploited. Three data types are used for evaluation:

- synthetic data, which denotes data generated by a mathematical expression,
- simulated data, which denotes data generated by Field II, *i.e* 3D simulation,
- experimental data, which denotes data recorded from an experimental ultrasound scanner at Duke University.

The synthetic, simulated, and experimental data are segmented according to the number of lines used for the estimate. For each segment, the actual signal power is calculated and used to determine the noise to be added. The mean and the standard deviation of the estimated mean velocities are calculated and displayed graphically. In appendix D all the results are listed in tables. The total number of synthetic calculated RF-data lines are scaled according to the number of realizations and the number of lines per realization. The total number of simulated and experimental data are limited or constant, which means that the number of realizations is reduced, when the number of lines per estimate is increased. The data segments are picked from the total number of RF-lines with a 50% overlap in order to increase the number of realizations.
The legends used in the plots are:

- solid: the mean of the estimated mean velocities,
- dashed: the standard deviation of the estimated mean velocities,
- dotted: the true mean velocity.

6.1 Evaluation parameters

The data used for evaluation are based on three variables:

- a number of angles, θ,

- a number of lines N_{lines} used for the estimate,
- a number of SNRs in dB, N_{SNR}.

The same number of lines and the signal-to-noise ratios are used for all data types and is chosen to be:

- $N_{lines} = 24, 20, 16, 12, 8$,
- $N_{SNR} = 40, 20, 16, 10, 6, 3, 0$ dB.

.
The number of angles differs from one data type to the other. The angles[1] used are

- synthetic: $\theta = 90°$,75°,60°,45°,30°,15°,0°,
- simulated: $\theta = 90°$,75°,60°,45°,30°,
- experimental: $\theta = 90°$,75°,60°,50°.

The angles for the experimental data were limited by practical restrictions in the experimental setup, because the angle was adjusted by tilting the transducer and the flow was emulated by moving the transducer, not the sponge. The range of angles for the simulated data is primarily generated for comparison with the experimental data. The synthetic data is generated for the full 90 degree angle span to show that the proposed estimators works when the fundamental 2D Hilbert relations are present.

6.1.1 Synthetic data

The synthetic data are generated using

- velocity: 0.5 m/s,
- realizations: 1000,
- lateral estimation: lag 4,
- RF averaging periods: 4,
- f_0: 6 MHz,
- f_x: 2 mm,
- f_s: 100 MHz,
- f_{prf} 10 kHz.

[1] as defined in Figure 5.1 *e.g.* 90 degrees is perpendicular to the propagation direction.

6.1.2 Simulated data

The simulated data are generated using

- velocity: 0.5 m/s,
- realizations: 1000,
- lateral estimation: lag 4,
- RF averaging periods: 4,
- number of elements: 128,
- f_0: 6 MHz,
- f_x: 2 mm,
- f_s: 100 MHz,
- f_{prf}: 10 kHz.

Two types of flow profiles were simulated, plug and parabolic. The flow setup is as described in Chapter 3.

6.1.3 Experimental data

The experimental data was recorded using a stepping unit to move the sponge between each recording. The sponge acts like a scattering media and mimics plug flow.

- step size: 40 μm, corresponding to a velocity 0.4 m/s @ f_{prf} 10 kHz,
- realizations: 250,
- number of transducer elements: 128,
- lateral estimation lag 4,
- RF averaging periods 4,
- f_0: 5.45 MHz,
- f_x: 1.8 mm,
- f_s: 36 MHz.

The acquired data were post-processed to remove glitches and DC-components, and interpolated up to 144 MHz.

6.2 Synthetic data

The performance of the estimators on data generated by the synthetic approach are shown in Figure 6.1 to Figure 6.7. Each figure is the result obtained for one angle and consists of 20 plots arranged in a matrix. Each row in the matrix corresponds to one number of emissions used for the estimation. Each plot shows the mean and the standard deviation of the estimated mean velocity as a function of SNR. The mean and the standard deviation is based on 1000 estimates of the mean velocity.

6.2.1 Angle of 90 degrees.

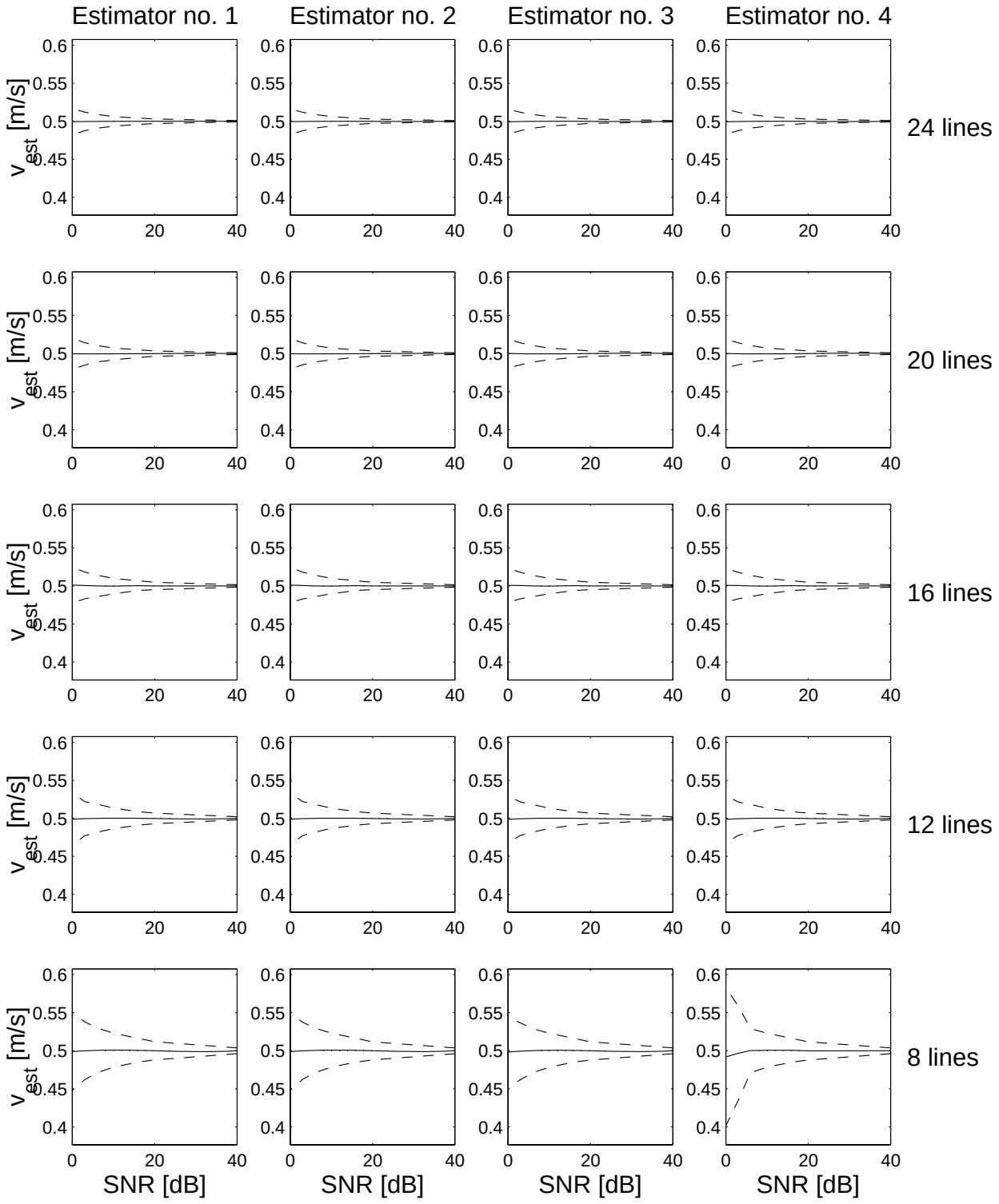

Figure 6.1: Mean and standard deviation of estimated velocities with a 90 degree angle.

6.2.2 Angle of 75 degrees.

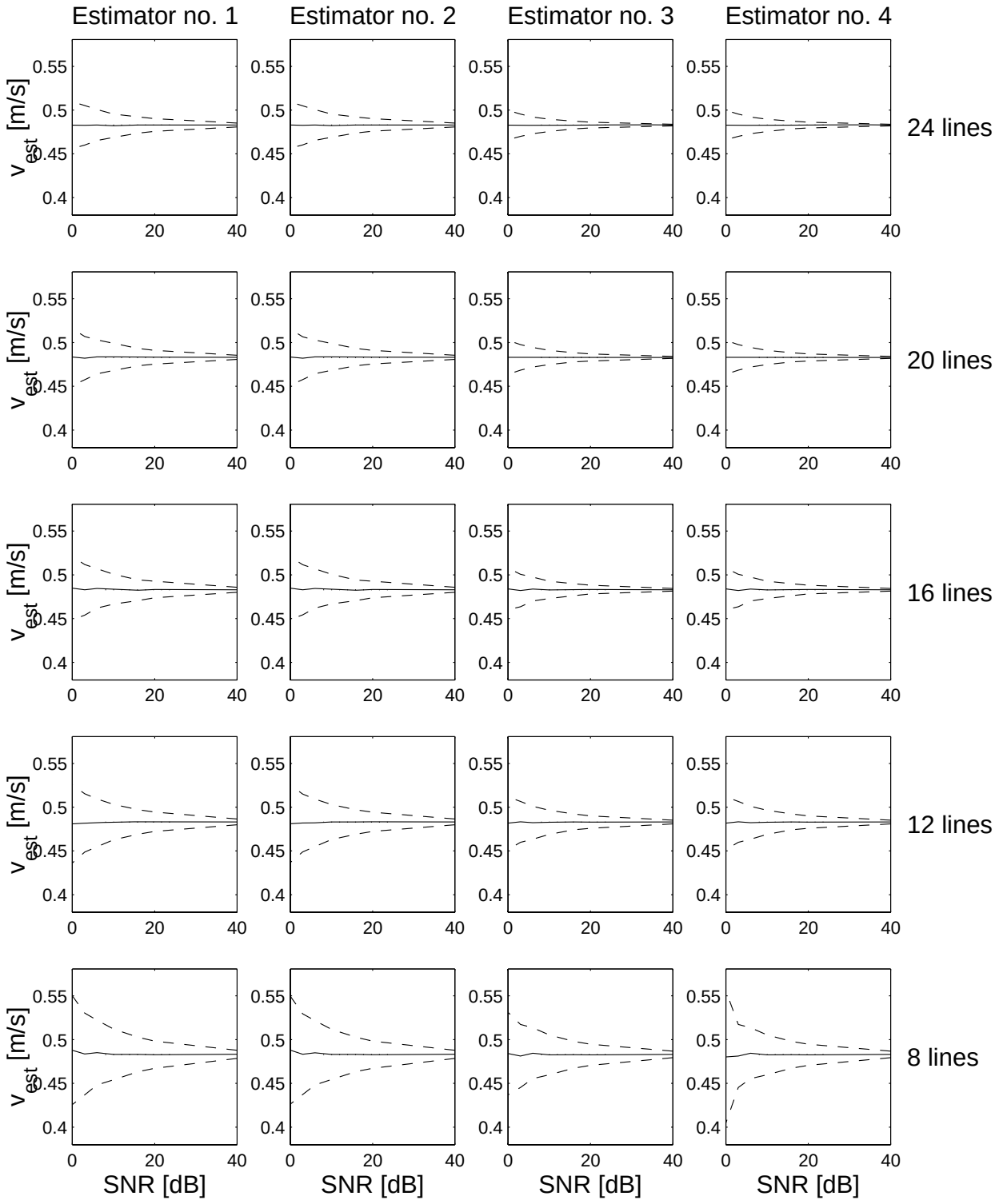

Figure 6.2: Mean and standard deviation of estimated velocities with a 75 degree angle.

6.2.3 Angle of 60 degrees.

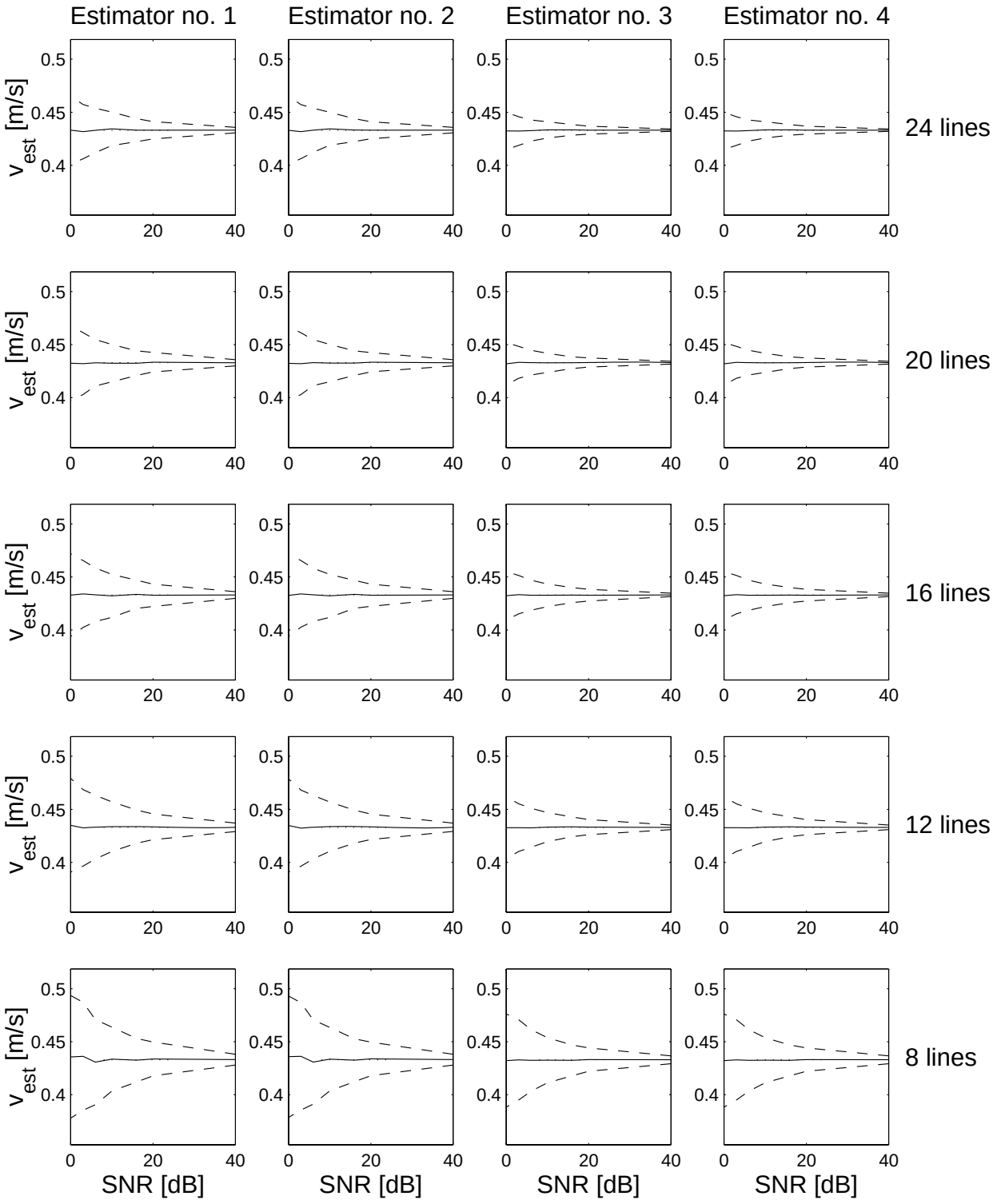

Figure 6.3: Mean and standard deviation of estimated velocities with a 60 degree angle.

6.2.4 Angle of 45 degrees.

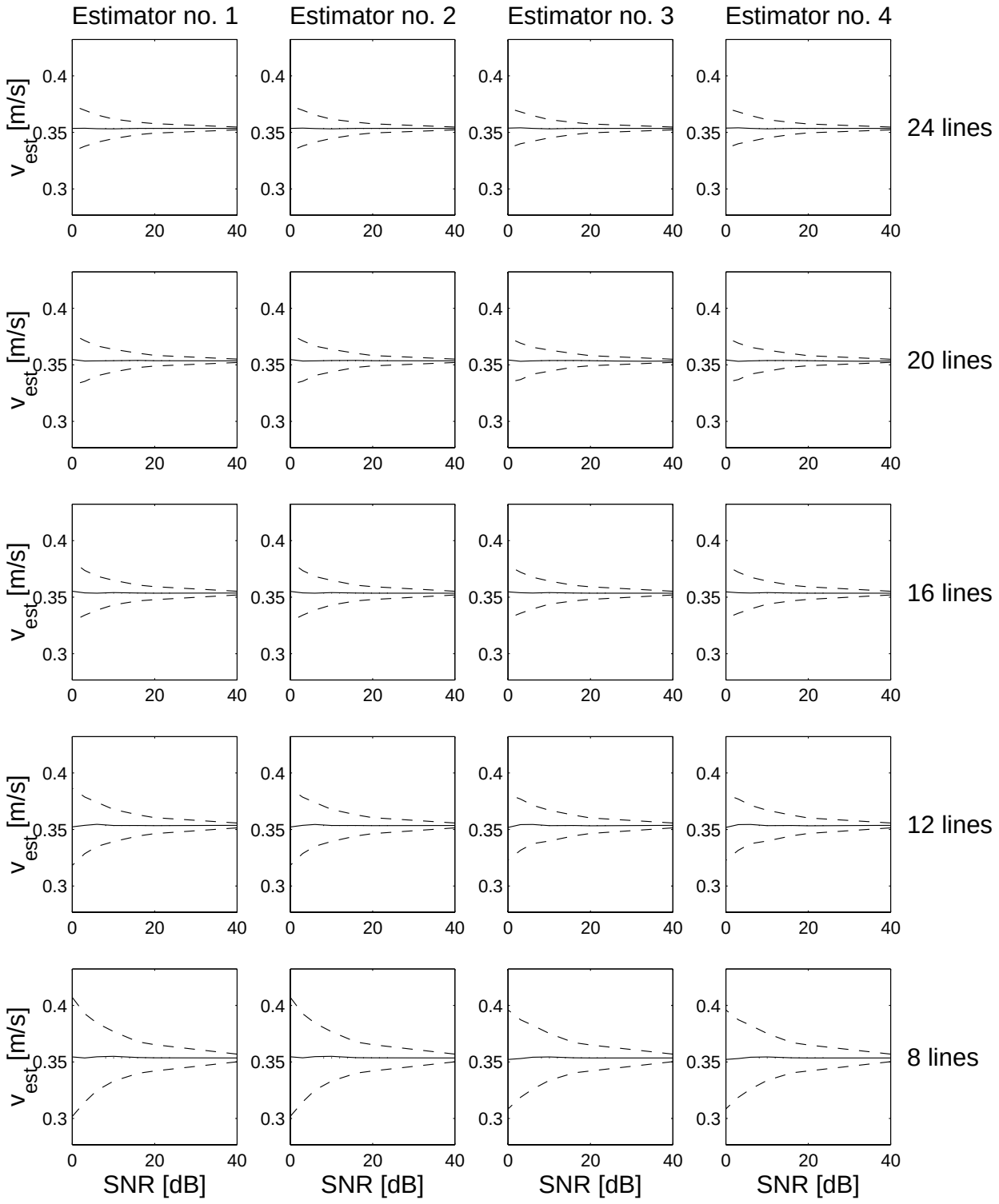

Figure 6.4: Mean and standard deviation of estimated velocities with a 45 degree angle.

6.2.5 Angle of 30 degrees.

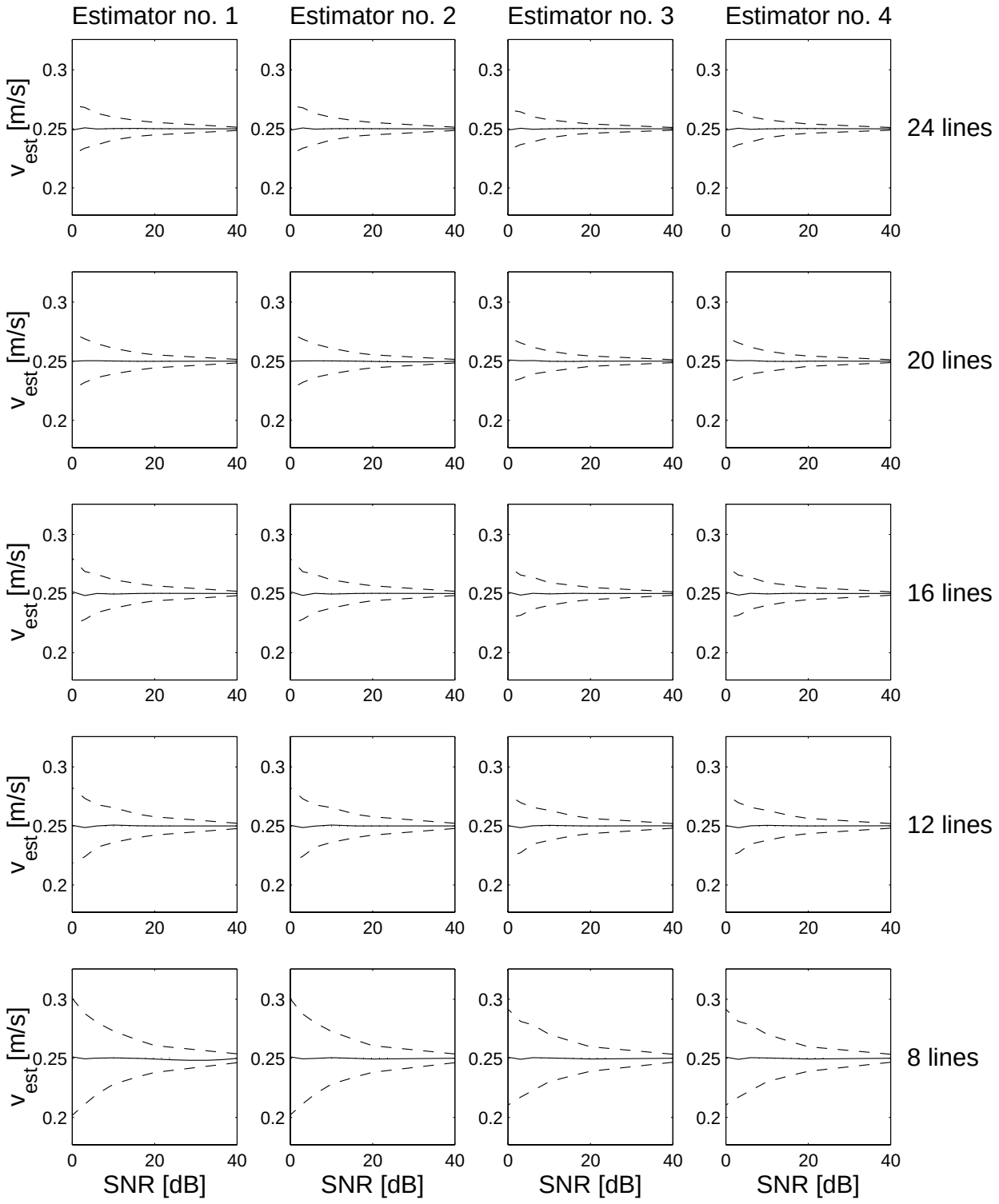

Figure 6.5: Mean and standard deviation of estimated velocities with a 30 degree angle.

6.2.6 Angle of 15 degrees.

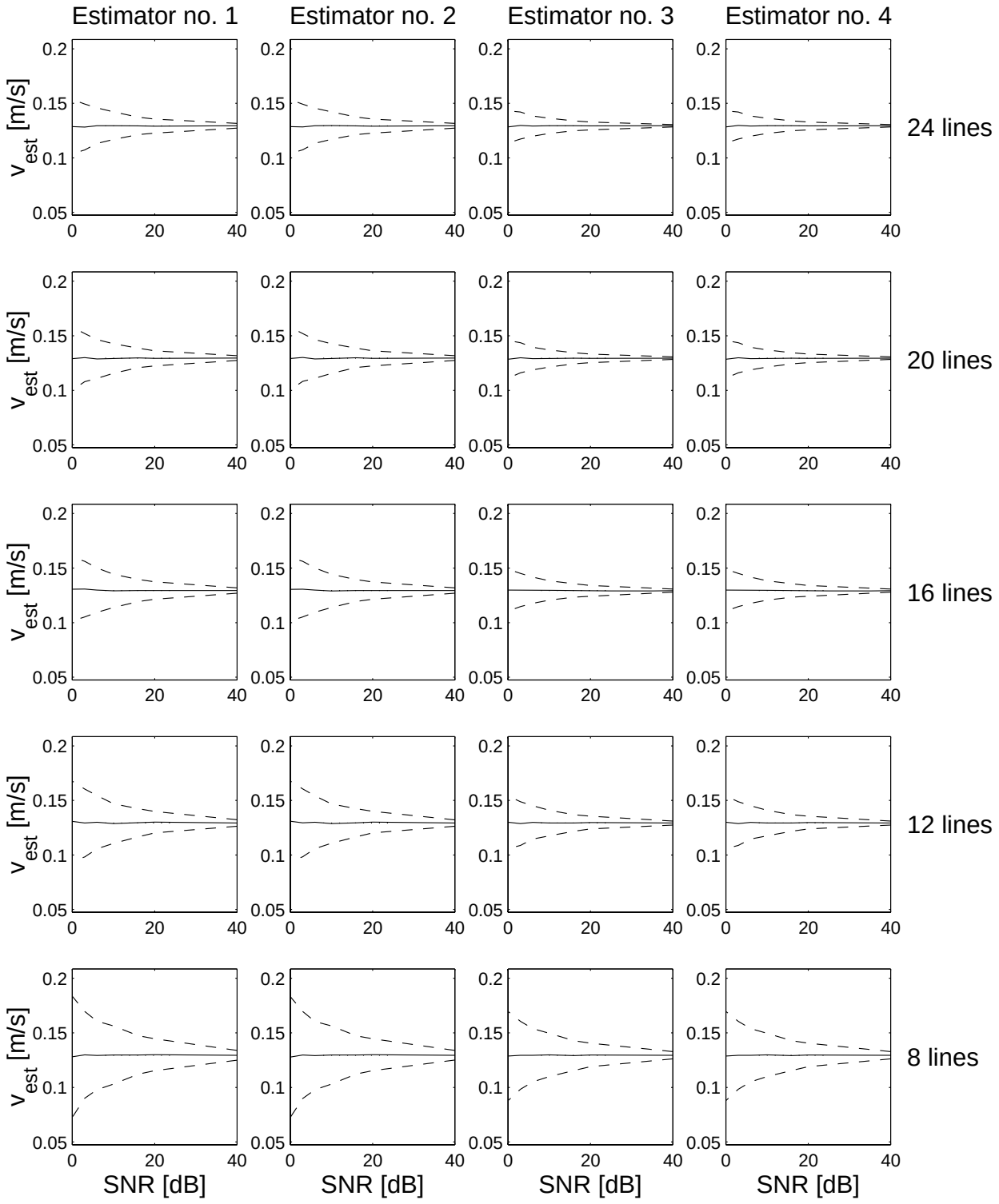

Figure 6.6: Mean and standard deviation of estimated velocities with a 15 degree angle.

6.2.7 Angle of 0 degrees.

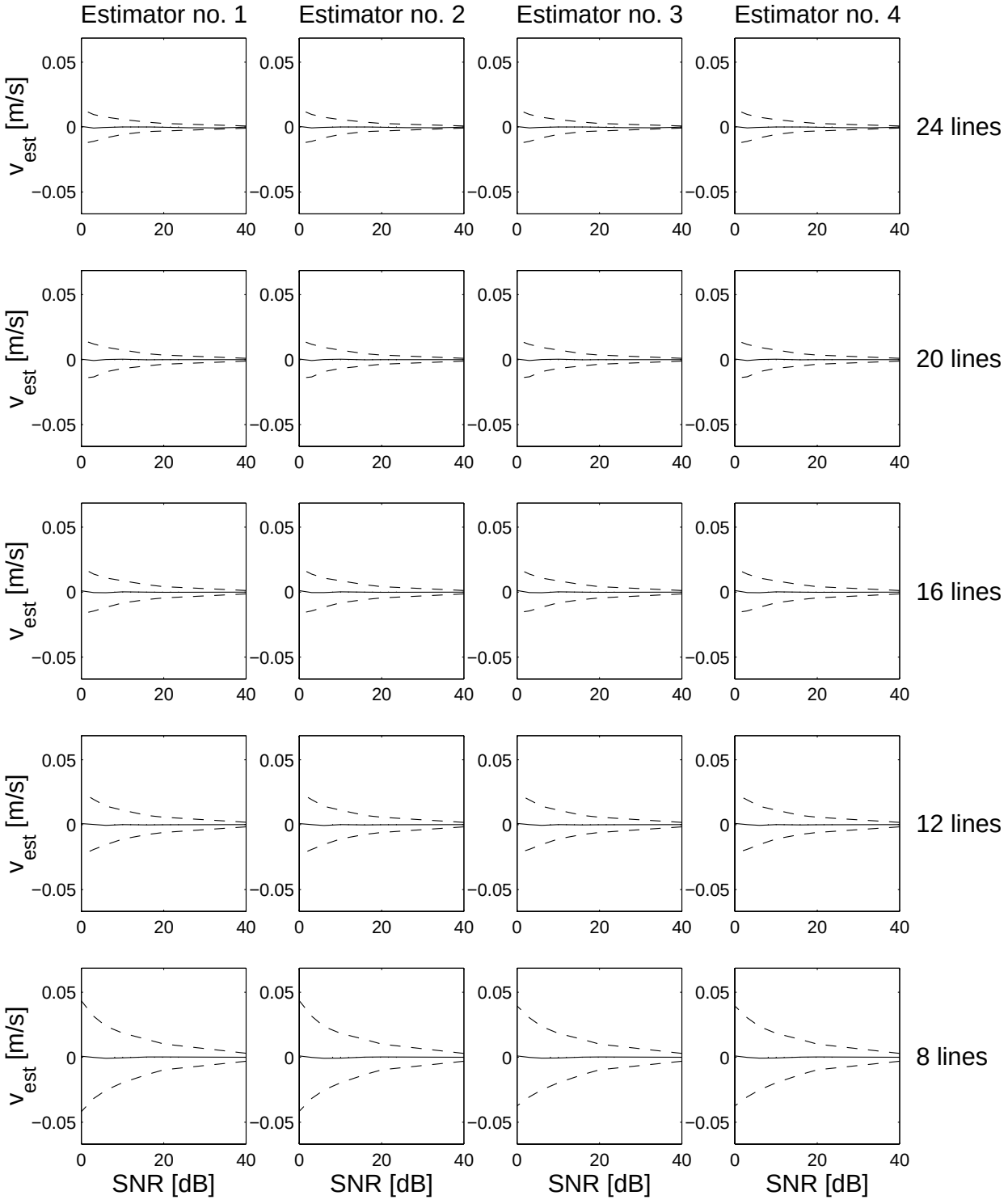

Figure 6.7: Mean and standard deviation of estimated velocities with a 0 degree angle.

6.2.8 Discussion

For all angles and all estimators the general tendency is that the variance of the estimate increases with a decrease in SNR or N_{lines}. A general observation is that all four estimators perform equally with a few exceptions. Estimator no. 4 have a worse performance at SNR=0dB in angle 90°and 75°, and estimator no. 3 and estimator no. 4. performs better in all cases, particularly at 60°. The estimates for all four estimators are unbiased. These results show that the combination of the four signals is not important, when they are in 2D quadrature.

6.3 Simulated data

The performance of the estimators on data generated by Field II using a plug flow profile are shown in Figure 6.8 to Figure 6.12, and by using a parabolic flow profile in Figure 6.13 to Figure 6.17 . Each figure is the result obtained for one angle and consists of 20 plots arranged in a matrix. Each row in the matrix corresponds to one number of emissions used for the estimation. Each plot shows the mean and the standard deviation of the estimated mean velocity as a function of SNR. The mean and the standard deviation is based on $1000/N_{lines}$ estimates of the mean velocity.

The performance of the estimators on data generated by the synthetic approach are shown in Figure 6.1 to Figure 6.7.

6.3.1 Plug flow, angle of 90 degrees

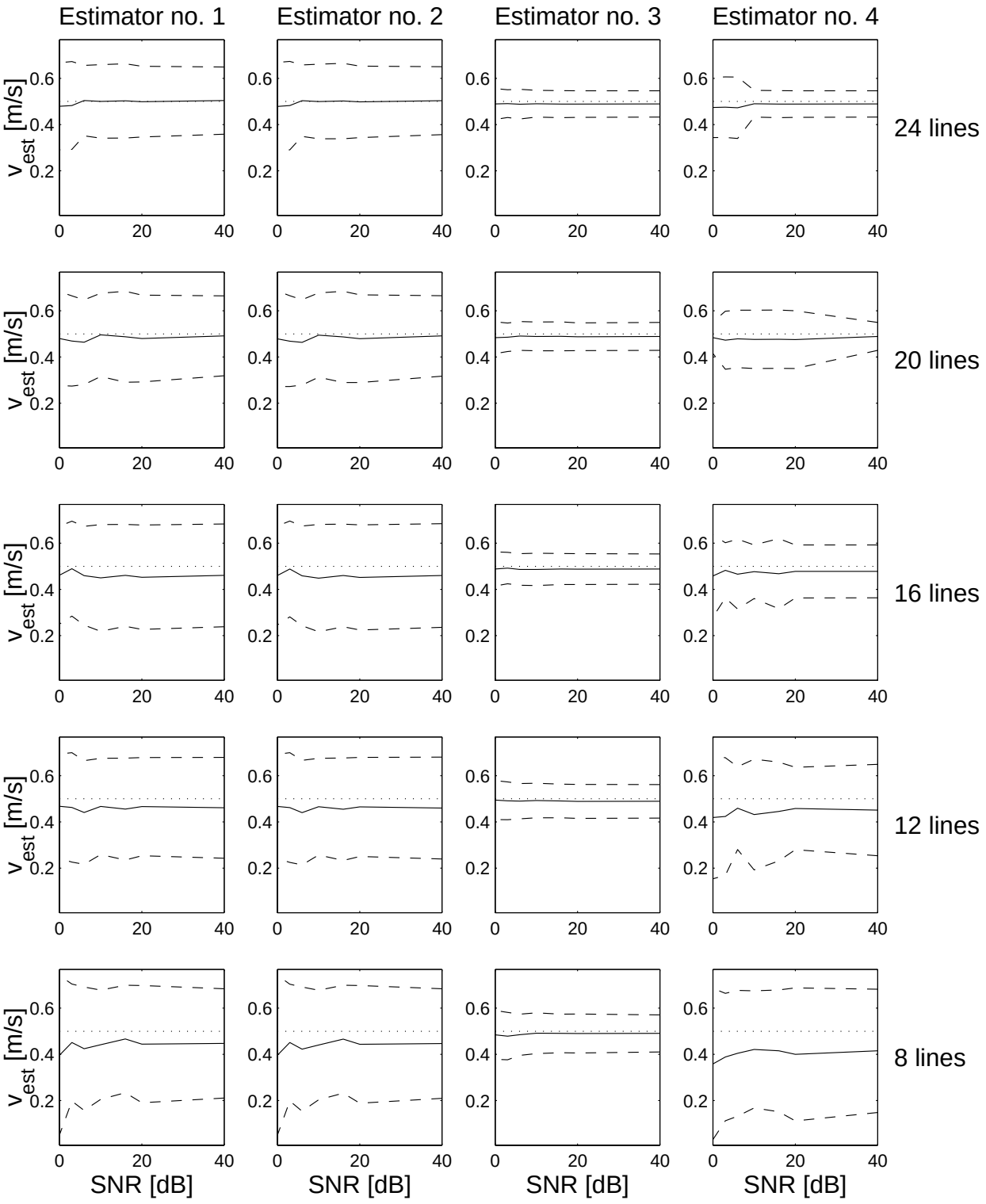

Figure 6.8: Mean and standard deviation of estimated velocities using plug flow profile with a 90 degree angle.

6.3.2 Plug flow, angle of 75 degrees

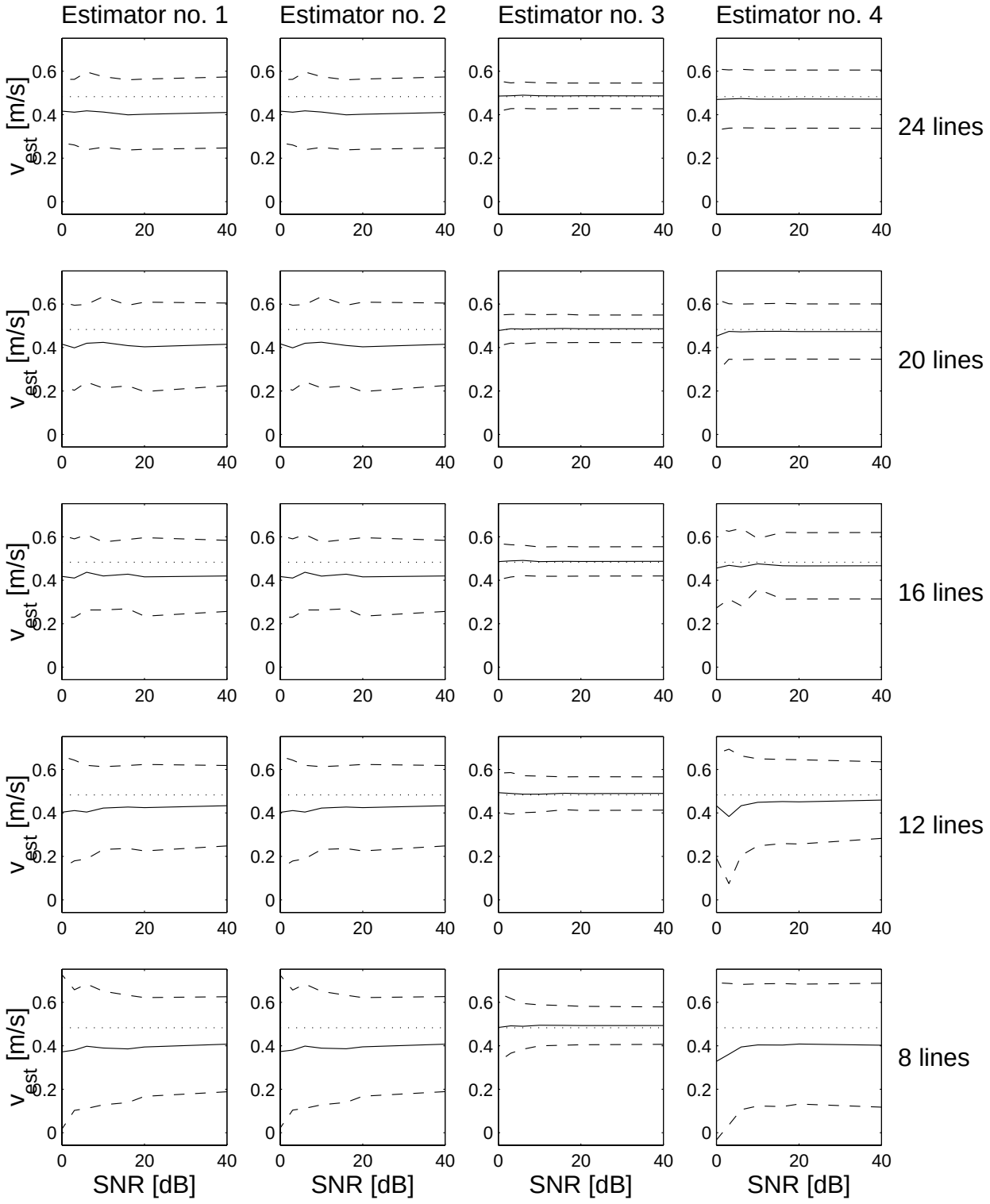

Figure 6.9: Mean and standard deviation of estimated velocities using plug flow profile with a 75 degree angle.

6.3.3 Plug flow, angle of 60 degrees

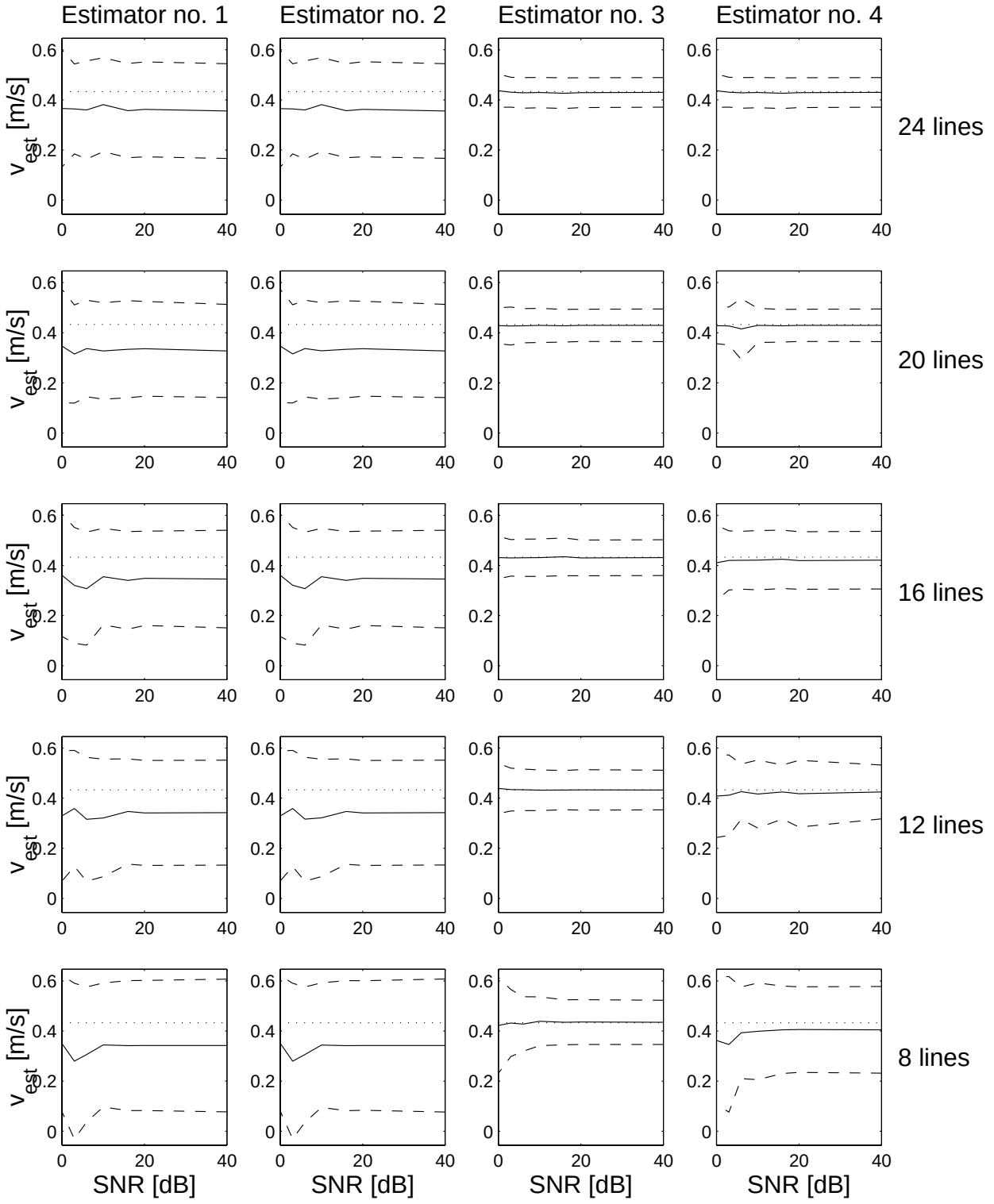

Figure 6.10: Mean and standard deviation of estimated velocities using plug flow profile with a 60 degree angle.

6.3.4 Plug flow, angle of 45 degrees

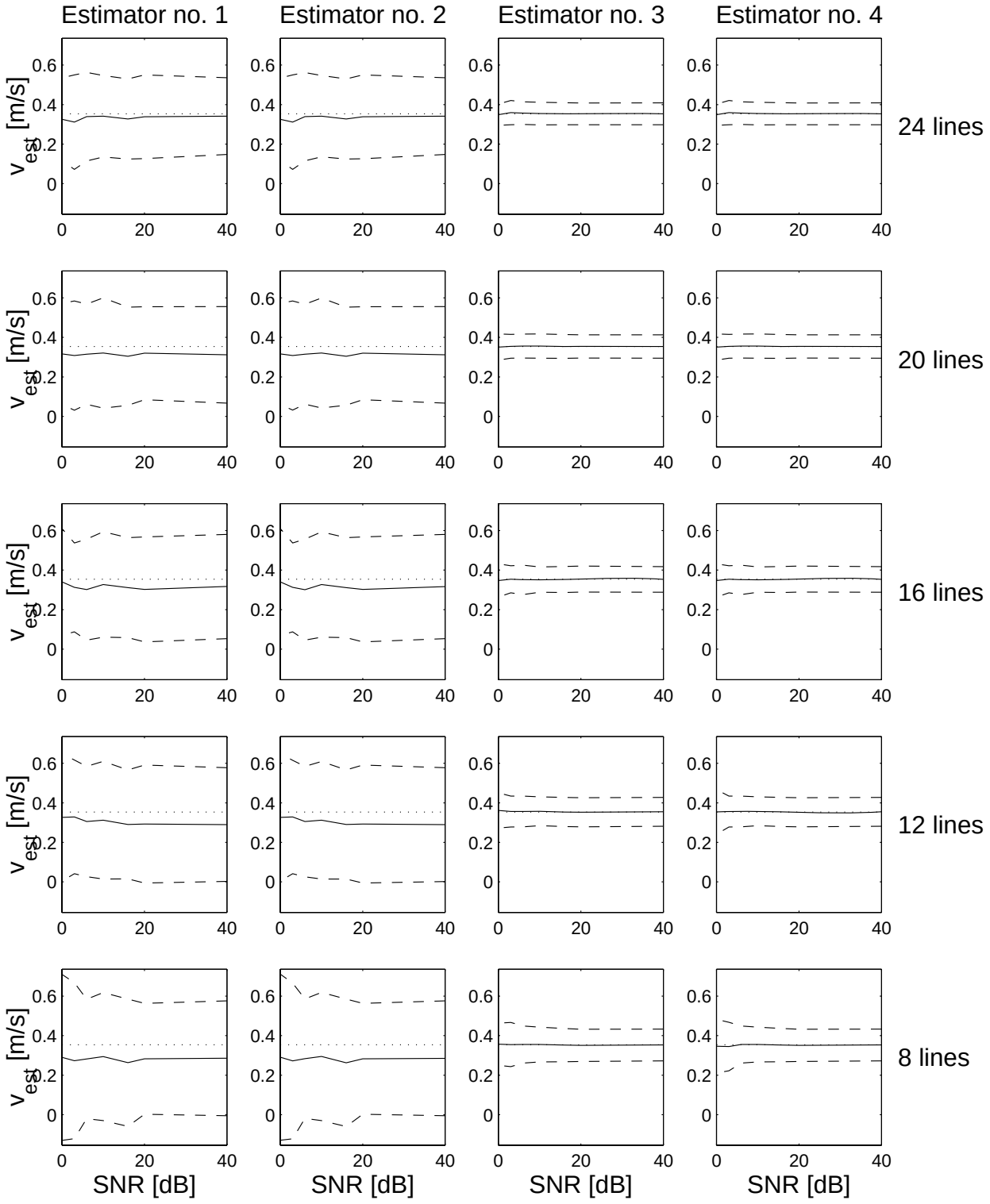

Figure 6.11: Mean and standard deviation of estimated velocities using plug flow profile with a 45 degree angle.

6.3.5 Plug flow, angle of 30 degrees

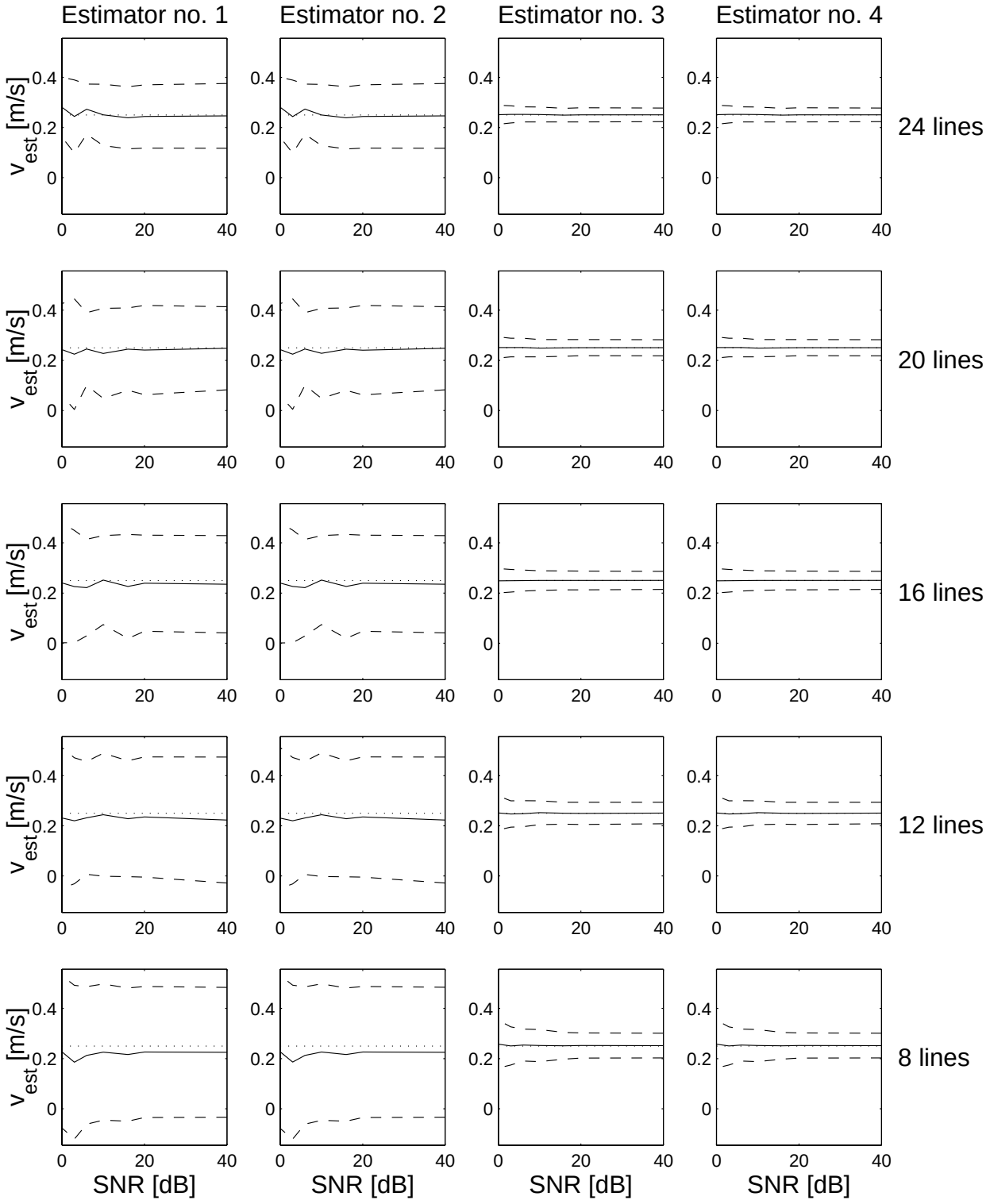

Figure 6.12: Mean and standard deviation of estimated velocities using plug flow profile with a 30 degree angle.

6.3.6 Parabolic flow, angle of 90 degrees

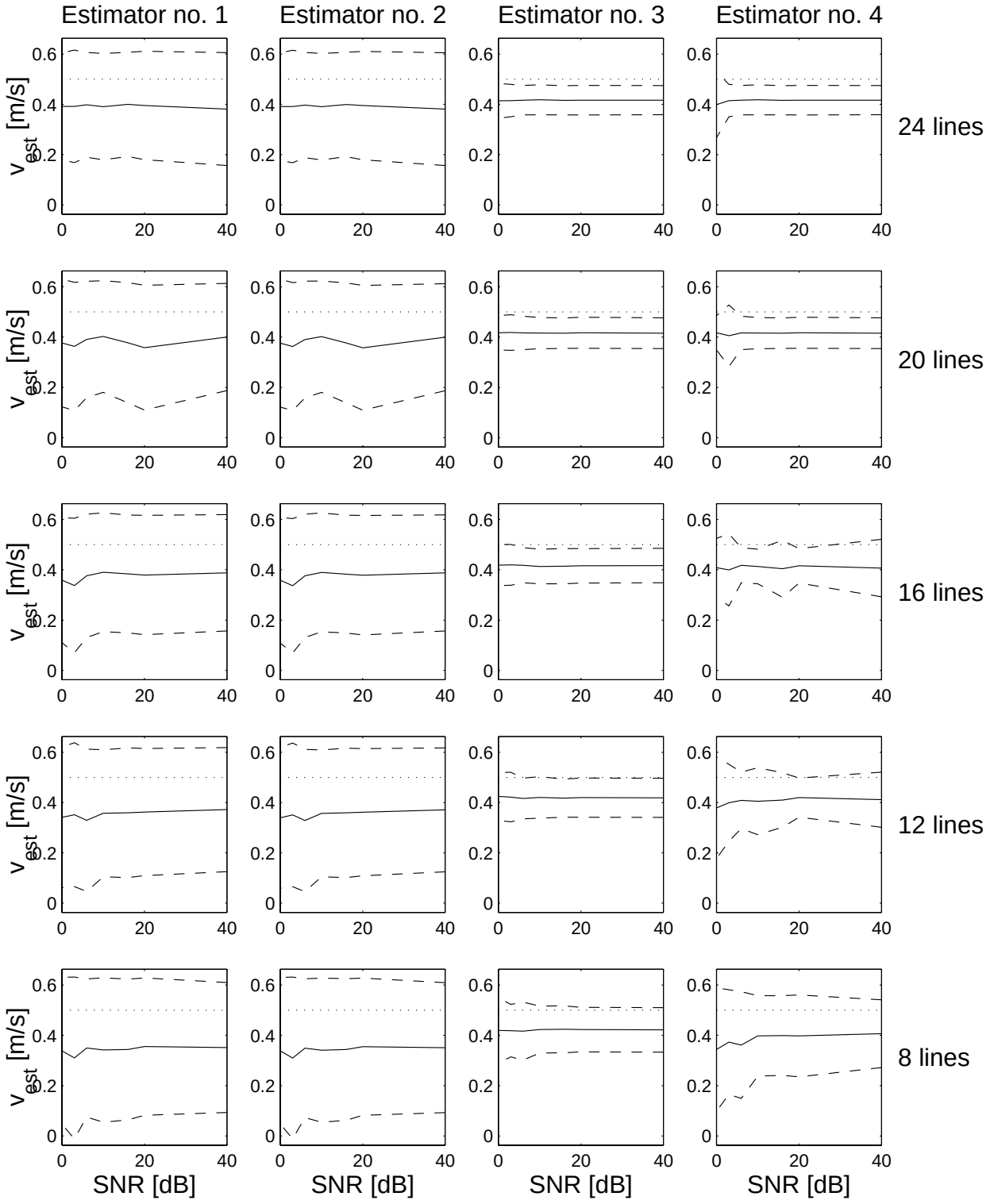

Figure 6.13: Mean and standard deviation of estimated velocities using parabolic flow profile with a 90 degree angle.

6.3.7 Parabolic flow, angle of 75 degrees

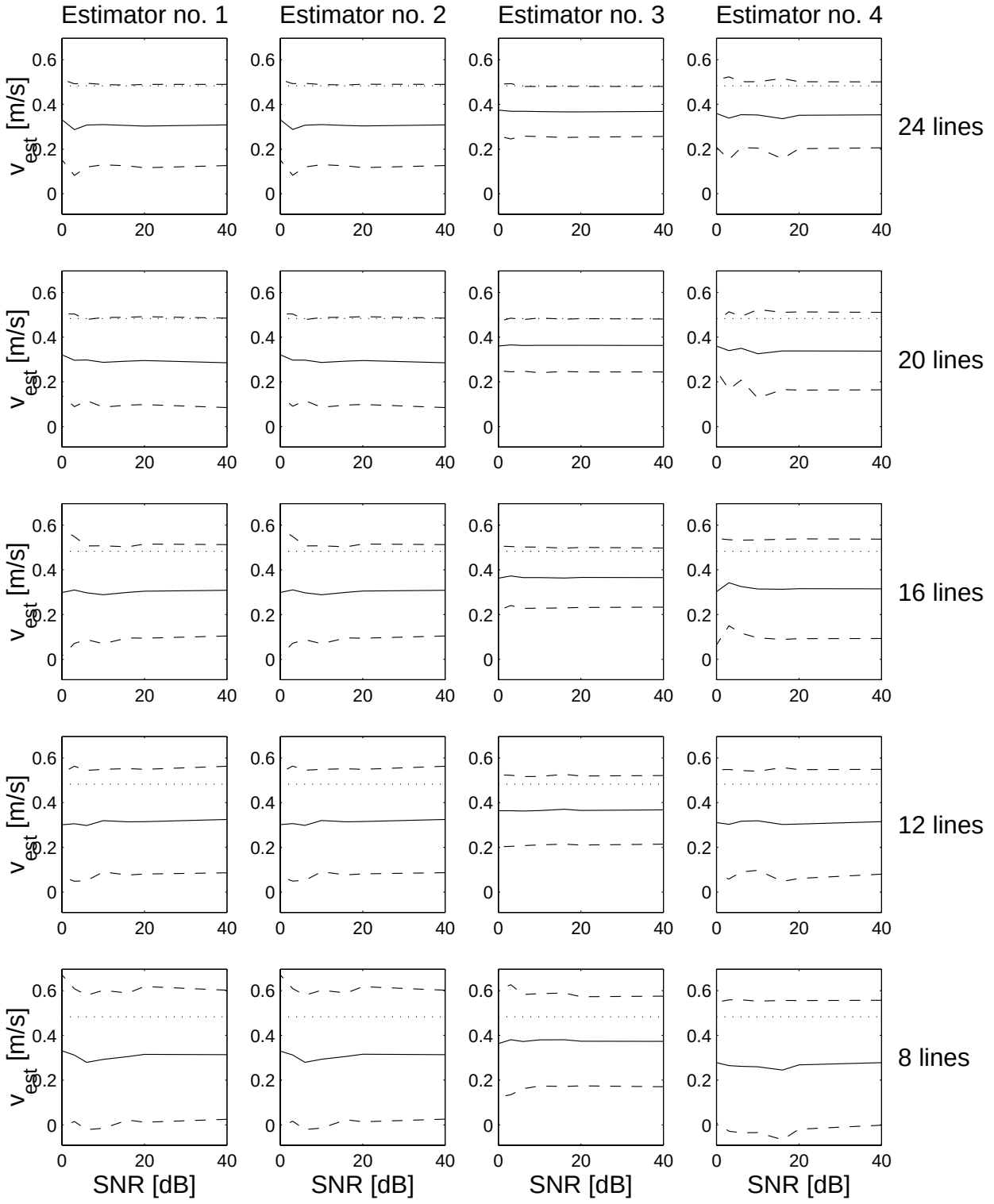

Figure 6.14: Mean and standard deviation of estimated velocities using parabolic flow profile with a 75 degree angle.

6.3.8 Parabolic flow, angle of 60 degrees

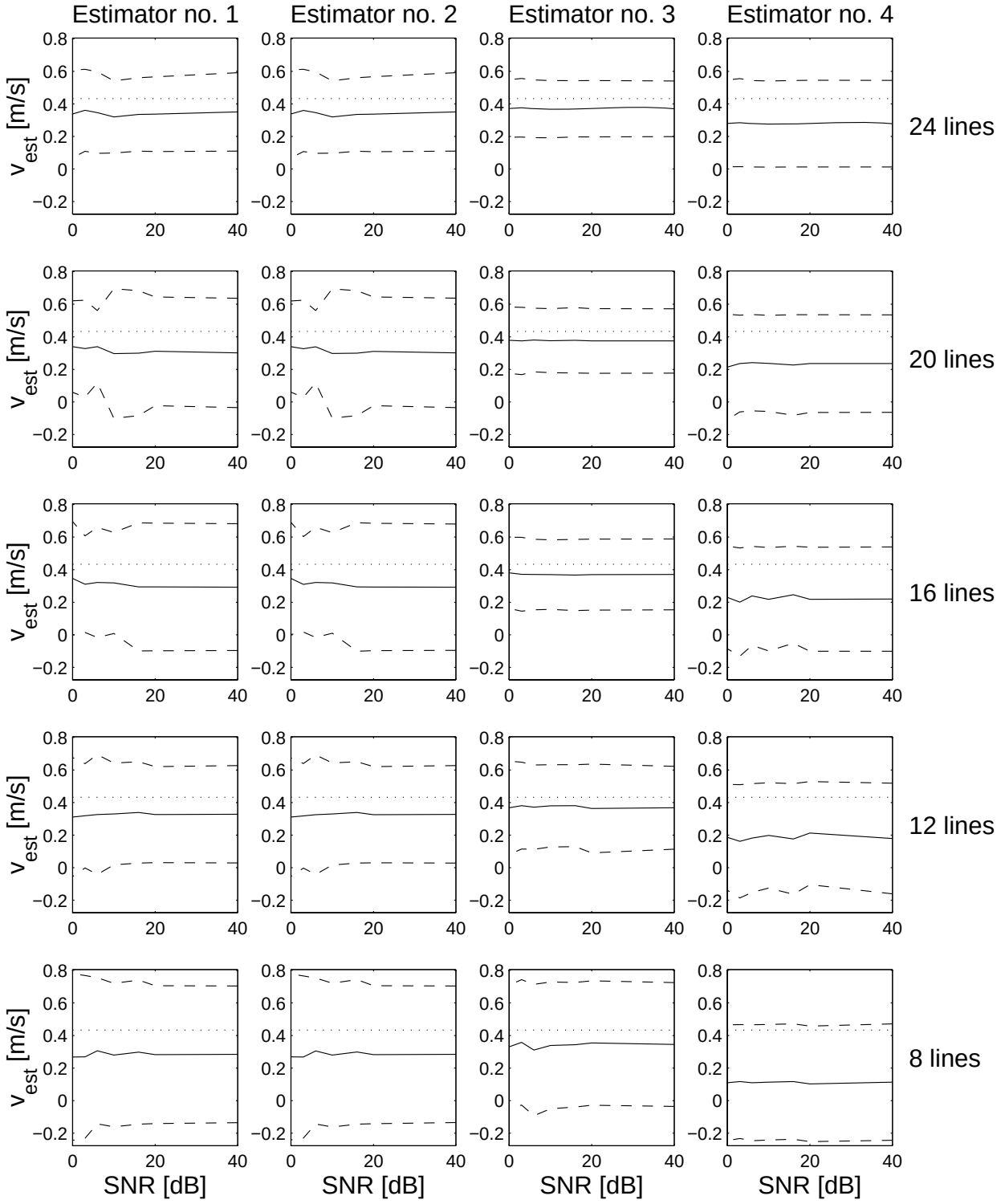

Figure 6.15: Mean and standard deviation of estimated velocities using parabolic flow profile with a 60 degree angle.

6.3.9 Parabolic flow, angle of 45 degrees

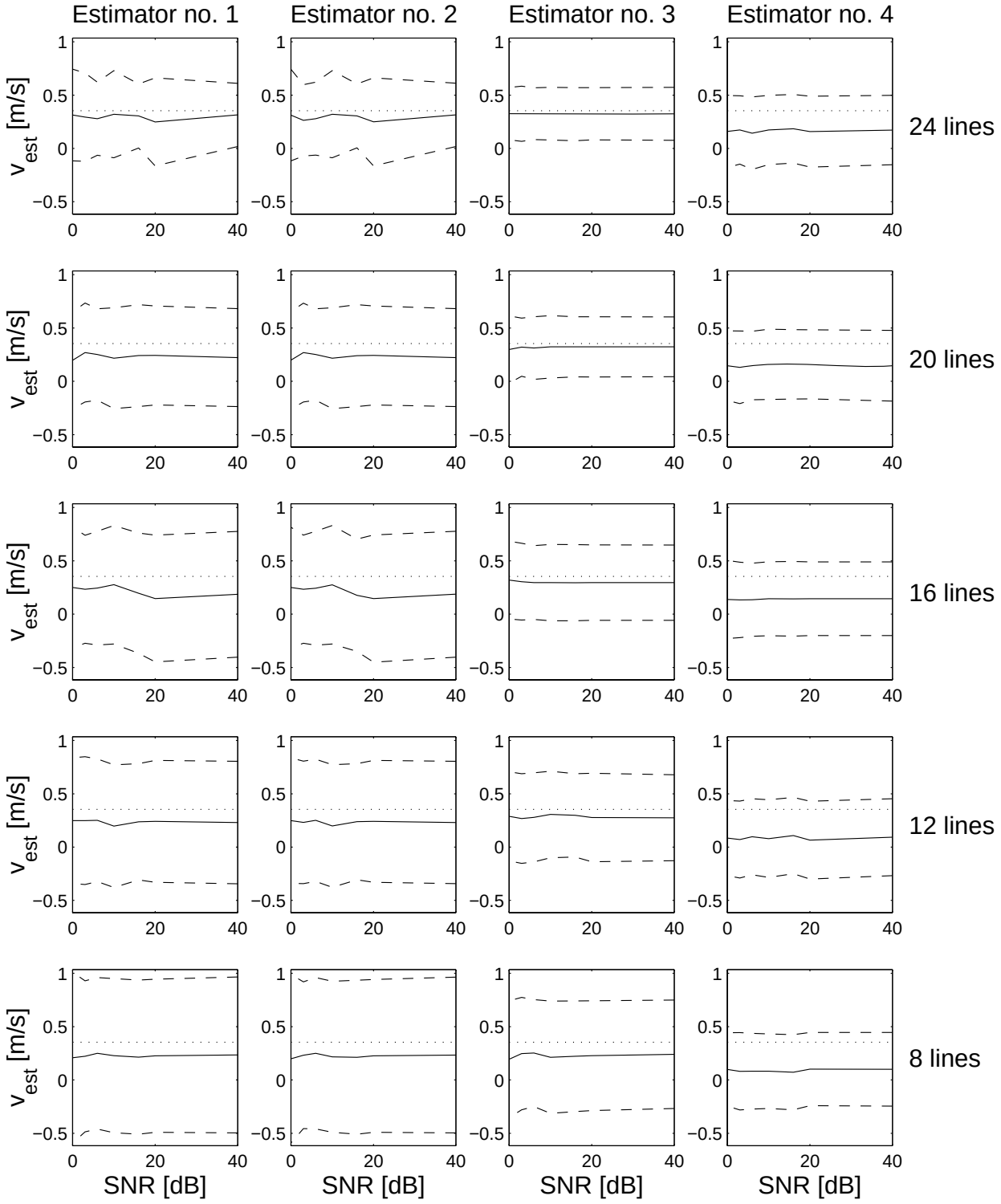

Figure 6.16: Mean and standard deviation of estimated velocities using parabolic flow profile with a 45 degree angle.

6.3.10 Parabolic flow, angle of 30 degrees

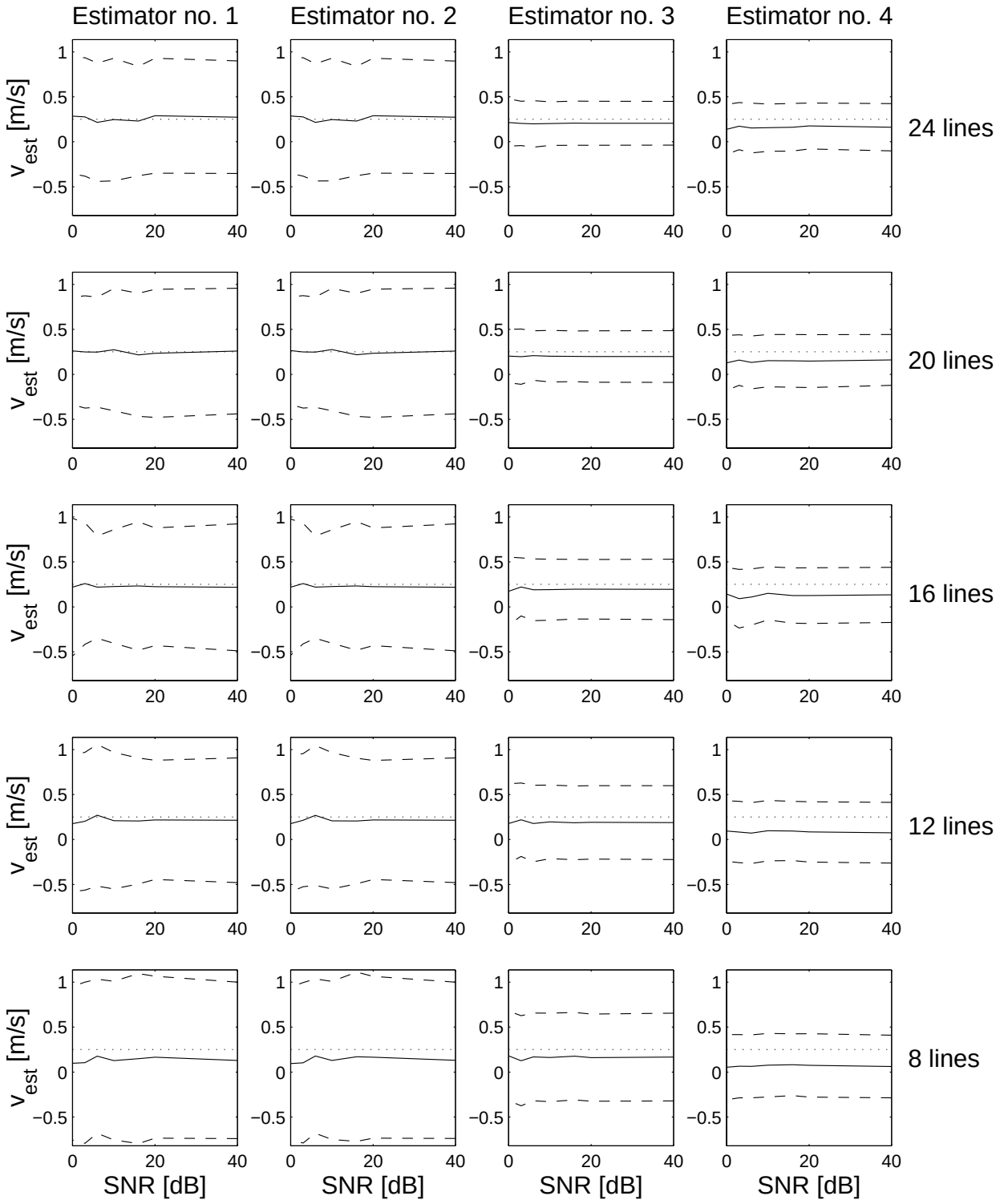

Figure 6.17: Mean and standard deviation of estimated velocities using parabolic flow profile with a 30 degree angle.

6.3.11 Discussion

The previous results using synthetic data showed how the variance of the mean velocity estimate increases with a decrease in SNR or N_{lines}. This is not the case with the simulated data. The standard deviation is approximately constant as a function of SNR, which indicates that the added noise is of no significance to the performance of the estimators compared to the spatial quadrature mismatch introduced by the speckle characteristics in the two channels. In general, estimator no. 3 is superior followed by no. 4 and with no. 1 and no. 2 performing equally poor. The variance is much higher than in the synthetic case. The bias of the estimate differs from the plug flow profile to the parabolic flow profile being more profound with the parabolic flow profile. The two cases of plug and parabolic flow profile are discussed further on an individual basis.
The performance of the four estimators differs significantly under these signal conditions. Estimator no. 1 and no. 2 performs almost identically poor, which shows that the averaging introduced on each channel does not have any impact of the performance. Estimator no. 3 seems to apply an appropiate combination of the available signals. Estimator no. 4 combines all four signals to both a real and an imaginary part of the complex signal used for estimation of the velocity.

Plug flow profile

On average, estimator no. 1 and no. 2 are most biased for all SNRs and N_{lines}. Estimator no. 4 performs to a second position and estimator no. 3 performs best being the less biased estimator. In the case of 90°and 75°, estimator no. 3 performs superior. At 60°, estimator no. 4 starts to perform equally to estimator no.3 for a high number of lines per estimate. At 45°and 30°, estimator 3 and 4 performs equal and superior to estimator no. 1 and no. 2.

Parabolic flow profile

In the parabolic case the estimates are more biased for all four estimators when compared to the results obtained by using a plug flow profile. The performance of estimator no. 3 is still the best even though the variance has increased considerably. Estimator no. 3 performs with the smallest bias and variance except for the case of 45°and a low number of lines. Here estimator no. 4 has a smaller variance, but has a higher bias.

6.4 Experimental data

The performance of the estimators on experimental data are shown in Figure 6.18 to Figure 6.21, Each figure is the result obtained for one angle and consists of 20 plots arranged in a matrix. Each row in the matrix corresponds to one number of emissions used for the estimation. Each plot shows the mean and the standard deviation of the estimated mean velocity as a function of SNR. The mean and the standard deviation is based on $250/N_{lines}$ estimates of the mean velocity.

6.4.1 Angle of 90 degrees

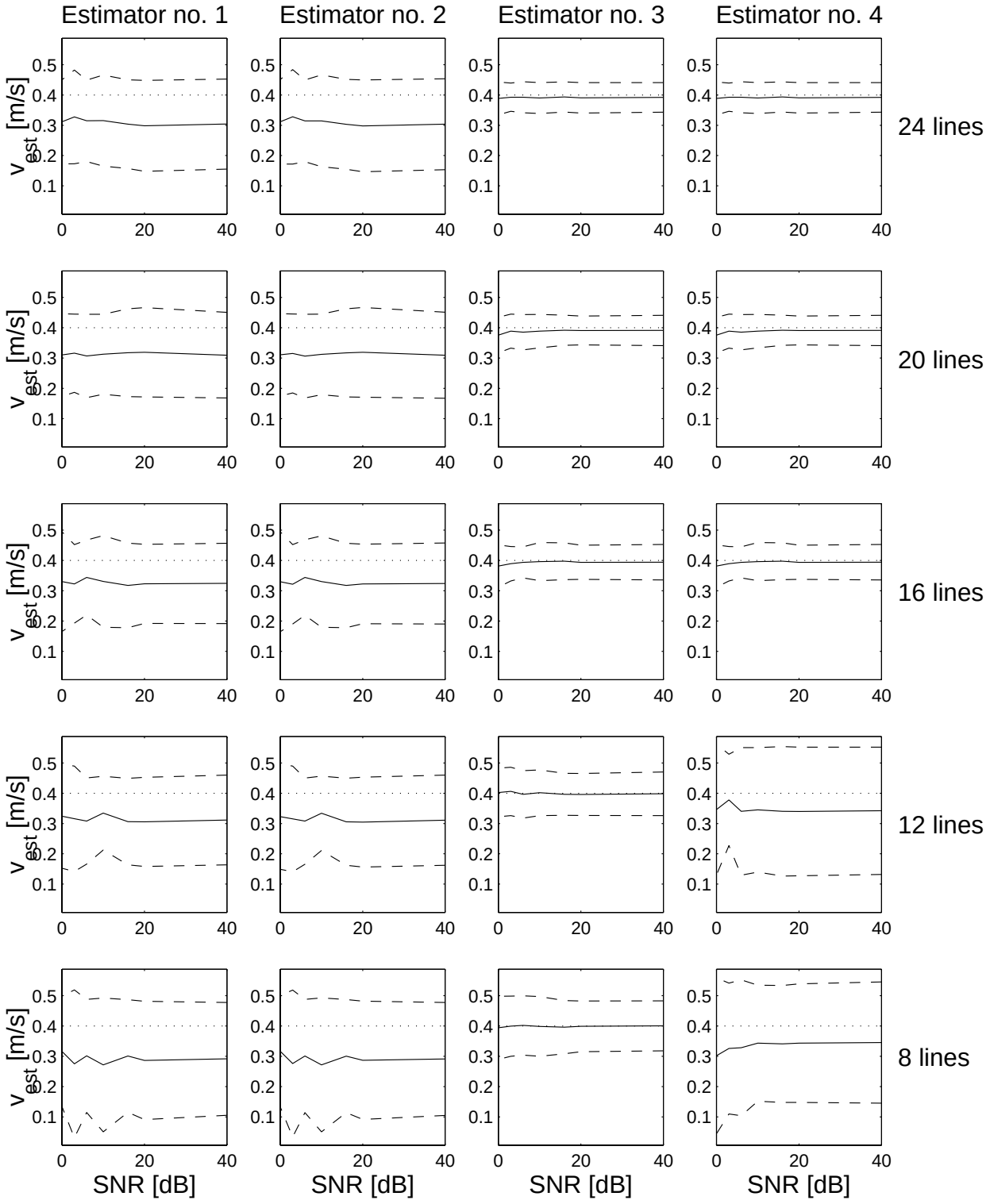

Figure 6.18: Mean and standard deviation of estimated velocities using a moving sponge with a 90 degree angle.

6.4.2 Angle of 75 degrees

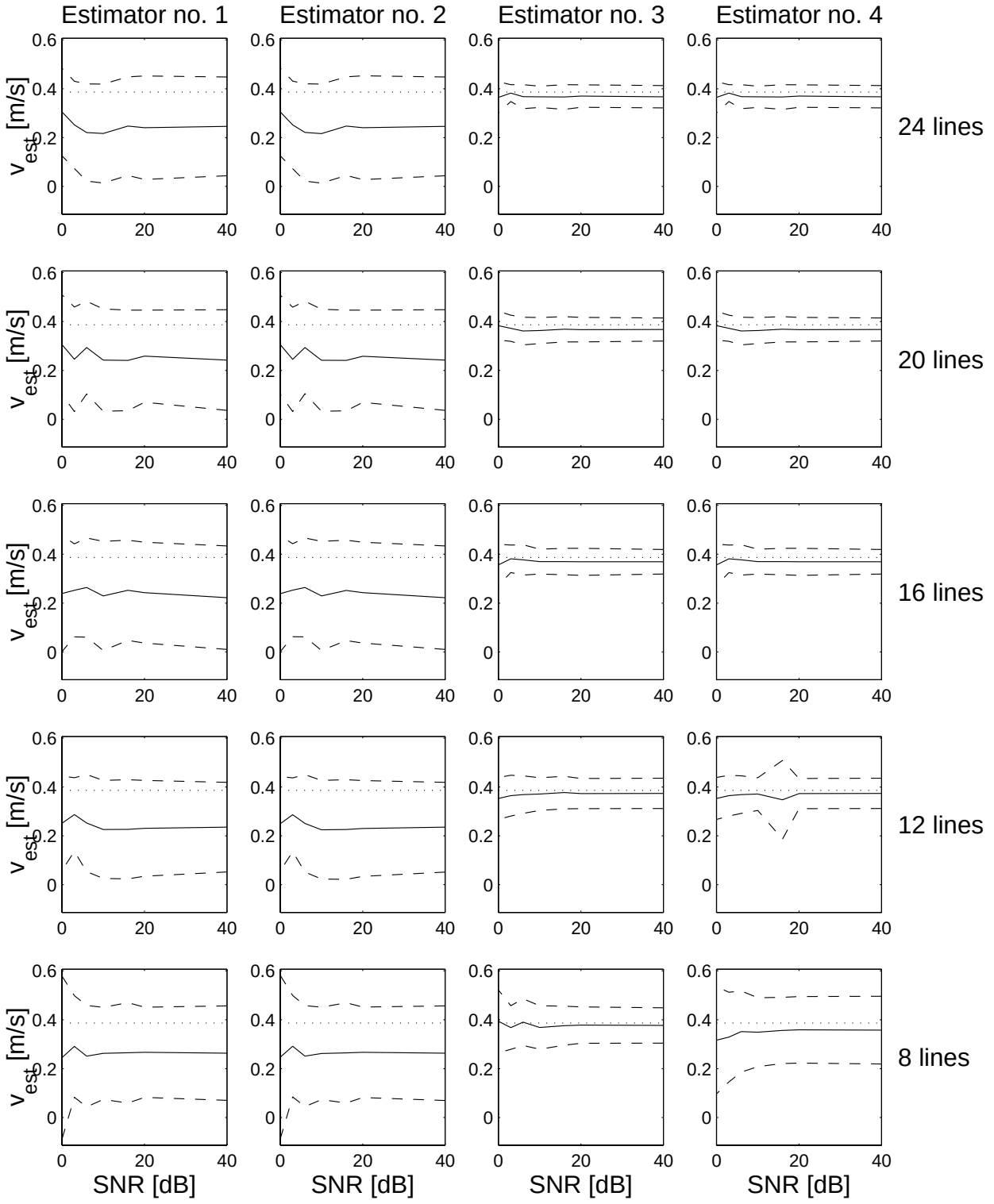

Figure 6.19: Mean and standard deviation of estimated velocities using a moving sponge with a 75 degree angle.

6.4.3 Angle of 60 degrees

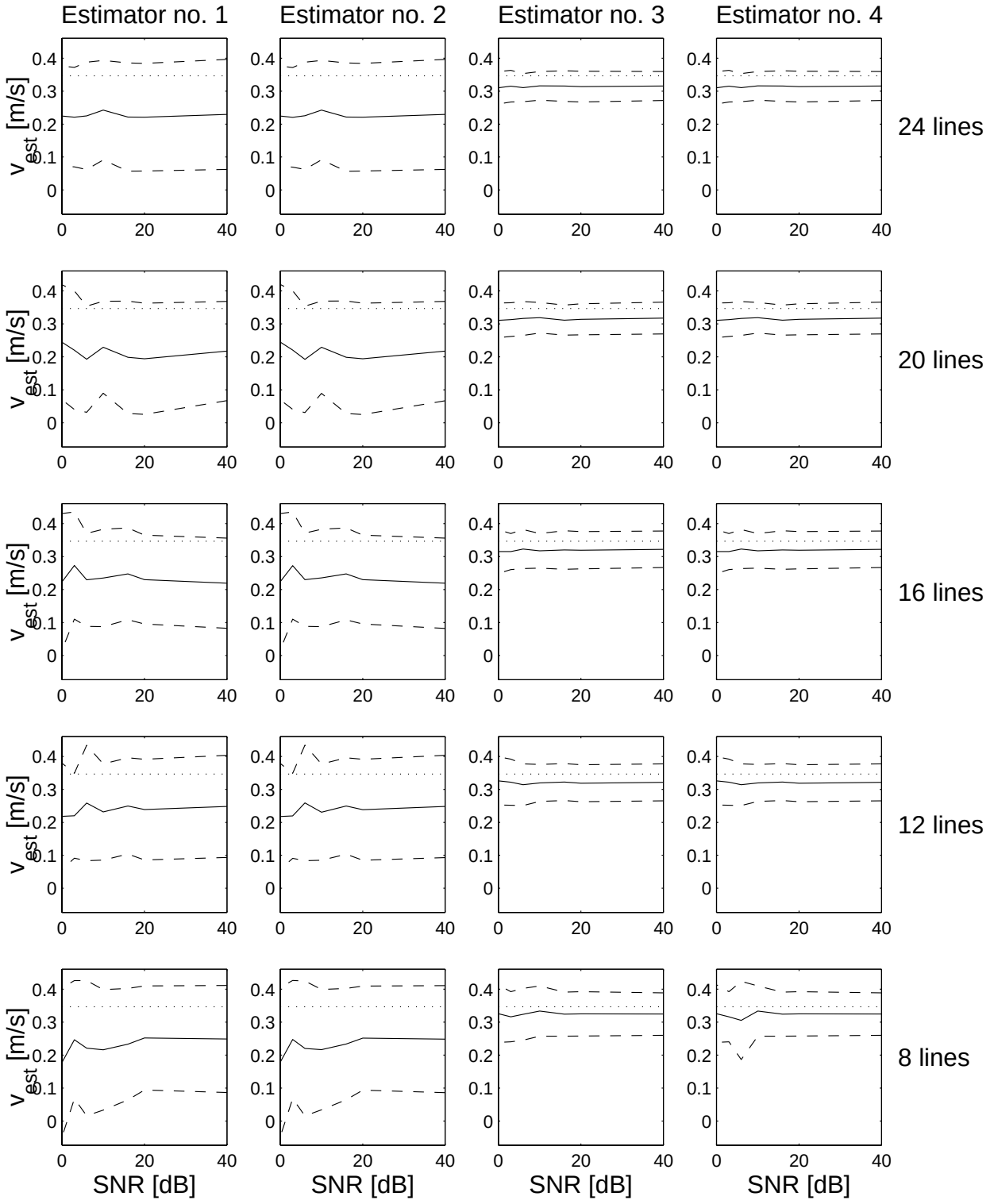

Figure 6.20: Mean and standard deviation of estimated velocities using a moving sponge with a 60 degree angle.

6.4.4 Angle of 50 degrees

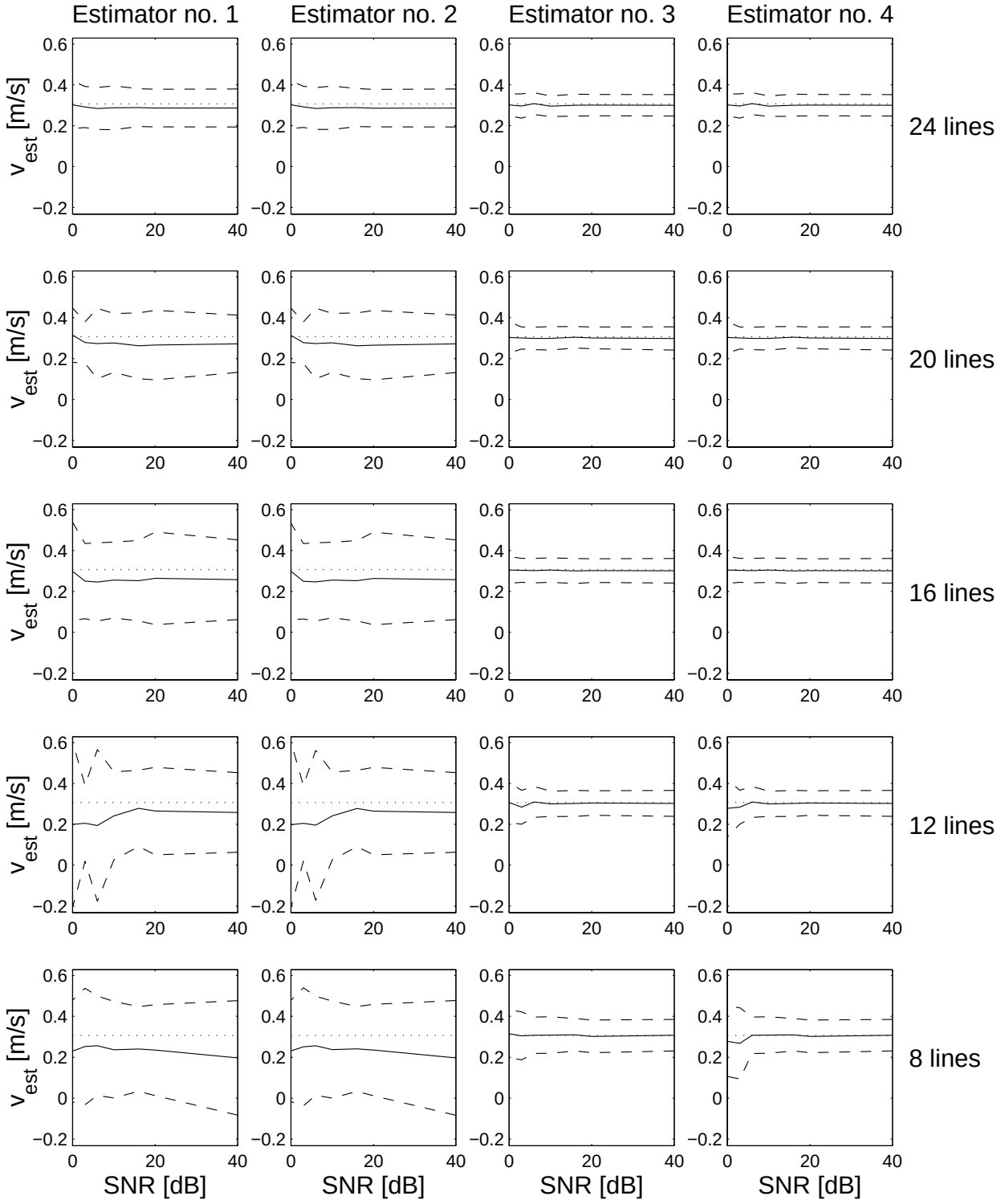

Figure 6.21: Mean and standard deviation of estimated velocities using a moving sponge with a 50 degree angle.

6.4.5 Discussion

In general, estimator no. 3 and no. 4 performs better than estimator no. 1 and no. 2. Compared to the results obtained by the synthetic and the simulated approach, estimator no. 4 shows to a larger extent, the approximate same performance as no. 3. In the case of angle 90°and 75°however estimator no. 3 is superior. At 90°the performance is only equal with N_{lines}= 16, 20, 24. At 75°estimator no. 3 performs better in all cases.

6.4.6 Multiple angles

Based on the previous results, numerous choices can be made in order to present the results obtained. Here it is chosen to show the performance of estimator no. 1, which approximately corresponds to the estimator originally used in previous work [Mun96], in comparison with estimator no. 3, which has the best performance. The number of lines is choosen to 16 and the SNR to 10 dB. Results for all angles are plotted for each estimator. The true mean velocity is indicated by a dashed line and a star. The estimated mean velocity is indicated by a solid line and a circle. For each estimated mean value, the corresponding standard deviation is indicated by the ellipse for both the axial and the lateral direction. The lateral standard deviation is the semi-major axis, and the axial standard deviation is the semi-minor axis. The performance of estimator no. 1 and 3 are shown in Figure 6.22 and in Figure 6.23. The improvement of the estimates using estimator no. 3 is clearly seen as a reduction in standard deviation and bias of the estimate. The numbers used for estimator no. 1 are found in tables in Appendix D.3.1, D.3.2, D.3.3 and D.3.4. The average bias for all angles is

- Estimator no. 1: 26.6 %
- Estimator no. 3: 3.8 %

and the relative standard deviation, calculated as the standard deviation divided by the estimated mean, is

- Estimator no. 1: 67.5 %
- Estimator no. 3: 17.0 %

which shows a significant improvement in the performance of the estimator.

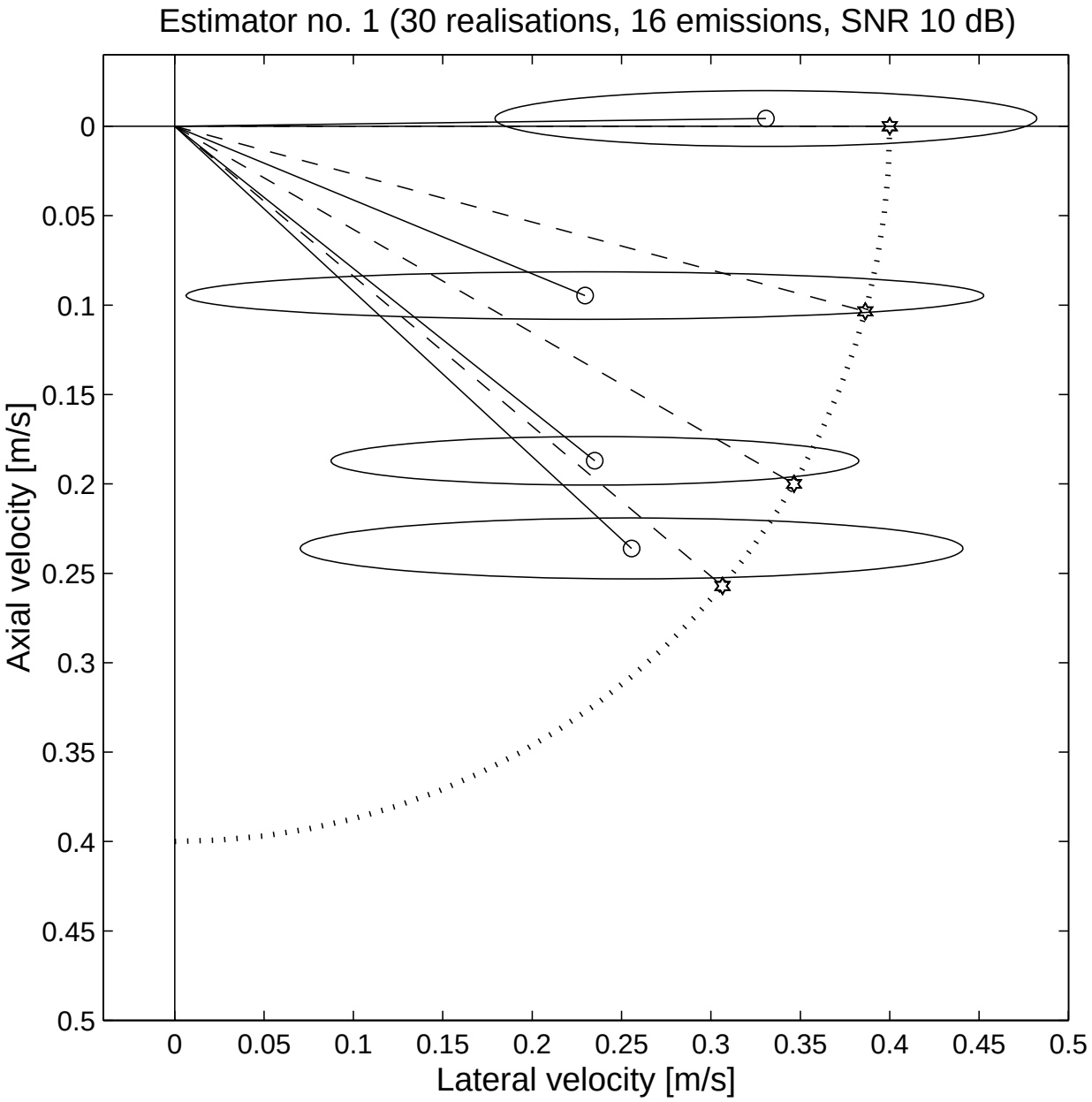

Figure 6.22: Performance of estimator no. 1 for angle 90, 75, 60 and 50 degrees.

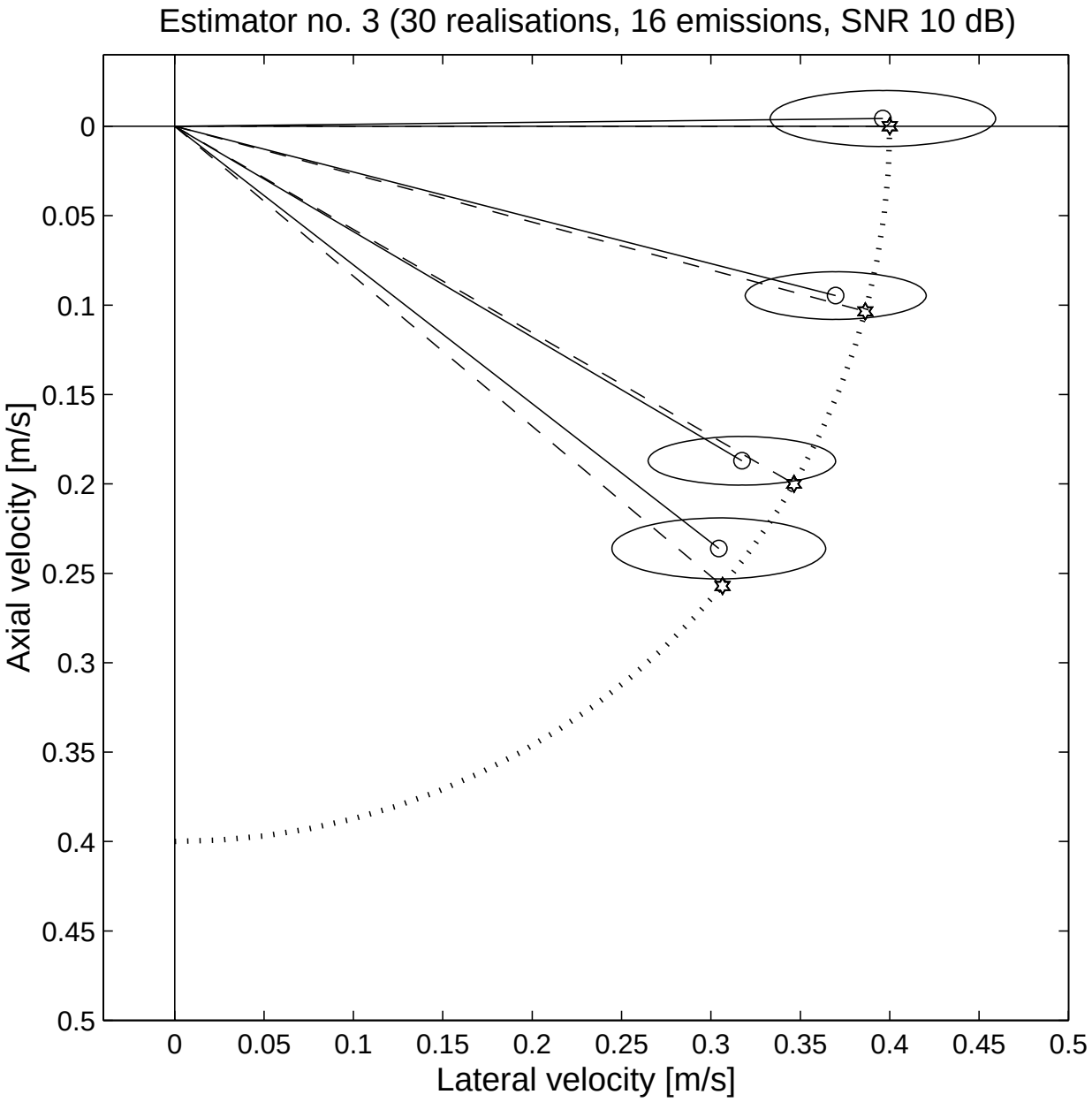

Figure 6.23: Performance of estimator no. 3 for angle 90, 75, 60 and 50 degrees.

Chapter 7

Conclusion

The major purposes of this Ph.D. work were to improve the performance of the method for estimation of vector flow presented in previous M.Sc. work [Mun96], to verify theoretical and simulated work by experimental results, and finally to make an initial implementation of the further developed method in a commercial scanner. The evolution of the project, and the development of a new digital scanner at the company B-K Medical A/S did not allow an implementation within the time frame of the project.
The work in [Mun96] verified the basic idea behind the method. It was shown that it is possible to create a received signal in a beamformer which is sensitive to movement perpendicular to the pulse propagation direction, and that the encoded information of the movement in the signal made it possible to use a modified version of the traditional autocorrelation method for velocity estimation.
The results obtained in this Ph.D. study can be summarized as follows: the method for estimating velocity vectors has been improved in the measurement situation by increased sensitivity, increased spatial resolution, and dynamic modulation. The estimation method has been improved by a decreased bias and decreased variance in the estimated velocities. Also, the pulsed plane wave decomposition and a new axial estimation scheme has been proposed.

In the following, the different contributions are described in more details.

In Chapter 2 a further development of a method originally presented by Leeman is given. A global and local time and a corrected propagation velocity is introduced. The method is applicable for decomposition of pulsed acoustic fields into a set of pulsed plane waves. The method can be used to decompose a pulsed acoustic field, propagate all the pulsed plane waves to another location, and reconstruct the resulting propagated pulsed acoustic field. The method exploits the benefit introduced by a projection scheme. In this work, it is used to devise the beamformer setup to be used for an array transducer in order to obtain a desired acoustic field. With this tool it is possible to come up with a setup for a filter-and-sum beamformer that creates a smooth Gaussian enveloped, double oscillating field sensitivity to be used for vector estimation.
Chapter 4 presents a new axial velocity estimator. The estimator is based on the 2D Fourier transform of the 2D RF data matrix normally used for axial velocity estimation. In the Fourier domain a Radon transform is performed for lines rotated in the origin of the 2D frequency domain. The result is a 1D function in which the mean value around the maximum value is a good estimate of the mean velocity. On the basis of simulated 3D acoustic data the new method showed an improved performance of up to 4 times compared to the standard

autocorrelation method on the standard deviation at a SNR level of -3 to 0 dB.
In Chapter 5 experimental work verifies the ability to create laterally oscillating fields by using a ruby (diameter 1/64") as an approximation to an ideal point reflector. The validation is performed with a focused transmit field and the lateral extension is reduced to approximately one lateral oscillation period which improves the sensitivity and the resolution of the flow imaging. Further, dynamic control in the receive beamforming is introduced, named dynamic oscillation, which allows the control of the lateral oscillation period as a function of depth. The framework of 2D Hilbert transformation is used to give a unified description of the measurement situation and of the proposed estimators.
In Chapter 6 all the results obtained by simulation and measurements are given. Experimental data recorded from a moving sponge in four different angles to the transducer show the ability to estimate the velocity independently of the angle. Simulated data are used to evaluated different estimators in terms of bias and variance. Results for different angles and for different velocities are given for varying SNRs and number of lines per estimate. In the case of a SNR of 10 dB and 16 lines, the results show a bias of 3.8 % and a relative standard deviation of 17 %.
Future work will include an implementation of the method on a scanner, based on a digital beamformer, to start the evaluation of the clinical aspects. The implementation will give rise to new issues that must be solved before a commercial introduction becomes a reality. One important aspect is the stationary echo-canceler, which perhaps could benefit from a two channel input. The estimators might further be improved by imposing a closer 2D Hilbert relation on the four signals generated by the measurement setup. The idea could be a new 2D filtering scheme. The impact on the performance of the estimator using a filter-and-sum beamformer must be clarified in order to evaluate the cost/benefit of using such a beamformer.

Bibliography

[AB95] Sheikh Kaisar Alam and Kevin J. Baker. The buttefly search technique for estimation of blood velocity. *Ultrasound Med. Biol.*, 21(5):657–670, 1995.

[AFH81] M. Arditi, F. S. Forster, and J. Hunt. Transient fields of concave annular arrays. *Ultrason. Imaging*, 3:37–61, 1981.

[AG96] M. E. Allam and J. F. Greenleaf. Isomorphism between pulsed-wave doppler ultrasound and direction-of-arrival estimation - part i: Basic principles. *IEEE Trans. Ultrason., Ferroelec., Freq. Contr.*, 43(5):911–922, 1996.

[AIU97] AIUM. *Recommended Ultrasound Terminology*. AUIM, second edition, 1997.

[AK83] B. A. Angelsen and Kjell Kristoffersen. Discrete time estimation of the mean doppler frequency in ultrasonic blood velocity measurements. *IEEE Trans. Biomed. Eng.*, 30(4):207–214, April 1983.

[And97] M. E. Anderson. Spatial quadrature: A novel technique for multi-dimensional velocity estimation. In *Proc. IEEE Ultrason. Symp.*, volume 45, pages 1233–1238, 1997.

[And98] M. E. Anderson. Spatial quadrature: A novel technique for multi-dimensional velocity estimation. *IEEE Trans. Ultrason., Ferroelec., Freq. Contr.*, 45:852–681, 1998.

[Ang80] B. A. J. Angelsen. A theoretical study of the scattering of ultrasound from blood. *IEEE Trans. Biomed. Eng.*, 27(2):61–67, February 1980.

[Ang81] B. A. Angelsen. Instantaneous frequency, mean frequency and variance of mean frequency estimators for ultrasonic blood velocity doppler signals. *IEEE Trans. Biomed. Eng.*, 28(11):733–741, November 1981.

[Bak70] D. W. Baker. Pulsed ultrasonic doppler blood-flow sensing. *IEEE Trans. Son. Ultrason.*, 17(3):170–185, 1970.

[BC81] B. G. Bardsley and D. A. Christensen. Beam patterns from pulsed ultrasonic transducers using linear system theory. *J. Acoust. Soc. Am.*, 69(1):25–30, January 1981.

[BEK85] W. D. Barber, J. W. Eberhard, and S. G. Karr. A new time domain technique for velocity measurements using doppler ultrasound. *IEEE Trans. Biomed. Eng.*, 32(3):213–229, March 1985.

[Bha67] A. B. Bhatia. *Ultrasonic Absorption, An Introduction to the Theory of Sound Absorption and Dispersion in Gases, Liquids and Solids*, chapter 4,8–10, pages 49–70, 168–263. Dover Publications, Inc., first edition, 1967.

[BM74] W. R. Brody and J. D. Meindl. Theoretical analysis of the CW doppler ultrasonic flowmeter. *IEEE Trans. Biomed. Eng.*, 21:183–192, 1974.

[Bon88] O. Bonnefous. Measurement of the complete (3D) velocity vector of blood flows. In *Proc. IEEE Ultrason. Symp.*, pages 795–799, 1988.

[BP86] O. Bonnefous and P. Pesqué. Time domain formulation of pulse-Doppler ultrasound and blood velocity estimation by cross correlation. *Ultrason. Imaging*, 8:73–85, 1986.

[BPB86] O. Bonnefous, P. Pesqué, and X. Bernard. A new velocity estimator for color flow mapping. In *Proc. IEEE Ultrason. Symp.*, pages 855–860, 1986.

[Bra78] R. N. Bracewell. *The Fourier Transform and its Applications.* McGraw Hill, second edition, 1978.

[CL89] E. T. Costa and S. Leeman. Diffraction artefacts and their removal. In *Acoust. Imaging*, pages 403–411, 1989.

[CLH88] E. T. Costa, S. Leeman, and J. C. Hoddinoott. *A New Approach Towards Measurement of Three-Dimensional Pulses: Linear and Nonlinear Fields*, volume 2, chapter 12. IPSM York, UK, first edition, 1988. Editor D. H. Evans and K. Martin.

[CLJ90] E. T. Costa, S. Leeman, and J. P. Jones. Reflectivity measurements using a large aperture PVDF hydrofone. In *Proc. IEEE Ultrason. Symp.*, pages 1043–1046, 1990.

[CLRS86] E. T. Costa, S. Leeman, P. A. C. Richardson, and D. A. Seggie. Measurements and calibration of transducer fields. In *Proc. Inst. Acoustics 8*, pages 113–118, 1986. Editor R. Lawrence Inst. of Acoustics Edinburgh UK.

[CNVO88] D. Censor, V. L. Newhouse, T. Vontz, and Hector V. Ortega. Theory of ultrasound doppler-spectra velocimetry for arbitrary beam and flow configurations. *IEEE Trans. Biomed. Eng.*, 35(9):740–751, September 1988.

[Cob84] W. N. Cobb. Frequency domain method for the prediction of the ultrasonic field patterns of pulsed, focused radiators. *J. Acoust. Soc. Am.*, 75(1):72–79, January 1984.

[Cou73] J. Coulthard. Ultrasonic cross-correlation flowmeters. *Ultrasonics*, pages 83–88, March 1973.

[Cou83] J. Coulthard. Cross-correlation flow measurement - a history and state of the art. *Meas. Cont.*, 16:214–218, 1983.

[Dea93] S. R. Deans. *The Radon Transform and some of its applications.* Krieger Publishing Company, second edition, 1993.

[DGS+76] D. Dotti, E. Gatti, V. Svelto, A. Uggè, and P. Vidali. Blood flow measurements by ultrasound correlation techniques. *Energia Nucleare*, 23:571–575, 1976.

[Dud84] D. E. Dudgeon. *Multidimensional Digital Signal processing*. Prentice-Hall, first edition, 1984.

[Eva2a] D. H. Evans. Some aspects of the relationship between instantaneous volumetric blood flow and continuous wave Doppler ultrasound recordings I. *Ultrasound Med. Biol.*, 9:605–609, 1982a.

[Eva2b] D. H. Evans. Some aspects of the relationship between instantaneous volumetric blood flow and continuous wave Doppler ultrasound recordings III. *Ultrasound Med. Biol.*, 9:617–623, 1982b.

[FC84] M. A. Fink and J.-F. Cardoso. Diffraction effects in pulse-echo measurements. *IEEE Trans. Son. Ultrason.*, 31(4):313–329, July 1984.

[FFBK94] D.-Y. Fei, C.-T. Fu, W. H. Brewer, and K. A. Kraft. Angle independent doppler color imaging: Determination of accuracy and a method of display. *Ultrasound Med. Biol.*, 20(2):147–155, 1994.

[FG88] M. D. Fox and W. M. Gardiner. Three-dimensional doppler velocimetry of flow jets. *IEEE Trans. Biomed. Eng.*, 35(10):834–841, October 1988.

[FHLC90] F. Forsberg, A. J. Healey, S. Leeman, and E. T. Costa. Measuring nonlinear fields without diffraction correction. In *Proc. IEEE Ultrason. Symp.*, pages 1033–1036, 1990.

[Fox78] M. D. Fox. Multiple crossed beam ultrasound doppler velocimetry. *IEEE Trans. Son. Ultrason.*, 25(5):281–286, September 1978.

[Fre70a] A. Freedman. Sound field of plane of gently curved pulsed radiators. *J. Acoust. Soc. Am.*, 48(1):221–227, 1970.

[Fre70b] A. Freedman. Transient fields of acoustic radiators. *J. Acoust. Soc. Am.*, 48(1):135–138, 1970.

[Fre94] A. Freedman. Acoustic field of a pulsed circular piston. *J. Sound and Vibration*, 170(4):495–519, 1994.

[GL77] J. C. Gore and S. Leeman. Ultrasonic backscattering from human tissue : A realistic model. *Phys. Med. Biol.*, 22(2):317–326, 1977.

[Goo68] J. W. Goodman. *Introduction to Fourier Optics*. McGraw-Hill Physical and Quantum Electronics Series. McGraw Hill, first edition, 1968.

[Goo96] J. W. Goodman. *Introduction to Fourier optics*. McGraw Hill Inc., New York, second edition edition, 1996.

[GP85] D. Guyomar and J. Powers. A fourier approach to diffraction of pulsed ultrasonic waves in lossless media. In *Proc. IEEE Ultrason. Symp.*, pages 692–695, 1985.

[HAF83] J. W. Hunt, M. Arditi, and F. Stuart Foster. Ultrasound transducers for pulse-echo medical imaging. *IEEE Trans. Biomed. Eng.*, 30(8):453–481, August 1983.

[Hah96] S. L. Hahn. *Hilbert Transforms in Signal Processing.* Artech House, Boston London, first edition, 1996.

[Han76] E. B. Hansen. *Sædvanlige differentialligninger fra fysikken.* Polyteknisk Forlag, second edition, 1976.

[Har81a] G. R. Harris. Review of transient field theory for baffled planar piston. *J. Acoust. Soc. Am.*, 70(1):10–20, July 1981.

[Har81b] G. R. Harris. Transient field of a baffled planar piston having an arbitrary vibration amplitude distribution. *J. Acoust. Soc. Am.*, 70(1):186–204, July 1981.

[HBL94] A. J. Healey, M. Betts, and S. Leeman. Field prediction in lossy media. In *Proc. IEEE Ultrason. Symp.*, pages 1769–1772, 1994.

[Hei93] I. A. Hein. Multi-directional ultrasonic blood flow measurement with a triple lens. In *Proc. IEEE Ultrason. Symp.*, pages 1065–1069, 1993.

[Hei95] I. A. Hein. Triple-beam lens transducer for three-dimensional ultrasonic fluid flow estimation. *IEEE Trans. Ultrason., Ferroelec., Freq. Contr.*, 42(5):854–869, September 1995.

[HL97] A. J. Healey and S. Leeman. Spacetime imaging of transient ultrasound fields. *International Journal of Imaging Systems and Technology*, 8(1):45–51, 1997.

[Hus75] M. Hussey. *Diagnostic Ultrasound, An Introduction to the Interactions between Ultrasound and Biological Tissue*, chapter 7, pages 146–199. Blackie Lmtd., first edition, 1975.

[Ish78a] A. Ishimaru. *Wave Propagation and Scattering in Random Media, Multiple Scattering, Turbulence, Rough Surfaces and Remote Sensing*, volume 2. Academic Press, first edition, 1978.

[Ish78b] A. Ishimaru. *Wave Propagation and Scattering in Random Media, Single Scattering and Transport Theory*, volume 1. Academic Press, first edition, 1978.

[JD93] D. H. Johnson and D. E. Dudgeon. *Array Signal Processing, Consepts and Techniques.* Prentice-Hall, first edition, 1993.

[Jen91] J. A. Jensen. A model for the propagation and scattering of ultrasound in tissue. *J. Acoust. Soc. Am.*, 89:182–191, 1991.

[Jen96a] J. A. Jensen. *Estimation of Blood Velocities using Ultrasound - A Signal Processing Approach.* Cambridge University Press, New York, first edition, 1996.

[Jen96b] J. A. Jensen. Ultrasound fields from triangular apertures. *J. Acoust. Soc. Am.*, 100(4):2049–2056, 1996.

[Jen99] J. A. Jensen. A new estimator for vector velocity estimation. *IEEE Trans. Ultrason., Ferroelec., Freq. Contr.*, page Submitted for review, 1999.

[JM97] J. A. Jensen and P. Munk. Computer phantoms for simulating ultrasound b-mode and cfm images. In S. Lees and L. A. Ferrari, editors, *Acoustical Imaging*, volume 23, pages 75–80, 1997.

[JM98] J. A. Jensen and P. Munk. A new method for estimation of velocity vectors. *IEEE Trans. Ultrason., Ferroelec., Freq. Contr.*, 45:837–851, 1998.

[Jøe87] O. G. Jøersbo. *Sandsynlighedsregning*, chapter 6, pages 39–55. Matematisk Institut, DTU, second edition, 1987.

[JS92] J. A. Jensen and N. B. Svendsen. Calculation of pressure fields from arbitrary shaped, apodized and ecxited ultrasound transducers. *IEEE Trans. Ultrason., Ferroelec., Freq. Contr.*, 39:262–267, 1992.

[Kin82] L. E. Kinsler. *Fundamentals of Acoustics*. John Wiley & Sons, third edition, 1982.

[Kin87] G. S. Kino. *Acoustic Waves: Devices, Imaging and Analog Signal Processing*. Prentice-Hall, first edition, 1987.

[KNKO85] C. Kasai, K. Namekawa, A. Koyano, and R. Omoto. Real-time two-dimensional blood flow imaging using an autocorrelation technique. *IEEE Trans. Son. Ultrason.*, 32:458–463, 1985.

[LCH91] S. Leeman, E. T. Costa, and A. J. Healey. Large aperture hydrophones for field characterisation. In *Proc. IEEE Ultrason. Symp.*, pages 679–682, 1991.

[LG94] T. Loupas and R. W. Gill. Multifrequency Doppler: Improving the quality of spectral estimation by making full use of the information present in the backscattered rf echoes. *IEEE Trans. Ultrason., Ferroelec., Freq. Contr.*, 41:522–531, 1994.

[LH97] S. Leeman and A. J. Healey. Field propagation via the angular spectrum method. In *Acoust. Imaging*, volume 23, pages 363–368, 1997.

[LHFJ90] S. Leeman, A. J. Healey, F. Forsberg, and J. A. Jensen. On output measurements via radiation pressure. In *Proc. IEEE Ultrason. Symp.*, pages 1389–1392, 1990.

[LPG95a] T. Loupas, R. B. Peterson, and R. W. Gill. Experimental evaluation of velocity and power estimation for blood flow imaging, by means of a two-dimensional autocorrelation approach. *IEEE Trans. Ultrason., Ferroelec., Freq. Contr.*, 42:689–699, 1995.

[LPG95b] T. Loupas, J. T. Powers, and R. W. Gill. An axial velocity estimator for ultrasound blood flow imaging, based on a full evaluation of the Doppler equation by means of a two-dimensional autocorrelation approach. *IEEE Trans. Ultrason., Ferroelec., Freq. Contr.*, 42:672–688, 1995.

[LSF+85] S. Leeman, D. A. Seggie, L. A. Ferrari, P. V. Sankar, and M. Doherty. Diffraction-free attenuation estimation. In *Ultrasonics International*, pages 128–132, 1985.

[LW73] J. C. Lockwood and J. G. Willette. High speed method for computing the exact solution for the pressure variations in the nearfield of a baffled piston. *J. Acoust. Soc. Am.*, 53:735–741, 1973.

[Mag86] P. A. Magnin. Doppler effect: History and theory. *HP-Journal*, 37(6):26–31, June 1986.

[Mag87] P. A. Magnin. A review of Doppler flow mapping techniques. In *Proc. IEEE Ultrason. Symp.*, pages 969–977, 1987.

[Mai94] R. J. Mailloux. *Phased Array Antenna Handbook*, chapter 3. Artech House, Boston London, first edition, 1994.

[MC86] L. Y. L. Mo and R. S. C. Cobbold. A stochastic model of the backscattered doppler ultrasound from blood. *IEEE Trans. Biomed. Eng.*, 33(1):20–27, January 1986.

[MC92] L. Y. L. Mo and R S. C. Cobbold. A unified approach to modelling the backscattered doppler ultrasound from blood. *IEEE Trans. Biomed. Eng.*, 39(5):450–461, May 1992.

[MCJ94] T. A. Maniatis, R. S. C. Cobbold, and K. W. Johnston. Two-dimensioanl velocity reconstruction strategies for color flow doppler ultrasound images. *Ultrasound Med. Biol.*, 20(2):137–145, 1994.

[MEAG96] R. R. Kinnick M. E. Allam and J. F. Greenleaf. Isomorphism between pulsed-wave doppler ultrasound and direction-of-arrival estimation - part ii: Experimental results. *IEEE Trans. Ultrason., Ferroelec., Freq. Contr.*, 43(5):922–935, 1996.

[MI68] P. M. Morse and K. U. Ingard. *Theoretical Acoustics*. McGraw-Hill, first edition, 1968.

[MJ98] P. Munk and J. A. Jensen. Performance of a vector velocity estimator. In *Proc. IEEE Ultrason. Symp.*, pages 1489–1493, 1998.

[MR72] K. S. Miller and M. M. Rochwarger. A covariance approach to spectral moment estimation. *IEEE Transaction on Information Theory*, 18(5):588–596, September 1972.

[MSB+83] J. Machi, B. Siegel, J.C. Beitler, J. C. U. Coelcho, and J. R. Justin. Relation of in vivo blood flow to ultrasound echogenicity. *J. Clin. Ultrasound*, 11:3–10, 1983.

[Mun96] P. Munk. Estimation of the 2-D flow vector in ultrasonic imaging: a new approach. Master's thesis, Deparment of Information Technology, Technical University of Denmark, 1996.

[Mun97] P. Munk. Uddannelsesplan for peter munk, ph.d.96-0152/atv.ef632. Technical report, Department of Information Technology, DTU, 1997.

[MZ83] P. R. Mahapatra and D. S. Zrnic. Practical algorithms for mean velocity estimation in pulse doppler weather radars using a small number of samples. *IEEE Transactions on Geoscience and Remote Sensing*, 21(4):491–501, October 1983.

[NBV76] V. L. Newhouse, P. J. Bendick, and L. W. Varner. Analysis of transit time effects on doppler flow measurement. *IEEE Trans. Biomed. Eng.*, 23(5):381–387, September 1976.

[NCC91] V. L. Newhouse, D. Cathignol, and J.Y. Chapelon. Study of flow estimation with transverse Doppler. In *Proc. IEEE Ultrason. Symp.*, pages 1259–1263, 1991.

[NCV+87] V. L. Newhouse, D. Censor, T. Vontz, J. A. Cisneros, and B. Goldberg. Ultrasound doppler probing of flow transverse with respect to beam axis. *IEEE Trans. Biomed. Eng.*, 34:779–789, October 1987.

[NDCC94a] V. L. Newhouse, K. S. Dickerson, D. Cathignol, and J.-Y. Chapelon. Three-dimensional vector flow estimation using two transducers and spectral width. *IEEE Trans. Ultrason., Ferroelec., Freq. Contr.*, 41(1):90–95, January 1994.

[NDCC94b] V. L. Newhouse, K. S. Dickerson, D. Cathignol, and J.-Y. Chapelon. Three-dimensional vector flow estimation using two transducers and spectral width. *IEEE Trans. Ultrason., Ferroelec., Freq. Contr.*, 41:90–95, 1994.

[NKKO82] K. Namekawa, C. Kasai, A. Koyano, and R. Omoto. Realtime bloodflow imaging utilizing auto-correlation techniques. *Ultrasound*, pages 203–208, 1982.

[NKTK82] K. Namekawa, C. Kasai, M. Tsukamoto, and A. Koyano. Imaging of blood flow using auto-correlation. *Ultrasound Med. Biol, Supplement*, 8:138, 1982.

[NO90] W. W. Nichols and M. F. O'Rourke. *McDonald's Blood Flow in Arteries, Theoretical, Experimental and Clinical Principles.* Lea & Febiger, second edition, 1990.

[OB92] J. R. Overbeck and K. W. Beach. Vector doppler: Accurate measurements of blood velocity in two dimensions. *Ultrasound Med. Biol.*, 18(1):19–31, 1992.

[Obe61a] F. Oberhettinger. Note on the "baffled piston" problem. *J. Res. Natl. Bur. Stand*, 65(3):203–204, July 1961. Volume 65B.

[Obe61b] F. Oberhettinger. On transient solutions of the "baffled piston" problem. *J. Res. Natl. Bur. Stand*, 65(1):1–6, March 1961. Volume 65B.

[OS89] A. V. Oppenheim and R. W. Schafer. *Discrete-Time Signal Processing.* Prentice Hall Signal Processing Series, international edition, 1989.

[Pap84] A. Papoulis. *Signal Analysis.* McGraw-Hill, first edition, 1984.

[Pie81] A. D. Pierce. *Acoustics, An Introduction to its Physical Principles and Applications*, chapter 1, pages 1–53. McGraw-Hill Series in Mechanical Engineering. McGraw-Hill Book Compagny, first edition, 1981.

[PL76] A. Penttinen and M. Luukkala. The impulse response and nearfield of a curved ultrasonic radiator. *J. Phys. D. Appl. Phys.*, 9:1547–1557, 1976.

[PS83] R. E. Passarelli and A. D. Siggia. The autocorrelation function and doppler spectral moments : Geometric and asymptotic interpretations. *Journal Of Climate and Applied Meteorology*, 22:1776–1787, October 1983.

[RMZ90] N. Rao, S. Mehra, and H. Zhu. Ultrasound speckle statistics variations with imaging systems impulse response. In *Proc. IEEE Ultrason. Symp.*, pages 1435–1440, 1990.

[Rob82] E. A. Robinson. Spectral approach to geophysical inversion by lorentz, fourier and radon transforms. *IEEE Trans. Acous., Speech, Sig. Pro.*, 70:1039–1054, 1982.

[Rum68a] W. D. Rummler. Introduction of a new estimator for velocity spectral parameters. *Technical Memo*, 1968. Reference MM-68-4121-5 at Bell Telephone Labs. Whippany NJ.

[Rum68b] W. D. Rummler. Two pulse spectral measurements. *Technical Memo*, 1968. Reference MM-68-4121-15 at Bell Telephone Labs. Whippany NJ.

[Sku71] E. Skudrzyk. *The Foundations of Acoustics, Basic Mathematics and Basic Acoustics.* Springer-Verlag, first edition, 1971.

[Sou94] Mehrdad Soumekh. *Fourier Array Imaging.* Prentice-Hall, first edition, 1994.

[SSR76] K. K. Shung, R. A. Siegelman, and J. M. Reid. Scattering of ultrasound by blood. *IEEE Trans. Biomed. Eng.*, 23(6):460–467, November 1976.

[Ste71a] P. R. Stephanishen. The time dependent force and radiation impedance on a piston in a rigid infinite planar baffle. *J. Acoust. Soc. Am.*, 49:841–849, 1971.

[Ste71b] P. R. Stephanishen. Transient radiation from pistons in an infinite planar baffle. *J. Acoust. Soc. Am.*, 49:1629–1638, 1971.

[Ste76a] B. D. Steinberg. *Principle of Aperture and Array System Design.* John Wiley & Sons, first edition, 1976.

[Ste76b] B. D. Steinberg. *Principles of aperture and array system design.* John Wiley & Sons, New York, 1976.

[Ste77] P. R. Stephanishen. Wide bandwidth acoustic near and farfield transients from baffled pistons. In *Proc. IEEE Ultrason. Symp.*, 1977.

[Ste81] P. R. Stephanishen. Pulsed transmit/receive response of ultrasonic piezoelectric transducers. *J. Acoust. Soc. Am.*, 69(6):1815–1827, June 1981.

[TAL93] R. Tolimieri, M. An, and C. Lu. *Mathematics of Multidimensional Fourier Transform Algorithms.* Springer-Verlag, first edition, 1993.

[TAvR87] G. E. Trahey, J. W. Allison, and O. T. von Ramm. Angle independent ultrasonic detection of blood flow. *IEEE Trans. Biomed. Eng.*, BME-34:965–967, 1987.

[TCJ90] T. Tamura, R. S. C. Cobbold, and K. W. Johnston. Determination of 2-D velocity vectors using color doppler ultrasound. In *Proc. IEEE Ultrason. Symp.*, pages 1537–1540, 1990.

[TGGA94] P. Tortoli, G. Guidi, F. Guidi, and C. Atzeni. A review of experimental transverse doppler studies. *IEEE Trans. Ultrason., Ferroelec., Freq. Contr.*, 41(1):84–89, January 1994.

[THvR88] G. E. Trahey, S. M. Hubbard, and O. T. von Ramm. Angle independent ultrasonic blood flow detection by frame-to-frame correlation of B-mode images. *Ultrasonics*, 26:271–276, 1988.

[Tof96] Peter Toft. *The Radon Transform, Theory and Implementation.* PhD thesis, Technical University of Denmark, Lyngby, Denmark, 1996.

[TSvR86] G. E. Trahey, S. W. Smith, and O. T. von Ramm. Speckle pattern correlation with lateral aperture translation: Experimental results and implications for spatial compounding. *IEEE Trans. Ultrason., Ferroelec., Freq. Contr.*, UFFC-33:257–264, 1986.

[TT82] J. N. Tjoetta and S. Tjoetta. Nearfield and farfield of pulsed acoustic radiators. *J. Acoust. Soc. Am.*, 71(4):824–834, April 1982.

[Wil91] L. S. Wilson. Description of broad-band pulsed Doppler ultrasound processing using the two-dimensional Fourier transform. *Ultrason. Imaging*, 13:301–315, 1991.

[Wom55] J. R. Womersley. Oscillatory motion of a viscous liquid in a thin-walled elastic tube. I: The linear approximation for long waves. *Phil. Mag.*, 46:199–221, 1955.

[WT94] W. F. Walker and G. E. Trahey. A fundamental limit on the performance of correlation based phase correction and flow estimation techniques. *IEEE Trans. Ultrason., Ferroelec., Freq. Contr.*, 41:644–654, 1994.

[Zrn77] D. S. Zrnic. Spectral moment estimates from correlated pulse pairs. *IEEE Transactions on Aerospace and Electronic Systems Journal*, 13(4):344–354, July 1977.

[Zrn79] D. S. Zrnic. Spectrum width estimates for weather echos. *IEEE Transactions on Aerospace and Electronic Systems Journal*, 15(5):613–619, September 1979.

Appendices

Appendix A

Solutions to the wave equation for different coordinate systems.

The wave equation is stated without any reference to a coordinate system. The choice of coordinate system implies geometrical properties of simple solutions for the wave equation. Typically three reference systems are of interest. The rectangular, the spherical and the cylindrical coordinate system. The following coordinate signature will be used:

- the rectangular coordinate system: x, y, z
- the spherical coordinate system: r, ϑ, φ
- the cylindrical coordinate system: h, φ, z

The relations between the different coordinate systems can be expressed on the basis of figure A.1 with trigonometric relations through the rectangular coordinates.

$$\begin{aligned} x &= r \sin\vartheta \cos\varphi \\ y &= r \sin\vartheta \sin\varphi \\ z &= r \cos\vartheta \end{aligned} \tag{A.1}$$

and

$$\begin{aligned} x &= h \cos\varphi \\ y &= h \sin\varphi \\ z &= z \end{aligned} \tag{A.2}$$

The differential operators in (2.12) and (2.14) will take form according to the applied coordinate system. The gradient of a scalar function will be a vector with components of the actual system. In rectangular coordinates

$$\begin{aligned} \nabla_x &= \mathrm{grad}_x() = \frac{\partial}{\partial x} \\ \nabla_y &= \mathrm{grad}_y() = \frac{\partial}{\partial y} \\ \nabla_z &= \mathrm{grad}_z() = \frac{\partial}{\partial z} \end{aligned} \tag{A.3}$$

in spherical coordinates

$$\begin{aligned} \nabla_r &= \mathrm{grad}_r() = \frac{\partial}{\partial r} \\ \nabla_\vartheta &= \mathrm{grad}_\vartheta() = \frac{1}{r}\frac{\partial}{\partial \vartheta} \\ \nabla_\varphi &= \mathrm{grad}_\varphi() = \frac{1}{r\sin\vartheta}\frac{\partial}{\partial x} \end{aligned} \tag{A.4}$$

in cylindrical coordinates

$$\begin{aligned} \nabla_h &= \mathrm{grad}_h() = \frac{\partial}{\partial h} \\ \nabla_\varphi &= \mathrm{grad}_\varphi() = \frac{1}{h}\frac{\partial}{\partial \varphi} \\ \nabla_z &= \mathrm{grad}_z() = \frac{\partial}{\partial z} \end{aligned} \tag{A.5}$$

For the Laplace operator $\nabla^2() = \mathrm{divgrad}()$ is given by:
in rectangular coordinates

$$\nabla^2 = \frac{\partial^2}{\partial x^2} + \frac{\partial^2}{\partial y^2} + \frac{\partial^2}{\partial z^2} \tag{A.6}$$

in spherical coordinates

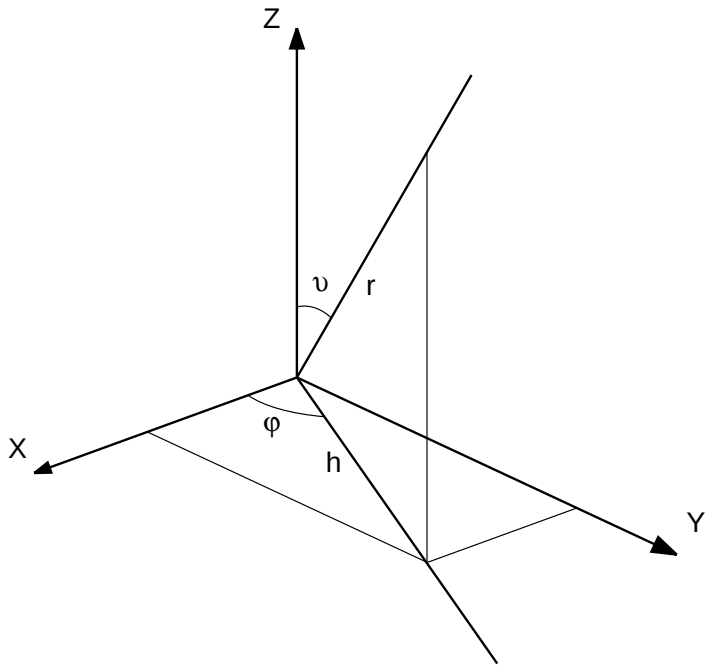

Figure A.1: Geometric relation for the coordinate signature for rectangular, spherical and cylindrical coordinate systems

$$\nabla^2 = \frac{1}{r^2}\frac{\partial}{\partial r}(r^2\frac{\partial}{\partial r}) + \frac{1}{r^2\sin\vartheta}\frac{\partial}{\partial\vartheta}(\sin\vartheta\frac{\partial}{\partial\vartheta}) + \frac{1}{r^2\sin^2\vartheta}\frac{\partial}{\partial\varphi^2} \tag{A.7}$$

in cylindrical coordinates

$$\nabla^2 = \frac{1}{h}\frac{\partial}{\partial h}(h\frac{\partial}{\partial h}) + \frac{1}{h^2}\frac{\partial^2}{\partial\varphi^2} + \frac{\partial^2}{\partial z^2} \tag{A.8}$$

On the basis of these transformations, different fundamental wave types can be found.

Appendix B

Integrals used for projections

Definite integrals in closed form of an exponential multiplied by either a sine or a cosine used for calculation of the pulsed field projections onto a plane in space.

$$\int_{-\infty}^{+\infty} \exp\left[-(ax^2+2bx+c)\right] \cdot \sin(px^2+2qx+r)dx$$

$$= \frac{\sqrt{\pi}}{\sqrt[4]{a^2+p^2}} \exp \frac{a(b^2-ac)-(aq^2-2bpq+cp^2)}{a^2+p^2}$$
$$\times \sin\left[\frac{1}{2}\arctan\frac{p}{a} - \frac{p(q^2-pr)-(b^2p-2abq+a^2r)}{a^2+p^2}\right]$$

$$[a>0]\,.$$

$$\int_{-\infty}^{+\infty} \exp\left[-(ax^2+2bx+c)\right] \cdot \cos(px^2+2qx+r)dx$$

$$= \frac{\sqrt{\pi}}{\sqrt[4]{a^2+p^2}} \exp \frac{a(b^2-ac)-(aq^2-2bpq+cp^2)}{a^2+p^2}$$
$$\times \cos\left[\frac{1}{2}\arctan\frac{p}{a} - \frac{p(q^2-pr)-(b^2p-2abq+a^2r)}{a^2+p^2}\right]$$

$$[a>0]\,.$$

Appendix C

Womersley parameters

The relation between pressure difference, ΔP, and volume flow rate, Q, for a sinusoidal flow is given in 3.8. Womersley's number α is complex and Womersley's parameters, M'_{10} and ϵ_{10} are a function of α given by

$$M'_{10}(\alpha) = \sqrt{1 + h_{10}^2 - 2h_{10}\cos(\delta_{10})} \tag{C.1}$$

$$\epsilon'_{10}(\alpha) = \arctan\left(\frac{h_{10}\sin(\delta_{10})}{1 - h_{10}\cos(\delta_{10})}\right), \tag{C.2}$$

with h_{10} and δ_{10} defined as

$$h_{10} = \frac{2}{\alpha}\sqrt{\frac{\mathrm{ber}_1^2(\alpha) + \mathrm{bei}_1^2(\alpha)}{\mathrm{ber}_0^2(\alpha) + \mathrm{bei}_0^2(\alpha)}} \tag{C.3}$$

$$\delta_{10} = \frac{3\pi}{4} - \arctan\left(\frac{\mathrm{bei}_1(\alpha)}{\mathrm{ber}_1(\alpha)}\right) + \arctan\left(\frac{\mathrm{bei}_0(\alpha)}{\mathrm{ber}_0(\alpha)}\right). \tag{C.4}$$

where the two functions, $\mathrm{ber}_n(x), \mathrm{bei}_n(x)$, is the Kelvin function defined by:

$$\mathrm{ber}_n(x) + j\mathrm{bei}_n(x) = e^{n\pi j} J_n(xe^{-\pi j/4}) \tag{C.5}$$

where J_n is the nth order Bessel function of the first kind.

Appendix D

Summarized results in tables

D.1 Synthetic data

D.1.1 Angle of 90 degrees.

Estimator no.1

		SNR						
lines		0	3	6	10	16	20	24
24	μ_v :	0.4995	0.4997	0.4999	0.4998	0.5	0.5	0.5
	σ_v :	0.017	0.0123	0.0091	0.0063	0.0041	0.0029	0.0008
20	μ_v :	0.4998	0.4996	0.4998	0.4995	0.5	0.4999	0.5
	σ_v :	0.0204	0.0147	0.0108	0.0078	0.005	0.0035	0.0011
16	μ_v :	0.5011	0.5006	0.5001	0.4998	0.5004	0.5	0.5
	σ_v :	0.0236	0.0176	0.0142	0.0101	0.0064	0.0048	0.0015
12	μ_v :	0.499	0.4996	0.5001	0.5	0.4999	0.4999	0.5
	σ_v :	0.0346	0.0225	0.0185	0.0134	0.0089	0.007	0.0021
8	μ_v :	0.4988	0.5	0.5003	0.5008	0.5007	0.4998	0.4999
	σ_v :	0.0512	0.0379	0.0295	0.0223	0.0156	0.012	0.0038

Estimator no.2

		SNR						
lines		0	3	6	10	16	20	24
24	μ_v :	0.4995	0.4997	0.4999	0.4999	0.5	0.5	0.5
	σ_v :	0.0168	0.0121	0.009	0.0063	0.0041	0.0029	0.0008
20	μ_v :	0.4999	0.4997	0.4998	0.4995	0.5	0.4999	0.5
	σ_v :	0.0201	0.0145	0.0108	0.0077	0.005	0.0035	0.0011
16	μ_v :	0.5011	0.5005	0.5	0.4998	0.5004	0.5	0.5
	σ_v :	0.0233	0.0175	0.014	0.01	0.0064	0.0048	0.0015
12	μ_v :	0.4989	0.4997	0.5001	0.5001	0.4999	0.4999	0.5
	σ_v :	0.0343	0.0222	0.0182	0.0133	0.0088	0.0069	0.0021
8	μ_v :	0.4988	0.4998	0.5004	0.5008	0.5007	0.4998	0.4999
	σ_v :	0.0504	0.0375	0.0291	0.0223	0.0156	0.0119	0.0038

Estimator no.3

		SNR						
lines		0	3	6	10	16	20	24
24	μ_v :	0.4994	0.4997	0.4999	0.4999	0.5	0.5	0.5
	σ_v :	0.0164	0.012	0.009	0.0063	0.0041	0.0029	0.0008
20	μ_v :	0.5002	0.4997	0.4998	0.4995	0.5	0.4999	0.5
	σ_v :	0.0188	0.0145	0.0108	0.0077	0.005	0.0035	0.0011
16	μ_v :	0.5009	0.5005	0.5	0.4998	0.5004	0.5	0.5
	σ_v :	0.0223	0.0174	0.014	0.01	0.0064	0.0048	0.0015
12	μ_v :	0.4986	0.4995	0.5	0.5	0.4999	0.4999	0.5
	σ_v :	0.0309	0.0219	0.0182	0.0133	0.0089	0.0069	0.0021
8	μ_v :	0.4982	0.4993	0.5002	0.5005	0.5006	0.4997	0.4999
	σ_v :	0.0462	0.0372	0.0288	0.0223	0.0156	0.0119	0.0038

Estimator no.4

		SNR						
lines		0	3	6	10	16	20	24
24	μ_v :	0.4994	0.4997	0.4999	0.4999	0.5	0.5	0.5
	σ_v :	0.0164	0.012	0.009	0.0063	0.0041	0.0029	0.0008
20	μ_v :	0.5002	0.4997	0.4998	0.4995	0.5	0.4999	0.5
	σ_v :	0.0188	0.0145	0.0108	0.0077	0.005	0.0035	0.0011
16	μ_v :	0.5009	0.5005	0.5	0.4998	0.5004	0.5	0.5
	σ_v :	0.0223	0.0174	0.014	0.01	0.0064	0.0048	0.0015
12	μ_v :	0.4986	0.4995	0.5	0.5	0.4999	0.4999	0.5
	σ_v :	0.0309	0.0219	0.0182	0.0133	0.0089	0.0069	0.0021
8	μ_v :	0.4919	0.4968	0.5002	0.5005	0.5006	0.4997	0.4999
	σ_v :	0.0904	0.0619	0.0288	0.0223	0.0156	0.0119	0.0038

D.1.2 Angle of 75 degrees.

Estimator no.1

		SNR						
lines		0	3	6	10	16	20	24
24	μ_v :	0.4828	0.4827	0.4829	0.4822	0.483	0.483	0.483
	σ_v :	0.0267	0.0226	0.0177	0.0133	0.0092	0.0073	0.0022
20	μ_v :	0.4834	0.4821	0.4836	0.4835	0.4833	0.4832	0.4831
	σ_v :	0.0325	0.0247	0.0194	0.0155	0.0099	0.0079	0.0024
16	μ_v :	0.4847	0.4829	0.4845	0.4836	0.4823	0.4832	0.4829
	σ_v :	0.0361	0.0289	0.0225	0.017	0.0118	0.0094	0.0029
12	μ_v :	0.4809	0.482	0.4821	0.483	0.4831	0.4834	0.4832
	σ_v :	0.0447	0.0334	0.0274	0.0202	0.014	0.011	0.0033
8	μ_v :	0.4878	0.4835	0.4851	0.4831	0.483	0.4827	0.4832
	σ_v :	0.0622	0.0467	0.037	0.029	0.0197	0.0155	0.0046

Estimator no.2

		SNR						
lines		0	3	6	10	16	20	24
24	μ_v :	0.4829	0.4826	0.483	0.4823	0.483	0.483	0.483
	σ_v :	0.0265	0.0223	0.0176	0.0132	0.0092	0.0072	0.0022
20	μ_v :	0.4834	0.4821	0.4836	0.4836	0.4833	0.4832	0.4831
	σ_v :	0.0321	0.0244	0.0192	0.0153	0.0098	0.0078	0.0024
16	μ_v :	0.4848	0.4829	0.4844	0.4836	0.4823	0.4832	0.4829
	σ_v :	0.0357	0.0286	0.0224	0.0169	0.0118	0.0094	0.0028
12	μ_v :	0.4811	0.4819	0.4821	0.4831	0.4831	0.4834	0.4832
	σ_v :	0.0444	0.0331	0.0272	0.02	0.0139	0.011	0.0033
8	μ_v :	0.4879	0.4833	0.4849	0.4831	0.483	0.4827	0.4832
	σ_v :	0.0617	0.0461	0.0368	0.0287	0.0196	0.0154	0.0046

Estimator no.3

		SNR						
lines		0	3	6	10	16	20	24
24	μ_v :	0.4829	0.4828	0.4826	0.4826	0.483	0.4828	0.4829
	σ_v :	0.0168	0.0127	0.0095	0.007	0.0044	0.0033	0.0009
20	μ_v :	0.483	0.4829	0.4831	0.4829	0.4831	0.4829	0.483
	σ_v :	0.0194	0.0146	0.0112	0.0081	0.0052	0.004	0.0011
16	μ_v :	0.4839	0.4821	0.4837	0.4828	0.483	0.4831	0.4829
	σ_v :	0.0237	0.0185	0.0137	0.0098	0.0068	0.005	0.0015
12	μ_v :	0.4818	0.4832	0.4822	0.4827	0.4832	0.483	0.4831
	σ_v :	0.0301	0.0234	0.0188	0.0137	0.0091	0.0071	0.0021
8	μ_v :	0.484	0.4813	0.4845	0.4826	0.4826	0.4826	0.4831
	σ_v :	0.0471	0.036	0.029	0.0228	0.0153	0.012	0.0037

Estimator no.4

		SNR						
lines		0	3	6	10	16	20	24
24	μ_v :	0.4829	0.4828	0.4826	0.4826	0.483	0.4828	0.4829
	σ_v :	0.0168	0.0127	0.0095	0.007	0.0044	0.0033	0.0009
20	μ_v :	0.483	0.4829	0.4831	0.4829	0.4831	0.4829	0.483
	σ_v :	0.0194	0.0146	0.0112	0.0081	0.0052	0.004	0.0011
16	μ_v :	0.4839	0.4821	0.4837	0.4828	0.483	0.4831	0.4829
	σ_v :	0.0237	0.0185	0.0137	0.0098	0.0068	0.005	0.0015
12	μ_v :	0.4818	0.4832	0.4822	0.4827	0.4832	0.483	0.4831
	σ_v :	0.0301	0.0234	0.0188	0.0137	0.0091	0.0071	0.0021
8	μ_v :	0.4803	0.4813	0.4845	0.4826	0.4826	0.4826	0.4831
	σ_v :	0.0754	0.036	0.029	0.0228	0.0153	0.012	0.0037

D.1.3 Angle of 60 degrees.

Estimator no.1

		SNR						
lines		0	3	6	10	16	20	24
24	μ_v :	0.4331	0.4317	0.4329	0.4344	0.4331	0.4331	0.4331
	σ_v :	0.0321	0.0256	0.0209	0.0157	0.0109	0.0081	0.0026
20	μ_v :	0.4325	0.4321	0.4329	0.4325	0.4325	0.4335	0.4329
	σ_v :	0.0353	0.0292	0.0218	0.0176	0.0117	0.0091	0.003
16	μ_v :	0.4328	0.434	0.4332	0.4322	0.4337	0.4327	0.433
	σ_v :	0.039	0.0315	0.0252	0.0203	0.0133	0.0105	0.0032
12	μ_v :	0.435	0.4326	0.4332	0.4337	0.4337	0.4335	0.433
	σ_v :	0.0442	0.0361	0.0301	0.0234	0.0156	0.0121	0.0039
8	μ_v :	0.4357	0.4363	0.4308	0.4336	0.4326	0.4337	0.4331
	σ_v :	0.0578	0.0509	0.0401	0.0301	0.0205	0.0159	0.0051

Estimator no.2

		SNR						
lines		0	3	6	10	16	20	24
24	μ_v :	0.433	0.4317	0.433	0.4344	0.4332	0.433	0.4331
	σ_v :	0.0319	0.0255	0.0208	0.0156	0.0108	0.0081	0.0026
20	μ_v :	0.4323	0.4321	0.433	0.4326	0.4326	0.4335	0.4329
	σ_v :	0.0349	0.0291	0.0217	0.0176	0.0116	0.0091	0.0029
16	μ_v :	0.4327	0.434	0.4332	0.4321	0.4336	0.4328	0.433
	σ_v :	0.0388	0.0314	0.0251	0.0202	0.0131	0.0105	0.0031
12	μ_v :	0.4348	0.4323	0.4332	0.4336	0.4338	0.4335	0.4331
	σ_v :	0.044	0.0359	0.0299	0.0232	0.0155	0.012	0.0039
8	μ_v :	0.4359	0.4362	0.4309	0.4336	0.4325	0.4338	0.4331
	σ_v :	0.0572	0.0505	0.0397	0.0299	0.0203	0.0158	0.0051

Estimator no.3

		SNR						
lines		0	3	6	10	16	20	24
24	μ_v :	0.4325	0.4323	0.4327	0.4334	0.4334	0.4331	0.4331
	σ_v :	0.0176	0.0135	0.01	0.0077	0.005	0.0038	0.0011
20	μ_v :	0.432	0.4333	0.433	0.4328	0.4329	0.4332	0.433
	σ_v :	0.02	0.015	0.0117	0.009	0.0055	0.0044	0.0013
16	μ_v :	0.4323	0.4333	0.4327	0.4327	0.4329	0.4328	0.433
	σ_v :	0.0229	0.0181	0.0142	0.0107	0.0071	0.0055	0.0016
12	μ_v :	0.4327	0.4327	0.4326	0.4333	0.4335	0.4332	0.433
	σ_v :	0.0291	0.0225	0.0184	0.0136	0.0094	0.0071	0.0021
8	μ_v :	0.4322	0.4329	0.4324	0.4326	0.4324	0.4332	0.433
	σ_v :	0.0439	0.0378	0.0292	0.0212	0.0145	0.011	0.0036

Estimator no.4

		SNR						
lines		0	3	6	10	16	20	24
24	μ_v :	0.4325	0.4323	0.4327	0.4334	0.4334	0.4331	0.4331
	σ_v :	0.0176	0.0135	0.01	0.0077	0.005	0.0038	0.0011
20	μ_v :	0.432	0.4333	0.433	0.4328	0.4329	0.4332	0.433
	σ_v :	0.02	0.015	0.0117	0.009	0.0055	0.0044	0.0013
16	μ_v :	0.4323	0.4333	0.4327	0.4327	0.4329	0.4328	0.433
	σ_v :	0.0229	0.0181	0.0142	0.0107	0.0071	0.0055	0.0016
12	μ_v :	0.4327	0.4327	0.4326	0.4333	0.4335	0.4332	0.433
	σ_v :	0.0291	0.0225	0.0184	0.0136	0.0094	0.0071	0.0021
8	μ_v :	0.4322	0.4329	0.4324	0.4326	0.4324	0.4332	0.433
	σ_v :	0.0439	0.0378	0.0292	0.0212	0.0145	0.011	0.0036

D.1.4 Angle of 45 degrees.

Estimator no.1

		SNR						
lines		0	3	6	10	16	20	24
24	μ_v :	0.3535	0.3537	0.3533	0.3532	0.3535	0.3536	0.3535
	σ_v :	0.0203	0.0159	0.0121	0.0086	0.0055	0.0042	0.0013
20	μ_v :	0.3546	0.3534	0.3535	0.3537	0.3539	0.3536	0.3535
	σ_v :	0.0224	0.018	0.0132	0.01	0.0063	0.0047	0.0015
16	μ_v :	0.3551	0.3538	0.3534	0.354	0.3536	0.3535	0.3535
	σ_v :	0.0266	0.0198	0.015	0.0108	0.007	0.0058	0.0016
12	μ_v :	0.3523	0.3536	0.3545	0.3536	0.3536	0.3534	0.3536
	σ_v :	0.0341	0.0251	0.0195	0.0142	0.0093	0.0071	0.0022
8	μ_v :	0.3544	0.3535	0.3545	0.3549	0.3538	0.3536	0.3535
	σ_v :	0.0526	0.0391	0.0298	0.0219	0.0139	0.0116	0.0034

Estimator no.2

		SNR						
lines		0	3	6	10	16	20	24
24	μ_v :	0.3535	0.3538	0.3534	0.3531	0.3535	0.3536	0.3535
	σ_v :	0.02	0.0158	0.012	0.0085	0.0055	0.0041	0.0013
20	μ_v :	0.3547	0.3533	0.3535	0.3537	0.3539	0.3536	0.3535
	σ_v :	0.0221	0.0179	0.0129	0.01	0.0062	0.0046	0.0015
16	μ_v :	0.355	0.3537	0.3535	0.354	0.3536	0.3535	0.3535
	σ_v :	0.0264	0.0197	0.0148	0.0109	0.0069	0.0057	0.0016
12	μ_v :	0.3522	0.3536	0.3545	0.3536	0.3536	0.3534	0.3536
	σ_v :	0.0339	0.0249	0.0194	0.0142	0.0094	0.007	0.0022
8	μ_v :	0.3545	0.3536	0.3546	0.3549	0.3538	0.3536	0.3535
	σ_v :	0.0527	0.039	0.0296	0.0219	0.0138	0.0116	0.0034

Estimator no.3

		SNR						
lines		0	3	6	10	16	20	24
24	μ_v :	0.3537	0.3541	0.3535	0.3532	0.3535	0.3536	0.3535
	σ_v :	0.0177	0.0141	0.0114	0.008	0.0053	0.0039	0.0012
20	μ_v :	0.3543	0.353	0.3536	0.3537	0.3539	0.3536	0.3535
	σ_v :	0.0198	0.0161	0.0119	0.0093	0.0059	0.0044	0.0014
16	μ_v :	0.3546	0.3539	0.3536	0.354	0.3536	0.3535	0.3535
	σ_v :	0.0233	0.0181	0.014	0.0101	0.0068	0.0056	0.0016
12	μ_v :	0.3519	0.3543	0.3545	0.3534	0.3536	0.3533	0.3536
	σ_v :	0.0292	0.0227	0.017	0.0136	0.0091	0.0069	0.0021
8	μ_v :	0.3522	0.3529	0.3541	0.3544	0.3537	0.3535	0.3535
	σ_v :	0.0437	0.0343	0.0282	0.0207	0.0134	0.0115	0.0033

Estimator no.4

		SNR						
lines		0	3	6	10	16	20	24
24	μ_v :	0.3537	0.3541	0.3535	0.3532	0.3535	0.3536	0.3535
	σ_v :	0.0177	0.0141	0.0114	0.008	0.0053	0.0039	0.0012
20	μ_v :	0.3543	0.353	0.3536	0.3537	0.3539	0.3536	0.3535
	σ_v :	0.0198	0.0161	0.0119	0.0093	0.0059	0.0044	0.0014
16	μ_v :	0.3546	0.3539	0.3536	0.354	0.3536	0.3535	0.3535
	σ_v :	0.0233	0.0181	0.014	0.0101	0.0068	0.0056	0.0016
12	μ_v :	0.3519	0.3543	0.3545	0.3534	0.3536	0.3533	0.3536
	σ_v :	0.0292	0.0227	0.017	0.0136	0.0091	0.0069	0.0021
8	μ_v :	0.3522	0.3529	0.3541	0.3544	0.3537	0.3535	0.3535
	σ_v :	0.0437	0.0343	0.0282	0.0207	0.0134	0.0115	0.0033

D.1.5 Angle of 30 degrees.

Estimator no.1								
		SNR						
lines		0	3	6	10	16	20	24
24	μ_v :	0.249	0.2508	0.2498	0.2502	0.2503	0.2502	0.25
	σ_v :	0.0209	0.0173	0.0133	0.0096	0.0065	0.0053	0.0014
20	μ_v :	0.25	0.2504	0.2505	0.2501	0.2499	0.2499	0.2501
	σ_v :	0.0238	0.0184	0.0143	0.0108	0.0072	0.0055	0.0015
16	μ_v :	0.2516	0.2483	0.2501	0.2496	0.2501	0.2502	0.2501
	σ_v :	0.0281	0.0203	0.0161	0.012	0.0082	0.0064	0.0018
12	μ_v :	0.2505	0.2486	0.2499	0.2507	0.25	0.2499	0.25
	σ_v :	0.032	0.0247	0.018	0.0148	0.0098	0.0078	0.0023
8	μ_v :	0.2512	0.2495	0.25	0.2505	0.2498	0.2494	0.25
	σ_v :	0.0494	0.0384	0.0304	0.0225	0.0154	0.0114	0.0037

Estimator no.2								
		SNR						
lines		0	3	6	10	16	20	24
24	μ_v :	0.2489	0.2507	0.2497	0.2502	0.2503	0.2501	0.25
	σ_v :	0.0207	0.0171	0.0132	0.0096	0.0065	0.0053	0.0014
20	μ_v :	0.25	0.2504	0.2505	0.2501	0.2499	0.2499	0.2501
	σ_v :	0.0238	0.0183	0.0141	0.0108	0.0071	0.0055	0.0015
16	μ_v :	0.2516	0.2484	0.2501	0.2496	0.2501	0.2502	0.2501
	σ_v :	0.0279	0.0202	0.0161	0.0119	0.0082	0.0063	0.0018
12	μ_v :	0.2505	0.2486	0.2499	0.2508	0.25	0.25	0.25
	σ_v :	0.0319	0.0244	0.0179	0.0147	0.0098	0.0077	0.0022
8	μ_v :	0.2512	0.2495	0.2499	0.2505	0.2499	0.2494	0.25
	σ_v :	0.0491	0.0381	0.0302	0.0223	0.0154	0.0113	0.0037

Estimator no.3								
		SNR						
lines		0	3	6	10	16	20	24
24	μ_v :	0.249	0.2505	0.2496	0.25	0.2503	0.2502	0.25
	σ_v :	0.0171	0.0139	0.0106	0.0076	0.0051	0.0039	0.0011
20	μ_v :	0.2511	0.2504	0.2505	0.2499	0.2498	0.2501	0.25
	σ_v :	0.0191	0.0152	0.0114	0.0086	0.0057	0.0043	0.0013
16	μ_v :	0.2512	0.2486	0.2502	0.2496	0.2501	0.25	0.25
	σ_v :	0.0217	0.017	0.0135	0.0096	0.0067	0.0052	0.0014
12	μ_v :	0.2503	0.2485	0.2502	0.2505	0.2502	0.2499	0.2501
	σ_v :	0.0262	0.0212	0.0155	0.0127	0.0083	0.0065	0.0019
8	μ_v :	0.2509	0.2491	0.2505	0.2503	0.2497	0.2494	0.25
	σ_v :	0.0405	0.0321	0.0278	0.02	0.0141	0.0104	0.0034

Estimator no.4								
		SNR						
lines		0	3	6	10	16	20	24
24	μ_v :	0.249	0.2505	0.2496	0.25	0.2503	0.2502	0.25
	σ_v :	0.0171	0.0139	0.0106	0.0076	0.0051	0.0039	0.0011
20	μ_v :	0.2511	0.2504	0.2505	0.2499	0.2498	0.2501	0.25
	σ_v :	0.0191	0.0152	0.0114	0.0086	0.0057	0.0043	0.0013
16	μ_v :	0.2512	0.2486	0.2502	0.2496	0.2501	0.25	0.25
	σ_v :	0.0217	0.017	0.0135	0.0096	0.0067	0.0052	0.0014
12	μ_v :	0.2503	0.2485	0.2502	0.2505	0.2502	0.2499	0.2501
	σ_v :	0.0262	0.0212	0.0155	0.0127	0.0083	0.0065	0.0019
8	μ_v :	0.2509	0.2491	0.2505	0.2503	0.2497	0.2494	0.25
	σ_v :	0.0405	0.0321	0.0278	0.02	0.0141	0.0104	0.0034

D.1.6 Angle of 15 degrees.

Estimator no.1

		SNR						
lines		0	3	6	10	16	20	24
24	μ_v :	0.1287	0.1283	0.1295	0.1295	0.1293	0.1291	0.1295
	σ_v :	0.0249	0.021	0.0163	0.0126	0.008	0.0065	0.0021
20	μ_v :	0.1291	0.13	0.1287	0.1291	0.1297	0.1293	0.1295
	σ_v :	0.0287	0.022	0.0178	0.0135	0.0089	0.0069	0.0022
16	μ_v :	0.1307	0.1307	0.1298	0.1291	0.1294	0.1294	0.1294
	σ_v :	0.0291	0.0255	0.0203	0.0153	0.0101	0.0079	0.0024
12	μ_v :	0.1309	0.1294	0.1301	0.1289	0.1296	0.1301	0.1293
	σ_v :	0.0367	0.0311	0.0244	0.0181	0.0129	0.0098	0.0029
8	μ_v :	0.1281	0.1298	0.1292	0.1297	0.1297	0.1299	0.1294
	σ_v :	0.0554	0.0398	0.0314	0.0266	0.0176	0.0146	0.0044

Estimator no.2

		SNR						
lines		0	3	6	10	16	20	24
24	μ_v :	0.1286	0.1284	0.1295	0.1296	0.1294	0.1291	0.1295
	σ_v :	0.0248	0.0209	0.0161	0.0126	0.008	0.0064	0.0021
20	μ_v :	0.1291	0.1301	0.1287	0.1291	0.1298	0.1292	0.1295
	σ_v :	0.0287	0.022	0.0177	0.0136	0.0089	0.0069	0.0022
16	μ_v :	0.1305	0.1306	0.1298	0.129	0.1294	0.1294	0.1294
	σ_v :	0.029	0.0255	0.0203	0.0152	0.01	0.0079	0.0024
12	μ_v :	0.1309	0.1295	0.13	0.1288	0.1295	0.1302	0.1293
	σ_v :	0.0369	0.0311	0.0242	0.018	0.0129	0.0098	0.003
8	μ_v :	0.1278	0.1297	0.1292	0.1296	0.1297	0.1299	0.1295
	σ_v :	0.0553	0.0399	0.0312	0.0267	0.0175	0.0146	0.0044

Estimator no.3

		SNR						
lines		0	3	6	10	16	20	24
24	μ_v :	0.1284	0.1297	0.1292	0.1294	0.1294	0.1293	0.1294
	σ_v :	0.0147	0.0123	0.0093	0.007	0.0046	0.0036	0.0011
20	μ_v :	0.1284	0.1298	0.129	0.1291	0.1293	0.1293	0.1294
	σ_v :	0.0172	0.0138	0.0103	0.0078	0.005	0.004	0.0012
16	μ_v :	0.1298	0.1299	0.1297	0.1294	0.1295	0.1291	0.1293
	σ_v :	0.0191	0.0152	0.0121	0.0088	0.0062	0.0049	0.0014
12	μ_v :	0.13	0.1288	0.1298	0.1293	0.1293	0.1298	0.1293
	σ_v :	0.0242	0.02	0.0153	0.0117	0.0076	0.0058	0.0018
8	μ_v :	0.1288	0.1294	0.1294	0.1298	0.1292	0.1297	0.1295
	σ_v :	0.0408	0.0311	0.0244	0.0198	0.0136	0.0108	0.0033

Estimator no.4

		SNR						
lines		0	3	6	10	16	20	24
24	μ_v :	0.1284	0.1297	0.1292	0.1294	0.1294	0.1293	0.1294
	σ_v :	0.0147	0.0123	0.0093	0.007	0.0046	0.0036	0.0011
20	μ_v :	0.1284	0.1298	0.129	0.1291	0.1293	0.1293	0.1294
	σ_v :	0.0172	0.0138	0.0103	0.0078	0.005	0.004	0.0012
16	μ_v :	0.1298	0.1299	0.1297	0.1294	0.1295	0.1291	0.1293
	σ_v :	0.0191	0.0152	0.0121	0.0088	0.0062	0.0049	0.0014
12	μ_v :	0.13	0.1288	0.1298	0.1293	0.1293	0.1298	0.1293
	σ_v :	0.0242	0.02	0.0153	0.0117	0.0076	0.0058	0.0018
8	μ_v :	0.1288	0.1294	0.1294	0.1298	0.1292	0.1297	0.1295
	σ_v :	0.0408	0.0311	0.0244	0.0198	0.0136	0.0108	0.0033

D.1.7 Angle of 0 degrees.

Estimator no.1

		SNR						
lines		0	3	6	10	16	20	24
24	μ_v :	0.0004	-0.0007	-0.0003	0.0001	0.0001	-0.0001	0
	σ_v :	0.0133	0.0103	0.0079	0.0057	0.0037	0.0029	0.0008
20	μ_v :	0.0004	-0.0007	0.0001	0.0003	-0.0001	0	0
	σ_v :	0.0148	0.0127	0.0094	0.0071	0.0047	0.0035	0.0011
16	μ_v :	0.0011	-0.0004	-0.0004	0.0002	0	-0.0001	-0.0001
	σ_v :	0.0178	0.0142	0.0113	0.0085	0.0057	0.0043	0.0013
12	μ_v :	0.0009	0.0002	-0.0005	0	-0.0002	-0.0001	0.0001
	σ_v :	0.0243	0.0192	0.0149	0.0112	0.0073	0.0059	0.0017
8	μ_v :	0.0008	-0.0001	-0.0007	-0.0005	0.0002	0.0003	0
	σ_v :	0.0427	0.0316	0.0246	0.0191	0.0135	0.01	0.003

Estimator no.2

		SNR						
lines		0	3	6	10	16	20	24
24	μ_v :	0.0005	-0.0006	-0.0003	0	0.0001	-0.0001	0
	σ_v :	0.0132	0.0103	0.0079	0.0057	0.0036	0.0029	0.0008
20	μ_v :	0.0004	-0.0007	0.0001	0.0003	-0.0001	0	0
	σ_v :	0.0148	0.0126	0.0093	0.007	0.0047	0.0035	0.0011
16	μ_v :	0.0011	-0.0003	-0.0004	0.0002	0	-0.0002	-0.0001
	σ_v :	0.0176	0.0141	0.0112	0.0085	0.0057	0.0043	0.0013
12	μ_v :	0.0009	0.0001	-0.0006	0.0001	-0.0002	-0.0001	0.0001
	σ_v :	0.0241	0.0192	0.0148	0.0111	0.0073	0.0058	0.0017
8	μ_v :	0.001	-0.0001	-0.0008	-0.0006	0.0001	0.0003	0
	σ_v :	0.0426	0.0316	0.0245	0.019	0.0135	0.0099	0.003

Estimator no.3

		SNR						
lines		0	3	6	10	16	20	24
24	μ_v :	0.0004	-0.0006	-0.0003	0	0.0001	-0.0001	0
	σ_v :	0.0132	0.0103	0.0079	0.0057	0.0036	0.0029	0.0008
20	μ_v :	0.0004	-0.0007	0.0001	0.0003	-0.0001	0	0
	σ_v :	0.0147	0.0125	0.0093	0.007	0.0047	0.0035	0.0011
16	μ_v :	0.0012	-0.0003	-0.0004	0.0002	0	-0.0002	-0.0001
	σ_v :	0.0171	0.0141	0.0112	0.0085	0.0057	0.0043	0.0013
12	μ_v :	0.001	0	-0.0006	0.0001	-0.0002	-0.0001	0.0001
	σ_v :	0.0231	0.019	0.0147	0.0111	0.0073	0.0058	0.0017
8	μ_v :	0.001	-0.0001	-0.0007	-0.0006	0.0001	0.0003	0
	σ_v :	0.0385	0.0304	0.0244	0.0191	0.0135	0.0099	0.003

Estimator no.4

		SNR						
lines		0	3	6	10	16	20	24
24	μ_v :	0.0004	-0.0006	-0.0003	0	0.0001	-0.0001	0
	σ_v :	0.0132	0.0103	0.0079	0.0057	0.0036	0.0029	0.0008
20	μ_v :	0.0004	-0.0007	0.0001	0.0003	-0.0001	0	0
	σ_v :	0.0147	0.0125	0.0093	0.007	0.0047	0.0035	0.0011
16	μ_v :	0.0012	-0.0003	-0.0004	0.0002	0	-0.0002	-0.0001
	σ_v :	0.0171	0.0141	0.0112	0.0085	0.0057	0.0043	0.0013
12	μ_v :	0.001	0	-0.0006	0.0001	-0.0002	-0.0001	0.0001
	σ_v :	0.0231	0.019	0.0147	0.0111	0.0073	0.0058	0.0017
8	μ_v :	0.001	-0.0001	-0.0007	-0.0006	0.0001	0.0003	0
	σ_v :	0.0385	0.0304	0.0244	0.0191	0.0135	0.0099	0.003

D.2 Simulated data

D.2.1 Plug flow, angle of 90 degrees

Estimator no.1

		SNR						
lines		0	3	6	10	16	20	24
24	μ_v :	0.4793	0.4826	0.5038	0.5002	0.5024	0.499	0.5038
	σ_v :	0.1886	0.1903	0.1526	0.1593	0.161	0.1531	0.1455
20	μ_v :	0.48	0.4694	0.4638	0.4959	0.4876	0.4801	0.4917
	σ_v :	0.2031	0.1953	0.1833	0.1799	0.1965	0.188	0.1727
16	μ_v :	0.4616	0.4899	0.4594	0.4497	0.4608	0.4526	0.4608
	σ_v :	0.2117	0.2055	0.2135	0.231	0.2204	0.2257	0.2221
12	μ_v :	0.4678	0.4627	0.441	0.4669	0.4557	0.466	0.4611
	σ_v :	0.2258	0.2369	0.2244	0.2085	0.2205	0.2123	0.2182
8	μ_v :	0.3963	0.4511	0.4243	0.4417	0.4666	0.4445	0.4476
	σ_v :	0.345	0.2532	0.2669	0.2365	0.2326	0.2534	0.2362

Estimator no.2

		SNR						
lines		0	3	6	10	16	20	24
24	μ_v :	0.4784	0.482	0.5033	0.4997	0.5019	0.4984	0.5033
	σ_v :	0.1908	0.1915	0.1547	0.1613	0.1631	0.1548	0.1472
20	μ_v :	0.479	0.4687	0.4631	0.4949	0.4871	0.4794	0.4912
	σ_v :	0.2066	0.1964	0.1846	0.1822	0.1971	0.1898	0.1739
16	μ_v :	0.4602	0.4885	0.4586	0.449	0.4604	0.4519	0.4601
	σ_v :	0.214	0.2073	0.2157	0.2323	0.2218	0.2274	0.224
12	μ_v :	0.4672	0.4621	0.4402	0.466	0.4549	0.4648	0.4599
	σ_v :	0.2256	0.2374	0.2264	0.2095	0.2217	0.2144	0.2204
8	μ_v :	0.3962	0.451	0.4228	0.4405	0.4657	0.4434	0.4467
	σ_v :	0.3461	0.2524	0.2684	0.2368	0.2333	0.2546	0.2368

Estimator no.3

		SNR						
lines		0	3	6	10	16	20	24
24	μ_v :	0.4892	0.4907	0.4882	0.4903	0.4886	0.4887	0.4892
	σ_v :	0.0668	0.06	0.0643	0.0579	0.0585	0.0577	0.0569
20	μ_v :	0.4835	0.4854	0.4911	0.4891	0.4895	0.4879	0.4892
	σ_v :	0.0689	0.0614	0.0622	0.0624	0.0624	0.0601	0.0602
16	μ_v :	0.4886	0.4924	0.4864	0.4867	0.4883	0.4879	0.4881
	σ_v :	0.0736	0.0682	0.0684	0.0697	0.0673	0.0666	0.0656
12	μ_v :	0.4946	0.4914	0.4898	0.4924	0.4905	0.4885	0.4891
	σ_v :	0.0843	0.082	0.0763	0.0747	0.0729	0.0736	0.0723
8	μ_v :	0.4843	0.4789	0.485	0.4916	0.4907	0.4902	0.4905
	σ_v :	0.1058	0.1023	0.089	0.088	0.0832	0.0841	0.0802

Estimator no.4

		SNR						
lines		0	3	6	10	16	20	24
24	μ_v :	0.4739	0.4754	0.473	0.4903	0.4886	0.4887	0.4892
	σ_v :	0.1306	0.1309	0.133	0.0579	0.0585	0.0577	0.0569
20	μ_v :	0.4835	0.4728	0.4785	0.4765	0.4769	0.4752	0.4892
	σ_v :	0.0689	0.1255	0.1244	0.1264	0.1262	0.1247	0.0602
16	μ_v :	0.4583	0.4823	0.4662	0.4766	0.4681	0.4778	0.478
	σ_v :	0.1774	0.1195	0.151	0.116	0.1515	0.1145	0.1145
12	μ_v :	0.4189	0.4232	0.4595	0.4318	0.4451	0.4582	0.4512
	σ_v :	0.2648	0.2548	0.1791	0.2396	0.2137	0.1784	0.1977
8	μ_v :	0.3588	0.3886	0.4046	0.4213	0.4154	0.3999	0.4152
	σ_v :	0.327	0.2756	0.272	0.2532	0.2635	0.288	0.2667

D.2.2 Plug flow, angle of 75 degrees

Estimator no.1

		SNR						
lines		0	3	6	10	16	20	24
24	μ_v :	0.4164	0.4118	0.4176	0.4126	0.3992	0.4025	0.4104
	σ_v :	0.1462	0.1514	0.1789	0.1622	0.1615	0.1615	0.1633
20	μ_v :	0.4153	0.3988	0.4195	0.4237	0.409	0.403	0.4144
	σ_v :	0.1935	0.1957	0.179	0.2099	0.1855	0.2056	0.1898
16	μ_v :	0.4173	0.4099	0.4363	0.4194	0.428	0.4151	0.4198
	σ_v :	0.1889	0.1802	0.173	0.1562	0.1593	0.1807	0.1636
12	μ_v :	0.4035	0.4114	0.4039	0.4227	0.4276	0.4244	0.4334
	σ_v :	0.257	0.2318	0.2153	0.1907	0.1911	0.1993	0.1851
8	μ_v :	0.372	0.3798	0.3979	0.3895	0.3858	0.3943	0.4072
	σ_v :	0.3551	0.2775	0.2862	0.2611	0.2468	0.2272	0.2186

Estimator no.2

		SNR						
lines		0	3	6	10	16	20	24
24	μ_v :	0.4162	0.4117	0.4177	0.4124	0.3994	0.4025	0.4104
	σ_v :	0.1456	0.1513	0.1789	0.1625	0.1615	0.1615	0.1634
20	μ_v :	0.4168	0.3986	0.4198	0.424	0.4091	0.4028	0.4144
	σ_v :	0.1943	0.1955	0.1781	0.21	0.1853	0.2058	0.1897
16	μ_v :	0.4169	0.4099	0.4364	0.4192	0.4279	0.4151	0.4198
	σ_v :	0.1882	0.1804	0.1735	0.1562	0.1594	0.1807	0.1637
12	μ_v :	0.4028	0.4108	0.4045	0.4229	0.4275	0.4244	0.4334
	σ_v :	0.2577	0.2322	0.2152	0.1906	0.1911	0.1993	0.1852
8	μ_v :	0.373	0.3801	0.3982	0.3892	0.3858	0.3948	0.4074
	σ_v :	0.3516	0.2765	0.2858	0.261	0.2463	0.2267	0.2187

Estimator no.3

		SNR						
lines		0	3	6	10	16	20	24
24	μ_v :	0.4857	0.4873	0.4898	0.487	0.4866	0.4873	0.4866
	σ_v :	0.07	0.0592	0.061	0.0602	0.0592	0.0585	0.0594
20	μ_v :	0.4781	0.4864	0.4847	0.4864	0.4875	0.4861	0.4858
	σ_v :	0.0711	0.0658	0.0681	0.0642	0.0652	0.0635	0.0637
16	μ_v :	0.4855	0.4889	0.4911	0.4855	0.4865	0.4861	0.4868
	σ_v :	0.0827	0.0743	0.0701	0.0675	0.0683	0.0672	0.0676
12	μ_v :	0.4933	0.4902	0.4867	0.4868	0.4906	0.4891	0.4897
	σ_v :	0.0901	0.0955	0.0849	0.0827	0.0754	0.0776	0.0765
8	μ_v :	0.484	0.4918	0.4894	0.4941	0.4936	0.4931	0.4928
	σ_v :	0.1578	0.1258	0.1051	0.0941	0.091	0.0883	0.086

Estimator no.4

		SNR						
lines		0	3	6	10	16	20	24
24	μ_v :	0.4704	0.4721	0.4746	0.4718	0.4713	0.472	0.4714
	σ_v :	0.1401	0.1342	0.1348	0.133	0.1342	0.1336	0.1342
20	μ_v :	0.4528	0.4737	0.4721	0.4738	0.4749	0.4734	0.4732
	σ_v :	0.1681	0.1276	0.1279	0.1275	0.1283	0.1267	0.1272
16	μ_v :	0.4553	0.4687	0.4608	0.4754	0.4664	0.4659	0.4666
	σ_v :	0.183	0.1562	0.1778	0.1163	0.1537	0.1527	0.153
12	μ_v :	0.4327	0.3841	0.4337	0.4489	0.4527	0.4513	0.4594
	σ_v :	0.2413	0.3094	0.2291	0.2005	0.1936	0.1943	0.1761
8	μ_v :	0.3284	0.3613	0.3941	0.4038	0.4032	0.4077	0.4024
	σ_v :	0.3614	0.3255	0.2878	0.2808	0.2828	0.2758	0.285

D.2.3 Plug flow, angle of 60 degrees

Estimator no.1

lines		SNR 0	3	6	10	16	20	24
24	μ_v :	0.3662	0.3642	0.36	0.3811	0.3572	0.3625	0.3558
	σ_v :	0.2333	0.1794	0.196	0.1875	0.188	0.1897	0.1891
20	μ_v :	0.347	0.315	0.3369	0.3273	0.3339	0.3359	0.3273
	σ_v :	0.2259	0.1957	0.1927	0.1923	0.1936	0.1892	0.1859
16	μ_v :	0.3611	0.3205	0.3075	0.3551	0.3402	0.3483	0.3456
	σ_v :	0.2443	0.231	0.2254	0.1926	0.1946	0.1882	0.1946
12	μ_v :	0.3295	0.359	0.3156	0.3212	0.3471	0.3412	0.3424
	σ_v :	0.2602	0.2318	0.2473	0.2345	0.2103	0.2095	0.2093
8	μ_v :	0.3497	0.2795	0.3062	0.3441	0.3417	0.342	0.342
	σ_v :	0.2716	0.3106	0.2691	0.2476	0.2591	0.2592	0.2649

Estimator no.2

lines		SNR 0	3	6	10	16	20	24
24	μ_v :	0.3655	0.3643	0.36	0.3812	0.3572	0.3625	0.3559
	σ_v :	0.233	0.1797	0.1959	0.1877	0.1878	0.1897	0.1891
20	μ_v :	0.3468	0.3154	0.3369	0.3276	0.3339	0.3359	0.3272
	σ_v :	0.2257	0.1959	0.1928	0.1924	0.1934	0.1893	0.1859
16	μ_v :	0.3606	0.3205	0.3073	0.3551	0.3403	0.3485	0.3456
	σ_v :	0.2438	0.231	0.2255	0.1927	0.1945	0.188	0.1947
12	μ_v :	0.3293	0.3591	0.3161	0.3216	0.347	0.3411	0.3425
	σ_v :	0.2598	0.2319	0.2476	0.234	0.2104	0.2094	0.2092
8	μ_v :	0.3507	0.2798	0.306	0.3436	0.3414	0.342	0.3418
	σ_v :	0.2704	0.3103	0.2698	0.2485	0.2596	0.2585	0.2653

Estimator no.3

lines		SNR 0	3	6	10	16	20	24
24	μ_v :	0.4371	0.4308	0.4285	0.4295	0.4269	0.4291	0.43
	σ_v :	0.0662	0.0595	0.0611	0.0604	0.0611	0.0594	0.059
20	μ_v :	0.428	0.4269	0.4276	0.429	0.4277	0.4293	0.4294
	σ_v :	0.0715	0.0758	0.0681	0.0683	0.0651	0.0645	0.0653
16	μ_v :	0.4308	0.4301	0.4306	0.4309	0.4344	0.4296	0.4311
	σ_v :	0.0843	0.073	0.0744	0.0746	0.0751	0.0713	0.0714
12	μ_v :	0.4389	0.4345	0.4337	0.4318	0.4324	0.4331	0.4326
	σ_v :	0.1003	0.0857	0.0829	0.0812	0.0782	0.0808	0.0792
8	μ_v :	0.4223	0.4317	0.4278	0.4387	0.4347	0.4355	0.4344
	σ_v :	0.1915	0.134	0.1087	0.0972	0.0896	0.0895	0.0883

Estimator no.4

lines		SNR 0	3	6	10	16	20	24
24	μ_v :	0.4371	0.4308	0.4285	0.4295	0.4269	0.4291	0.43
	σ_v :	0.0662	0.0595	0.0611	0.0604	0.0611	0.0594	0.059
20	μ_v :	0.428	0.4269	0.415	0.429	0.4277	0.4293	0.4294
	σ_v :	0.0715	0.0758	0.121	0.0683	0.0651	0.0645	0.0653
16	μ_v :	0.4106	0.42	0.4205	0.4208	0.4243	0.4196	0.421
	σ_v :	0.1487	0.118	0.1153	0.1185	0.1162	0.1147	0.1152
12	μ_v :	0.4086	0.4117	0.4262	0.4167	0.4248	0.4179	0.425
	σ_v :	0.1652	0.1606	0.1104	0.136	0.1077	0.1335	0.1074
8	μ_v :	0.3621	0.3464	0.3927	0.3986	0.4046	0.4054	0.4043
	σ_v :	0.2548	0.2702	0.1829	0.1929	0.1743	0.171	0.1729

D.2.4 Plug flow, angle of 45 degrees

Estimator no.1

		SNR						
lines		0	3	6	10	16	20	24
24	μ_v :	0.3256	0.3113	0.339	0.3414	0.3272	0.3385	0.3417
	σ_v :	0.2095	0.2388	0.2239	0.2061	0.2028	0.212	0.194
20	μ_v :	0.3164	0.308	0.3146	0.321	0.3044	0.3199	0.3117
	σ_v :	0.2554	0.2763	0.2534	0.2787	0.2479	0.235	0.2441
16	μ_v :	0.3403	0.3123	0.3012	0.3271	0.3112	0.302	0.3168
	σ_v :	0.27	0.2243	0.2552	0.2665	0.2528	0.2656	0.2633
12	μ_v :	0.3266	0.3289	0.3054	0.3122	0.2906	0.2926	0.2901
	σ_v :	0.3223	0.2877	0.279	0.2977	0.2757	0.2986	0.2879
8	μ_v :	0.2901	0.2733	0.282	0.2942	0.263	0.2827	0.2854
	σ_v :	0.4197	0.3946	0.3022	0.3236	0.3219	0.2802	0.2905

Estimator no.2

		SNR						
lines		0	3	6	10	16	20	24
24	μ_v :	0.3257	0.3113	0.3391	0.3413	0.3272	0.3384	0.3417
	σ_v :	0.2089	0.2391	0.2233	0.2058	0.2028	0.212	0.194
20	μ_v :	0.3166	0.3078	0.3148	0.321	0.3046	0.3198	0.3117
	σ_v :	0.2558	0.2758	0.253	0.2779	0.2478	0.235	0.2441
16	μ_v :	0.34	0.3124	0.301	0.3269	0.3112	0.3021	0.3167
	σ_v :	0.2702	0.2246	0.2551	0.2664	0.2527	0.2656	0.2633
12	μ_v :	0.3266	0.3287	0.3053	0.312	0.2907	0.2926	0.2901
	σ_v :	0.3223	0.2868	0.2793	0.2975	0.2758	0.2986	0.288
8	μ_v :	0.2909	0.2722	0.2833	0.2944	0.2627	0.2829	0.2853
	σ_v :	0.4199	0.3937	0.302	0.324	0.3222	0.2804	0.2907

Estimator no.3

		SNR						
lines		0	3	6	10	16	20	24
24	μ_v :	0.349	0.3593	0.3567	0.3546	0.3539	0.3533	0.3534
	σ_v :	0.0538	0.0612	0.0572	0.0569	0.0556	0.055	0.0556
20	μ_v :	0.3509	0.3548	0.3561	0.3558	0.3541	0.3544	0.3538
	σ_v :	0.0661	0.0602	0.0606	0.0613	0.0602	0.0587	0.0592
16	μ_v :	0.3472	0.3536	0.3505	0.3517	0.3522	0.3547	0.3527
	σ_v :	0.0839	0.0683	0.0746	0.0638	0.0657	0.0657	0.0647
12	μ_v :	0.3619	0.3561	0.3564	0.3574	0.3538	0.3524	0.3548
	σ_v :	0.089	0.0782	0.0781	0.0727	0.0741	0.0735	0.0728
8	μ_v :	0.3566	0.3548	0.3551	0.355	0.3522	0.3506	0.3527
	σ_v :	0.1066	0.1119	0.0939	0.088	0.0842	0.0814	0.0801

Estimator no.4

		SNR						
lines		0	3	6	10	16	20	24
24	μ_v :	0.349	0.3593	0.3567	0.3546	0.3539	0.3533	0.3534
	σ_v :	0.0538	0.0612	0.0572	0.0569	0.0556	0.055	0.0556
20	μ_v :	0.3509	0.3548	0.3561	0.3558	0.3541	0.3544	0.3538
	σ_v :	0.0661	0.0602	0.0606	0.0613	0.0602	0.0587	0.0592
16	μ_v :	0.3472	0.3536	0.3505	0.3517	0.3522	0.3547	0.3527
	σ_v :	0.0839	0.0683	0.0746	0.0638	0.0657	0.0657	0.0647
12	μ_v :	0.3544	0.3561	0.3564	0.3574	0.3538	0.3524	0.3548
	σ_v :	0.1131	0.0782	0.0781	0.0727	0.0741	0.0735	0.0728
8	μ_v :	0.3466	0.3447	0.3551	0.355	0.3522	0.3506	0.3527
	σ_v :	0.1356	0.1224	0.0939	0.088	0.0842	0.0814	0.0801

D.2.5 Plug flow, angle of 30 degrees

Estimator no.1

		SNR						
lines		0	3	6	10	16	20	24
24	μ_v :	0.2809	0.244	0.2734	0.2505	0.2389	0.2443	0.2465
	σ_v :	0.1193	0.1456	0.1002	0.1222	0.124	0.1259	0.1293
20	μ_v :	0.2425	0.2244	0.2453	0.2277	0.2447	0.2408	0.2482
	σ_v :	0.1833	0.2205	0.145	0.1792	0.1642	0.1778	0.1656
16	μ_v :	0.2403	0.2259	0.2217	0.2517	0.2264	0.2392	0.2352
	σ_v :	0.2383	0.2236	0.1923	0.1773	0.2073	0.1913	0.194
12	μ_v :	0.2311	0.2202	0.2317	0.2442	0.2284	0.2353	0.223
	σ_v :	0.2808	0.2512	0.2249	0.2455	0.231	0.2396	0.251
8	μ_v :	0.2267	0.1856	0.2127	0.2257	0.216	0.2263	0.2252
	σ_v :	0.3035	0.3062	0.274	0.2713	0.2652	0.2608	0.2586

Estimator no.2

		SNR						
lines		0	3	6	10	16	20	24
24	μ_v :	0.2808	0.2437	0.2735	0.2502	0.2389	0.2443	0.2466
	σ_v :	0.1195	0.1456	0.1001	0.1221	0.1241	0.1259	0.1292
20	μ_v :	0.2426	0.2248	0.2454	0.2277	0.2445	0.2406	0.2481
	σ_v :	0.1834	0.2201	0.1446	0.1793	0.1644	0.1781	0.1657
16	μ_v :	0.24	0.2262	0.2214	0.2518	0.2263	0.2391	0.2352
	σ_v :	0.2389	0.2243	0.1923	0.1773	0.2071	0.1914	0.1939
12	μ_v :	0.2308	0.2203	0.2315	0.2444	0.2281	0.2353	0.223
	σ_v :	0.2809	0.2523	0.2254	0.2463	0.2314	0.2397	0.2513
8	μ_v :	0.2265	0.1859	0.2125	0.226	0.216	0.2261	0.2252
	σ_v :	0.3046	0.3064	0.2736	0.2718	0.2652	0.261	0.2589

Estimator no.3

		SNR						
lines		0	3	6	10	16	20	24
24	μ_v :	0.2511	0.2525	0.2525	0.2521	0.2496	0.2508	0.2508
	σ_v :	0.0378	0.034	0.0303	0.0296	0.0269	0.0285	0.0271
20	μ_v :	0.2512	0.2511	0.2511	0.2485	0.2497	0.2507	0.2503
	σ_v :	0.0421	0.0371	0.037	0.0345	0.0333	0.0323	0.032
16	μ_v :	0.2489	0.2489	0.2497	0.2496	0.2504	0.2503	0.2504
	σ_v :	0.0488	0.0453	0.042	0.0392	0.0375	0.0374	0.0358
12	μ_v :	0.2514	0.2471	0.2483	0.2523	0.2503	0.2494	0.2508
	σ_v :	0.0677	0.0526	0.0519	0.0476	0.0437	0.0442	0.0427
8	μ_v :	0.2576	0.2506	0.2538	0.252	0.2511	0.2522	0.2517
	σ_v :	0.095	0.0761	0.0636	0.0638	0.0531	0.0503	0.0491

Estimator no.4

		SNR						
lines		0	3	6	10	16	20	24
24	μ_v :	0.2511	0.2525	0.2525	0.2521	0.2496	0.2508	0.2508
	σ_v :	0.0378	0.034	0.0303	0.0296	0.0269	0.0285	0.0271
20	μ_v :	0.2512	0.2511	0.2511	0.2485	0.2497	0.2507	0.2503
	σ_v :	0.0421	0.0371	0.037	0.0345	0.0333	0.0323	0.032
16	μ_v :	0.2489	0.2489	0.2497	0.2496	0.2504	0.2503	0.2504
	σ_v :	0.0488	0.0453	0.042	0.0392	0.0375	0.0374	0.0358
12	μ_v :	0.2514	0.2471	0.2483	0.2523	0.2503	0.2494	0.2508
	σ_v :	0.0677	0.0526	0.0519	0.0476	0.0437	0.0442	0.0427
8	μ_v :	0.2576	0.2506	0.2538	0.252	0.2511	0.2522	0.2517
	σ_v :	0.095	0.0761	0.0636	0.0638	0.0531	0.0503	0.0491

D.2.6 Parabolic flow, angle of 90 degrees

Estimator no.1

		SNR						
lines		0	3	6	10	16	20	24
24	μ_v :	0.3385	0.3103	0.3498	0.3418	0.3437	0.3555	0.3516
	σ_v :	0.2923	0.3215	0.2745	0.2872	0.28	0.2731	0.2583
20	μ_v :	0.3409	0.3519	0.3296	0.3574	0.3597	0.3624	0.3721
	σ_v :	0.28	0.2861	0.2833	0.2526	0.258	0.2528	0.2466
16	μ_v :	0.359	0.3373	0.3763	0.3904	0.3835	0.3793	0.3881
	σ_v :	0.2487	0.2674	0.2451	0.2363	0.2342	0.2372	0.2314
12	μ_v :	0.3768	0.3629	0.3907	0.4024	0.3774	0.3578	0.4004
	σ_v :	0.2539	0.2546	0.2314	0.2218	0.2389	0.2481	0.213
8	μ_v :	0.3918	0.3921	0.398	0.3909	0.3997	0.3955	0.3812
	σ_v :	0.2132	0.2238	0.2087	0.2114	0.2076	0.2157	0.2249

Estimator no.2

		SNR						
lines		0	3	6	10	16	20	24
24	μ_v :	0.3387	0.3098	0.3488	0.341	0.344	0.3547	0.3511
	σ_v :	0.2913	0.3219	0.276	0.2864	0.2816	0.2728	0.2581
20	μ_v :	0.3394	0.3511	0.3289	0.357	0.3592	0.3616	0.3713
	σ_v :	0.2798	0.2857	0.2831	0.2523	0.2575	0.2529	0.2466
16	μ_v :	0.3584	0.3365	0.3761	0.3897	0.3828	0.3785	0.3876
	σ_v :	0.25	0.267	0.245	0.2365	0.2343	0.2375	0.2308
12	μ_v :	0.3759	0.3628	0.3901	0.4018	0.3769	0.3574	0.3997
	σ_v :	0.254	0.2539	0.232	0.2215	0.2385	0.2479	0.2129
8	μ_v :	0.3909	0.3913	0.3971	0.3904	0.3993	0.3951	0.3809
	σ_v :	0.2138	0.2239	0.2093	0.2117	0.2078	0.2159	0.2244

Estimator no.3

		SNR						
lines		0	3	6	10	16	20	24
24	μ_v :	0.4193	0.4186	0.4167	0.423	0.4242	0.4229	0.4217
	σ_v :	0.1293	0.1044	0.1153	0.0934	0.0933	0.0884	0.0886
20	μ_v :	0.4245	0.422	0.4163	0.4206	0.4177	0.4198	0.4191
	σ_v :	0.0956	0.0987	0.0813	0.0826	0.076	0.0782	0.0777
16	μ_v :	0.4185	0.4197	0.4181	0.4131	0.4142	0.416	0.4169
	σ_v :	0.0814	0.0811	0.0697	0.069	0.07	0.0685	0.0687
12	μ_v :	0.4172	0.4182	0.4166	0.416	0.4156	0.4171	0.4156
	σ_v :	0.0683	0.0707	0.0666	0.062	0.0605	0.0617	0.061
8	μ_v :	0.4141	0.4149	0.4167	0.418	0.4161	0.4165	0.4166
	σ_v :	0.0694	0.0646	0.0586	0.0597	0.0578	0.0589	0.0579

Estimator no.4

		SNR						
lines		0	3	6	10	16	20	24
24	μ_v :	0.344	0.3734	0.3614	0.3979	0.3991	0.3978	0.4066
	σ_v :	0.2452	0.2081	0.2121	0.1599	0.1585	0.163	0.1347
20	μ_v :	0.379	0.3993	0.4087	0.4054	0.4102	0.4198	0.4115
	σ_v :	0.2021	0.1529	0.1125	0.1332	0.1087	0.0782	0.1099
16	μ_v :	0.4084	0.3996	0.4181	0.4131	0.4041	0.416	0.4068
	σ_v :	0.1161	0.1433	0.0697	0.069	0.113	0.0685	0.1143
12	μ_v :	0.4172	0.4055	0.4166	0.416	0.4156	0.4171	0.4156
	σ_v :	0.0683	0.1225	0.0666	0.062	0.0605	0.0617	0.061
8	μ_v :	0.3989	0.4149	0.4167	0.418	0.4161	0.4165	0.4166
	σ_v :	0.131	0.0646	0.0586	0.0597	0.0578	0.0589	0.0579

D.2.7 Parabolic flow, angle of 75 degrees

Estimator no.1

		SNR						
lines		0	3	6	10	16	20	24
24	μ_v :	0.3308	0.3117	0.2791	0.2928	0.3055	0.3151	0.3135
	σ_v :	0.3396	0.2964	0.3001	0.3083	0.2836	0.3031	0.2886
20	μ_v :	0.3012	0.3052	0.2976	0.3195	0.3142	0.3148	0.3244
	σ_v :	0.232	0.2571	0.2465	0.2294	0.2378	0.2341	0.2384
16	μ_v :	0.2985	0.3097	0.2971	0.2885	0.2992	0.3048	0.3083
	σ_v :	0.2838	0.2385	0.2094	0.2186	0.2033	0.2104	0.204
12	μ_v :	0.3213	0.2964	0.2976	0.287	0.2926	0.2951	0.2853
	σ_v :	0.1828	0.207	0.1812	0.2002	0.1962	0.1964	0.1999
8	μ_v :	0.3315	0.287	0.3072	0.3092	0.3054	0.303	0.3078
	σ_v :	0.1797	0.2052	0.1872	0.1798	0.1806	0.1865	0.1818

Estimator no.2

		SNR						
lines		0	3	6	10	16	20	24
24	μ_v :	0.3297	0.3127	0.2793	0.2935	0.3061	0.3155	0.3137
	σ_v :	0.3409	0.2963	0.3001	0.308	0.2829	0.3019	0.288
20	μ_v :	0.3018	0.3059	0.2984	0.3198	0.3142	0.3151	0.3247
	σ_v :	0.2325	0.2572	0.2464	0.2292	0.2375	0.2339	0.2383
16	μ_v :	0.2986	0.3103	0.2973	0.2885	0.2992	0.305	0.3083
	σ_v :	0.2831	0.2386	0.2094	0.2189	0.2033	0.2104	0.2042
12	μ_v :	0.321	0.2972	0.2973	0.2869	0.2926	0.2951	0.2852
	σ_v :	0.1832	0.2061	0.1811	0.2005	0.1961	0.1961	0.1998
8	μ_v :	0.3312	0.2877	0.3069	0.3094	0.3056	0.3032	0.3079
	σ_v :	0.1795	0.2052	0.187	0.1793	0.1809	0.1865	0.1816

Estimator no.3

		SNR						
lines		0	3	6	10	16	20	24
24	μ_v :	0.3636	0.3804	0.3722	0.38	0.3806	0.3736	0.3731
	σ_v :	0.2393	0.2456	0.2102	0.2063	0.2088	0.1991	0.2025
20	μ_v :	0.3635	0.3636	0.3621	0.3641	0.3704	0.3649	0.3675
	σ_v :	0.1611	0.159	0.1545	0.1529	0.1561	0.1544	0.1535
16	μ_v :	0.3628	0.3724	0.3651	0.3651	0.3633	0.366	0.3655
	σ_v :	0.1434	0.1318	0.1369	0.1363	0.1337	0.1342	0.1322
12	μ_v :	0.3598	0.365	0.3626	0.3633	0.3634	0.3631	0.3627
	σ_v :	0.1101	0.1198	0.1153	0.1221	0.1169	0.119	0.1183
8	μ_v :	0.3741	0.3688	0.3691	0.3679	0.3665	0.3666	0.3684
	σ_v :	0.1157	0.1236	0.111	0.1119	0.1143	0.1135	0.1118

Estimator no.4

		SNR						
lines		0	3	6	10	16	20	24
24	μ_v :	0.2782	0.2649	0.2618	0.2595	0.245	0.2682	0.2777
	σ_v :	0.2695	0.2937	0.2969	0.2937	0.3113	0.2872	0.279
20	μ_v :	0.3105	0.303	0.3167	0.3186	0.3022	0.3043	0.3144
	σ_v :	0.2366	0.245	0.227	0.2217	0.2547	0.2434	0.2346
16	μ_v :	0.3023	0.3421	0.3247	0.3147	0.3129	0.3156	0.3151
	σ_v :	0.2379	0.192	0.2077	0.2192	0.2234	0.223	0.2219
12	μ_v :	0.3598	0.3398	0.35	0.3254	0.3382	0.3379	0.3374
	σ_v :	0.1101	0.1736	0.1423	0.1979	0.1723	0.1748	0.1732
8	μ_v :	0.3588	0.3383	0.3538	0.3526	0.336	0.3514	0.3531
	σ_v :	0.1512	0.185	0.1475	0.1484	0.1795	0.1496	0.1473

D.2.8 Parabolic flow, angle of 60 degrees

Estimator no.1

		SNR						
lines		0	3	6	10	16	20	24
24	μ_v :	0.2684	0.269	0.3059	0.2803	0.298	0.2823	0.2847
	σ_v :	0.5113	0.4999	0.4486	0.4405	0.4427	0.4233	0.4197
20	μ_v :	0.3112	0.3192	0.3265	0.3301	0.3397	0.3262	0.3282
	σ_v :	0.3651	0.3204	0.368	0.3128	0.3115	0.2946	0.299
16	μ_v :	0.3464	0.3111	0.3215	0.3185	0.2946	0.2939	0.2929
	σ_v :	0.3481	0.2965	0.3377	0.3101	0.3932	0.3916	0.3889
12	μ_v :	0.3402	0.3275	0.3394	0.2975	0.2997	0.3112	0.3014
	σ_v :	0.2809	0.2977	0.2223	0.3983	0.3829	0.3341	0.3355
8	μ_v :	0.3388	0.3614	0.3471	0.3202	0.3358	0.3373	0.351
	σ_v :	0.2694	0.2521	0.2508	0.2221	0.2257	0.2298	0.2407

Estimator no.2

		SNR						
lines		0	3	6	10	16	20	24
24	μ_v :	0.2687	0.2682	0.3049	0.2794	0.299	0.2822	0.2848
	σ_v :	0.509	0.4976	0.4481	0.4414	0.4437	0.4238	0.4195
20	μ_v :	0.3108	0.3189	0.3262	0.3303	0.3398	0.3258	0.328
	σ_v :	0.3642	0.321	0.3672	0.314	0.3116	0.2951	0.2996
16	μ_v :	0.3461	0.3101	0.3218	0.3188	0.2942	0.2938	0.2929
	σ_v :	0.3443	0.2926	0.3384	0.3091	0.3947	0.3911	0.3878
12	μ_v :	0.3401	0.3269	0.3393	0.298	0.2996	0.3112	0.3013
	σ_v :	0.2801	0.2976	0.2217	0.3965	0.3833	0.3342	0.336
8	μ_v :	0.3386	0.3605	0.3468	0.3201	0.3354	0.3372	0.3509
	σ_v :	0.2704	0.2525	0.2503	0.2221	0.2259	0.2301	0.241

Estimator no.3

		SNR						
lines		0	3	6	10	16	20	24
24	μ_v :	0.3311	0.3583	0.3105	0.3391	0.3432	0.354	0.3449
	σ_v :	0.3771	0.3851	0.4031	0.3889	0.3822	0.3819	0.3804
20	μ_v :	0.3684	0.3816	0.3719	0.3805	0.3812	0.3642	0.3685
	σ_v :	0.2869	0.2671	0.2589	0.2527	0.2514	0.2727	0.2547
16	μ_v :	0.3809	0.372	0.3703	0.3694	0.3674	0.3696	0.3709
	σ_v :	0.2189	0.227	0.2163	0.2135	0.2186	0.2177	0.2177
12	μ_v :	0.379	0.375	0.3805	0.3764	0.3785	0.3749	0.3748
	σ_v :	0.2038	0.2065	0.1954	0.1966	0.2007	0.1984	0.1978
8	μ_v :	0.3722	0.3765	0.37	0.3679	0.3701	0.3708	0.3704
	σ_v :	0.1768	0.18	0.1774	0.1755	0.1724	0.1732	0.1711

Estimator no.4

		SNR						
lines		0	3	6	10	16	20	24
24	μ_v :	0.1102	0.1173	0.1097	0.1132	0.1173	0.103	0.1139
	σ_v :	0.3553	0.3498	0.356	0.3544	0.3546	0.3549	0.3574
20	μ_v :	0.1865	0.1619	0.1825	0.1987	0.1767	0.2126	0.1791
	σ_v :	0.3252	0.3479	0.3344	0.3238	0.3397	0.3171	0.3398
16	μ_v :	0.2297	0.2006	0.2392	0.2182	0.2465	0.2184	0.2197
	σ_v :	0.3151	0.3326	0.3039	0.3174	0.2978	0.3191	0.32
12	μ_v :	0.2148	0.2362	0.2416	0.2375	0.227	0.236	0.2359
	σ_v :	0.3239	0.2972	0.2956	0.2952	0.3088	0.3002	0.299
8	μ_v :	0.2807	0.285	0.2786	0.2765	0.2787	0.2794	0.2789
	σ_v :	0.2664	0.2704	0.2652	0.2647	0.2657	0.266	0.2661

D.2.9 Parabolic flow, angle of 45 degrees

Estimator no.1

lines		SNR 0	3	6	10	16	20	24
24	μ_v :	0.2093	0.2221	0.2506	0.2278	0.214	0.2271	0.235
	σ_v :	0.8011	0.7079	0.7103	0.7228	0.7224	0.7179	0.7308
20	μ_v :	0.2481	0.248	0.2512	0.1966	0.237	0.2413	0.2301
	σ_v :	0.5897	0.5997	0.5754	0.5753	0.5452	0.5719	0.5746
16	μ_v :	0.2505	0.2337	0.244	0.276	0.1968	0.1465	0.1868
	σ_v :	0.566	0.5059	0.5329	0.5554	0.5637	0.5945	0.5894
12	μ_v :	0.1975	0.2702	0.2511	0.2172	0.2413	0.2428	0.2225
	σ_v :	0.454	0.4636	0.4286	0.4728	0.4777	0.4641	0.4592
8	μ_v :	0.3136	0.2933	0.2786	0.3205	0.3044	0.2485	0.3141
	σ_v :	0.4304	0.414	0.3429	0.4089	0.3001	0.4133	0.2968

Estimator no.2

lines		SNR 0	3	6	10	16	20	24
24	μ_v :	0.1993	0.2325	0.2507	0.2175	0.2132	0.2261	0.2342
	σ_v :	0.79	0.6882	0.7092	0.7085	0.7223	0.7162	0.7305
20	μ_v :	0.2478	0.2316	0.2507	0.1976	0.2378	0.2412	0.2303
	σ_v :	0.5884	0.5744	0.5735	0.5758	0.5448	0.5714	0.574
16	μ_v :	0.2508	0.2338	0.2438	0.2757	0.1769	0.1463	0.1873
	σ_v :	0.5644	0.507	0.5341	0.5554	0.5262	0.596	0.5903
12	μ_v :	0.1983	0.2698	0.2517	0.2168	0.2408	0.2428	0.2224
	σ_v :	0.4565	0.4629	0.429	0.4729	0.478	0.4642	0.4595
8	μ_v :	0.3125	0.2628	0.2789	0.3207	0.3045	0.2491	0.3143
	σ_v :	0.4297	0.3346	0.3424	0.4087	0.2999	0.4132	0.297

Estimator no.3

lines		SNR 0	3	6	10	16	20	24
24	μ_v :	0.1947	0.2469	0.2527	0.2129	0.2229	0.2276	0.2407
	σ_v :	0.5474	0.5272	0.5016	0.5263	0.5188	0.5145	0.5084
20	μ_v :	0.2888	0.2675	0.2781	0.3061	0.2975	0.2775	0.2749
	σ_v :	0.4179	0.42	0.4178	0.4059	0.3903	0.4154	0.4036
16	μ_v :	0.3195	0.3047	0.2964	0.296	0.2949	0.2961	0.2955
	σ_v :	0.3648	0.36	0.3458	0.358	0.3573	0.3533	0.3531
12	μ_v :	0.2983	0.3205	0.3119	0.3234	0.3239	0.3232	0.3236
	σ_v :	0.3159	0.2722	0.2932	0.293	0.2815	0.2819	0.2804
8	μ_v :	0.3264	0.3252	0.3255	0.3255	0.3215	0.325	0.3248
	σ_v :	0.2457	0.2594	0.243	0.247	0.2491	0.245	0.2483

Estimator no.4

lines		SNR 0	3	6	10	16	20	24
24	μ_v :	0.0993	0.0813	0.082	0.0824	0.0723	0.1021	0.1001
	σ_v :	0.344	0.3628	0.3554	0.3497	0.3522	0.3432	0.3456
20	μ_v :	0.0843	0.0706	0.0963	0.0789	0.1081	0.0654	0.0931
	σ_v :	0.353	0.3608	0.3567	0.3644	0.3583	0.3651	0.3612
16	μ_v :	0.1381	0.1333	0.1351	0.1448	0.1437	0.1449	0.1443
	σ_v :	0.3664	0.3534	0.3425	0.3473	0.3501	0.3458	0.3455
12	μ_v :	0.1468	0.1311	0.1478	0.1592	0.1598	0.1591	0.1468
	σ_v :	0.3265	0.3404	0.3213	0.3289	0.3251	0.3239	0.3315
8	μ_v :	0.1587	0.1727	0.1425	0.1731	0.1843	0.1573	0.1723
	σ_v :	0.3378	0.3206	0.3405	0.3255	0.3216	0.3321	0.3258

D.2.10 Parabolic flow, angle of 30 degrees

Estimator no.1

lines		SNR 0	3	6	10	16	20	24
24	μ_v :	0.0979	0.1042	0.1762	0.1276	0.1496	0.1653	0.13
	σ_v :	0.855	0.8954	0.8564	0.8813	0.9442	0.8992	0.8694
20	μ_v :	0.1755	0.2032	0.2693	0.2095	0.2056	0.2178	0.214
	σ_v :	0.7563	0.7661	0.7881	0.759	0.6993	0.6625	0.6936
16	μ_v :	0.2191	0.259	0.2198	0.2266	0.2322	0.2239	0.2174
	σ_v :	0.7653	0.6748	0.5686	0.631	0.713	0.6545	0.7049
12	μ_v :	0.2607	0.249	0.2467	0.2741	0.2171	0.2339	0.2591
	σ_v :	0.5979	0.6238	0.6111	0.679	0.6837	0.7116	0.6981
8	μ_v :	0.2851	0.2763	0.2162	0.2471	0.2306	0.2894	0.2724
	σ_v :	0.6412	0.6585	0.658	0.682	0.6078	0.6393	0.6261

Estimator no.2

lines		SNR 0	3	6	10	16	20	24
24	μ_v :	0.0956	0.1029	0.1781	0.1287	0.1698	0.1649	0.1313
	σ_v :	0.8503	0.891	0.8575	0.8782	0.9409	0.8992	0.8688
20	μ_v :	0.1754	0.2144	0.2675	0.2077	0.2057	0.2172	0.2142
	σ_v :	0.7589	0.7398	0.7784	0.7584	0.6984	0.6626	0.6931
16	μ_v :	0.2201	0.2589	0.22	0.2261	0.2325	0.2237	0.2172
	σ_v :	0.7567	0.6702	0.5683	0.6307	0.7137	0.6549	0.7053
12	μ_v :	0.2633	0.2496	0.2469	0.2754	0.2176	0.2343	0.2594
	σ_v :	0.5989	0.625	0.6137	0.6796	0.6835	0.7124	0.6985
8	μ_v :	0.287	0.2761	0.2161	0.2468	0.2297	0.2896	0.2724
	σ_v :	0.6376	0.6592	0.6526	0.6818	0.608	0.6389	0.6257

Estimator no.3

lines		SNR 0	3	6	10	16	20	24
24	μ_v :	0.1797	0.1258	0.1686	0.1624	0.1771	0.1601	0.1676
	σ_v :	0.4975	0.5003	0.4874	0.4919	0.4861	0.4843	0.4873
20	μ_v :	0.1775	0.2196	0.1778	0.1961	0.1856	0.1902	0.1883
	σ_v :	0.4423	0.4084	0.4259	0.4096	0.4097	0.4083	0.4107
16	μ_v :	0.1729	0.2218	0.1901	0.1915	0.1967	0.196	0.1943
	σ_v :	0.3808	0.3231	0.3438	0.3391	0.3314	0.331	0.3364
12	μ_v :	0.203	0.1963	0.2088	0.2023	0.2007	0.1981	0.1987
	σ_v :	0.2974	0.3069	0.2754	0.2869	0.2808	0.2859	0.2872
8	μ_v :	0.2145	0.2036	0.1984	0.2018	0.207	0.2061	0.2065
	σ_v :	0.2628	0.2461	0.2587	0.2424	0.2453	0.2452	0.2432

Estimator no.4

lines		SNR 0	3	6	10	16	20	24
24	μ_v :	0.0542	0.0656	0.0632	0.0771	0.0817	0.0748	0.0621
	σ_v :	0.3623	0.3511	0.35	0.353	0.3436	0.3521	0.3481
20	μ_v :	0.0942	0.0832	0.0717	0.0976	0.0947	0.0842	0.0746
	σ_v :	0.3367	0.3408	0.3385	0.3358	0.3294	0.3359	0.3374
16	μ_v :	0.1426	0.0908	0.1095	0.1512	0.1261	0.1254	0.1338
	σ_v :	0.2948	0.3254	0.3115	0.2955	0.3076	0.31	0.3065
12	μ_v :	0.1273	0.1584	0.133	0.1518	0.1502	0.1476	0.1608
	σ_v :	0.3057	0.2809	0.294	0.2909	0.293	0.2943	0.2826
8	μ_v :	0.1383	0.1732	0.1526	0.156	0.1613	0.1756	0.1608
	σ_v :	0.2782	0.2623	0.2767	0.2631	0.2643	0.2559	0.2629

D.3 Experimental data

D.3.1 Angle of 90 degrees

Estimator no.1								
		SNR						
lines		0	3	6	10	16	20	24
24	μ_v :	0.3163	0.2751	0.3012	0.2715	0.3009	0.2863	0.2915
	σ_v :	0.1821	0.2441	0.1866	0.2211	0.1859	0.1953	0.1864
20	μ_v :	0.3242	0.3157	0.3083	0.3342	0.3061	0.3054	0.3117
	σ_v :	0.1718	0.1742	0.1423	0.1221	0.1429	0.1473	0.1482
16	μ_v :	0.3302	0.3225	0.3437	0.3307	0.3177	0.3228	0.3243
	σ_v :	0.1647	0.1296	0.1238	0.1516	0.1396	0.1305	0.1326
12	μ_v :	0.31	0.3161	0.3068	0.3126	0.3174	0.3191	0.3095
	σ_v :	0.1365	0.1291	0.1378	0.1321	0.145	0.1475	0.1415
8	μ_v :	0.3114	0.3278	0.3147	0.3154	0.3037	0.2981	0.3039
	σ_v :	0.139	0.1549	0.1347	0.1506	0.1467	0.1502	0.1488

Estimator no.2								
		SNR						
lines		0	3	6	10	16	20	24
24	μ_v :	0.3167	0.2761	0.301	0.2718	0.3005	0.2868	0.2913
	σ_v :	0.1836	0.2426	0.187	0.2211	0.1868	0.1952	0.1864
20	μ_v :	0.3228	0.3153	0.3078	0.3337	0.3058	0.3049	0.3112
	σ_v :	0.1739	0.1747	0.1423	0.123	0.1438	0.1486	0.1491
16	μ_v :	0.3296	0.3213	0.3439	0.3303	0.3174	0.3223	0.3238
	σ_v :	0.1651	0.1312	0.1248	0.151	0.1394	0.1313	0.1338
12	μ_v :	0.3105	0.3153	0.3064	0.3121	0.317	0.3188	0.3092
	σ_v :	0.1358	0.1303	0.1383	0.1331	0.1454	0.148	0.142
8	μ_v :	0.3113	0.328	0.3146	0.3146	0.3033	0.2979	0.3035
	σ_v :	0.1398	0.1561	0.1352	0.1517	0.1485	0.1517	0.1504

Estimator no.3								
		SNR						
lines		0	3	6	10	16	20	24
24	μ_v :	0.394	0.3995	0.4019	0.3987	0.3962	0.3989	0.4008
	σ_v :	0.1041	0.0994	0.098	0.0986	0.0879	0.0839	0.0825
20	μ_v :	0.4026	0.4062	0.3963	0.4017	0.3965	0.396	0.3983
	σ_v :	0.0804	0.0799	0.0785	0.0757	0.0693	0.0696	0.0722
16	μ_v :	0.3816	0.3891	0.3938	0.3962	0.3976	0.3939	0.3944
	σ_v :	0.0697	0.0567	0.0511	0.0631	0.0608	0.0562	0.0586
12	μ_v :	0.3758	0.3888	0.3853	0.3889	0.3918	0.3909	0.3911
	σ_v :	0.0587	0.056	0.0583	0.0553	0.0498	0.0476	0.0503
8	μ_v :	0.3888	0.3927	0.3927	0.39	0.3934	0.3907	0.3921
	σ_v :	0.0542	0.0467	0.0514	0.0511	0.0498	0.0502	0.0487

Estimator no.4								
		SNR						
lines		0	3	6	10	16	20	24
24	μ_v :	0.3018	0.3257	0.3281	0.3434	0.3408	0.3436	0.3454
	σ_v :	0.2576	0.216	0.2244	0.1917	0.1932	0.1958	0.2004
20	μ_v :	0.3463	0.378	0.3401	0.3454	0.3403	0.3398	0.3421
	σ_v :	0.2163	0.151	0.2106	0.2057	0.2139	0.2124	0.2103
16	μ_v :	0.3816	0.3891	0.3938	0.3962	0.3976	0.3939	0.3944
	σ_v :	0.0697	0.0567	0.0511	0.0631	0.0608	0.0562	0.0586
12	μ_v :	0.3758	0.3888	0.3853	0.3889	0.3918	0.3909	0.3911
	σ_v :	0.0587	0.056	0.0583	0.0553	0.0498	0.0476	0.0503
8	μ_v :	0.3888	0.3927	0.3927	0.39	0.3934	0.3907	0.3921
	σ_v :	0.0542	0.0467	0.0514	0.0511	0.0498	0.0502	0.0487

D.3.2 Angle of 75 degrees

Estimator no.1								
		SNR						
lines		0	3	6	10	16	20	24
24	μ_v :	0.2453	0.2908	0.2513	0.2623	0.2648	0.2669	0.2635
	σ_v :	0.3338	0.2076	0.2075	0.1884	0.2053	0.1846	0.1931
20	μ_v :	0.2516	0.2872	0.2525	0.2262	0.2268	0.2309	0.2358
	σ_v :	0.1933	0.1509	0.1987	0.2006	0.2032	0.1959	0.1835
16	μ_v :	0.2391	0.2522	0.2637	0.2295	0.2523	0.2427	0.2222
	σ_v :	0.2375	0.1904	0.2028	0.2232	0.2051	0.2059	0.2118
12	μ_v :	0.3055	0.2455	0.2932	0.2418	0.2407	0.2582	0.2424
	σ_v :	0.2035	0.2138	0.1894	0.2092	0.2055	0.1885	0.2061
8	μ_v :	0.3052	0.2519	0.2209	0.2168	0.2469	0.2407	0.2461
	σ_v :	0.1795	0.1787	0.1987	0.2025	0.202	0.212	0.2019

Estimator no.2								
		SNR						
lines		0	3	6	10	16	20	24
24	μ_v :	0.247	0.2916	0.2512	0.2621	0.2644	0.267	0.2633
	σ_v :	0.3347	0.2076	0.2065	0.1889	0.205	0.185	0.1937
20	μ_v :	0.2499	0.2864	0.2511	0.225	0.2262	0.2303	0.2355
	σ_v :	0.1933	0.1509	0.1995	0.2017	0.2039	0.1963	0.1839
16	μ_v :	0.2383	0.2529	0.264	0.2296	0.252	0.2425	0.2222
	σ_v :	0.2371	0.1902	0.2023	0.2231	0.2054	0.2062	0.2118
12	μ_v :	0.3054	0.2452	0.2937	0.2414	0.2406	0.2578	0.2423
	σ_v :	0.2024	0.2132	0.189	0.2086	0.2056	0.1884	0.2062
8	μ_v :	0.3052	0.2521	0.2212	0.2164	0.247	0.2404	0.2459
	σ_v :	0.1795	0.1792	0.1991	0.2027	0.2017	0.2124	0.2022

Estimator no.3								
		SNR						
lines		0	3	6	10	16	20	24
24	μ_v :	0.3937	0.3681	0.3904	0.3685	0.3758	0.3782	0.3769
	σ_v :	0.1286	0.0894	0.0955	0.0891	0.0799	0.0744	0.0723
20	μ_v :	0.3532	0.3645	0.3687	0.3712	0.3772	0.3731	0.374
	σ_v :	0.0857	0.0834	0.0769	0.0669	0.0664	0.0617	0.0621
16	μ_v :	0.3566	0.3813	0.3766	0.3698	0.3698	0.3688	0.369
	σ_v :	0.0845	0.0564	0.062	0.0506	0.0543	0.0556	0.0501
12	μ_v :	0.383	0.3723	0.3611	0.3629	0.3682	0.3666	0.3671
	σ_v :	0.0584	0.0533	0.0566	0.0532	0.0519	0.05	0.0473
8	μ_v :	0.3648	0.3823	0.3678	0.367	0.3663	0.3702	0.3673
	σ_v :	0.0637	0.0345	0.049	0.0436	0.0506	0.0458	0.0457

Estimator no.4								
		SNR						
lines		0	3	6	10	16	20	24
24	μ_v :	0.3162	0.3293	0.3517	0.3491	0.3564	0.3588	0.3575
	σ_v :	0.2192	0.1832	0.166	0.1409	0.1357	0.136	0.1385
20	μ_v :	0.3532	0.3645	0.3687	0.3712	0.3475	0.3731	0.374
	σ_v :	0.0857	0.0834	0.0769	0.0669	0.161	0.0617	0.0621
16	μ_v :	0.3566	0.3813	0.3766	0.3698	0.3698	0.3688	0.369
	σ_v :	0.0845	0.0564	0.062	0.0506	0.0543	0.0556	0.0501
12	μ_v :	0.383	0.3723	0.3611	0.3629	0.3682	0.3666	0.3671
	σ_v :	0.0584	0.0533	0.0566	0.0532	0.0519	0.05	0.0473
8	μ_v :	0.3648	0.3823	0.3678	0.367	0.3663	0.3702	0.3673
	σ_v :	0.0637	0.0345	0.049	0.0436	0.0506	0.0458	0.0457

D.3.3 Angle of 60 degrees

Estimator no.1

		SNR						
lines		0	3	6	10	16	20	24
24	μ_v :	0.1778	0.2467	0.2211	0.2161	0.2332	0.252	0.2487
	σ_v :	0.2263	0.179	0.205	0.1827	0.1692	0.1578	0.1623
20	μ_v :	0.2183	0.2201	0.2588	0.2315	0.2498	0.2386	0.2485
	σ_v :	0.1615	0.1288	0.1752	0.146	0.1461	0.1528	0.155
16	μ_v :	0.2235	0.273	0.2295	0.2351	0.2477	0.2301	0.2193
	σ_v :	0.2068	0.1625	0.141	0.1477	0.1394	0.1348	0.1369
12	μ_v :	0.2444	0.2204	0.1927	0.2291	0.1987	0.1941	0.2176
	σ_v :	0.1744	0.1798	0.1609	0.1393	0.1705	0.1686	0.1506
8	μ_v :	0.2245	0.2211	0.2251	0.2423	0.2213	0.2207	0.2295
	σ_v :	0.1517	0.1509	0.1629	0.1509	0.1641	0.1634	0.1669

Estimator no.2

		SNR						
lines		0	3	6	10	16	20	24
24	μ_v :	0.1785	0.2474	0.2202	0.2165	0.2335	0.2518	0.2486
	σ_v :	0.2262	0.179	0.2044	0.1826	0.1689	0.1578	0.1623
20	μ_v :	0.2177	0.2198	0.2591	0.231	0.2497	0.2383	0.2482
	σ_v :	0.1611	0.1289	0.1755	0.1463	0.1464	0.1532	0.1553
16	μ_v :	0.2238	0.2728	0.23	0.2352	0.2476	0.2302	0.2191
	σ_v :	0.2067	0.1624	0.1414	0.1479	0.1396	0.1349	0.137
12	μ_v :	0.2446	0.2207	0.1924	0.2291	0.1987	0.194	0.2175
	σ_v :	0.1749	0.1798	0.1615	0.1399	0.1706	0.1688	0.1506
8	μ_v :	0.2245	0.2204	0.2252	0.2424	0.2212	0.2209	0.2293
	σ_v :	0.1516	0.1511	0.1628	0.1508	0.1644	0.1635	0.167

Estimator no.3

		SNR						
lines		0	3	6	10	16	20	24
24	μ_v :	0.3257	0.3163	0.3237	0.3336	0.3242	0.3251	0.3245
	σ_v :	0.0871	0.0761	0.0785	0.0762	0.0668	0.0674	0.0645
20	μ_v :	0.3259	0.3218	0.3142	0.3197	0.3224	0.3189	0.3213
	σ_v :	0.0732	0.07	0.0634	0.0561	0.0561	0.0561	0.0562
16	μ_v :	0.3152	0.3152	0.3229	0.3173	0.32	0.3193	0.3221
	σ_v :	0.0662	0.0547	0.0592	0.0525	0.0586	0.0565	0.0554
12	μ_v :	0.3108	0.313	0.3165	0.3186	0.3114	0.314	0.3175
	σ_v :	0.0524	0.0512	0.0513	0.0465	0.0457	0.0472	0.0482
8	μ_v :	0.3101	0.3151	0.3106	0.3161	0.3154	0.3138	0.3155
	σ_v :	0.0491	0.048	0.0425	0.0434	0.0463	0.0468	0.044

Estimator no.4

		SNR						
lines		0	3	6	10	16	20	24
24	μ_v :	0.3257	0.3163	0.3052	0.3336	0.3242	0.3251	0.3245
	σ_v :	0.0871	0.0761	0.1187	0.0762	0.0668	0.0674	0.0645
20	μ_v :	0.3259	0.3218	0.3142	0.3197	0.3224	0.3189	0.3213
	σ_v :	0.0732	0.07	0.0634	0.0561	0.0561	0.0561	0.0562
16	μ_v :	0.3152	0.3152	0.3229	0.3173	0.32	0.3193	0.3221
	σ_v :	0.0662	0.0547	0.0592	0.0525	0.0586	0.0565	0.0554
12	μ_v :	0.3108	0.313	0.3165	0.3186	0.3114	0.314	0.3175
	σ_v :	0.0524	0.0512	0.0513	0.0465	0.0457	0.0472	0.0482
8	μ_v :	0.3101	0.3151	0.3106	0.3161	0.3154	0.3138	0.3155
	σ_v :	0.0491	0.048	0.0425	0.0434	0.0463	0.0468	0.044

D.3.4 Angle of 50 degrees

Estimator no.1								
		SNR						
lines		0	3	6	10	16	20	24
24	μ_v :	0.23	0.2527	0.2561	0.2367	0.24	0.2349	0.1971
	σ_v :	0.2493	0.2848	0.2431	0.2361	0.2069	0.2223	0.2799
20	μ_v :	0.199	0.2048	0.1945	0.2411	0.2779	0.2649	0.2581
	σ_v :	0.4042	0.1858	0.3708	0.215	0.1868	0.2138	0.1947
16	μ_v :	0.2981	0.2505	0.2462	0.2556	0.2527	0.2639	0.2573
	σ_v :	0.2393	0.1838	0.1913	0.1854	0.1968	0.2265	0.1949
12	μ_v :	0.3144	0.2783	0.2734	0.2767	0.2623	0.2662	0.2724
	σ_v :	0.1327	0.1012	0.1719	0.1439	0.1607	0.1696	0.1402
8	μ_v :	0.3024	0.2912	0.2838	0.2876	0.2884	0.2861	0.2865
	σ_v :	0.1158	0.1006	0.1027	0.1071	0.0924	0.0922	0.0928

Estimator no.2								
		SNR						
lines		0	3	6	10	16	20	24
24	μ_v :	0.2308	0.2509	0.256	0.2373	0.2408	0.2348	0.1968
	σ_v :	0.2482	0.2885	0.2425	0.2373	0.2073	0.2234	0.2807
20	μ_v :	0.1979	0.2049	0.1955	0.2411	0.2774	0.2648	0.258
	σ_v :	0.4057	0.1851	0.3667	0.2147	0.1866	0.2136	0.1948
16	μ_v :	0.2978	0.2499	0.2469	0.2556	0.2524	0.2635	0.2573
	σ_v :	0.2354	0.1845	0.1911	0.185	0.1964	0.2264	0.1948
12	μ_v :	0.3136	0.2781	0.2738	0.2767	0.2626	0.2657	0.2723
	σ_v :	0.1328	0.1011	0.1723	0.144	0.1604	0.1695	0.1406
8	μ_v :	0.3024	0.2919	0.284	0.2877	0.2887	0.2858	0.2865
	σ_v :	0.1169	0.1004	0.1022	0.1066	0.0928	0.0919	0.0928

Estimator no.3								
		SNR						
lines		0	3	6	10	16	20	24
24	μ_v :	0.315	0.3046	0.3074	0.3082	0.3099	0.302	0.3075
	σ_v :	0.1173	0.1172	0.0887	0.0894	0.0791	0.0797	0.0771
20	μ_v :	0.3064	0.2837	0.3095	0.3002	0.3018	0.3046	0.3022
	σ_v :	0.0984	0.083	0.0756	0.0618	0.0637	0.0601	0.0633
16	μ_v :	0.3048	0.3033	0.3013	0.3044	0.3	0.3017	0.3007
	σ_v :	0.0653	0.0585	0.06	0.0598	0.061	0.0579	0.0601
12	μ_v :	0.3033	0.3006	0.2989	0.2987	0.3044	0.3012	0.2982
	σ_v :	0.0765	0.0538	0.0549	0.0573	0.0524	0.0533	0.0568
8	μ_v :	0.3014	0.2965	0.3082	0.2954	0.3002	0.3004	0.2996
	σ_v :	0.0535	0.0592	0.0535	0.0501	0.0541	0.0521	0.0524

Estimator no.4								
		SNR						
lines		0	3	6	10	16	20	24
24	μ_v :	0.2781	0.2677	0.3074	0.3082	0.3099	0.302	0.3075
	σ_v :	0.1715	0.1742	0.0887	0.0894	0.0791	0.0797	0.0771
20	μ_v :	0.2783	0.2837	0.3095	0.3002	0.3018	0.3046	0.3022
	σ_v :	0.1405	0.083	0.0756	0.0618	0.0637	0.0601	0.0633
16	μ_v :	0.3048	0.3033	0.3013	0.3044	0.3	0.3017	0.3007
	σ_v :	0.0653	0.0585	0.06	0.0598	0.061	0.0579	0.0601
12	μ_v :	0.3033	0.3006	0.2989	0.2987	0.3044	0.3012	0.2982
	σ_v :	0.0765	0.0538	0.0549	0.0573	0.0524	0.0533	0.0568
8	μ_v :	0.3014	0.2965	0.3082	0.2954	0.3002	0.3004	0.2996
	σ_v :	0.0535	0.0592	0.0535	0.0501	0.0541	0.0521	0.0524